JACC
Basic to Translational Science

A Journal of the American College of Cardiology

JACC
Basic to Translational Science

A Journal of the American College of Cardiology

CORRESPONDENCE FOR AMERICAN COLLEGE OF CARDIOLOGY

All correspondence for the College, other than that related to *JACC: Basic to Translational Science* should be sent to Resource Center, American College of Cardiology, 2400 N Street, NW, Washington, DC 20037

JACC: BASIC TO TRANSLATIONAL SCIENCE VOL. 4, NO. 6, 2019

CLINICAL RESEARCH

First-in-Man Study of a Cardiac Extracellular Matrix Hydrogel in Early and Late Myocardial Infarction Patients

Jay H. Traverse, MD,[a] Timothy D. Henry, MD,[b] Nabil Dib, MD,[c] Amit N. Patel, MD,[d] Carl Pepine,[e] Gary L. Schaer, MD,[f] Jessica A. DeQuach, PhD,[g] Adam M. Kinsey, PhD,[g] Paul Chamberlin, MD,[g] Karen L. Christman, PhD[h]

VISUAL ABSTRACT

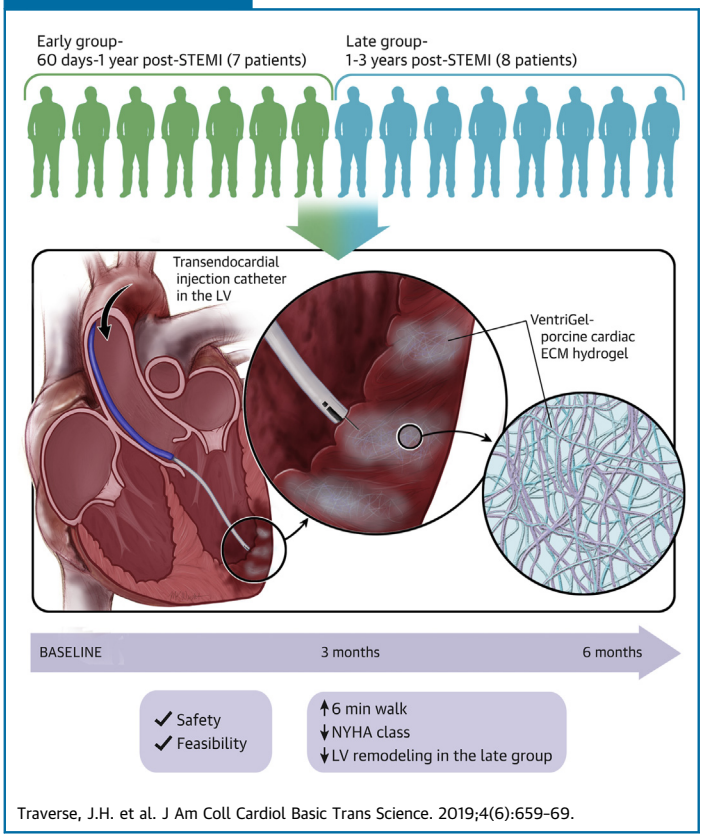

Traverse, J.H. et al. J Am Coll Cardiol Basic Trans Science. 2019;4(6):659-69.

HIGHLIGHTS

- **A first-in-man clinical trial was completed with VentriGel, an extracellular matrix hydrogel derived from decellularized porcine myocardium, in post-MI patients.**
- **Results from the trial support the safety and feasibility of transendocardial injection of VentriGel in post-MI patients with left ventricular dysfunction.**
- **Although the study was not designed to evaluate efficacy, there were suggestions of improvements including increases in 6-min walk test distance and decreases in New York Heart Association functional class across the entire cohort of patients.**
- **Improvements in left ventricular remodeling were mainly observed in patients who were treated >1-year post-MI as opposed to <1 year.**
- **Results from the trial warrant further evaluation in larger randomized, controlled clinical trials.**

ISSN 2452-302X https://doi.org/10.1016/j.jacbts.2019.07.012

ABBREVIATIONS AND ACRONYMS

BNP = B-type natriuretic peptide

CMR = cardiac magnetic resonance

ECM = extracellular matrix

EF = ejection fraction

LV = left ventricular

LVEDV = left ventricular end-diastolic volume

LVESV = left ventricular end-systolic volume

MI = myocardial infarction

MLWHFQ = Minnesota Living with Heart Failure Questionnaire

NYHA = New York Heart Association

SUMMARY

This study evaluated the safety and feasibility of transendocardial injections of VentriGel, a cardiac extracellular matrix hydrogel, in early and late post-myocardial infarction (MI) patients with left ventricular (LV) dysfunction. VentriGel was delivered in 15 patients with moderate LV dysfunction (25% ≤ LV ejection fraction ≤ 45%) who were between 60 days to 3 years post-MI and were revascularized by percutaneous coronary intervention. The primary endpoints were incidence of adverse events and abnormal clinical laboratory results. This first-in-man study established the safety and feasibility of delivering VentriGel in post-MI patients, thus warranting further evaluation in larger, randomized clinical trials. (J Am Coll Cardiol Basic Trans Science 2019;4:659–69)

Over the past 2 decades, there has been extensive interest in using regenerative medicine to treat patients with myocardial infarction (MI) and ischemic heart failure. Although several growth factor and gene therapeutics have been explored, the vast majority of trials have tested different types of stem cells (1). However, tissues are not just comprised of cells but also include a scaffolding framework, the extracellular matrix (ECM). The ECM contains numerous proteins and proteoglycans with a unique tissue-specific composition that provides cues, which influence all aspects of cell behavior necessary for proper tissue function as well as repair (2). After an MI, there is not only cell death but also an inflammatory response and upregulation of matrix metalloproteinases that degrade the native cardiac ECM (3). After the initial inflammation, the area is replaced by a collagen-rich scar. With the goal of replacing this abnormal microenvironment with healthy myocardial ECM cues to facilitate cardiac repair, we developed an injectable, catheter-deliverable hydrogel derived from porcine decellularized myocardial ECM (4). This material can be stored in a lyophilized form and rehydrated with sterile water to form a liquid that gels into a porous and fibrous scaffold upon intramyocardial injection, enabling endogenous cell infiltration and cardiac repair (4,5). In vitro analyses showed the potential of the material to promote recruitment and/or proliferation of vascular cells and stem cells as well as cardiac differentiation of stem cells (4,6–10). In rat MI models, the hydrogel promoted a pro-remodeling instead of a proinflammatory environment, increased neovascularization, and reduced fibrosis. The hydrogel also decreased border zone cardiomyocyte apoptosis, led to a shift in cardiomyocyte metabolism, and increased cardiac muscle leading to improvements in global cardiac function (5,11). In a more translatable porcine MI model, the material increased cardiac muscle, reduced fibrosis, and led to significant improvements in both global and regional function after percutaneous, transendocardial delivery (12). Importantly, preclinical safety studies showed biocompatibility, hemocompatibility, and lack of arrhythmias (5,12). This work motivated testing the material, commercially termed VentriGel (Ventrix, Inc., San Diego, California), in post-MI patients.

Accordingly, we developed a first-in-man, single-arm, multicenter trial to evaluate the safety, feasibility, and preliminary efficacy of percutaneous transendocardial delivery of VentriGel in early and late MI patients with left ventricular (LV) dysfunction. This injectable biomaterial approach represents

From the [a]Minneapolis Heart Institute, Minneapolis, Minnesota; [b]The Carl and Edyth Lindner Center for Research and Education at The Christ Hospital, Cincinnati, Ohio; [c]Dignity Health Mercy Gilbert Medical Center, Gilbert, Arizona; [d]Dewitt Daughtry Family Department of Surgery, Division of Cardiothoracic Surgery, University of Miami, Leonard M. Miller School of Medicine, Miami, Florida; [e]University of Florida College of Medicine, Gainesville, Florida; [f]Division of Cardiology, Rush University Medical Center, Chicago, Illinois; [g]Ventrix, Inc., San Diego, California; and the [h]Department of Bioengineering, Sanford Consortium for Regenerative Medicine, La Jolla, California. This study was supported by Ventrix, Inc., San Diego, California. Drs. Kinsey and Christman and KLC are cofounders of Ventrix, Inc.; Drs. DeQuach, Chamberlin, and Christman are consultants and receive income from Ventrix, Inc.; Drs. Kinsey and Christman are board members of Ventrix, Inc.; Dr. Kinsey is an employee of Ventrix, Inc.; Drs. Dib, DeQuach, Kinsey, and Chamberlin hold equity interest in Ventrix, Inc. Dr. Dib is owner of Tri LLC and UltraNav Medical LLC; and a consultant for BDS and CSI. All other authors have reported that they have no relationships relevant to the contents of this paper to disclose. The authors attest they are in compliance with human studies committees and animal welfare regulations of the authors' institutions and Food and Drug Administration guidelines, including patient consent where appropriate. For more information, visit the *JACC: Basic to Translational Science* author instructions page.

Manuscript received June 20, 2019; revised manuscript received July 26, 2019, accepted July 27, 2019.

an alternative paradigm to cell-based regenerative medicine strategies (13).

METHODS

TRIAL DESIGN AND PATIENT POPULATION. This phase 1 trial was approved by the Food and Drug Administration and the institutional review boards of each participating clinical center. Eligibility for the trial included patients with their first ST-segment elevation MI treated by percutaneous coronary intervention within the past 60 days to 3 years who had moderate LV dysfunction (25% ≤ LV ejection fraction [EF] ≤ 45%). The enrollment criteria were intentionally broad so that we could begin to evaluate the safety and potential efficacy of VentriGel in both early and late MI patients. The primary objective was to investigate the safety and feasibility of a single dose of VentriGel delivered via multiple sequential endomyocardial injections using the MyoStar catheter guided by the NOGA cardiac mapping system (Biologics Delivery Systems, Cordis Corporation, Hialeah, Florida). The primary endpoints were incidence of adverse events and abnormal clinical laboratory results.

The secondary objective was to investigate the preliminary efficacy of VentriGel by measuring the changes in various parameters from baseline to 3 and 6 months after the procedure. The secondary endpoints included evaluation of LV volumes, EF, and scar size by cardiac magnetic resonance (CMR), serum B-type natriuretic peptide (BNP) level, the 6-min walk test distance, quality of life using the Minnesota Living with Heart Failure Questionnaire (MLWHFQ), and New York Heart Association (NYHA) functional classification assessment.

Patients who experienced their first ST-segment elevation MI treated by percutaneous coronary intervention within the past 60 days to 3 years and had an LVEF between 25% and 45% by baseline screening echocardiogram were recruited and enrolled at 6 sites. LVEF was determined by 2-dimensional transthoracic echocardiography performed in accordance with the American Society of Echocardiography guidelines. Key exclusion criteria included sustained ventricular tachycardia, LV thrombus, significant coronary artery stenosis requiring percutaneous or surgical revascularization within 6 months of enrollment, heart failure due to any cause other than index MI, and NYHA functional class IV heart failure in the prior 6 months. Additional details including full inclusion/exclusion criteria are provided in the Supplemental Appendix. An independent safety advisory board was chartered to review safety data after the first 9 patients and ad hoc.

PROCEDURES. VentriGel, an ECM hydrogel derived from decellularized porcine myocardium, was manufactured at a single Good Manufacturing Practice facility and provided to trial sites as lyophilized material in sterile vials and stored frozen. Immediately before the procedure, VentriGel was resuspended in sterile water and loaded into 1-ml syringes for injection. All patients underwent electromechanical mapping with the NOGA XP system (Biosense Webster, Irvine, California). The area of infarct was determined by <6.9 mV univoltage potential. All patients received sequential injections of VentriGel (0.3-ml individual injections up to a total of 18 injections or 5.4 ml) using a MyoStar catheter into the infarct and border zone areas with a wall thickness >8 mm as defined by the screening echocardiogram. Each injection was delivered over 45 s through a 27-gauge needle. A limited echocardiogram was obtained immediately post-injection to rule out pericardial effusion. Patients were routinely discharged at 24 h post-procedure with a cardiac event monitor for 30 days. Patients received a follow-up phone call on day 5 post-discharge; returned for safety visits on days 7 (±2 days), 14 (±2 days), 30 (±2 days), 90 (±4 days), and 180 (±7 days); and received a telephone follow-up at 12 months (±14 days). The 24-h Holter monitoring was performed at screening and at 90 and 180 days. Cardiac MRI was performed according to imaging guidelines provided by the Yale Cardiovascular Research Group at baseline and at 90 and 180 days. The 6-min walk test was performed according to American Thoracic Society guidelines at baseline and at 90 and 180 days. NYHA functional classification and MLWHFQ were obtained at baseline and at 30, 90, and 180 days.

DATA AND STATISTICAL ANALYSIS. Data were recorded in case report forms and monitored against source documentation for accuracy by clinical study monitors. Independent centralized core laboratories (Yale Cardiovascular Research Group, New Haven, Connecticut, and KCRI, Krakow, Poland) provided all MRI image analysis. Statistical analysis was performed with GraphPad Prism version 8.01 (GraphPad Software, La Jolla, California). Categorical variables are summarized by counts and proportions. Descriptive data of continuous variables are summarized using mean and standard error of the mean. Data were compared using a repeated-measures mixed-effects model in Prism. This mixed model uses a compound symmetry covariance matrix and is fit using restricted maximum likelihood. A Geisser-Greenhouse correction was used where sphericity could not be assumed.

TABLE 1 Patient Demographics and Baseline Characteristics

	VentriGel Treatment (N = 15)	Patients <12 Months Post-MI at Treatment (n = 7)	Patients >12 Months Post-MI at Treatment (n = 8)
Age, yrs	59.6 ± 8.8	57.7 ± 10.3	61.3 ± 7.5
Female	3 (20.0)	2 (28.6)	1 (12.5)
White, non-Hispanic	12 (80.0)	6 (85.7)	6 (75.0)
White, Hispanic	1 (6.7)	1 (12.5)	0 (0)
African American	2 (13.3)	0 (0)	2 (28.6)
Body mass index, kg/m^2	30.0 (4.4)	29.1 (4.1)	30.7 (4.7)
Tobacco use			
Former	10 (66.7)	5 (71.4)	5 (62.5)
Current	1 (6.7)	1 (14.3)	0 (0)
Diabetes mellitus	3 (20.0)	2 (28.6)	1 (12.5)
Hypertension	7 (46.7)	4 (57.1)	3 (37.5)
Dyslipidemia	12 (80.0)	4 (57.1)	8 (100)
Previous PCI	15 (100)	7 (100)	8 (100)
Previous CABG	3 (20.0)	0 (0)	3 (37.5)
NYHA functional class			
I	3 (20.0)	1 (14.3)	2 (25.0)
II	11 (73.3)	5 (71.4)	6 (75.0)
III	1 (6.7)	1 (14.3)	0 (0)
Time from MI to injection (months)	15.2 ± 10.6	6.5 ± 2.9	22.8 ± 8.7

Values are mean ± SD or n(%).

CABG = coronary artery bypass grafting; MI = myocardial infarction; NYHA = New York Heart Association; PCI = percutaneous coronary intervention.

FIGURE 1 Changes in Exercise Capacity, Heart Failure Class, and Quality of Life

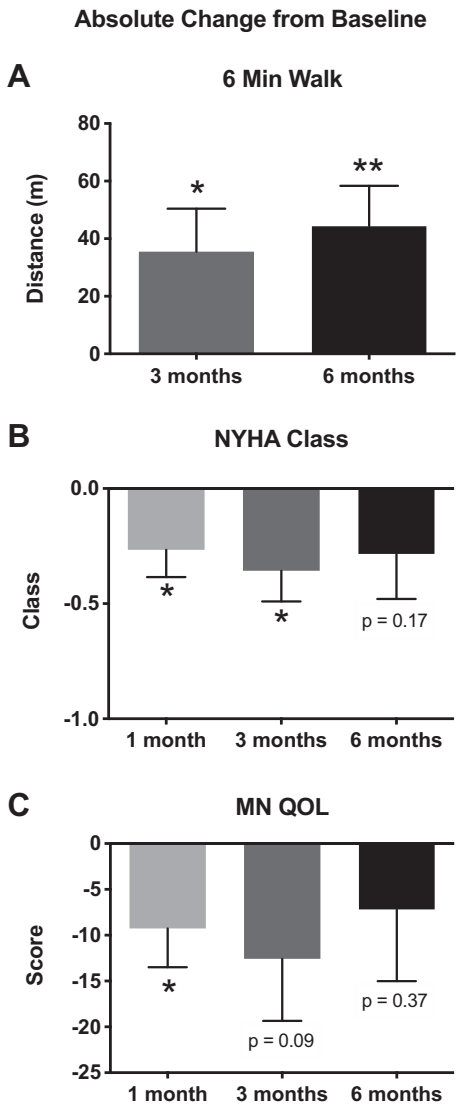

Absolute changes in **(A)** the 6-min walk test distance, **(B)** NYHA functional class, and **(C)** Minnesota Living With Heart Failure Questionnaire (MNLWHFQ) score from baseline to follow-up visits are shown for the total cohort. The p value is for the paired Student's t-test between follow-up and baseline. *p < 0.05. **p < 0.01. MN = Minnesota; NYHA = New York Heart Association; QOL = quality of life.

Each follow-up time point was compared with baseline with a paired Student's *t*-test. Significance was accepted at $p < 0.05$. Given the small, exploratory nature of this study, there were no adjustments for multiple comparisons.

RESULTS

PATIENTS. All patients gave written informed consent; 22 patients were consented and screened, and 15 patients were subsequently enrolled between September 2015 and July 2017 (Supplemental Table 1). The majority of patients were men (n = 12) and had Class II heart failure (n = 11). Age ranged from 45 to 69 years, and other pertinent baseline characteristics are summarized in **Table 1**. Concomitant medications are listed in Supplemental Table 2. VentriGel was delivered between 3 and 35.5 months post-MI. Enrolled patients were divided with approximately one-half of the patients treated <12 months post-MI and one-half of the patients treated >12 months post-MI (**Table 1**). Thirteen of the 15 patients received all 18 injections. The 2 remaining patients received 15 and 16 injections due to injection requirement restrictions such as wall thickness minimum.

SAFETY. Overall, VentriGel was well tolerated, and there were no deaths or patients who discontinued from the study. No adverse event was reported as definitely related to VentriGel (Supplemental Table 3) or the mapping/injection procedure. One major adverse cardiac event, cardiogenic shock, and 1 moderate event, complete heart block, both in the first patient treated were reported as possibly related for study treatment. This patient's history included trifascicular block, which was added as an exclusion

FIGURE 2 **Changes in Exercise Capacity, Heart Failure Class, and Quality of Life in Early and Late MI Patients**

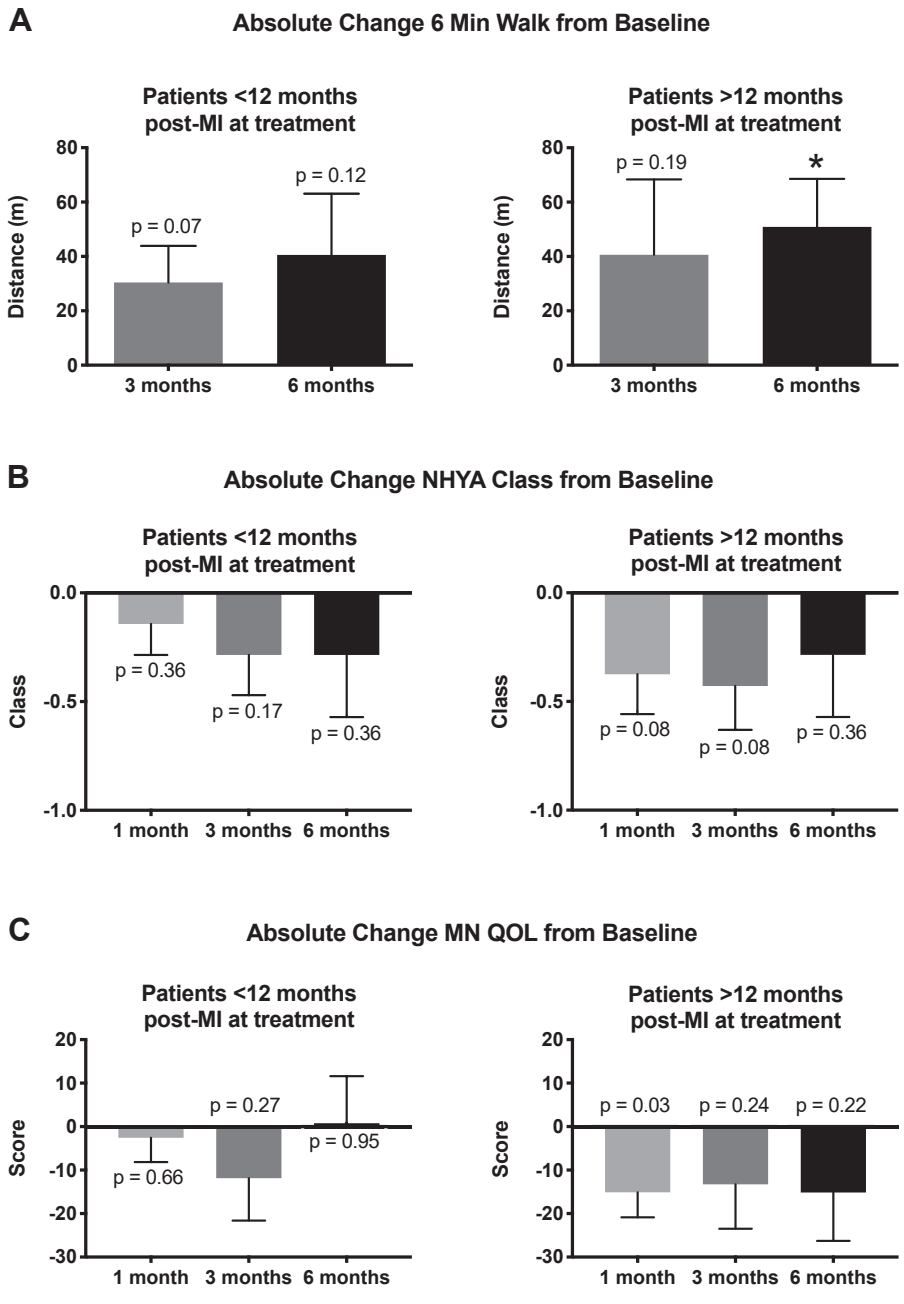

Absolute changes in **(A)** the 6-min walk test distance, **(B)** NYHA functional class, and **(C)** MNLWHFQ score from baseline to follow-up visits are shown for patients <12 months post-MI and >12 months post-MI at treatment. The p value is for the paired Student's *t*-test between follow-up and baseline. *p < 0.05. MI = myocardial infarction; other abbreviation as in Figure 1.

criterion based on recommendations by the safety advisory board for the final 13 patients. One intracardiac thrombus was reported as possible for the mapping/injection procedure. No significant ventricular arrhythmias were found by Holter monitoring. One episode of nonsustained ventricular tachycardia was reported as not related to VentriGel. There were no clinically meaningful changes in the clinical laboratory results. As expected by the injection procedure, a small, nonsignificant increase in C-reactive

FIGURE 3 MRI Parameters

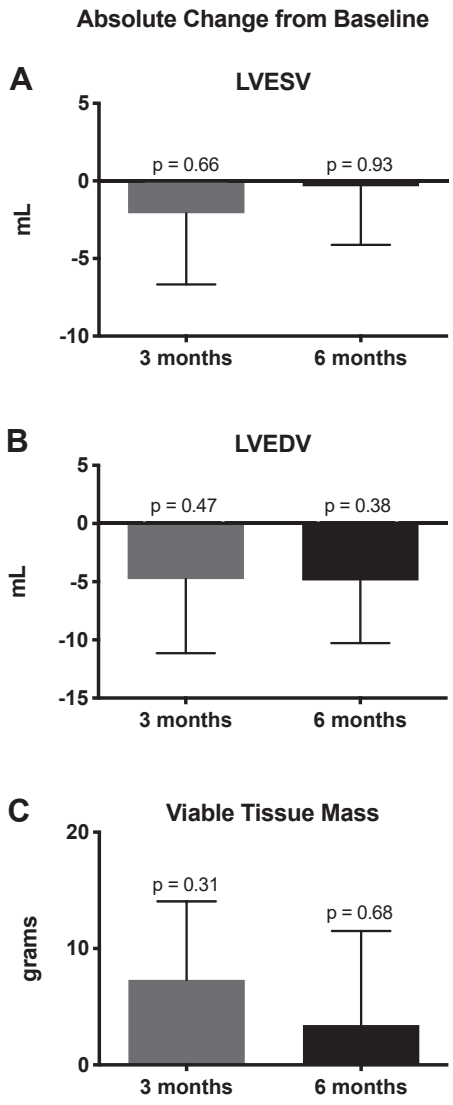

Absolute changes in **(A)** LVESV, **(B)** LVEDV, and **(C)** viable mass from baseline to follow-up visits are shown for the total cohort. The p value is for the paired Student's *t*-test between follow-up and baseline. LVEDV = left ventricular end-diastolic volume; LVESV = left ventricular end-systolic volume; MRI = magnetic resonance imaging.

protein was observed 1 day after the injection procedure but not at other time points (Supplemental Table 4).

EFFICACY SIGNS. A 6-min walk test was evaluated at baseline and 3- and 6-month follow-up visits as a measure of functional exercise capacity. In the total cohort, treatment with VentriGel significantly increased the maximum walk distance with time post-injection ($p = 0.004$) at 3 and 6 months. The walk distance was significantly greater than at baseline with average changes of +35.6 m ($p = 0.033$) and +44.4 m ($p = 0.007$), respectively (**Figure 1A**, Supplemental Figure 1A, Supplemental Table 5). This corresponded to improvements in NYHA functional class and the MLWHFQ quality of life score. NYHA functional class significantly decreased at 1-month post-treatment ($p = 0.041$), and this overall decrease was similar at 3 and 6 months (**Figure 1B**, Supplemental Figure 1B, Supplemental Table 6). The MLWHFQ score likewise significantly decreased at 1 month ($p = 0.045$), and a similar decrease was observed at 3 and 6 months but was nonsignificant (**Figure 1C**, Supplemental Figure 1C, Supplemental Table 6). Improvements in the walk distance (**Figure 2A**, Supplemental Figure 2A), NYHA functional class (**Figure 2B**, Supplemental Figure 2B), and the MLWHFQ score (**Figure 2C**, Supplemental Figure 2C) tended to be better in the late MI subset (>12 months post-MI) versus the early MI subset (<12 months post-MI).

Cardiac function was evaluated using MRI at baseline and at the 3- and 6-month follow-up visits. Thirteen of 15 patients were evaluated at 3 months, and 14 of 15 patients were evaluated at 6 months. In the 14 patients who were evaluated with MRI at 6 months, 11 patients had maintained or decreased LV end-diastolic volume (LVEDV) or LV end-systolic volume (LVESV) compared with baseline at the final follow-up. Although numerical averages for the total cohort decreased (**Figure 3**, Supplemental Figure 3), post hoc analysis revealed that decreases in LV volumes occurred predominantly in the late MI subset (>12 months post-MI) versus the early MI subset (<12 months post-MI) (**Figures 4A and 4B**, Supplemental Figures 4A and 4B, Supplemental Table 7). At 6 months, both LVESV and LVEDV decreased by approximately 8 ml ($p = 0.051$ and $p = 0.280$, respectively) in those patients treated >12 months post-MI. Similarly, changes in viable mass were more notable in the late MI population (**Figure 4C**, Supplemental Figure 4C, Supplemental Table 7). No major changes were observed in EF or scar size (Supplemental Table 7). The first treated patient received a pacemaker, which prevented follow-up MRI analysis; however, echocardiography was performed at 3 and 6 months and analyzed by the core laboratories. This patient's EF increased from 40.6% at baseline to 44.6% and 46.9% at 3 and 6 months, respectively. LV diameters likewise improved compared with baseline. The LV end-systolic diameter decreased from 4.16 cm at baseline to 4.15 cm and 4.13 cm at 3 and 6 months, respectively, whereas the LV end-diastolic diameter

FIGURE 4 MRI Parameters in Early and Late MI Patients

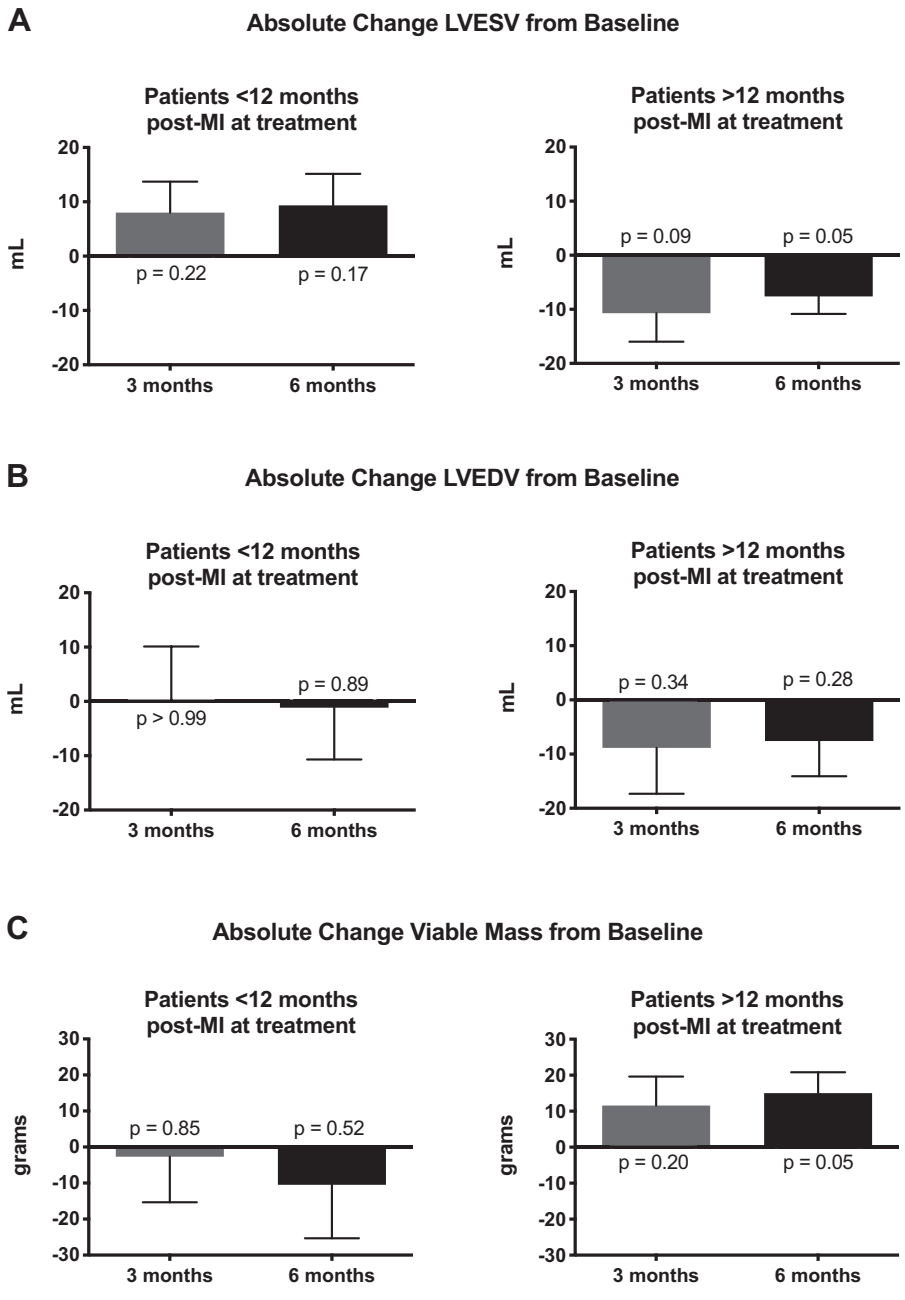

Absolute changes in **(A)** LVESV, **(B)** LVEDV, and **(C)** viable mass from baseline to follow-up visits are shown for patients <12 months post-MI and >12 months post-MI at treatment. The p value is for the paired Student's *t*-test between follow-up and baseline. Abbreviations as in Figures 2 and 3.

decreased from 5.23 cm at baseline to 4.80 cm and 5.01 cm at 3 and 6 months, respectively.

BNP decreased by approximately 5% and 12% at 3 and 6 months in the 13 patients with follow-up, although this was not significant (**Figure 5A**, Supplemental Figure 5A, Supplemental Table 8). Similar to LV volumes, those in the late MI subset (>12 months post-MI) had the greatest decreases in BNP (**Figures 5B and 5C**, Supplemental Figures 5B and 5C).

FIGURE 5 BNP

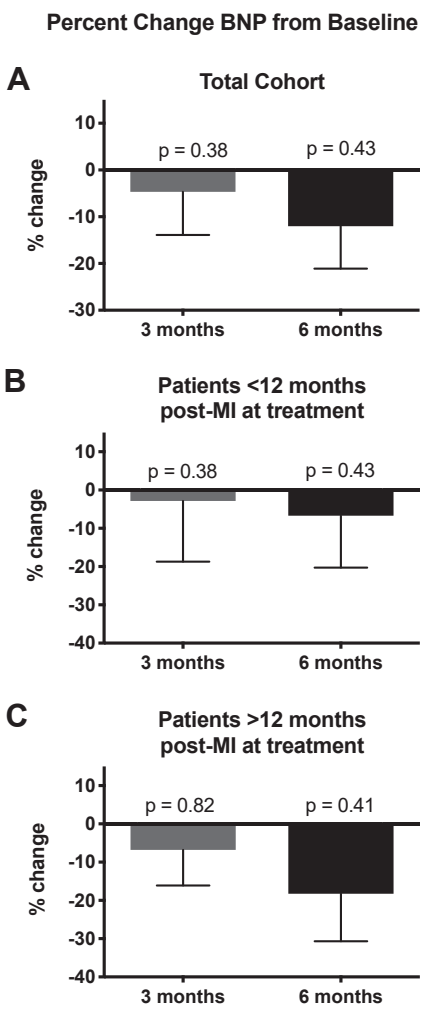

Percent changes in BNP from baseline to follow-up visits are shown for the **(A)** total cohort and patients **(B)** <12 months and **(C)** >12 months post-MI at treatment. The p value is for the paired Student's *t*-test between follow-up and baseline. BNP = B-type natriuretic peptide; other abbreviation as in Figure 2.

DISCUSSION

To the best of our knowledge, this study is the first clinical trial to evaluate an injectable biomaterial delivered via percutaneous transendocardial injections for cardiac repair. We observed findings that support the initial safety and feasibility of injecting VentriGel, an ECM hydrogel derived from porcine myocardium, in post-MI patients with LV dysfunction. The trial was also the first demonstration of using a decellularized ECM hydrogel in any tissue in patients.

The concept of injectable biomaterials for treating MI was first introduced in the early 2000s (14–17). At that time, it was postulated that an injectable biomaterial may improve cardiac function by acting as an internal wall support to increase infarct wall thickness. Other materials were developed based on this hypothesis, including 2 alginate-based materials (polysaccharide hydrogels derived from seaweed) that were evaluated in clinical trials. Algisyl-LVR (LoneStar Heart, Inc., Laguna Hills, California) was delivered via surgical-based epicardial injections in patients with heart failure with both ischemic and nonischemic etiologies, whereas BL-1040/IK-5001 (Bellerophon Therapeutics, Warren, New Jersey) was delivered via intracoronary infusion in patients with acute MI (18,19). In phase 2 studies, Algisyl-LVR significantly improved exercise capacity but not measures of LV remodeling (20,21), and IK-5001 likewise failed to reduce progressive LV remodeling (22). Later preclinical studies have shown that passively supporting the infarct wall does not improve long-term cardiac function and suggest that the cell and tissue response to injected biomaterials play a dominant role in cardiac remodeling (23,24). VentriGel is a relatively weak hydrogel, about 2 orders of magnitude lower than the stiffness of healthy myocardium (25), and therefore would not be expected to act as a mechanical support; rather, it was designed to be delivered via a catheter and upon injection assemble into an open porous and fibrous scaffold to allow for endogenous cells to repopulate and remodel the matrix. By acting as a new physical scaffold with appropriate pore size and fiber dimeter as well as containing the ECM cues of normal, healthy myocardium, the goal was to recreate a new microenvironment in the heart. Therefore, this trial was the first to evaluate a proreparative hydrogel in the heart.

Although numerous injectable biomaterials have now been evaluated in preclinical studies in MI and heart failure models, few have actually been delivered via a catheter because this poses unique material design constraints (26,27). The quick gelling nature, high viscosity, and/or lack of hemocompatibility prevent the majority of injectable biomaterials from this type of minimally invasive delivery modality. VentriGel was specifically designed to have the appropriate viscosity and gelation kinetics to facilitate transendocardial delivery, and extensive preclinical safety studies have shown hemocompatibility and a lack of arrhythmias (5,12). This study demonstrated the safety and feasibility of transendocardial delivery of VentriGel in post-MI patients with 15 to 18 injections being performed in all patients and without

serious adverse events observed to be definitely related to material or mapping/injection procedure. The first patient, whose pre-treatment history included a trifascicular block, had 2 adverse events (cardiogenic shock and heart block) that were deemed as possibly related to the study treatment; however, this patient improved in measures of LV remodeling (as determined by echocardiography), the 6-min walk test distance, and BNP levels at 3 and 6 months. Based on the safety advisory board's review, modest changes to the inclusion criteria (around arrhythmias) and additional early visits to the clinical site 1-week post-treatment were added to the study for the remaining 13 patients who were enrolled. No such serious adverse events were subsequently observed.

Although this phase 1 study was not designed to evaluate efficacy, there were suggestions of improvements including increases in the 6-min walk test distance and decreases in NYHA functional class across the entire cohort of patients. Enrollment criteria were set between 60 days and 3 years because it was unknown whether VentriGel would be more effective in earlier- versus later-stage MI patients. Therefore, 1 goal of this study was to inform the appropriate patient population to enroll in future studies. Post hoc analysis revealed that improvements in LV remodeling data, viable mass, and BNP levels were mainly observed in patients who had their MI >12 months before treatment. The lack of observed improvements in early MI patients (<12 months post-MI) may be a result of a more variate baseline in these patients as the infarct and peri-infarct regions recover from ischemic injury. In patients, infarct remodeling is typically thought to occur over the first several months, although studies have suggested that the dynamic time period of infarct healing is, in fact, a longer process (28,29). Overall, there were few increases in cardiac medications, and those that did occur were in the early subset of patients. No discernable changes were noted in EF, although this is not surprising given that parallel changes in LVEDV and LVESV can result in calculation of the same EF; this phenomenon has been observed in other heart failure trials (30,31). The suggested improvements in patients treated >12 months post-MI largely mirror results across the small and large animal preclinical studies with VentriGel in which the most notable changes were in LVESV and increases in cardiac muscle. In these later patients, there were trending decreases in LVESV and increases in viable mass at 6 months after treatment. In a rat MI model, analysis of gene expression in the infarct wall using whole transcript microarrays showed changes in several tissue processes that suggests the hydrogel creates a new template for healing in the infarct (11). After injection, the fibrous and porous nature facilitates endogenous cell infiltration; over approximately 3 weeks, host cells remodel the temporary matrix similar to a healing wound (12). Altered pathways included blood vessel and cardiac development. Other shifts included a decrease in cell death, an altered inflammatory response, reduced cardiomyocyte hypertrophy, reduced fibrosis, and an altered myocardial metabolism (11). Although these studies were performed in a subacute MI model, we anticipate that in the later chronic MI patients, VentriGel is likely acting through similar pathways. In patients with ischemic cardiomyopathy, cardiomyocyte apoptosis continues to occur through the stages of acute MI, subacute MI, and all the way to end-stage heart failure (32). Moreover, cardiac metabolism is dysregulated in patients with heart failure (33), and it is now known that the collagen scar is, in fact, a dynamic tissue with collagen turnover and myofibroblasts, which are present for years in patients and continue to generate fibrogenic signals (34).

Although initial attempts at regenerative medicine for the heart focused on cell transplantation, there has been increasing focus in preclinical studies on biomaterials or matrix-based approaches to recreate a more appropriate microenvironment for tissue repair (35). In both cardiovascular and noncardiovascular applications, translation of biomaterial-alone therapies to facilitate endogenous repair is recently on this rise (13). Overall, these technologies, such as VentriGel, have significant advantages over the traditional regenerative medicine paradigm. For example, they can be off-the-shelf and cost-effective and do not have the burdens associated with supplying a living product. In the case of VentriGel, the cost of manufacturing is at least 2 orders of magnitude less than cell therapies, and, therefore, it could be a scalable and potentially cost-effective treatment for heart failure.

STUDY LIMITATIONS. The major limitation of this phase 1 study is that it was an uncontrolled, single-arm trial with a small number of patients not powered to evaluate efficacy. A single-arm trial was performed in this first-in-man study because of the difficulty of applying a transendocardial injection procedure in a control group, especially in earlier MI patients where there is less evidence of safety. Moreover, VentriGel is regulated as a device in Europe and Japan given that it acts as a new physical

scaffold to enable cell infiltration, and early device trials do not typically include a control group. Another limitation is that the patients' MIs spanned a relatively large post-infarction time period when the biologic response to VentriGel may vary. Thus, the optimum time to deliver VentriGel remains to be determined and will require a larger trial. However, the beneficial response of patients whose infarcts were >12 months appears to be an encouraging starting point going forward. Importantly, the study used state-of-the-art MRI imaging rather than echocardiography, which helped reduce variability. Because injections were limited to wall thickness of >8 mm, we were frequently precluded from injecting into the infarct zone as was performed in the preclinical porcine studies (12).

CONCLUSIONS

These results support the safety and feasibility of transendocardial injection of VentriGel in post-MI patients with LV dysfunction and introduces a new potential treatment for patients with heart failure. This trial was novel in many regards including the first injectable biomaterial to be delivered in patients using transendocardial injections, translation of the first proreparative hydrogel for the heart, and translation of the first decellularized ECM hydrogel in any tissue. As such, the significance of this trial reaches beyond the cardiac field because there have been numerous preclinical studies evaluating decellularized ECM hydrogels in various applications in other tissues (36). Although there is a long precedence of using porcine-derived materials, including decellularized ECM patches (37), this trial was the first to test an injectable hydrogel form of decellularized ECM in patients and therefore provides important safety and feasibility data and opens up the possibility of using ECM hydrogels in many other applications. Importantly, this study also provides support for the safety and feasibility of treating post-MI patients with VentriGel and warrants further evaluation in larger randomized clinical trials.

ACKNOWLEDGMENTS The authors thank the patients that participated in this study. They thank Kelly Wilson, Tracey Early, Marilyn Mendez, Carlyn Sander, Matthew Brobeck, Jennifer Vermillion, Nusrat Jahan, Kelli Jones, Nicole Bostick, and Sarah Long for assistance with recruitment and follow-up of patients. They also thank Warren Sherman and Anthony DeMaria for thoughtful advice regarding the clinical trial design.

ADDRESS FOR CORRESPONDENCE: Dr. Karen L. Christman, Department of Bioengineering, Sanford Consortium for Regenerative Medicine, 2880 Torrey Pines Scenic Drive, La Jolla, California 92037. E-mail: christman@eng.ucsd.edu. OR Dr. Jay H. Traverse, Minneapolis Heart Institute, 920 East 28th Street, Suite 300, Minneapolis, Minnesota 55407. E-mail: trave004@umn.edu.

PERSPECTIVES

COMPETENCY IN MEDICAL KNOWLEDGE: Initial safety and feasibility of percutaneous transendocardial injections of VentriGel, a porcine-derived decellularized ECM hydrogel, was established in post-MI patients with potential effects on LV remodeling in patients >12 months post-MI.

TRANSLATIONAL OUTLOOK: Larger randomized controlled trials should be performed to further evaluate the safety and efficacy of transendocardial injections of VentriGel in post-MI patients.

REFERENCES

1. Perin EC, Miller L, Taylor DA, Willerson JT, editors. Stem Cell and Gene Therapy for Cardiovascular Disease. Cambridge, MA: Academic Press, 2016.

2. Swinehart IT, Badylak SF. Extracellular matrix bioscaffolds in tissue remodeling and morphogenesis. Dev Dyn 2016;245:351–60.

3. Mann DL. Mechanisms and models in heart failure: a combinatorial approach. Circulation 1999;100:999–1008.

4. Singelyn JM, DeQuach JA, Seif-Naraghi SB, Littlefield RB, Schup-Magoffin PJ, Christman KL. Naturally derived myocardial matrix as an injectable scaffold for cardiac tissue engineering. Biomaterials 2009;30:5409–16.

5. Singelyn JM, Sundaramurthy P, Johnson TD, et al. Catheter-deliverable hydrogel derived from decellularized ventricular extracellular matrix increases endogenous cardiomyocytes and preserves cardiac function post-myocardial infarction. J Am Coll Cardiol 2012;59:751–63.

6. DeQuach JA, Mezzano V, Miglani A, et al. Simple and high yielding method for preparing tissue specific extracellular matrix coatings for cell culture. PLoS One 2010;5:e13039.

7. French KM, Boopathy AV, DeQuach JA, et al. A naturally derived cardiac extracellular matrix enhances cardiac progenitor cell behavior in vitro. Acta Biomater 2012;8:4357–64.

8. French KM, Maxwell JT, Bhutani S, et al. Fibronectin and cyclic strain improve cardiac progenitor cell regenerative potential in vitro. Stem Cells Int 2016;2016:8364382.

9. Gaetani R, Yin C, Srikumar N, et al. Cardiac derived extracellular matrix enhances cardiogenic properties of human cardiac progenitor cells. Cell Transplant 2016;25:1653–63.

10. Bejleri D, Streeter BW, Nachlas AL, et al. A bioprinted cardiac patch composed of cardiac-specific extracellular matrix and progenitor cells for heart repair. Adv Healthc Mater 2018;7:e1800672.

11. Wassenaar JW, Gaetani R, Garcia JJ, et al. Evidence for mechanisms underlying the functional

benefits of a myocardial matrix hydrogel for post-MI treatment. J Am Coll Cardiol 2016;67:1074–86.

12. Seif-Naraghi SB, Singelyn JM, Salvatore MA, et al. Safety and efficacy of an injectable extracellular matrix hydrogel for treating myocardial infarction. Sci Transl Med 2013;5:173ra25.

13. Christman KL. Biomaterials for tissue repair. Science 2019;363:340–1.

14. Christman KL, Fok HH, Sievers RE, Fang Q, Lee RJ. Fibrin glue alone and skeletal myoblasts in a fibrin scaffold preserve cardiac function after myocardial infarction. Tissue Eng 2004;10:403–9.

15. Christman KL, Vardanian AJ, Fang Q, Sievers RE, Fok HH, Lee RJ. Injectable fibrin scaffold improves cell transplant survival, reduces infarct expansion, and induces neovasculature formation in ischemic myocardium. J Am Coll Cardiol 2004;44:654–60.

16. Christman KL, Lee RJ. Biomaterials for the treatment of myocardial infarction. J Am Coll Cardiol 2006;48:907–13.

17. Rane AA, Christman KL. Biomaterials for the treatment of myocardial infarction a 5-year update. J Am Coll Cardiol 2011;58:2615–29.

18. Frey N, Linke A, Suselbeck T, et al. Intracoronary delivery of injectable bioabsorbable scaffold (IK-5001) to treat left ventricular remodeling after ST-elevation myocardial infarction: a first-in-man study. Circ Cardiovasc Interv 2014;7:806–12.

19. Lee RJ, Hinson A, Bauernschmitt R, et al. The feasibility and safety of Algisyl-LVR as a method of left ventricular augmentation in patients with dilated cardiomyopathy: initial first in man clinical results. Int J Cardiol 2015;199:18–24.

20. Anker SD, Coats AJ, Cristian G, et al. A prospective comparison of alginate-hydrogel with standard medical therapy to determine impact on functional capacity and clinical outcomes in patients with advanced heart failure (AUGMENT-HF trial). Eur Heart J 2015;36:2297–309.

21. Mann DL, Lee RJ, Coats AJ, et al. One-year follow-up results from AUGMENT-HF: a multicentre randomized controlled clinical trial of the efficacy of left ventricular augmentation with Algisyl in the treatment of heart failure. Eur J Heart Fail 2016;18:314–25.

22. Rao SV, Zeymer U, Douglas PS, et al. Bioabsorbable intracoronary matrix for prevention of ventricular remodeling after myocardial infarction. J Am Coll Cardiol 2016;68:715–23.

23. Rane AA, Chuang JS, Shah A, et al. Increased infarct wall thickness by a bio-inert material is insufficient to prevent negative left ventricular remodeling after myocardial infarction. PLoS One 2011;6:e21571.

24. McGarvey JR, Pettaway S, Shuman JA, et al. Targeted injection of a biocomposite material alters macrophage and fibroblast phenotype and function following myocardial infarction: relation to left ventricular remodeling. J Pharmacol Exp Ther 2014;350:701–9.

25. Johnson TD, Lin SY, Christman KL. Tailoring material properties of a nanofibrous extracellular matrix derived hydrogel. Nanotechnology 2011;22:494015.

26. Johnson TD, Christman KL. Injectable hydrogel therapies and their delivery strategies for treating myocardial infarction. Expert Opin Drug Deliv 2013;10:59–72.

27. Hernandez MJ, Christman KL. Designing acellular injectable biomaterial therapeutics for treating myocardial infarction and peripheral artery disease. JACC Basic Transl Sci 2017;2:212–26.

28. Schroeder AP, Houlind K, Pedersen EM, Nielsen TT, Egeblad H. Serial cardiac magnetic resonance of global and regional left ventricular remodeling during 1 year after acute myocardial infarction. Cardiology 2001;96:106–14.

29. Pokorney SD, Rodriguez JF, Ortiz JT, Lee DC, Bonow RO, Wu E. Infarct healing is a dynamic process following acute myocardial infarction. J Cardiovasc Magn Reson 2012;14:62.

30. Jessup M, Greenberg B, Mancini D, et al. Calcium Upregulation by Percutaneous Administration of Gene Therapy in Cardiac Disease (CUPID): a phase 2 trial of intracoronary gene therapy of sarcoplasmic reticulum Ca2+-ATPase in patients with advanced heart failure. Circulation 2011;124:304–13.

31. Perin EC, Borow KM, Silva GV, et al. A phase II dose-escalation study of allogeneic mesenchymal precursor cells in patients with ischemic or nonischemic heart failure. Circ Res 2015;117:576–84.

32. Abbate A, Biondi-Zoccai GG, Baldi A. Pathophysiologic role of myocardial apoptosis in post-infarction left ventricular remodeling. J Cell Physiol 2002;193:145–53.

33. Rowe GC, Jiang A, Arany Z. PGC-1 coactivators in cardiac development and disease. Circ Res 2010;107:825–38.

34. Sun Y, Weber KT. Infarct scar: a dynamic tissue. Cardiovasc Res 2000;46:250–6.

35. Taylor DA, Chandler AM, Gobin AS, Sampaio LC. Maximizing cardiac repair: should we focus on the cells or on the matrix? Circ Res 2017;120:30–2.

36. Spang MT, Christman KL. Extracellular matrix hydrogel therapies: in vivo applications and development. Acta Biomater 2018;68:1–14.

37. Badylak SF. The extracellular matrix as a biologic scaffold material. Biomaterials 2007;28:3587–93.

KEY WORDS biomaterial, catheter, heart failure, injectable, myocardial infarction

APPENDIX For supplemental material, please see the online version of this paper.

JACC: BASIC TO TRANSLATIONAL SCIENCE VOL. 4, NO. 6, 2019

PRECLINICAL RESEARCH

Quantification of DNA Damage in Heart Tissue as a Novel Prediction Tool for Therapeutic Prognosis of Patients With Dilated Cardiomyopathy

Toshiyuki Ko, MD, PhD,[a,*] Kanna Fujita, MD,[a,*] Seitaro Nomura, MD, PhD,[a,*] Yukari Uemura, PhD,[b] Shintaro Yamada, MD,[a] Takashige Tobita, MD,[c] Manami Katoh, MD, PhD,[d] Masahiro Satoh, MD, PhD,[e] Masamichi Ito, MD, PhD,[a] Yukako Domoto, MD, PhD,[f] Yumiko Hosoya, MD, PhD,[a] Eisuke Amiya, MD, PhD,[a] Masaru Hatano, MD, PhD,[a] Hiroyuki Morita, MD, PhD,[a] Masashi Fukayama, MD, PhD,[f] Hiroyuki Aburatani, MD, PhD,[d] Issei Komuro, MD, PhD[a]

VISUAL ABSTRACT

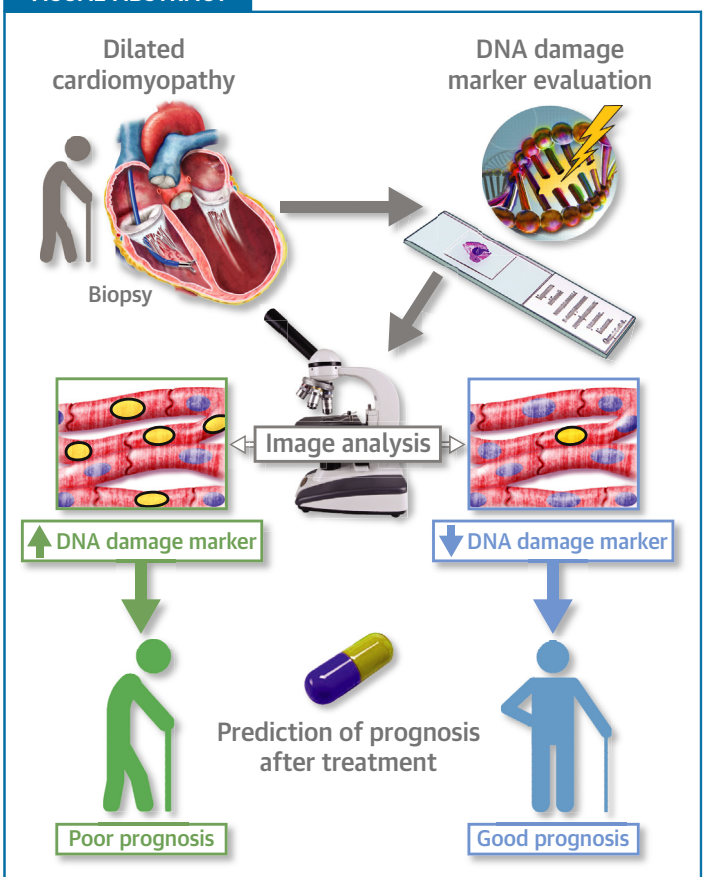

Ko, T. et al. J Am Coll Cardiol Basic Trans Science. 2019;4(6):670–80.

ISSN 2452-302X https://doi.org/10.1016/j.jacbts.2019.05.010

HIGHLIGHTS

- **Patients with dilated cardiomyopathy who achieved LVRR have a favorable prognosis, but it is still difficult to precisely predict LVRR in the clinical setting.**
- **Immunostaining of DNA damage markers such as PAR in biopsy specimens from patients with dilated cardiomyopathy revealed that patients with LVRR showed a significantly smaller proportion of PAR-positive nuclei compared with those without LVRR.**
- **The high proportion of PAR-positive nuclei was an independent prognostic factor for LVRR. Besides, it can predict clinical prognosis (death, heart transplantation, and ventricular assist device implantation) with good sensitivity and specificity.**

ABBREVIATIONS AND ACRONYMS

BMI = body mass index

BNP = B-type natriuretic peptide

CI = confidence interval

DAPI = 4′,6-diamidino-2-phenylindole

DCM = dilated cardiomyopathy

IQR = interquartile range

LVAD = left ventricular assist device

LVEF = left ventricular ejection fraction

LVRR = left ventricular reverse remodeling

NYHA = New York Heart Association

ROC = receiver-operating characteristic

PAR = poly(ADP-ribose)

WGA = wheat germ agglutinin

SUMMARY

This study evaluated myocardial nuclear staining for the DNA damage markers poly(ADP-ribose) (PAR) and γ-H2A.X in 58 patients with dilated cardiomyopathy. Patients with left ventricular reverse remodeling (LVRR) showed a significantly smaller proportion of PAR-positive nuclei and γ-H2A.X-positive nuclei in biopsy specimens compared with those without LVRR. Propensity analysis showed that the proportion of both PAR-positive and γ-H2A.X-positive nuclei were independent prognostic factors for LVRR. In conclusion, we showed the utility of DNA damage-marker staining to predict the probability of LVRR, thus revealing a novel prognostic predictor of medical therapy for dilated cardiomyopathy.

Heart failure is a global problem, with an estimated prevalence of 38 million patients worldwide, and a major cause of morbidity and mortality despite advances in cardiovascular therapy throughout the past decades (1,2). Among the various etiologies of heart failure, dilated cardiomyopathy (DCM) is a common cause. DCM is typically diagnosed by left ventricular dilation and impaired systolic function without any known cause (e.g., pressure overload or coronary artery disease) sufficient to explain the myocardial dysfunction (3). Common pharmacological and device therapies such as β-blockers, renin-angiotensin-aldosterone system inhibitors, and cardiac resynchronization therapy induce left ventricular reverse remodeling (LVRR), characterized by a decrease in left ventricular volume and improvement in systolic function in a certain population of patients with DCM (4). In many clinical trials studying patients with DCM, mortality rates decreased with increasing left ventricular ejection fraction (LVEF) and decreasing left ventricular end-diastolic and end-systolic volumes (4–6).

The potential for left ventricular recovery is probably intrinsically conserved in the setting of cardiac

From the [a]Department of Cardiovascular Medicine, Graduate School of Medicine, University of Tokyo, Tokyo, Japan; [b]Biostatistics Division, Clinical Research Support Center, University of Tokyo Hospital, Tokyo, Japan; [c]Department of Cardiology, Tokyo Women's Medical University, Tokyo, Japan; [d]Genome Science Division, Research Center for Advanced Science and Technology, University of Tokyo, Tokyo, Japan; [e]Department of Cardiovascular Medicine, Graduate School of Medicine, Chiba University, Chiba, Japan; and the [f]Department of Pathology, Graduate School of Medicine, University of Tokyo, Tokyo, Japan. *Drs. Ko, Fujita, and Nomura contributed equally to this paper and are joint first authors. This work was supported by grants from a Grant-in-Aid for Young Scientists (to Dr. Ko), the Japan Foundation for Applied Enzymology (to Dr. Nomura), the SENSHIN Medical Research Foundation (to Dr. Nomura), the KANAE Foundation for the Promotion of Medical Science (to Dr. Nomura), MSD Life Science Foundation (to Dr. Nomura), The Tokyo Biomedical Research Foundation (to Dr. Nomura), Astellas Foundation for Research on Metabolic Disorders (to Dr. Nomura), The NOVARTIS Foundation (Japan) for the Promotion of Science (to Dr. Nomura), the Japanese Circulation Society (to Dr. Nomura), a Grant-in-Aid for Scientific Research (B) (to Dr. Nomura), a Grant-in-Aid for Scientific Research (A) (to Dr. Komuro), and AMED (JP19ek0210118, JP19gm6210010, JP19bm0804010, JP19gm0810013, JP19km0405209, JP19bm0704026, JP19ek0109406) (to Drs. Ko, Nomura, Aburatani, and Komuro). The authors have reported that they have no relationships relevant to the contents of this paper to disclose.

The authors attest they are in compliance with human studies committees and animal welfare regulations of the authors' institutions and Food and Drug Administration guidelines, including patient consent where appropriate. For more information, visit the *JACC: Basic to Translational Science* author instructions page.

Manuscript received March 7, 2019; revised manuscript received May 27, 2019, accepted May 28, 2019.

JACC: BASIC TO TRANSLATIONAL SCIENCE VOL. 4, NO. 6, 2019
OCTOBER 2019:670–80

dysfunction, and even in the presence of apparently severe myocardial dysfunction (7). However, the recovery of left ventricular function is not universal, occurring in only about 40% of patients with DCM (4,5). Therefore, a major unmet need in the clinical setting is the identification of patients who retain this potential for heart function recovery. Even in the United States, a shortage of donor hearts is a critical problem. Over the past 2 decades, there have been increasingly long waiting times for heart transplantation because the number of available hearts has decreased substantially, from 38% in 2000 to 32% in 2010 (8). In Japan, DCM is the primary cause of end-stage heart failure requiring heart transplantation. The waiting time for patients is much longer in Japan than in other countries, and a substantial proportion of patients die while on the waiting list. If we can anticipate the patients unlikely to achieve remodeling, then these patients can be preferentially referred for mechanical circulatory support and heart transplantation at an earlier stage. The long-term management and prognostic stratification of patients with DCM would benefit from the identification of reliable clinical predictors of LVRR to optimize the treatment strategy and improve patient prognosis.

SEE PAGE 681

Many studies have attempted to identify a predictor of LVRR in patients with DCM (9–11). At present, hemodynamic parameters such as blood pressure, echocardiographic parameters such as left ventricular end-diastolic diameter, and interstitial fibrosis evaluated by late gadolinium enhancement of cardiac magnetic resonance are reported as useful predictors of LVRR. However, common examinations such as blood pressure measurement and echocardiography are not strong predictors of LVRR. Likewise, late gadolinium enhancement evaluation by cardiac magnetic resonance is burdened with the issue of false positives and cannot be performed in patients with renal dysfunction. Therefore, we still lack an accurate method to predict LVRR in patients with DCM (7).

In previous studies of animal models, accumulation of unrepaired oxidative DNA damage was observed in the failing heart (12,13). Our group has previously reported that the accumulation of unrepaired DNA single-strand breaks plays a causative role in the pathogenesis of heart failure (14). Furthermore, using single-cardiomyocyte RNA sequencing, we have also reported that p53 in cardiomyocytes increases cell-to-cell transcriptional heterogeneity and drives pathogenic gene programs, which shows how the accumulation of DNA damage leads to heart failure (15). However, all of these studies were conducted using animal models, and there have been few studies on DNA damage in human heart failure.

Poly(ADP-ribose) (PAR) is a major marker of DNA damage; it solely regulates diverse biological processes known as DNA damage responses (16). The DNA damage responses include DNA repair, chromatin remodeling, transcription, and cell death (17). A recent report by Hoch et al. (18) has shown that PAR in brain tissues could reflect the disease severity of cerebellar ataxia caused by a mutation of *XRCC1*, a gene involved in DNA single-strand break repair. This report raises the possibility that PAR staining could be used to measure DNA damage in human tissues. In the present study, we conducted immunofluorescence staining of PAR in endomyocardial biopsy specimens obtained from patients with DCM to confirm whether there is a DNA damage signature in the failing human heart. We also aimed to verify the utility of immunostaining of DNA damage markers for the prediction of response to heart failure therapy in patients with DCM.

METHODS

STUDY POPULATION AND DESIGN. We retrospectively enrolled patients who were diagnosed with DCM and underwent endomyocardial biopsy between 2009 and 2016 at the University of Tokyo Hospital, a tertiary referral center in Japan for cardiomyopathies. No statistical methods were used to estimate a priori sample size. The DCM diagnosis was made according to current guidelines and based on various modalities including coronary angiography, echocardiography, and endomyocardial biopsy (19,20). As this study is intended to evaluate the utility of immunostaining DNA damage markers in biopsy specimens for the prognostic stratification of patients, patients who have already received optimal medical therapy at the time of biopsy were excluded. According to the general consensus, β-blockers are one of the most important and established medical agents used as the standard therapeutic strategy to achieve LVRR in DCM. As β-blockers are known to improve heart function in a dose-dependent manner, we excluded patients who had already received therapeutic doses of β-blockers (equivalents of carvedilol >5 mg) at the time of biopsy.

In advance, we excluded hemodynamically-unstable patients who had received intravenous catecholamine infusion therapy or mechanical support therapy such as intra-aortic balloon pump therapy and percutaneous cardiopulmonary support within the 30 days preceding biopsy, and patients treated

with left ventricular assist device (LVAD) implantation or heart transplantation. As this study is intended to evaluate the utility of immunostaining DNA damage markers in biopsy specimens for the prognostic stratification of patients, patients who have already received optimal medical therapy at the time of biopsy were excluded. According to the general consensus, β-blockers are 1 of the most important and established medical agents used as the standard therapeutic strategy to achieve LVRR in DCM. As β-blockers are known to improve heart function in a dose-dependent manner, we excluded patients who had already received therapeutic doses of β-blockers (equivalents of carvedilol >5 mg) at the time of biopsy.

The collection of clinical data, the conduction of immunofluorescence staining for PAR, and the combining of those data to perform statistical analyses were all independently performed by 3 different researchers. The endpoint was a combined endpoint, defined as a composite outcome of death, ventricular assist device implantation, and heart transplantation. Optimal medical therapy for heart failure, including the administration of angiotensin-converting enzyme inhibitors or angiotensin II receptor blockers, antimineralocorticoids, and up-titration of β-blocker dosages, were initiated shortly after the patients underwent endomyocardial biopsy and a diagnosis of DCM was confirmed. LVRR was defined as an absolute increase in LVEF from ≥10% to a final value of >35%, accompanied by a decrease in left ventricular end-diastolic diameter ≥10% assessed by echocardiography 12 months after the initiation of optimal medical therapy (10). Patients who had events defined as combined endpoint before 12 months after initiation of therapy were categorized into the LVRR-negative group.

Our study was conducted according to the guidelines of the Declaration of Helsinki. Previous approval was obtained from the institutional research ethics committee, which waived the need for individual informed consent (Approval Number 11801).

CLINICAL MEASUREMENTS. Demographic data previously reported to be associated with LVRR in patients with DCM were collected during chart reviews. Demographic variables included age, sex, body mass index (BMI), hemodynamic status at presentation (blood pressure, heart rate), family history, past medical history, medication, and device therapy information. Familial DCM was defined as patients with at least 1 additional family member with DCM. We also reviewed laboratory data and clinical parameters such as electrocardiography and echocardiography collected both at the time of biopsy and 12 months after the initiation of optimal medical therapy.

IMMUNOHISTOCHEMICAL STUDIES. Immunofluorescence staining was used to investigate the expression of PAR and γ-H2A.X in formalin-fixed, paraffin-embedded biopsy specimens from patients with DCM. Briefly, 4-μm sections were cut from paraffin blocks and placed onto slides. After deparaffinization and rehydration, antigens were unmasked by boiling the slides for 20 min in Dako S1699 antigen retrieval solution (Agilent, Santa Clara, California) using an MI-33 microwave processor (Azumaya Co. Ltd., Tokyo, Japan). Slides were blocked in 5% normal goat serum for 60 min at room temperature and subsequently incubated with anti-PAR polymer antibody (ab14459, 1:100, Abcam, Cambridge, Massachusetts) overnight. After washing with phosphate-buffered saline, samples were stained with anti-mouse IgG-Alexa 647 (1:300, Thermo Fisher Scientific, Waltham, Massachusetts) for 1 h at room temperature. Cell membranes and nuclei were counterstained with wheat germ agglutinin (WGA)-Alexa 488 (1:200; Thermo Fisher Scientific), and 4′,6-diamidino-2-phenylindole (DAPI) (1:1,000; Dojindo Molecular Technologies, Inc., Kumamoto, Japan). Other antibodies and dyes used in this study include γ-H2A.X (ab81299, 1:200, Abcam), γ-H2A.X (MA1-2022, 1:200, Thermo Fisher Scientific), WGA-Alexa 350 (1:200; Thermo Fisher Scientific), vimentin (ab92547, 1:200, Abcam), PECAM1 (HPA004690, 1:100, Sigma-Aldrich), and anti-mouse IgG-Alexa 488 and 594 (1:300, Thermo Fisher Scientific). We used 2 sections from the residual biopsy specimens per patient: 1 for PAR staining and another for γ-H2A.X staining. Images were obtained under an inverted fluorescence microscope (BZ-X700, Keyence Corporation, Itasca, Illinois) with 20× objective, which covered the most area of the biopsy specimen in one visual field. Raw imaging data were analyzed using BZ-X analyzer software (Keyence Corporation) to quantify the fluorescence intensity of the PAR signal merged with DAPI in each nucleus. Subsequently, we set the threshold to detect PAR-positive nuclei based on a histogram of the fluorescence intensity and confirmed that each PAR-positive region recognized by the software showed high PAR signal intensity on each section. Supplemental Figure 1 shows an example of the distribution of fluorescence intensity for each nucleus stained with either PAR or γ-H2A.X in either LVRR-positive or LVRR-negative patients. The software automatically calculated the proportion of PAR-positive nuclei (% PAR nuclei) ([PAR stained nuclei] / [all nuclei stained by DAPI]). All raw imaging data were analyzed using

FIGURE 1 Enrollment and F/U of Study Population

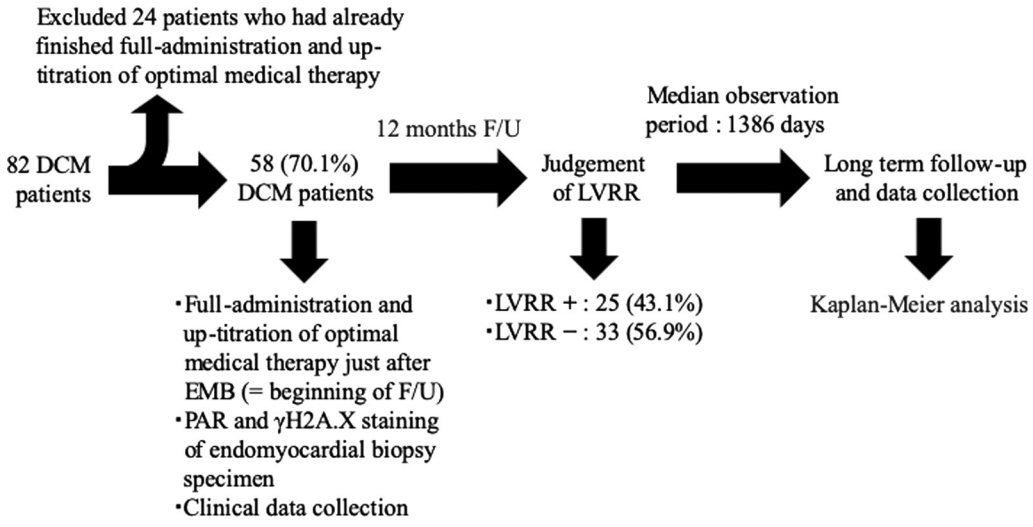

DCM = dilated cardiomyopathy; F/U = follow-up; EMB = endomyocardial biopsy; LVRR = left ventricular reverse remodeling; PAR = poly(ADP-ribose).

the same algorithm. The same analysis was also performed for the immunostaining of γ-H2A.X. To analyze the types of PAR-positive cells, 2 researchers jointly reviewed all imaging data of PAR-stained cells to determine whether each stained cell was a cardiomyocyte or noncardiomyocyte; determinations were made based on morphological differences. Noncardiomyocytes are very small compared with typical large mature cardiomyocytes, and their nuclei are located close to the cell membrane, which is detected by WGA staining (15,21).

STATISTICAL ANALYSIS. Continuous variables were expressed as the mean ± SD, and categorical variables as count and proportion. For those variables with skewed distributions, median (interquartile range [IQR]) were reported and compared using the Wilcoxon rank sum test. Statistical significance between the 2 groups was determined by an unpaired 2-tailed Student's *t*-test.

Univariable screening of all parameters of the patients at baseline was first performed. Student's *t* test was used for continuous variables. Fisher's exact test was used for categorical variables and mid-p values were calculated. We used the Kaplan-Meier method and the log-rank test to assess the impact of LVRR on the endpoint. We estimated the effect of %PAR as well as %γ-H2A.X for the combined endpoint by inverse probability weighted Cox proportional hazards regression models with robust standard errors. The weight for each subject was calculated using the generalized propensity score, including the following variables in the model to adjust for baseline confounding factors: age, BMI, family history, duration of heart failure, New York Heart Association (NYHA) functional class, systolic blood pressure, B-type natriuretic peptide (BNP), left ventricular end-diastolic diameter, severe mitral regurgitation (grade III or IV). The associations between %PAR and LVRR as well as between %γ-H2A.X and LVRR were also examined using the propensity score method in logistic regression modeling (22). Receiver-operating characteristic (ROC) analysis was performed to assess the performance of %PAR nuclei as well as %γ-H2A.X to predict LVRR. Cutpoint analysis was performed to determine the optimal cutoff value to maximize the Youden index [sensitivity − (1 − specificity)]. Areas under the ROC curve were calculated using logistic regression.

All analyses were carried out using SAS software version 9.4 (SAS Institute, Inc., Cary, North Carolina). For all tests, a probability value of $p < 0.05$ was considered significant.

RESULTS

CHARACTERISTICS OF THE STUDY POPULATION. A total of 82 patients underwent endomyocardial biopsy and were diagnosed with DCM during the study period. Among these, 24 (29.9%) patients were excluded mainly because they had already received full administration of optimal medical therapy with

high doses of β-blockers at the time of endomyocardial biopsy. As a result, we enrolled 58 (70.1%) patients in this study (Figure 1). The clinical characteristics and laboratory data at the time of biopsy for both LVRR-positive and LVRR-negative groups are presented in Table 1. The patients were predominantly men. The mean age of patients at diagnosis was 44.3 ± 15.0 years. A family history of DCM was identified in 25.9% of all cases. More than one-half of the patients belonged to NYHA functional class III or IV at baseline (58.6%), with a severe reduction of left ventricular systolic function (LVEF 24.2 ± 9.7%). The patients in the LVRR-negative group had significantly lower blood pressure, BMI, and peak oxygen consumption levels. They had a longer QRS duration and more complete left bundle branch block on electrocardiography; larger left ventricular dimensions, with severe mitral regurgitation in echocardiography; and higher BNP levels. However, analyses of these parameters showed no statistically significant differences.

TABLE 1 Baseline Characteristics of the Patients

	LVRR-Negative Group (n = 33)	LVRR-Positive Group (n = 25)	p Value
Age, yrs	45.3 ± 15.4	42.9 ± 14.6	0.558
Male	25 (75.8)	21 (84.0)	0.394
BMI, kg/m^2	21.6 ± 2.9	24.3 ± 5.5	0.019
Smoking	13 (39.4)	10 (40.0)	0.691
Familial DCM	12 (36.4)	3 (12.0)	0.054
Duration of HF, days	231 (101–1,108)	67 (33–107)	0.001
NYHA functional class III, IV	18 (54.5)	16 (44.0)	0.603
SBP, mm Hg	96.0 ± 14.6	111.1 ± 21.1	0.002
DBP, mm Hg	60.7 ± 12.8	70.9 ± 18.6	0.017
HR, beats/min	78.7 ± 19.1	81.6 ± 18.8	0.568
CLBBB	7 (21.2)	4 (16.0)	0.623
Atrial fibrillation	7 (21.2)	3 (12.0)	0.396
QRS duration, ms	115 (108–160)	110 (98–120)	0.085
LAD, mm	43.5 ± 9.4	43.9 ± 8.6	0.857
IVS, mm	7.9 ± 1.8	8.5 ± 1.6	0.214
LVPW, mm	8.4 ± 1.6	9.0 ± 1.7	0.132
LVDd, mm	68.1 ± 9.4	66.1 ± 11.3	0.472
LVDs, mm	60.9 ± 10.8	58.8 ± 11.7	0.465
LVEF (%)	24.5 ± 10.8	23.8 ± 8.1	0.795
MR severity grade			0.447
0 (no MR)	4 (12.1)	6 (24.0)	
I, II	23 (69.7)	16 (64.0)	
III, IV	6 (18.2)	3 (12.0)	
Peak Vo_2, ml/min/kg	15.8 ± 4.3	21.3 ± 3.4	0.002
Hb, g/dl	14.1 ± 2.1	14.9 ± 1.9	0.130
Alb, g/dl	4 ± 0.5	3.9 ± 0.6	0.575
Cr, mg/dl	1 ± 0.2	0.9 ± 0.2	0.428
eGFR, ml/min/1.73 m^2	68.7 ± 19.2	75.3 ± 19.4	0.204
Na, mEq/l	133.9 ± 17.7	139.7 ± 1.8	0.109
BNP, pg/ml	435.9 (203.6–844.0)	348.3 (153.7–617.7)	0.367
ACE inhibitor	16 (48.5)	10 (40.0)	0.513
ARB	9 (27.3)	5 (20.0)	0.454
β-blocker	23 (69.7)	11 (44.0)	0.082
Antimineralocorticoids	20 (60.6)	10 (40.0)	0.152
Loop diuretics	20 (60.6)	12 (48.0)	0.340
Anticoagulant agents	18 (54.5)	7 (28.0)	0.048
ICD implantation	3 (9.1)	0 (0)	0.163
CRT-D implantation	3 (9.1)	0 (0)	0.163

Values are mean ± SD, n (%), or median (interquartile range).

ACE = angiotensin-converting enzyme; Alb = albumin; ARB = angiotensin II receptor blocker; BNP = B-type natriuretic peptide; BMI = body mass index; CLBBB = complete left bundle branch block; Cr = creatinine; CRT-D = cardiac resynchronization therapy with defibrillator; DBP = diastolic blood pressure; DCM = dilated cardiomyopathy; eGFR = estimated glomerular filtration rate; Hb = hemoglobin; HF = heart failure; HR = heart rate; ICD = implantable cardioverter-defibrillator; IVS = interventricular septum; LAD = left atrial diameter; LVDd = left ventricular end-diastolic diameter; LVDs = left ventricular end-systolic diameter; LVEF = left ventricular ejection fraction; LVPW = left ventricular posterior wall; LVRR = left ventricular reverse remodeling; MR = mitral regurgitation; NYHA = New York Heart Association; SBP = systolic blood pressure.

PAR STAINING OF MYOCARDIAL BIOPSY SPECIMENS. Figure 2 shows an example of PAR and γ-H2A.X staining and the analysis via imaging software. Figures 2A to 2D are raw images of immunofluorescence staining for PAR using an endomyocardial biopsy specimen from LVRR-negative and LVRR-positive patients, respectively. Figures 2E and 2F are the same image after automatic assessment by a hybrid cell counting program; PAR-positive nuclei recognized by the program were marked as yellow. Figures 2G to 2L are raw images and program-processed images for γ-H2A.X. Supplemental Figure 1 shows the distribution of fluorescence intensity for each nucleus stained with either PAR or γ-H2A.X measured by the image software. Generally, both PAR and γ-H2A.X were stained in each nucleus (Supplemental Figure 2A). Nuclei with positivity to DNA damage markers were mainly thought to belong to cardiomyocytes. All PAR-positive noncardiomyocytes belonged to the cardiac fibroblast population (Supplemental Figures 2B and 2C). The average proportions of cardiomyocytes and noncardiomyocytes among all PAR-positive cells of all biopsy specimens from 58 patients (1,068 cells) were 94.5% and 5.5%, respectively (Supplemental Figure 2D).

As each biopsy specimen contained different numbers of cells, the numbers of the nuclei varied. The mean numbers of the analyzed nuclei of each PAR-stained specimen in LVRR-negative and LVRR-positive groups were 887 ± 41 and 903 ± 69, respectively (p = 0.832) (Figure 3A). Measurements of PAR staining revealed that patients with LVRR had significantly lower %PAR nuclei (3.7% [IQR: 0.6% to 3.9%] vs. 16.3% [IQR: 6.3% to 19.3%]; p < 0.001) as well as %γ-H2A.X nuclei (3.5% [IQR: 1.2% to 6.4%] vs. 11.7% [IQR: 6.0% to 14.6%]; p < 0.001) compared with those without LVRR (Figures 3B and 3C).

PATIENT OUTCOMES. The median observation period was 1,386 (IQR: 667 to 2,032) days in our study. During the judgement period of LVRR, 25 of 58 (43.1%) patients had achieved LVRR after multidisciplinary

FIGURE 2 Example of Analysis of PAR and γ-H2A.X Staining

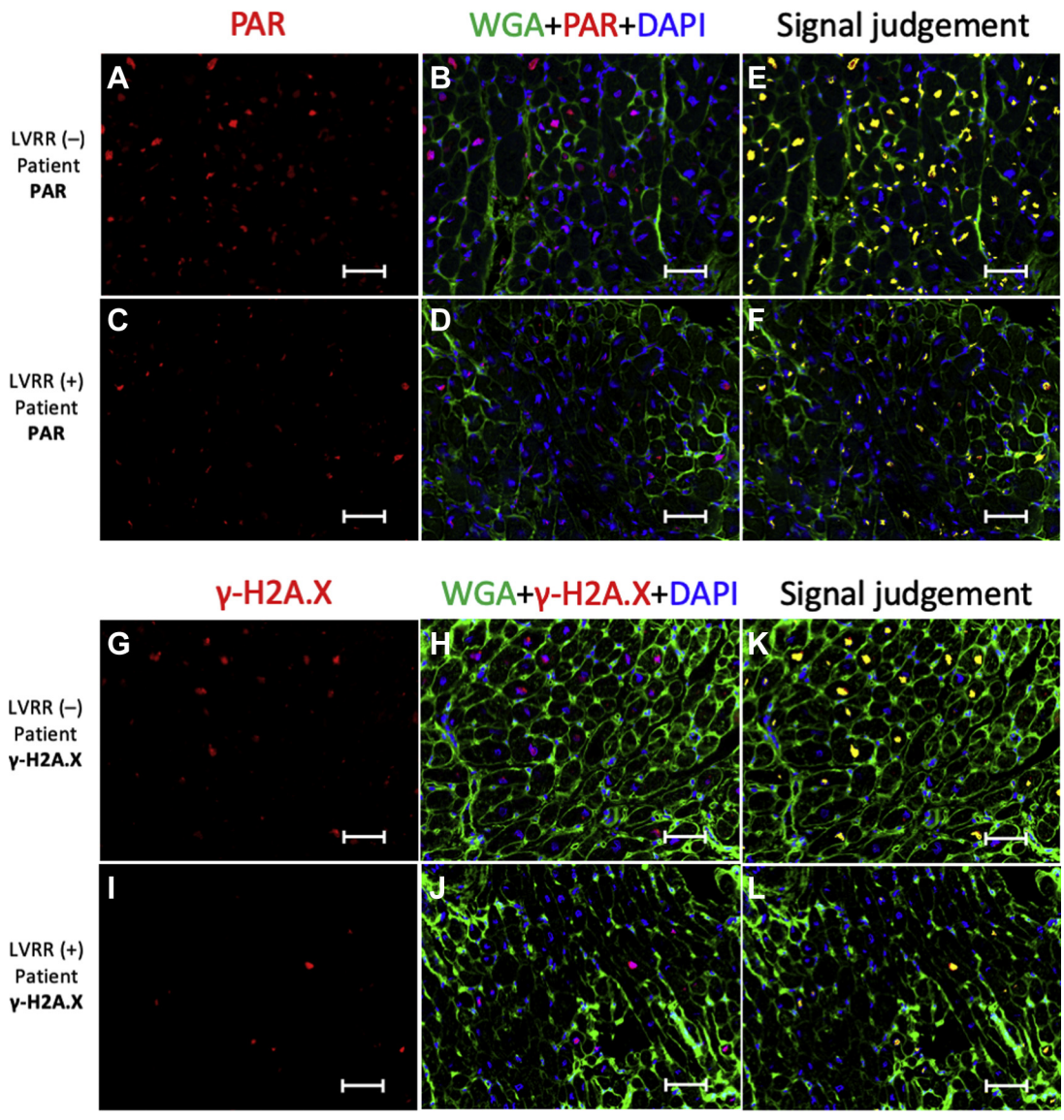

(A to D) Raw images of immunofluorescence staining for PAR **(red)** and wheat germ agglutinin (WGA) **(green)** with 4,6-diamidino-2-phenylindole (DAPI) **(blue)** nuclear counterstain using an endomyocardial biopsy specimen (**white bar** = 50 μm) from LVRR-negative and LVRR-positive patients, respectively. **(E, F)** The same image after automatic judgment by hybrid cell count program; PAR-positive nuclei were marked **(yellow)**. **(G to J)** Raw image of immunofluorescence staining for γ-H2A.X **(red)** and WGA **(green)** DAPI **(blue)** nuclear counterstain using an endomyocardial biopsy specimen (**white bar** = 50 μm) from LVRR-negative and LVRR-positive patients, respectively. **(K, L)** The same image after automatic judgment by a hybrid cell count program; γ-H2A.X-positive nuclei were marked **(yellow)**. Abbreviations as in Figure 1.

therapy including inhibition of the renin-angiotensin-aldosterone system, β-blockers, and cardiac resynchronization therapy. Neurohormonal drug treatment with angiotensin-converting enzyme inhibitors or angiotensin II receptor blockers, antimineralocorticoids, and β-blockers was tailored in the majority of patients (95%, 78%, and 100%, respectively) at target doses. No significant differences were noted between patients with LVRR and those without LVRR with respect to drug administration proportions of angiotensin-converting enzyme inhibitors (68.0% in patients with LVRR vs. 72.7% in patients without LVRR; $p = 0.775$), angiotensin II receptor blockers (28.0% vs. 21.2%; $p = 0.758$), antimineralocorticoids (72.0% vs. 81.8%;

FIGURE 3 Comparison of Analyzed Nuclei and Percentages of PAR-Positive and γ-H2A.X-Positive Nuclei in LVRR-Negative and LVRR-Positive Groups

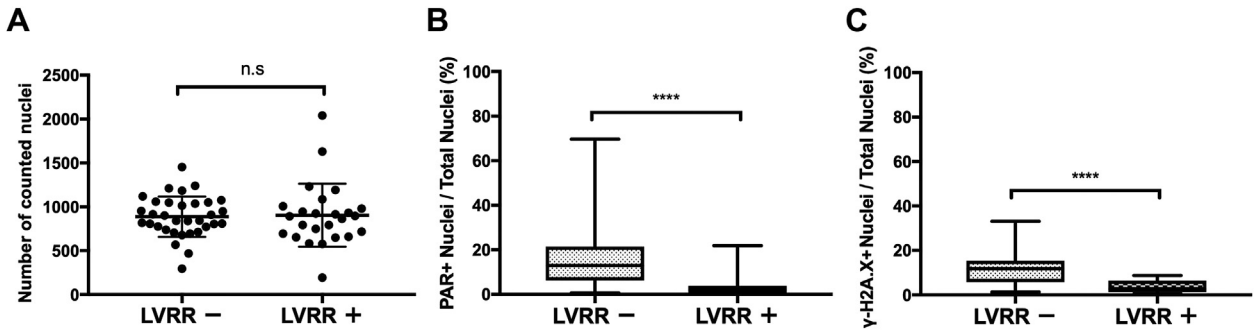

(A) Comparison of the number of counted nuclei on each specimen in the LVRR-negative and LVRR-positive groups. **(B, C)** Comparison of the proportion of PAR-positive or g-H2A.X positive nuclei in the LVRR-negative and LVRR-positive groups, respectively. Bar graph shows the mean proportion of PAR-positive or g-H2A.X-positive nuclei with SDs. ****$p < 0.001$. Abbreviations as in Figure 1.

$p = 0.527$), or β-blockers (both groups achieved 100% administration and the daily doses were 22.7 mg vs. 19.5 mg as equivalents of carvedilol; $p = 0.281$) at 12 months after the initiation of optimal medical therapy. The survival curves of the study population classified according to the presence or absence of LVRR are shown in Figure 4. The patients with LVRR had significantly better prognosis compared with those without LVRR (log-rank test, $p < 0.001$). The combined endpoint was reached during the follow-up period in 17 patients: 8 heart transplants (13.8%), 16 LVAD implants (27.6%), and 1 death (1.7%).

In this study, we used age, BMI, family history, duration of heart failure, NYHA functional classification, systolic blood pressure, BNP, left ventricular end-diastolic diameter, and severe mitral regurgitation (grade III or IV) as confounders for adjustment in propensity score analysis. Propensity score analysis for combined endpoint revealed that %PAR nuclei (for every 10% increase, hazard ratio: 1.36; 95% confidence interval [CI]: 1.02 to 1.81; $p = 0.035$) was a significant and independent prognostic factor after adjustment for other major clinical factors (Table 2). Other major prognostic factors predicting poor outcome in univariable Cox analysis were age, high NYHA functional class, low blood pressure, and low BMI. Because only a small number of patients in our cohort had undergone cardiac magnetic resonance (27.6%) and cardiopulmonary exercise testing (51.7%), we could not include late gadolinium enhancement extent and peak oxygen consumption in the model of propensity score analysis. The %PAR nuclei (for every 1% increase, odds ratio: 0.87; 95% CI: 0.79 to 0.95; $p = 0.003$) was also identified by propensity score analysis as a significant independent predictor of LVRR (Table 3). The results of the same analysis using the data for γ-H2A.X staining are shown in Tables 2 and 3, which revealed that %γ-H2A.X-stained nuclei can also independently predict LVRR.

Figure 5 shows the results of the ROC analysis. Compared with γ-H2A.X staining, PAR staining showed an incremental prognostic power for LVRR, but the statistical difference between these 2 models was not significant ($p = 1.000$). The ideal cutoff value of %PAR nuclei to predict LVRR in our study cohort was 5.74%. Using this threshold, the %PAR nuclei predicted LVRR with a sensitivity of 77.8% (95% CI: 57.7% to 91.4%) and a specificity of 87.1% (95% CI: 70.2% to 96.4%), and the area under the ROC curve was 0.879.

FIGURE 4 Long-Term Prognostic Impact of LVRR in DCM Patients

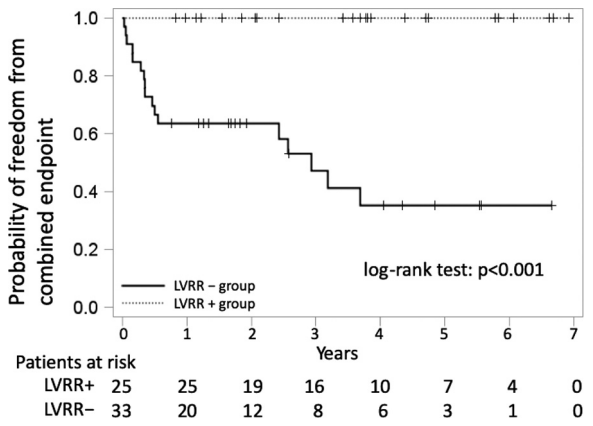

Survival curves of long-term freedom from major adverse cardiac events (death, ventricular assist device implantation, and heart transplantation) comparing the LVRR-positive and LVRR-negative patient subgroups. Abbreviations as in Figure 1.

TABLE 2 Univariable Cox Analysis and Propensity Score Analysis for Combined Endpoint

	HR (95% CI)	p Value
Age (10-yr increase)	0.66 (0.48–1.49)	0.015
BMI (5-yr increase)	0.46 (0.23–3.21)	0.028
Family history	2.21 (0.84–5.83)	0.110
Duration of HF (per 12-month increase)	1.07 (0.97–1.20)	0.190
NYHA functional class (1 increase in grade)	2.14 (1.14–1.88)	0.018
SBP (10-mm Hg increase)	0.50 (0.34–1.98)	<0.001
BNP (10-pg/ml increase)	1.00 (0.99–1.03)	0.730
LVDd (10-mm increase)	1.13 (0.71–1.44)	0.620
Severe MR (III/IV)	1.48 (0.43–5.17)	0.536
%PAR nuclei (10% increase)	1.25 (0.96–1.63)	0.100
%γ-H2A.X nuclei (10% increase)	1.16 (0.55–2.44)	0.700
Inverse probability weighting using propensity score		
%PAR nuclei (10% increase)	1.36 (1.02–1.81)	0.035
%γ-H2A.X nuclei (10% increase)	1.28 (0.75–2.21)	0.370

CI = confidence interval; HR = hazard ratio; PAR = poly(ADP-ribose); other abbreviations as in Table 1.

DISCUSSION

There is consensus that a distinct subset of patients with DCM can achieve LVRR after medical therapy, and that their clinical prognosis is better than those without LVRR (2,3). Over many years, several clinical trials have been conducted to evaluate potential predictors of cardiac recovery in patients with DCM. These trials were generally divided into 2 categories. The first category was the measurement of parameters associated with left ventricular dysfunction such as left ventricular end-diastolic diameter, QRS duration or complete left bundle branch block, and BNP. The second category was the evaluation of myocardial fibrosis assessed by late gadolinium enhancement in cardiac magnetic resonance. Compared with these examinations, the role of endomyocardial biopsy has been very limited. endomyocardial biopsy is mainly used to rule out diseases that are similar to DCM, such as myocarditis and sarcoidosis. Previous reports have established a relationship between quantitative histological findings on endomyocardial biopsy and left ventricular contractile function in patients with DCM (23). In recent years, however, the value of histopathological findings correlated with clinical and hemodynamic parameters has become controversial or even unfavorable (9,24). Therefore, one could question the clinical merit and rationale of assessing myocardial histology by endomyocardial biopsy given the risk of various complications (25). However, late gadolinium enhancement measured by cardiac magnetic resonance provides limited information on interstitial fibrosis, and echocardiography can estimate only myocardial status by compiling information on dysfunction and loss of cardiomyocytes. In contrast, endomyocardial biopsy analysis has the potential to directly assess all of the molecular characteristics of cardiac cells. In this study, we demonstrated the utility of immunostaining DNA damage markers using endomyocardial biopsy specimens to predict the probability of LVRR and even the patient's outcome. Among the analyzed specimens, the predictive ability of PAR for prognoses (combined endpoint and LVRR) is slightly better than that of γ-H2A.X. A previous study involving a small number of patients with heart failure (not limited to DCM) showed that mechanical unloading by LVAD implantation reduced DNA damage responses (26). Taken together with our results, DNA damage seems to be a very important pathophysiological component of heart failure. DCM-causative genes encode a heterogeneous group of molecules that participate in force generation, force transmission, sarcomere integrity, and cytoskeletal and nuclear architecture (27). We have previously reported the prognostic value of genetic mutations in Japanese patients with DCM (28). At first glance, it looks like the majority of DCM-causative genes such as sarcomere and cytoskeletal genes have no relationship with DNA damage. However, the linker of the nucleoskeleton and cytoskeleton complex physically couples the nuclear membrane with the cytoskeleton (29). Therefore, sarcomere and cytoskeletal impairment may also have a harmful impact on the nucleus. Although we do not know the genetic mutations among our study population, the significantly high proportions of PAR-positive nuclei seen in poor-prognosis patients suggests that the accumulation of DNA damage is a common pathogenetic trait in severe

TABLE 3 Univariable Logistic Regression Analysis and Propensity Score Analysis for LVRR

	OR (95% CI)	p Value
Age (10-yr increase)	0.90 (0.63–1.28)	0.551
BMI (5-yr increase)	2.20 (1.08–4.46)	0.029
Family history	0.24 (0.06–0.97)	0.045
Duration of HF (per 12-month increase)	0.72 (0.52–0.99)	0.044
NYHA functional class (1 increase in grade)	1.18 (0.63–2.21)	0.610
SBP (10-mm Hg increase)	1.62 (1.15–2.28)	0.006
BNP (10-pg/ml increase)	0.99 (0.98–1.00)	0.260
LVDd (10-mm increase)	0.82 (0.49–1.39)	0.460
Severe MR (III/IV)	0.61 (0.14–2.74)	0.522
%PAR nuclei (1% increase)	0.81 (0.71–0.92)	<0.001
%γ-H2A.X nuclei (1% increase)	0.68 (0.55–0.84)	<0.001
Inverse probability weighting using propensity score		
%PAR nuclei (10% increase)	0.87 (0.79–0.95)	0.003
%γ-H2A.X nuclei (10% increase)	0.68 (0.55–0.84)	<0.001

OR = odds ratio; other abbreviations as in Tables 1 and 2.

FIGURE 5 ROC Curve to Evaluate the Performance of %PAR or %γ-H2A.X Nuclei to Predict LVRR

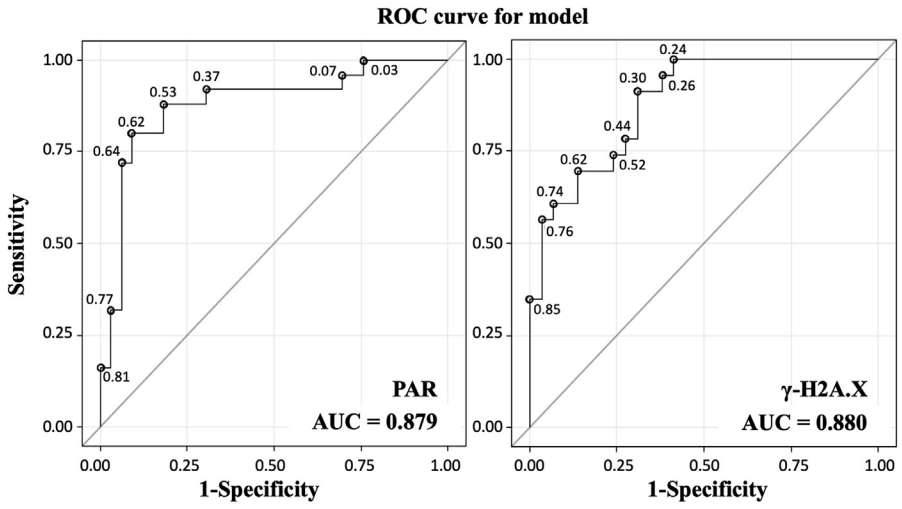

AUC = area under the curve; ROC = receiver-operating characteristic; other abbreviations as in Figure 1.

heart failure patients with DCM. Although familial DCM patients were much more common in the LVRR-negative group than in the LVRR-positive group, Tables 2 and 3 show %PAR could independently predict combined endpoint and LVRR even after adjustment for various factors, including family history. In fact, LVRR-negative patients showed high %PAR in both the familial and nonfamilial DCM groups (Supplemental Figures 3A and 3B). To our knowledge, this is the first clinical study to show that the evaluation of DNA damage is useful for the prediction of prognosis in patients with heart failure. Considering the high specificity and sensitivity, this kind of evaluation of DNA damage may also prove useful in patients with heart failure from etiologies other than DCM.

STUDY LIMITATIONS. Despite the significance of the findings, our study has several limitations. First, because our hospital conducts most of the heart transplants in Japan, the majority of patients with DCM who are referred to our hospital are at end-stage heart failure, and are treated with LVAD implantation or heart transplantation. Therefore, our study population imposes a selection bias with respect to the characteristics of DCM among the general population. For many patients referred to our hospital, some pharmacological medications such as renin-angiotensin-aldosterone system inhibitors and β-blockers have already been administered in the referring hospital, even before a diagnosis of DCM has been confirmed. Although we excluded patients who had already completed full administration and up-titration of medications for heart failure at the time of endomyocardial biopsy, the remaining patients still had an incomplete course of medication, as shown in Table 1. Thus, low-dose drugs might have had a small impact on DNA damage in the patients with heart failure. This is an unavoidable consequence of a retrospective study conducted in a large referral center. We need to prospectively enroll patients who have not received any pharmacological agents for heart failure.

Second, the sample size in our study population is small and, as mentioned before, we could not include the extent of late gadolinium enhancement or peak oxygen consumption in the propensity score analysis, which makes it impossible to compare % PAR nuclei with these gold standards for assessing prognosis. Third, although we paid careful attention to the immunofluorescence staining of the endomyocardial biopsy specimens, this process requires effort and time. Besides, the results of immunostaining will be affected by many factors such as the quality of antibodies, the storage conditions of endomyocardial biopsy specimens, and the technical skills of the staff. Therefore, simpler methods to measure DNA damage should be developed.

CONCLUSIONS

In this study, we demonstrated the utility of PAR staining to predict the probability of LVRR. Our

study underscores the importance of utilizing endomyocardial biopsy specimens to evaluate DNA damage at baseline and to improve the prognostic stratification in patients with DCM. Further prospective multicenter studies are needed to assess the prognostic significance of PAR staining and to establish the most effective strategies for the diagnosis of DCM and identify patients who have a poor prognosis. Optimal treatment could then be initiated earlier, thereby improving patient outcome.

ACKNOWLEDGMENT The authors thank Y. Yokota for experimental support.

ADDRESS FOR CORRESPONDENCE: Dr. Issei Komuro, Department of Cardiovascular Medicine, Graduate School of Medicine, University of Tokyo, 7-3-1 Hongo, Bunkyo-ku, Tokyo 113-8655, Japan. E-mail: komuro-tky@umin.ac.jp.

PERSPECTIVES

COMPETENCY IN MEDICAL KNOWLEDGE: DNA damage has been reported to cause heart failure in animal models. This was the first study that clearly showed the existence of DNA damage in human cardiomyopathy heart tissues and the correlation between degree of DNA damage and clinical prognosis. Staining of PAR, a pathogenic signature of DNA damage responses, is useful to anticipate the probability of left ventricular reverse remodeling and prognosis in patients with DCM.

TRANSLATIONAL OUTLOOK: Further prospective multicenter studies are needed to assess the clinical usefulness of PAR staining for predicting the prognosis among heart failure patients.

REFERENCES

1. Braunwald E. The war against heart failure: the Lancet lecture. Lancet 2015;385:812–24.

2. Savarese G, Lund LH. Global public health burden of heart failure. Card Fail Rev 2017;3:7–11.

3. Weintraub RG, Semsarian C, Macdonald P. Dilated cardiomyopathy. Lancet 2017;390:400–14.

4. Merlo M, Pyxaras SA, Pinamonti B, Barbati G, Di Lenarda A, Sinagra G. Prevalence and prognostic significance of left ventricular reverse remodeling in dilated cardiomyopathy receiving tailored medical treatment. J Am Coll Cardiol 2011;57:1468–76.

5. Matsumura Y, Hoshikawa-Nagai E, Kubo T, et al. Left ventricular reverse remodeling in long-term (>12 years) survivors with idiopathic dilated cardiomyopathy. Am J Cardiol 2013;111:106–10.

6. Merlo M, Stolfo D, Anzini M, et al. Persistent recovery of normal left ventricular function and dimension in idiopathic dilated cardiomyopathy during long-term follow-up: does real healing exist? J Am Heart Assoc 2015;4:e001504.

7. Tayal U, Prasad SK. Myocardial remodeling and recovery in dilated cardiomyopathy. JRSM Cardiovasc Dis 2017;6: 2048004017734476.

8. Khush KK, Zaroff JG, Nguyen J, Menza R, Goldstein BA. National decline in donor heart utilization with regional variability: 1995-2010. Am J Transplant 2015;15:642–9.

9. McNamara DM, Starling RC, Cooper LT, et al. Clinical and demographic predictors of outcomes in recent onset dilated cardiomyopathy: results of the IMAC (Intervention in Myocarditis and Acute Cardiomyopathy)-2 study. J Am Coll Cardiol 2011;58:1112–8.

10. Kubanek M, Sramko M, Maluskova J, et al. Novel predictors of left ventricular reverse remodeling in individuals with recent-onset dilated cardiomyopathy. J Am Coll Cardiol 2013;61:54–63.

11. Broch K, Murbræch K, Andreassen AK, Hopp E, Aakhus S, Gullestad L. Contemporary outcome in patients with idiopathic dilated cardiomyopathy. Am J Cardiol 2015;116:952–9.

12. Siggens L, Figg N, Bennett M, Foo R. Nutrient deprivation regulates DNA damage repair in cardiomyocytes via loss of the base-excision repair enzyme OGG1. FASEB J 2012;26:2117–24.

13. Sano M, Minamino T, Toko H, et al. p53-induced inhibition of Hif-1 causes cardiac dysfunction during pressure overload. Nature 2007;446:444–8.

14. Higo T, Naito AT, Sumida T, et al. DNA single-strand break-induced DNA damage response causes heart failure. Nat Commun 2017;8:15104.

15. Nomura S, Satoh M, Fujita T, et al. Cardiomyocyte gene programs encoding morphological and functional signatures in cardiac hypertrophy and failure. Nat Commun 2018;9:4435.

16. Bai P. Biology of poly(ADP-Ribose) polymerases: the factotums of cell maintenance. Mol Cell 2015;58:947–58.

17. Leung AK. Poly(ADP-ribose): an organizer of cellular architecture. J Cell Biol 2014;205:613–9.

18. Hoch NC, Hanzlikova H, Rulten SL, et al. XRCC1 mutation is associated with PARP1 hyperactivation and cerebellar ataxia. Nature 2017;541:87–91.

19. McNamara DM, Starling RC, Cooper LT, et al. Clinical and demographic predictors of outcomes in recent onset dilated cardiomyopathy: results of the IMAC (Intervention In Myocarditis and Acute Cardiomyopathy)-2 study. J Am Coll Cardiol 2011;58:1112–8.

20. Japp AG, Gulati A, Cook SA, Cowie MR, Prasad SK. The diagnosis and evaluation of dilated cardiomyopathy. J Am Coll Cardiol 2016;67:2996–3010.

21. Satoh M, Nomura S, Harada M, et al. High-throughput single-molecule RNA imaging analysis reveals heterogeneous responses of cardiomyocytes to hemodynamic overload. J Mol Cell Cardiol 2019;128:77–89.

22. Austin PC. Assessing the performance of the generalized propensity score for estimating the effect of quantitative or continuous exposures on binary outcomes. Stat Med 2018;37:1874–94.

23. Schwarz F, Mall G, Zebe H, et al. Quantitative morphologic findings of the myocardium in idiopathic dilated cardiomyopathy. Am J Cardiol 1983;51:501–6.

24. Shimura S, Matsui Y, Yutani C, et al. Histopathological study of specimens obtained by left ventricular biopsy during ventriculoplasty for idiopathic dilated cardiomyopathy. Tokai J Exp Clin Med 2009;34:1–7.

25. Holzmann M, Nicko A, Kühl U, et al. Complication rate of right ventricular endomyocardial biopsy via the femoral approach: a retrospective and prospective study analyzing 3048 diagnostic procedures over an 11-year period. Circulation 2008;118:1722–8.

26. Canseco DC, Kimura W, Garg S, et al. Human ventricular unloading induces cardiomyocyte proliferation. J Am Coll Cardiol 2015;65:892–900.

27. Burke MA, Cook SA, Seidman JG, Seidman CE. Clinical and mechanistic insights into the genetics of cardiomyopathy. J Am Coll Cardiol 2016;68:2871–86.

28. Tobita T, Nomura S, Fujita T, et al. Genetic basis of cardiomyopathy and the genotypes involved in prognosis and left ventricular reverse remodeling. Sci Rep 2018;8:1998.

29. Stroud MJ, Banerjee I, Veevers J, Chen J. Linker of nucleoskeleton and cytoskeleton complex proteins in cardiac structure, function, and disease. Circ Res 2014;114:538–48.

KEY WORDS dilated cardiomyopathy, DNA damage, left ventricular reverse remodeling, poly ADP-ribose

APPENDIX For supplemental figures, please see the online version of this paper.

JACC: BASIC TO TRANSLATIONAL SCIENCE VOL. 4, NO. 6, 2019

EDITORIAL COMMENT

DNA Damage Prediction Tool in Dilated Cardiomyopathy

Don't Go Breaking My Heart*

Jesus Jimenez, MD, PhD,[a,b] Stacey L. Rentschler, MD, PhD[a,b]

Dilated nonischemic cardiomyopathy (DCM) is the most common indication for heart transplantation (1). DCM is characterized by systolic dysfunction and enlargement of 1 or both ventricles. The causes of DCM vary widely and include idiopathic, genetic, pregnancy, toxin, infectious, metabolic/endocrine, inflammatory/infiltrative/autoimmune, and neuromuscular disease mechanisms (2). There are additional mechanisms that can lead to cardiomyopathy which overlap phenotypically with DCM, including ischemic cardiomyopathy, hypertensive heart disease, and athlete's heart. The wide-ranging phenotypic overlap and diverse mechanisms which can result in DCM make the management challenging, especially with respect to predicting which individual patients will undergo left ventricular reverse remodeling (LVRR) in response to therapy. Although treatment includes removing the stressor, such as discontinuing alcohol for alcoholic DCM patients or starting methimazole for thyrotoxicosis, standard guideline-directed medical treatment (GDMT) also requires beta-blocker and renin-angiotensin-aldosterone system inhibitor therapy to promote reverse remodeling and recovery of systolic function. Unfortunately, despite our best efforts, many DCM patients do not recover cardiac function and subsequently progress to end-stage heart failure requiring advanced heart failure therapies (3).

SEE PAGE 670

Evaluation for DCM often begins upon incidentally finding cardiomegaly on chest radiography; and typically, a careful history, physical examination, and echocardiography study yields clues to the cause. Additional work-up often requires cardiac magnetic resonance to evaluate for late gadolinium enhancement and, in many cases, an endomyocardial biopsy for histological analysis. Prior animal studies performed by Ko et al. (4) in this issue of *JACC: Basic to Translational Science* demonstrated that unrepaired DNA damage increases expression of inflammatory and DNA damage response signaling that play a causative role in the pathogenesis of heart failure (5). Ko et al. (4) hypothesized that DNA damage in DCM patients can be assessed from endomyocardial biopsy results and that these markers of DNA damage may be useful in predicting LVRR in response to GDMT. Specifically, the study evaluated 2 major markers of DNA damage, poly (ADP-ribose) (PAR) and γ-H2A.X, by using immunohistochemical analysis of endomyocardial samples from 58 DCM patients prior to initiating 12 months of optimal GDMT. A total of 43% of these patients demonstrated LVRR, defined in the study as an absolute increase in LV ejection fraction ≥10% to a final value of >35% with a concomitant decrease in LV end-diastolic diameter ≥10%, whereas 57% of patients did not have LVRR in response to GDMT (i.e., they were LVRR-negative). PAR and γ-H2A.X nuclear staining was significantly reduced in LVRR-positive patients, and propensity score analysis demonstrated that the proportions of PAR (%PAR) and %γ-H2A.X staining

*Editorials published in *JACC: Basic to Translational Science* reflect the views of the authors and do not necessarily represent the views of *JACC: Basic to Translational Science* or the American College of Cardiology.

From the [a]Department of Medicine, Cardiovascular Division, Washington University School of Medicine, St. Louis, Missouri; and the [b]Department of Developmental Biology, Washington University School of Medicine, St Louis, Missouri. Both authors have reported that they have no relationships relevant to the contents of this paper to disclose.

The authors attest they are in compliance with human studies committees and animal welfare regulations of the authors' institutions and Food and Drug Administration guidelines, including patient consent where appropriate. For more information, visit the *JACC: Basic to Translational Science* author instructions page.

ISSN 2452-302X https://doi.org/10.1016/j.jacbts.2019.08.005

were significant and independent risk factors for DCM as well as independent predictors of LVRR. Finally, receiver-operating characteristic analysis demonstrated the incremental prognostic power of %PAR staining with a sensitivity of 78% and a specificity of 87% to predict LVRR. An exciting finding was that markers of DNA damage could be used retrospectively to predict LVRR and patient clinical outcomes in DCM patients. If it is possible to predict which patients are unlikely to recover cardiac function, then advanced heart failure therapies can be deployed earlier.

A strength of this study is the bench-to-bedside approach used by the team, whereby findings of DNA damage in animal models of heart failure were translated to a novel prediction tool for patients with DCM. One pertinent question this study raises is what was the mechanism underlying the differential response observed in DCM patients with less DNA damage who underwent LVRR? One possibility is that the patients with LVRR had accumulated less DNA damage overall, as represented by lower %PAR-stained nuclei. Was this, perhaps, due to having had DCM for a shorter period of time? Because we know that "time is muscle" in the setting of acute myocardial infarction, does a similar prediction model hold true in nonischemic DCM with respect to LVRR? A potential future follow-up study could measure DNA damage in serial biopsies over time after removal of the stressor and/or GDMT to correlate these DNA damage markers with the level of cardiac recovery. To this end, it would also be interesting to evaluate patients who have undergone LVRR and subsequently have had recurrence of LV systolic dysfunction, as is often seen clinically and as reported in the TRED-HF trial (6). Of note, prior preclinical studies using a pressure-overload heart failure model demonstrated that, after the stressor was removed (i.e., debanding), there was incomplete reversal of transcriptional changes despite recovery of LV systolic function (7). This "memory" of a prior injury suggests a potential epigenetic basis. Given that 1 of the markers used in this study, γ-H2A.X, is a histone variant, these markers may herald a molecular signature of epigenetic changes that have reached a "point of no return" and progress to irreversible LVRR. Therefore, this study raises interesting directions for further elucidation of downstream bench research.

Although there are several study limitations related to sample size and selection bias for primarily end-stage heart failure patients as described by the authors, a second major strength is that DNA damage was an independent prognostic marker in all types of DCM. Although the authors did not report the types of DCM encountered, if the ratios were similar to previously studied cohorts, evaluation of DNA damage in all DCM patients could meet criteria for a screening test (8). With a larger, prospective study cohort, a subgroup analysis of the types of DCM may uncover that the patients without LVRR will fall primarily into certain types of DCM, further allowing targeted therapies and model validation. This point was partially illustrated in this study, given that familial DCM patients were primarily in the LVRR-negative group (4). Because the prevalence of DCM in Japan is estimated to be 14/100,000 compared to the US prevalence of 36.5/100,000, it is imperative to determine if the findings of this study can be applied globally and across the various types of DCM (9,10).

In conclusion, the findings by Ko et al. (4) validated a novel prognostic tool to determine LVRR in DCM patients. By assessing DNA damage by using PAR-stained cardiomyocyte nuclei from an endomyocardial biopsy, it may be possible to predict the clinical prognosis of DCM patients, with adequate sensitivity and specificity. A future prospective study is warranted to determine whether this can be used to dictate future clinical care.

ADDRESS FOR CORRESPONDENCE: Dr. Stacey L. Rentschler, Department of Medicine, Cardiovascular Division, Washington University School of Medicine, 309 McDonnell Science Building, Campus Box 8103, 660 South Euclid Avenue, St. Louis, Missouri 63110. E-mail: stacey.rentschler@wustl.edu.

REFERENCES

1. Khush KK, Cherikh WS, Chambers DC, et al. The International Thoracic Organ Transplant Registry of the International Society for Heart and Lung Transplantation: thirty-fifth adult heart transplantation report—2018; focus theme: multiorgan transplantation. J Heart Lung Transplant 2018;37:1155–68.

2. Japp AG, Gulati A, Cook SA, Cowie MR, Prasad SK. The diagnosis and evaluation of dilated cardiomyopathy. J Am Coll Cardiol 2016;67:2996–3010.

3. Tayal U, Prasad SK. Myocardial remodelling and recovery in dilated cardiomyopathy. JRSM Cardiovasc Dis 2017;6. 2048004017734476.

4. Ko T, Fujita K, Nomura S, et al. Quantification of DNA damage in heart tissue as a novel prediction tool for therapeutic prognosis of patients with dilated cardiomyopathy. J Am Coll Cardiol Basic Trans Science 2019;4:670–80.

5. Higo T, Naito AT, Sumida T, et al. DNA single-strand break-induced DNA damage response causes heart failure. Nat Commun 2017;8:15104.

6. Halliday BP, Wassall R, Lota AS, et al. Withdrawal of pharmacological treatment for heart failure in patients with recovered dilated cardiomyopathy (TRED-HF): an open-label, pilot, randomised trial. Lancet 2019;393:61–73.

7. Weinheimer CJ, Kovacs A, Evans S, Matkovich SJ, Barger PM, Mann DL. Load-dependent changes in left ventricular structure and function in a pathophysiologically relevant murine model of reversible heart failure. Circ Heart Fail 2018;11:e004351.

8. Wilson JM, Jungner YG. [Principles and practice of mass screening for disease] in Spanish. Bol Oficina Sanit Panam 1968;65:281–393.

9. Miura K, Nakagawa H, Morikawa Y, et al. Epidemiology of idiopathic cardiomyopathy in Japan: results from a nationwide survey. Heart 2002;87:126–30.

10. Codd MB, Sugrue DD, Gersh BJ, Melton LJ III. Epidemiology of idiopathic dilated and hypertrophic cardiomyopathy. A population-based study in Olmsted County, Minnesota, 1975–1984. Circulation 1989;80:564–72.

KEY WORDS dilated cardiomyopathy, DNA damage, PAR, stratification

JACC: BASIC TO TRANSLATIONAL SCIENCE VOL. 4, NO. 6, 2019

PRECLINICAL RESEARCH

JAK2^{V617F}-Mediated Clonal Hematopoiesis Accelerates Pathological Remodeling in Murine Heart Failure

Soichi Sano, MD, PhD,[a] Ying Wang, MD, PhD,[a] Yoshimitsu Yura, MD, PhD,[a] Miho Sano, MD, PhD,[a] Kosei Oshima, MD, PhD,[b] Yue Yang, PhD,[c] Yasufumi Katanasaka, PhD,[d] Kyung-Duk Min, MD, PhD,[a] Shinobu Matsuura, DVM, PhD,[e] Katya Ravid, DSc,[e] Golam Mohi, PhD,[c] Kenneth Walsh, PhD[a]

VISUAL ABSTRACT

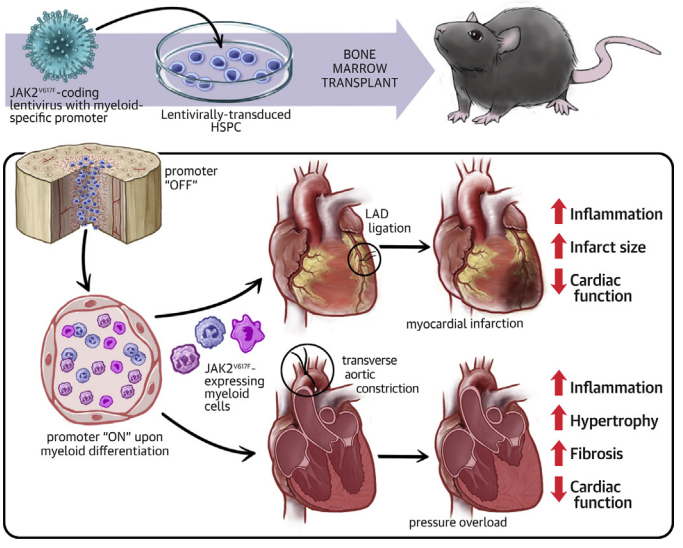

Sano, S. et al. J Am Coll Cardiol Basic Trans Science. 2019;4(6):684–97.

HIGHLIGHTS

- **Clonal hematopoiesis can develop from *JAK2*^{V617F} mutant cells, but mouse models harboring this mutation are confounded by myeloproliferative disease phenotypes.**
- **To establish a model of *JAK2*^{V617F} clonal hematopoiesis, a lentivirus vector was used to transduce hematopoietic stem and progenitor cells with a construct that expresses this mutation from a myeloid-specific promoter.**
- **When transduced hematopoietic stem and progenitor cells were implanted into mice, *JAK2*^{V617F} chimerism was achieved in monocytes and neutrophils in the absence of changes in blood cell counts, and these mice exhibited greater myocardial inflammation and accelerated heart failure when subjected to models of cardiac injury.**
- **These data suggest that clonal hematopoiesis can arise from the acquisition of *JAK2*^{V617F} mutations in a progenitor cell subpopulation that gives rise to circulating myeloid cells, and that this condition can promote cardiovascular disease through proinflammatory mechanisms.**

ISSN 2452-302X https://doi.org/10.1016/j.jacbts.2019.05.013

SUMMARY

Janus kinase 2 (valine to phenylalanine at residue 617) ($JAK2^{V617F}$) mutations lead to myeloproliferative neoplasms associated with elevated myeloid, erythroid, and megakaryocytic cells. Alternatively these same mutations can lead to the condition of clonal hematopoiesis with no impact on blood cell counts. Here, a model of myeloid-restricted $JAK2^{V617F}$ expression from lineage-negative bone marrow cells was developed and evaluated. This model displayed greater cardiac inflammation and dysfunction following permanent left anterior descending artery ligation and transverse aortic constriction. These data suggest that $JAK2^{V617F}$ mutations arising in myeloid progenitor cells may contribute to cardiovascular disease by promoting the proinflammatory properties of circulating myeloid cells. (J Am Coll Cardiol Basic Trans Science 2019;4:684–97)

ABBREVIATIONS AND ACRONYMS

AIM2 = absence in melanoma 2

ANOVA = analysis of variance

ARCH = age-related clonal hematopoiesis

BMT = bone marrow transplant

CCL2 = C-C motif chemokine ligand 2

CHIP = clonal hematopoiesis of indeterminate potential

GFP = green fluorescent protein

HSC = hematopoietic stem cell

HSPC = hematopoietic stem and progenitor cell

IFNGR1 = interferon gamma receptor 1

IL = interleukin

JAK2 = Janus kinase 2

$JAK2^{V617F}$ = mutant Janus kinase 2 (valine to phenylalanine at residue 617)

$JAK2^{WT}$ = wild-type Janus kinase 2

LPS = lipopolysaccharide

LT-HSC = long-term hematopoietic stem cell

MI = myocardial infarction

MPN = myeloproliferative neoplasm

NET = neutrophil extracellular traps

STAT = signal transducer and activator of transcription

TAC = transverse aortic constriction surgery

Clonal hematopoiesis of indeterminate potential (CHIP) or age-related clonal hematopoiesis (ARCH) is a prevalent condition in elderly individuals in which a substantial portion of mature blood cells are derived from a single dominant hematopoietic stem cell (HSC) clone (1–3). In a portion of individuals, this clonal hematopoiesis event can be attributed to mutations in "driver" genes that are recurrently mutated in hematologic malignancies. These mutated genes include *DNMT3A*, *TET2*, *ASXL1*, and others. These mutations are thought to provide the HSC with a competitive advantage such that it undergoes clonal amplification and gives rise to differentiated blood cell progeny that also harbor pre-leukemic mutations. Notably, the mutations that give rise to clonal hematopoiesis do not overtly alter blood cell counts or give rise to other features of hematologic malignancy. The existence of clonal hematopoiesis has been known for decades (4,5), but it had generally been viewed as a benign condition and that it might provide a counterbalance to HSC exhaustion that occurs in elderly individuals (6). However, recent epidemiological studies have shown that clonal hematopoiesis is associated with an appreciable increase in mortality in the general population as well as in patient cohorts (7–12). In some instances, clonal hematopoiesis has been associated with an increased risk of cardiovascular disease, including coronary artery disease, ischemic stroke, and early onset myocardial infarction (10,13). Studies in experimental models have provided evidence that inactivating mutations in *TET2* can causally contribute to atherosclerosis and heart failure through an interleukin (IL)-1 beta-dependent mechanism (14,15). Similarly, experimental studies have shown that mutations in *DNMT3A* can contribute to myocardial inflammation and heart failure (16). Recently, hematopoietic mutations in *TET2* and *DNMT3A* have been associated with the progression and poor prognosis in patients with chronic ischemic heart failure (17).

SEE PAGE 698

Janus kinase 2 (JAK2) is a nonreceptor tyrosine kinase that transmits intracellular signals downstream of various cytokine receptors. While JAK2 is broadly expressed, the activating mutation *JAK2 G1849T (V617F)* ($JAK2^{V617F}$) in hematopoietic

From the [a]Hematovascular Biology Center, Robert M. Berne Cardiovascular Research Center, University of Virginia School of Medicine, Charlottesville, Virginia; [b]Molecular Cardiology, Whitaker Cardiovascular Institute, Boston University School of Medicine, Boston, Massachusetts; [c]Biochemistry and Molecular Genetics, University of Virginia School of Medicine, Charlottesville, Virginia; [d]Division of Molecular Medicine, Graduate School of Pharmaceutical Sciences, University of Shizuoka, Shizuoka, Japan; and the [e]Department of Medicine and Whitaker Cardiovascular Institute, Boston University School of Medicine, Boston, Massachusetts. This work was supported by National Institutes of Health grant nos. HL138014, HL132564 (to Dr. Walsh), HL139819 (to Dr. Walsh), HL141256 (to Dr. Walsh), HL095685 (to Dr. Mohi), and HL136363 (to Dr. Ravid); American Heart Association Post-Doctoral Fellowship 17POST33670076 and Kanae Foundation for the Promotion of Medical Science (to Dr. Sano), and a China Scholarship Council grant (to Dr. Wang). The authors have reported that they have no relationships relevant to the contents of this paper to disclose.

The authors attest they are in compliance with human studies committees and animal welfare regulations of the authors' institutions and Food and Drug Administration guidelines, including patient consent where appropriate. For more information, visit the *JACC: Basic to Translational Science* author instructions page.

Manuscript received January 16, 2019; revised manuscript received May 29, 2019, accepted May 29, 2019.

cells is commonly associated with rare myeloproliferative neoplasms (MPNs) including polycythemia vera, essential thrombocytopenia, and myelofibrosis that are generally associated with the aberrant production of red blood cells, platelets, and leukocytes (18,19). These diseases frequently lead to increased incidences of myocardial infarction, stroke, and deep vein thrombosis due to increased blood viscosity, clotting, and leukocytosis.

It is increasingly appreciated that there are many individuals who harbor the *JAK2*^{V617F} allele in leukocytes yet do not exhibit overt changes in levels of erythrocytes, platelets or leukocytes. A number of studies have detected the presence of the *JAK2*^{V617F} mutation in the leukocytes of individuals with no diagnosis of MPNs at frequencies ranging from 0.1% to 9.6% of the population depending on the method of detection and the cohort analyzed (20–23). More recently, the *JAK2*^{V617F} mutation in leukocytes has been appreciated to be associated with the condition of CHIP or ARCH (i.e., the detectable clonal amplification of the mutation with no associated changes in blood cell counts) (8,10,12,13,24–26). This *JAK2*^{V617F} -mediated clonal hematopoiesis has been associated with an increased incidence of cardiovascular disease (13). In light of these considerations, experimental studies are warranted to elucidate whether the *JAK2*^{V617F} mutation in the myeloid lineage can contribute to cardiovascular disease independently of high blood cell counts and the prothrombotic complications associated with MPNs. However, these experiments are confounded by the neoplasm phenotypes that are exhibited by murine models that harbor *Jak2*^{V617F} mutations (27–31).

In this study, we document that mice expressing *JAK2*^{V617F} display a strong bias toward amplification into the myeloid lineage in competitive bone marrow transplantation (BMT) experiments. Thus, a myeloid-specific lentivirus and BMT strategy was employed to specifically express *JAK2*^{V617F} exclusively in monocytes and neutrophils in blood following the transduction of lineage-negative bone marrow cells. These mice displayed normal levels of leukocytes, erythrocytes, and platelets. However, when challenged in 2 models of cardiac injury the *Jak2*^{V617F} mice displayed greater myocardial inflammation and pathological remodeling. These results raise the possibility that the acquisition and expansion of mutations within hypothetical monocyte or neutrophil-restricted progenitor cells could account for *JAK2*^{V617F}-mediated clonal hematopoiesis and subsequent cardiovascular disease.

METHODS

MICE. *Jak2*^{V617F} transgenic mice were provided by Zhizhuang Joe Zhao at the University of Oklahoma (31). Briefly, the human *JAK2*^{V617F} transgene is driven under the control of the vav1 promoter that drives expression in hematopoietic and vascular endothelial cells (32). The *JAK2*^{V617F} line was backcrossed with control C57BL6/J mice for several generations, and brought to homozygosity. All reported results were performed in animals homozygotes for the transgene. Genotyping was performed using quantitative reverse transcription polymerase chain reaction of the human *JAK2* gene (TaqMan primers from Applied Biosystems, Waltham, Massachusetts). Littermate wild-type mice were used as control animals. In lentivirus-mediated lineage-negative cell transfer experiments, wild-type C57BL/6J mice for both donor and recipient were purchased from The Jackson Laboratory (Stock# 000664) (Bar Harbor, Maine). Male mice were used for all the experiments. Mice were maintained on a 12-h light-dark schedule in a specific pathogen-free animal facility and given food and water ad libitum. The number of mice included in each study is indicated in the figures or the associated legends.

PLASMIDS AND LENTIVIRUS PRODUCTION. Myeloid-specific SP146-gp91 promoter-enhancer sequence was synthesized as described previously with some modifications (33). Full sequences are provided in Supplemental Figure 1. psPAX2 and pMD2.G were a gift from Didier Trono (Addgene, Watertown, Massachusetts, plasmids 12260 and 12259). Lentivirus particles were generated as described previously (34). Briefly, the plasmids (pLenti-SP146-gp91-JAK2, psPAX2, pMD2.G) were co-transfected to HEK293T cells with polyethylenimine (Cat# 24765-1, Polysciences, Warrington, Pennsylvania) and the supernatant was collected at 48 h after transfection. After filtration (40 μm), virus particles were concentrated by ultracentrifugation at a speed of 20,000 rpm for 3 h. The virus pellet was suspended with StemSpan medium (Cat# 09600, Stemcell Technologies, Cambridge, Massachusetts) without aeration and kept at -80°C. Lentiviral particle titer was determined using a Lenti-X qRT-PCR Titration Kit (Cat# 631235, Clontech, Mountain View, California).

ISOLATION OF LINEAGE-NEGATIVE CELLS AND LENTIVIRUS TRANSDUCTION. Lineage-negative cells were isolated from the bone marrow of C57BL/6J wild-type mice using a Lineage Cell Depletion Kit (Cat #130-090-858, Miltenyi Biotec, Somerville,

Massachusetts) according to manufacturer's instructions. Cells were pre-incubated with StemSpan medium for 1.5 h at 37°C. Lentivirus transduction was performed in the presence of 20 ng/ml of thrombopoietin, 50 ng/ml of stem cell factor 1, 4 μg/ml of polybrene, and 5 μg/ml of rapamycin for 16 to 20 h (35). Cells were washed and resuspended with RPMI medium before transplantation via the retro-orbital vein.

STATISTICS. Data are expressed as mean ± SEM, except for the boxplots which show minimum, 25th percentile, median, 75th percentile, and maximum. Shapiro-Wilk normality test was used to evaluate data distribution, and F test was used to evaluate homogeneity of variance. For normally distributed data with 1 experimental variable, unpaired (2-tailed) Student's *t*-test was used for comparing the difference between wild-type JAK2 ($JAK2^{WT}$) and $JAK2^{V617F}$ of transgenic mice strain in: CD41 expression of long-term hematopoietic stem cells (LT-HSCs), absolute numbers of white blood cells at 16 weeks after BMT, cardiac function parameters (posterior wall thickness at diastole, fractional shortening) at 2 months post-BMT; and also used for comparing the difference between $JAK2^{WT}$ and $JAK2^{V617F}$ of myeloid $JAK2^{V617F}$ mice strain in absolute numbers of white blood cells, hemoglobin, and platelets at 8 weeks after BMT; cardiac fibrosis at 14 days post-myocardial infarction (MI); absolute numbers of neutrophils and macrophages of enzymatically digested infarct area at 4 days post-MI; cardiac myocyte hypertrophy and cardiac fibrosis at 8 weeks post-transverse aortic constriction surgery (TAC); and transcript expression of *Col3a1* of heart tissue at 8 weeks post-TAC; and unequal variance *t* test was used for comparing the difference between $JAK2^{WT}$ and $JAK2^{V617F}$ of transgenic mice strain in absolute numbers of Hb at 16 weeks after BMT; and used for comparing the difference between $JAK2^{WT}$ and $JAK2^{V617F}$ of myeloid $JAK2^{V617F}$ mice strain in heart mass and lung weight at 8 weeks post-TAC, transcript expression of IL-6 and *Col1a1* of heart tissue at 8 weeks post-TAC; and used for comparing the difference of *JAK2* transgene expression between $CD11b^+$ cells and $CD31^+$ cells from hearts 7 days after MI; and 1-way analysis of variance (ANOVA) with post hoc Tukey's multiple comparison test was used for comparing the differences among green fluorescent protein (GFP), $JAK2^{WT}$ and $JAK2^{V617F}$ of THP-1 cells in gene expression (*Isg15, Mx1, Cxcl10*) at baseline. For non-normally distributed data with 1 experimental variable, Kruskal-Wallis test was used for comparing the difference between $JAK2^{WT}$ and $JAK2^{V617F}$ of transgenic mice strain in absolute numbers of platelets at 16 weeks after BMT; the difference between $JAK2^{WT}$ and $JAK2^{V617F}$ of myeloid $JAK2^{V617F}$ mice strain in absolute numbers of $Ly6C^{hi}$ monocytes of enzymatically digested infarct area at 4 days post-MI; macrophage accumulation in myocardium at 8 weeks post-TAC; transcript expression of *Anp*, *Bnp*, and *β/αMhc* of heart tissue at 8 weeks post-TAC; and the difference of *JAK2* transgene expression between $CD11b^+$ cells and $CD31^+$ cells from hearts 7 days after TAC. Kruskal-Wallis test with post hoc Dunn's multiple comparison test was used for comparing the differences among GFP, $Jak2^{WT}$, and $Jak2^{V617F}$ of THP-1 cells in gene expression (*Oas1*, *Oas2*) at baseline. For data with more than 1 experimental variable, 2-way ANOVA with post hoc Tukey's multiple comparison test was used for comparing the difference among GFP, $JAK2^{WT}$, and $JAK2^{V617F}$ of THP-1 cells in gene expression (IL-6, IL-1B, tumor necrosis factor alpha, C-C motif chemokine ligand 2[CCL2], absence in melanoma 2 [AIM2]) after lipopolysaccharide (LPS) stimulation; between $JAK2^{WT}$ and $JAK2^{V617F}$ of myeloid $JAK2^{V617F}$ mice strain in cytokine gene expression of heart tissue at both sham state and 7 days post-MI; and among GFP, $JAK2^{WT}$ and $JAK2^{V617F}$ of THP-1 cells in the gene expression (*Isg15*, *Mx1*, *Oas1*, *Oas2*) with or without treatment of ruxolitinib. Two-way repeated measures ANOVA with Sidak's multiple comparison test was selected as post hoc comparison for analysis between 2 groups at each time point. It was used for sequentially comparing the difference between $JAK2^{WT}$ and $JAK2^{V617F}$ of transgenic mice strain in the blood chimerism after BMT; and for sequentially comparing the difference between $JAK2^{WT}$ and $JAK2^{V617F}$ of myeloid $JAK2^{V617F}$ mice strain in cardiac function parameters (left ventricular end-systolic volume, left ventricular end-diastolic volume, ejection fraction) pre- and post-MI, and cardiac function parameters (posterior wall thickness at diastole, fractional shortening) pre- and post-TAC. Two-way repeated measures ANOVA with post hoc Tukey's multiple comparison test was selected as post hoc comparison for analysis among 3 groups at each time point. It was used for sequentially comparing the difference of blood chimerism among $JAK2^{WT}$-sham, $JAK2^{V617F}$-sham, and $JAK2^{V617F}$-MI mice pre- and post-surgery within each time point. All results were considered statistically significant at 0.05. All the statistical analyses were performed using GraphPad Prism 8 software (GraphPad Software, San Diego, California).

STUDY APPROVAL. Study protocols were approved by the Institutional Animal Care and Use Committees at Boston University and the University of Virginia.

Additional materials and methods are described in the Supplemental Appendix.

FIGURE 1 HSPCs Expressing *JAK2*^{V617F} Display a Competitive Advantage in a Competitive BMT Assay That Is Highly Restricted to the Myeloid Lineage

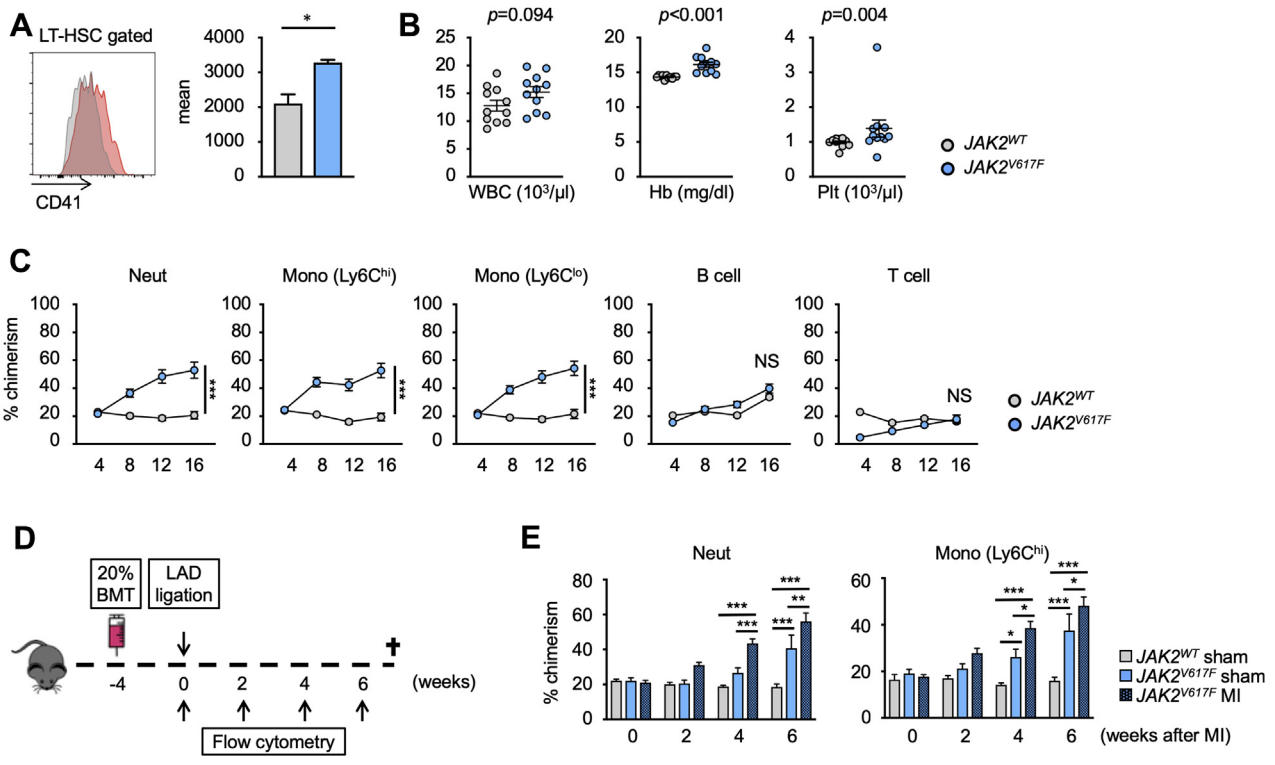

(A) Representative flow cytometry data to show that mutant Janus kinase 2 (valine to phenylalanine at residue 617) (*JAK2*^{V617F})–harboring long-term hematopoietic stem cell (LT-HSCs) display higher expression of CD41 protein compared with wild-type cells. LT-HSC population was defined as lineage$^-$, c-kit$^+$, Sca-1$^+$, CD48$^-$, and CD150$^+$ cells. n = 3 in each group. Data are presented as mean fluorescence intensity. Statistical analysis was performed using 2-tailed unpaired Student's *t*-test. **(B)** Absolute numbers of white blood cells, hemoglobin, and platelets of mice that underwent competitive transplantation with 20% *JAK2*^{V617F} bone marrow or 20% wild-type bone marrow at 16 weeks after bone marrow transplantation (BMT). Data are shown as mean ± SEM. Statistical analysis was performed using 2-tailed unpaired Student's *t* test (white blood cells [WBCs]), unequal variance *t* test (hemoglobin [Hb]), and Kruskal-Wallis test (platelets [Plt]). n = 11 in each group. **(C)** Flow cytometry analysis of peripheral blood showing that *JAK2*^{V617F} cells displayed a competitive advantage over wild-type Janus kinase 2 (*Jak2*^{WT}) competitor cells in a myeloid-biased manner. Peripheral blood was obtained at 4, 8, 12, and 16 weeks after BMT. n = 6 in *Jak2*^{WT} groups and n = 16 in *JAK2*^{V617F} groups. Statistical analysis was performed using 2-way repeated measures analysis of variance with Sidak's multiple comparison tests. Significance stars are from Sidak's tests. **(D)** Schematic that describes the experimental protocol. Left anterior descending artery (LAD) ligation surgery was performed 4 weeks after 20% competitive BMT. The chimerism of test cells in peripheral blood was evaluated by sequential flow cytometry analysis. **(E)** Flow cytometry analysis showing that experimental myocardial infarction (MI) induced by LAD ligation accelerates the expansion of *JAK2*^{V617F} myeloid cells in peripheral blood. n = 6 to 8 in each group. Statistical analysis was performed using 2-way repeated measures analysis of variance with Tukey's multiple comparison tests. Significance stars are from Tukey's tests. *p < 0.05, **p < 0.01, ***p < 0.001. NS = not significant.

RESULTS

HEMATOPOIETIC STEM AND PROGENITOR CELLS HARBORING *JAK2*^{V617F} PREFERENTIALLY EXPAND INTO MYELOID CELL POPULATIONS. LT-HSCs, defined as CD48$^-$ CD150$^+$ LSK cells, that harbor the *JAK2*^{V617F} mutation, have been reported to display increased expression of CD41, a marker of a myeloid-biased HSC population, in the experimental setting of BMT (36). Using a transgenic mouse strain that expresses human *JAK2*^{V617F} from the vav1 promoter (31), we find that the LT-HSC population also expresses an increased level of CD41 (p = 0.0125) (Figure 1A). To evaluate the functional characteristics of these LT-HSCs, we performed a competitive BMT assay in which lethally irradiated mice were transplanted with bone marrow cells containing 20% of test cells (vav1-*JAK2*^{V617F} or nonmutant cells expressing the CD45.2 variant) and 80% of wild-type competitor cells that expressed the CD45.1 variant. As shown in Figure 1B, analysis of the peripheral blood at 16 weeks after transplantation revealed a significant increase in hemoglobin levels (p < 0.001) and platelet counts (p = 0.004) in mice that were transplanted with bone

marrow cells from vav1-*Jak2*^{V617F} mice, consistent with MPN-like phenotypes. CD45.2 cell chimerism was also examined to evaluate the competitive fitness of the vav1-*Jak2*^{V617F} cells. The vav1-*Jak2*^{V617F} cells displayed a distinct bias to expand into neutrophils ($p < 0.001$) and monocytes ($p < 0.001$), and little or no evidence of expansion into lymphoid populations could be detected (**Figure 1C**). Mice that underwent competitive BMT with bone marrow from the vav1-*JAK2*^{V617F} mouse also displayed cardiac hypertrophy in the absence of surgical cardiac injury (posterior wall thickness at diastole, $p = 0.003$) (Supplemental Figure 2), consistent with a report showing that *Jak2*^{V617F} transgenic mice develop cardiac hypertrophy in the absence of experimental cardiac injury (37).

Because it has been reported that inflammation favors the expansion of *JAK2*^{V617F} cells relative to wild-type cells (38,39), we tested whether the systemic sterile inflammation caused by LAD ligation, a model of myocardial infarction, could accelerate the expansion of vav1-*Jak2*^{V617F} donor bone marrow–derived cells into myeloid cell populations (**Figure 1D**). LAD ligation or sham surgery was performed 1 month after competitive BMT with 20% vav1-*Jak2*^{V617F} or 20% wild-type bone marrow cells. LAD ligation was found to accelerate the expansion of vav1-*Jak2*^{V617F} cells into the myeloid lineage, suggesting that myocardial infarction confers an additional competitive advantage to the expansion of *Jak2* mutant cells (neutrophil: $p = 0.001$ at 4 weeks and $p = 0.003$ at 6 weeks post-MI; Ly6C^{hi} Monocyte: $p = 0.014$ at 4 weeks and $p = 0.043$ at 6 weeks post-MI) (**Figure 1E**). No differences were observed in the lymphoid populations (data not shown), and LAD ligation does not affect the frequencies of CD45.2-positive, wild-type cells in the different leukocyte populations (14).

MYELOID CELLS HARBORING THE *JAK2*^{V617F} MUTATION DISPLAY ENHANCED INFLAMMATORY PROPERTIES. To address the effect of *JAK2*^{V617F} mutation in myeloid populations, THP-1 cells were transduced with lentivirus expressing GFP, *JAK2*^{WT}, or *JAK2*^{V617F} from the SP146-gp47 myeloid-specific promoter/enhancer (Supplemental Figure 1A). Overexpression of exogenous wild-type JAK2 protein did not affect the activation status of signal transducer and activator of transcription (STAT) proteins by phosphorylation, but cells expressing *JAK2*^{V617F} displayed activation of STAT1 signaling that was indicated by robust phosphorylation of STAT1 at the Y701 and S727 residues (**Figure 2A**). The activation of STAT1 under these conditions was dependent on *JAK2*^{V617F} enzymatic activity, as it could be blocked by the JAK1/2 inhibitor ruxolitinib (**Figure 2B**). In the unstimulated state, THP-1 cells transduced with the mutated *Jak2*^{V617F} allele displayed upregulation of several interferon-responsive genes, *Isg15* ($p < 0.001$), *Mx1* ($p < 0.001$), *Oas1* ($p < 0.05$), *Oas2* ($p < 0.05$), and *Cxcl10* ($p < 0.001$) (Supplemental Figure 3), which is consistent with constitutive STAT1 activation. Ruxolitinib blocked the upregulation of these genes ($p < 0.001$) (Supplemental Figure 4).

Jak2^{V617F} requires interactions with homodimer type 1 cytokine receptors for growth factor–independent activation of JAK-STAT signaling (40). Thus, to identify the receptor in the monocytic cell line that fulfills this role, THP-1 cells were transduced with lentivirus encoding Cas9 clustered regularly interspaced short palindromic repeat-associated 9 (CRISPR), red fluorescent protein and a guide RNA targeting human interferon gamma receptor 1 (IFNGR1). Gene editing was confirmed by sequencing of the IFNGR1 locus (Supplemental Figure 5). This manipulation led to reductions in STAT1 phosphorylation in the *Jak2*^{V617F}-expressing cells (**Figure 2C**). These results indicate that *Jak2*^{V617F} requires IFNGR1 for downstream signal transduction in THP-1 cells. In contrast, similar manipulations targeting other cytokine receptors, including the interferon lambda receptor, the erythropoietin receptor, or the granulocyte colony-stimulating factor receptor, did not affect JAK2^{V617F}-STAT1 signaling (data not shown).

Upon stimulation with LPS, cells transduced with *Jak2*^{V617F} displayed significant upregulation of transcripts of various cytokines and chemokines, including IL-6 ($p < 0.001$), IL-1β ($p < 0.001$), tumor necrosis factor alpha ($p = 0.0001$) and CCL2 ($p < 0.001$), in addition to upregulation of the AIM2 inflammasome component ($p < 0.001$) (**Figure 2D**). In contrast, THP-1 cells expressing *Jak2*^{WT} did not exhibit enhanced inflammatory responses.

MYELOID *JAK2*^{V617F} EXPRESSION ACCELERATES HEART FAILURE IN RESPONSE TO EXPERIMENTAL MI. To address whether *Jak2*^{V617F}-mediated clonal expansion of myeloid cells contributes to cardiac dysfunction, we developed a strategy in which the expression of the *Jak2*^{V617F} mutation is restricted to myeloid populations. The goal was to avoid the expression of *Jak2*^{V617F} in vascular endothelial cells and in the erythroid and megakaryocyte populations that would lead to changes in erythrocyte and platelet numbers and confound the analysis of *Jak2*^{V617F}-mediated clonal hematopoiesis in the cardiovascular system. In this regard, the conditional Cre-mediated expression system that employs the

FIGURE 2 Myeloid Cells Transduced With the *JAK2*^{V617F} Allele Exhibit Enhanced Proinflammatory Properties

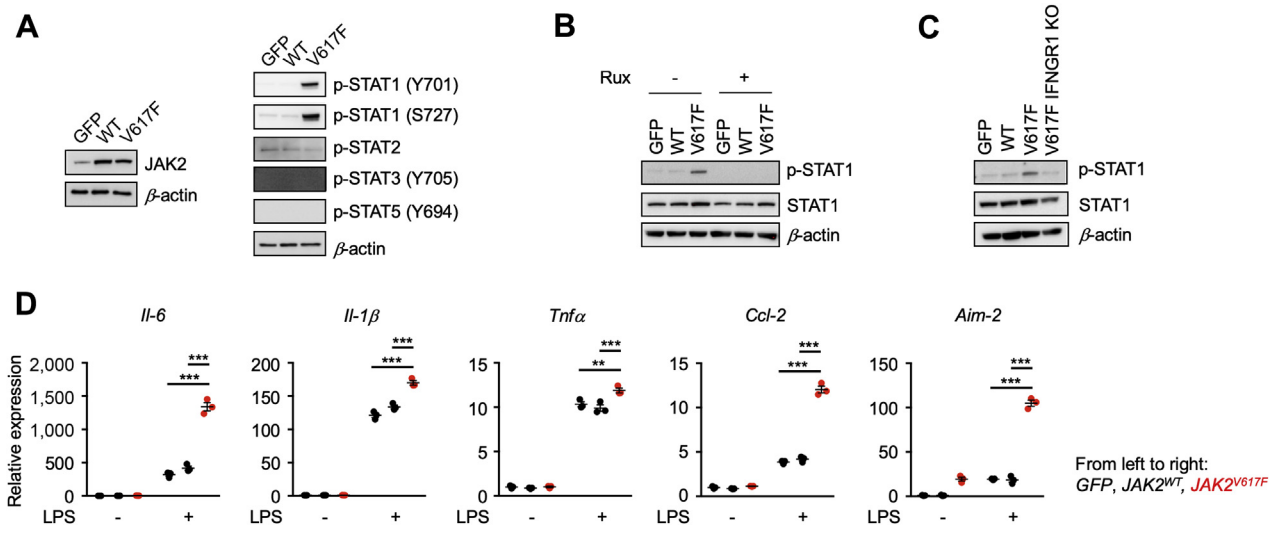

(A) Immunoblot analysis reveals modest overexpression of exogenous human *JAK2*^{WT} and *JAK2*^{V617F} in THP-1 cells using the lentivirus system **(left)**. Green fluorescent protein (GFP) was expressed in control cells. Signal transducer and activator of transcription (STAT) activities in each experimental group of cells were evaluated by immunoblot with antibodies that detect the level of activating phosphorylation. **(B)** THP-1 cells were treated with 1 μM of ruxolitinib or vehicle. STAT1 phosphorylation was evaluated by immunoblot analysis. **(C)** THP-1 cells harboring *JAK2*^{V617F} were transduced with a lentivirus encoding clustered regularly interspaced short palindromic repeats (CRISPR)/Cas9, red fluorescent protein, and single guide RNA targeting human interferon gamma receptor 1. STAT1 phosphorylation was evaluated by immunoblot analysis that detected decreased levels of phosphorylation in IFNGR1 knockout *Jak2*^{V617F} THP-1 cells. **(D)** Gene expression analysis of THP-1 cells transduced with lentivirus encoding GFP, *JAK2*^{WT}, or *JAK2*^{V617F} at 8 h after stimulation with 10 ng/ml lipopolysaccharide (LPS). n = 3 in each group. Data are shown as mean ± SEM. Statistical analysis was performed using 2-way analysis of variance with Tukey's multiple comparison tests. Significance stars are from Tukey's tests. *p < 0.05, **p < 0.01, ***p < 0.001. AIM2 = AIM2, interferon-inducible protein A2; CCL2 = C-C motif chemokine ligand 2; IL = interleukin; p-STAT = phosphorylated; signal transducer and activator of transcription; Rux = ruxolitinib; TNF = tumor necrosis factor; other abbreviations as in Figure 1.

Lyz2 promoter to drive *Jak2*^{V617F} expression in myeloid cells will also give rise to confounding MPN-like phenotypes due to a low level of Cre protein expression in hematopoietic stem and progenitor cell (HSPC) populations (30). Thus, we generated a lentivirus vector in which exogenous *Jak2* expression is under the control of the myeloid-specific SP146/gp91 promoter/enhancer, in which a minimal promoter sequence of human *gp91*^{phox} gene is fused to the synthetic SP146 element (33,41) (**Figure 3A**, Supplemental Figure 1B). To evaluate the fidelity of this system, we transduced lineage-negative bone marrow cells from wild-type mice with a lentivirus encoding GFP from the SP146/gp91 promoter/enhancer and transplanted these cells into lethally irradiated wild-type mice (**Figure 3B**). Flow cytometry analysis of peripheral blood at 8 weeks after transplantation revealed that GFP signal was predominantly observed in monocyte and neutrophil cell populations, with negligible GFP-positivity in lymphoid cells (**Figure 3C**). We also found little or no expression of exogenous *JAK2* gene in endothelial cells after cardiac injury models, further highlighting the specificity of our myeloid-specific promoter (Supplemental Figure 6). We also analyzed immune cell populations isolated from hearts at 4 days after LAD ligation and found that the lentivirus vector expressed the GFP transgene in cardiac neutrophils, monocytes, and macrophages (Supplemental Figure 7). Encouraged by these data, we then transduced lineage-negative cells from wild-type mice with a lentivirus encoding *JAK2*^{WT} or *JAK2*^{V617F} under the control of the myeloid-specific promoter and enhancer and transplanted these cells into lethally irradiated wild-type mice. Notably, these mice did not display MPN-like phenotypes and exhibited normal levels of hemoglobin and platelet counts at 8 weeks after transplantation (**Figure 3D**).

LAD ligation was then performed to establish a model of myocardial infarction, and the cardiac phenotypes of mice transduced with the myeloid-specific vectors expressing *JAK2*^{V617F} or *JAK2*^{WT} as control animals. At the 14 day termination of the experiment, mice transplanted with bone marrow

FIGURE 3 Mice With Myeloid-Specific *JAK2*^{V617F} Mutation Have Inferior Outcome After MI

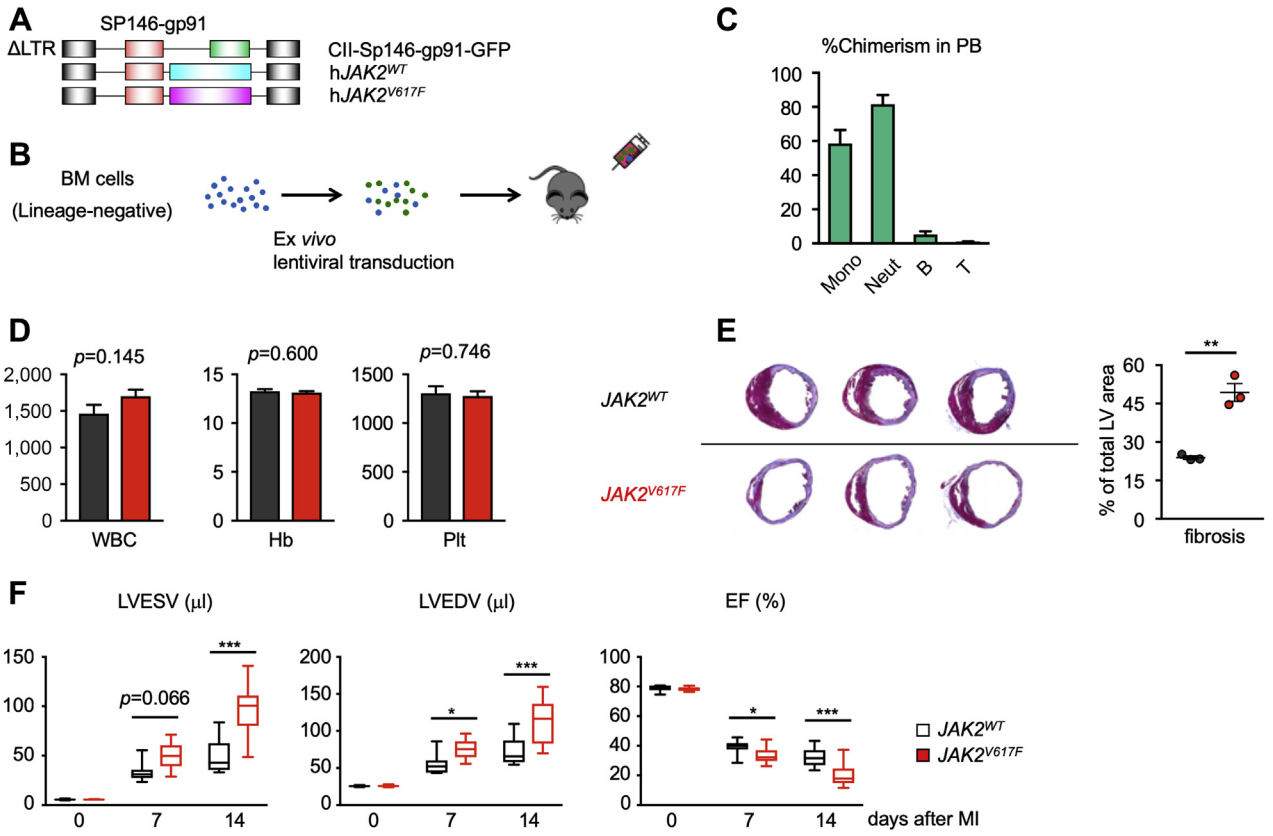

(A) Construction of the lentivirus vectors used in this study. SP146-gp91 is a myeloid-specific enhancer and promoter, respectively. **(B)** Schematic of the study. Bone marrow–derived lineage-negative cells were transduced with lentivirus ex vivo and transplanted to lethally irradiated mice. Mice were subjected to LAD ligation surgery 8 weeks after BMT and were observed for an additional 8 weeks. **(C)** The proportion of GFP-positive cells in the peripheral blood from mice reconstituted with lineage-negative cells transduced with GFP-encoding lentivirus vector. Blood cell populations were analyzed by flow cytometry. n = 3 in each group. Data are shown as mean ± SEM. **(D)** Analysis of peripheral blood parameters of mice from each group (*JAK2*^{WT} in **black** and *JAK2*^{V617F} in **red**, n = 6). Data are shown as mean ± SEM. Statistical analysis was performed using 2-tailed unpaired Student's *t* tests. **(E)** Representative cross-sectional images and analysis of Masson's trichrome staining for cardiac fibrosis from each group of mice (n = 3) after LAD ligation surgery at the end of the study. Data are shown as mean ± SEM. Statistical analysis was performed using 2-tailed unpaired Student's *t*-tests. **(F)** Sequential echocardiographic analysis of mice from each group (n = 11) before and after LAD ligation surgery at the indicated time points. Data are shown as minimum to maximum. Statistical analysis was performed using 2-way repeated measures analysis of variance with Sidak's multiple comparison tests. Significance stars are from Sidak's tests. **(G)** Analysis of transcript expression of proinflammatory cytokines in the infarct area were obtained from each group of mice 4 days after LAD ligation surgery. *36b4* was used as a reference for normalization. n = 8 in surgical groups and n = 4 in sham groups. Data are shown as mean ± SEM. Statistical analysis was performed by 2-way analysis of variance with Tukey's multiple comparison tests. Significance stars are from Tukey's tests. **(H)** Flow cytometry analysis of myeloid cell populations in the infarct area obtained from each group of mice 4 days after LAD ligation surgery. Cell numbers were normalized per 100-mg tissue weight. n = 6–7 in each group. Data are shown as mean ± SEM. Statistical analysis was performed using 2-tailed unpaired Student's *t* test (neutrophil [Neut], macrophage) or Kruskal-Wallis test (Ly6C^{hi}Mono). *p < 0.05, **p < 0.01, ***p < 0.001. B = B cell; EF = ejection fraction; LTR = long-terminal repeat; LVEDV = left ventricular end-diastolic volume; LVESV = left ventricular end-systolic volume; Mono = monocyte; PB = peripheral blood; T = T cell; other abbreviations as in Figures 1 and 2.

Continued on the next page

lineage-negative cells transduced with the myeloid-specific lentiviral vector expressing *JAK2*^{V617F} displayed enlarged infarct areas in histological analysis and an increase in fibrosis (p = 0.002) (Figure 3E). Before sacrifice, serial echocardiographic analysis revealed progressive dilatation of cardiac chamber size and deterioration of cardiac function in the *JAK2*^{V617F} group (p < 0.001) (Figure 3F). To evaluate the inflammatory status of the heart, quantitative polymerase chain reaction analysis was performed on tissues from the infarct areas at 7 days after LAD ligation in a separate group of mice. Consistent with

FIGURE 3 Continued

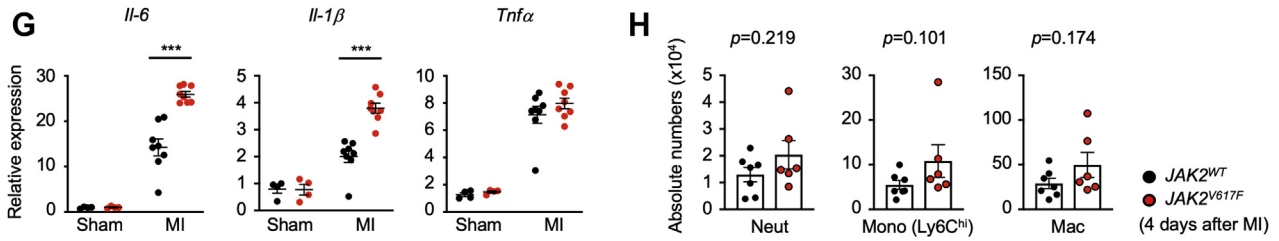

our observations in the transduced THP-1 cells (Figure 2), the infarcted myocardium of mice from the *JAK2*^{V617F} expression group displayed significantly increased expression of IL-6 ($p < 0.001$) and IL-1β ($p < 0.001$) transcript compared with mice from the *Jak2*^{WT} group (Figure 3G), indicating an enhanced inflammatory response in the infarct zone. Flow cytometry analysis of enzymatically digested infarct area 4 days after myocardial infarction showed trends toward increases in Ly6C^{hi} monocytes ($p = 0.101$), neutrophils ($p = 0.219$), and macrophages ($p = 0.174$) in the *JAK2*^{V617F} group (Figure 3H).

MYELOID *JAK2*^{V617F} EXPRESSION ACCELERATES NONISCHEMIC CARDIAC REMODELING. To corroborate and extend these findings in another model of heart failure, experiments were conducted in a model of pressure overload cardiac hypertrophy because there is a growing awareness that myeloid cell-mediated inflammatory responses contribute to pathological cardiac remodeling under these conditions (42-45). Thus, experimental groups of mice were transplanted with bone marrow lineage-negative cells transduced with the myeloid-specific lentiviral vector expressing the *JAK2*^{WT} and *JAK2*^{V617F} from the SP146/gp91 promoter/enhancer before TAC to promote cardiac hypertrophy (Figure 4A). Notably, these mice did not display cardiac hypertrophy in the absence of surgical cardiac injury (Figure 4C). This finding is in contrast to competitive BMT experiments employing bone marrow from mice that express *Jak2*^{V617F} under the vav1 promoter (Supplemental Figure 2), suggesting that cardiac hypertrophy in the absence of surgical cardiac injury is secondary to conditions associated with MPN phenotype and not a feature of myeloid restricted *Jak2*^{V617F} expression.

In response to pressure overload hypertrophy, the *JAK2*^{V617F} experimental group displayed significant increases in heart mass ($p < 0.001$) and lung weight ($p < 0.001$) indicative of congestion compared with mice from the *JAK2*^{WT} experimental group at 8 weeks post-surgery (Figure 4B). Sequential analysis of echocardiography revealed that the *JAK2*^{V617F} experimental group displayed significantly increased cardiac posterior wall thickness (Sidak's 95% confidence interval: -0.19 to -0.07; $p < 0.001$) and a progressive reduction of fractional shortening (Sidak's 95% confidence interval: 9.30 to 14.73; $p < 0.001$) (Figure 4C). Correspondingly, histological analyses revealed that the TAC-treated *JAK2*^{V617F} group displayed more cardiac myocyte hypertrophy ($p < 0.001$) (Figure 4D) and cardiac fibrosis ($p < 0.001$) (Figure 4E) following TAC. Immunohistological staining with Mac2 antibody revealed greater macrophage accumulation in the myocardium of the TAC *JAK2*^{V617F} group ($p = 0.012$) (Figure 4F), and these mice displayed greater IL-6 ($p = 0.002$), *Anp* ($p < 0.001$), *Bnp* ($p = 0.015$), *Col1a1* ($p = 0.010$), and *Col3a1* ($p = 0.058$) transcript expression and an increase in the ratio of β-to-α myosin heavy chain isoform ($p < 0.001$) (Figure 4G), indicative of greater inflammation, fibrosis, and cardiac dysfunction.

DISCUSSION

Myeloproliferative neoplasms are rare blood disorders that are frequently associated with somatic *JAK2*^{V617F} mutation in hematopoietic cells. These conditions lead to elevations in erythrocytes and platelets that have the potential to contribute to cardiovascular disease through increased blood viscosity and thrombotic complications (18,19,46). Additionally, these conditions are associated with leukocytosis that can also contribute to cardiovascular diseases (47-49). Recently, it has been recognized that asymptomatic adults display clonal events in their hematopoietic system that result from *JAK2*^{V617F} mutations, yet they do not display overt changes in leukocytes, erythrocytes, or platelets. This condition, referred to as clonal hematopoiesis (or CHIP or ARCH), is prevalent in the elderly population and has been associated with increased mortality and cardiovascular disease incidence (13). Clonal hematopoiesis associated with candidate genes that are

FIGURE 4 Mice With Myeloid-Specific *JAK2*^{V617F} Mutation Display Greater Dysfunction in a Model of Pressure-Overload Hypertrophy

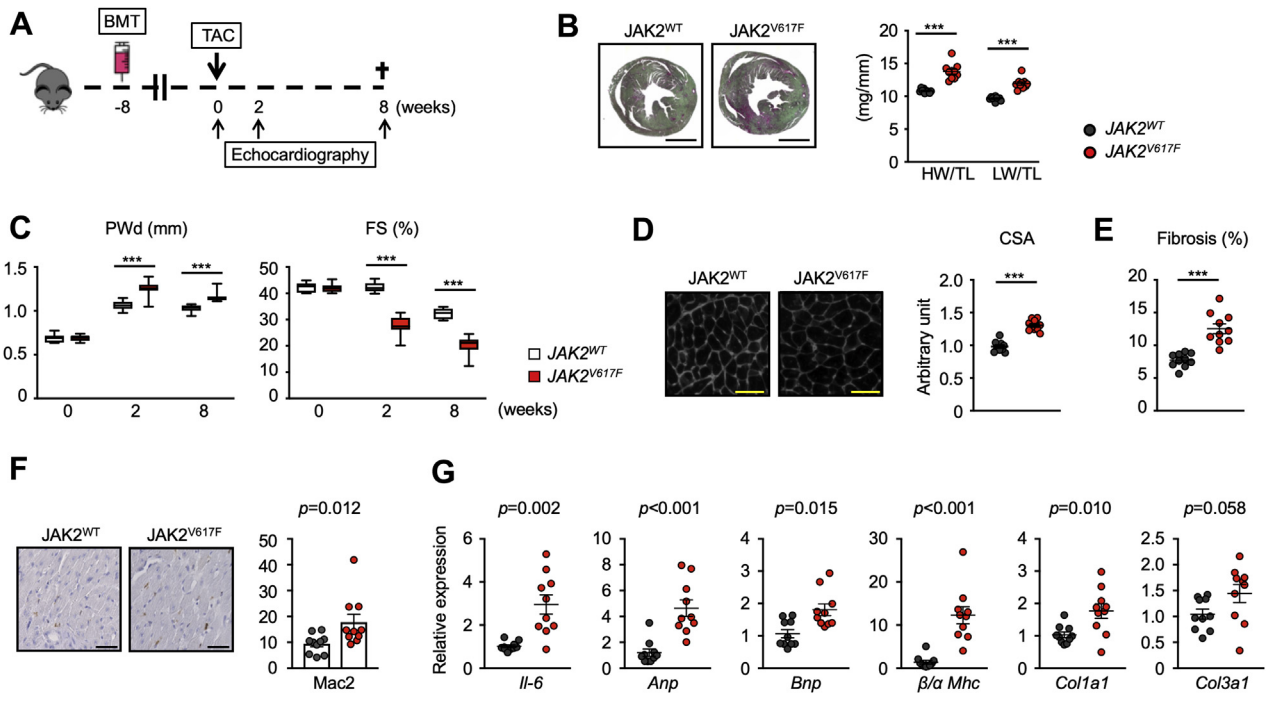

(A) Schematic of the study. Lethally irradiated wild-type mice were transplanted with lineage-negative cells that were transduced by myeloid-specific lentivirus expression vectors. These mice were subjected to transverse aortic constriction surgery (TAC) 8 weeks after BMT. Echocardiography was performed at the times indicated and mice were euthanized 8 weeks after TAC. **(B)** Representative images of Picrosirius red/Fast Green staining of the heart **(left)**, and heart weight and lung weight adjusted by tibia length **(right)** from each group (n = 10) at the end of the study. Scale bar = 3 mm. Data are shown as mean ± SEM. Statistical analysis was evaluated by unequal variance *t* test. **(C)** Sequential echocardiographic analysis of mice from each group (n = 10) before and after TAC at the indicated time points. Data are shown as minimum to maximum. Statistical analysis was evaluated by 2-way repeated measures analysis of variance with Sidak's multiple comparison tests. Significance stars are from Sidak's tests. **(D)** Representative images and analysis of wheat germ agglutinin staining of the heart sections from each group (n = 10) at the end of study. Scale bar = 100 μm. Data are shown as mean number per field. ± SEM. Statistical analysis was evaluated by 2-tailed unpaired Student's *t*-test. **(E)** Analysis of Picrosirius red/Fast Green staining of the heart sections from each group (n = 10) presented in **B**, at the end of study. Data are shown as mean ± SEM. Statistical analysis was evaluated by unequal variance *t* test. **(F)** Representative images and analysis of Mac2 staining of the sections of hearts from mice of each group (n = 10) at the end of study. Scale bar = 100 um. Data are shown as mean ± SEM, Mac2^{+} cells per field. Statistical analysis was evaluated by Kruskal-Wallis test. **(G)** Analysis of transcript expression in the myocardium obtained from each group of mice (n = 10) 8 weeks after TAC surgery. *36b4* was used as a reference for normalization. Data are shown as mean ± SEM. Statistical analysis was evaluated by 2-tailed unpaired Student's *t* test (*Col3a1*), unequal variance *t* test (IL-6, *Col1a1*) or by Kruskal-Wallis test (*Anp*, *Bnp*, *β/α MHC*). *p < 0.05, **p < 0.01, ***p < 0.001. CSA = cross-sectional area of myocyte; FS = fractional shortening; HW = heart weight; LW = lung weight; PWd = posterior wall thickness at diastole; TL = tibia length; other abbreviations as in Figure 1.

recurrently mutated in hematologic malignancies is estimated to occur in 10% of individuals who are older than 70 years of age. Of these, the activating *JAK2*^{V617F} mutation can account for a portion of the reported cases of clonal hematopoiesis cases, yet these individuals do not display abnormalities in total blood counts (10,13). Thus, the mechanisms leading to the increased cardiovascular disease incidence caused by *JAK2*^{V617F}-mediated clonal hematopoiesis are enigmatic.

Here, we evaluated the fitness of HSCs expressing a *JAK2*^{V617F} transgene to repopulate bone marrow in lethally irradiated mice using a competitive transplantation approach. Analysis of the blood of transplanted mice established that this BMT led to the preferential expansion of mutant *JAK2* hematopoietic cells to an extent that was comparable to the allelic fractions that are observed in individuals with clonal hematopoiesis (8,10,13). The kinetics of this expansion was similar to that previously observed in competitive transplantation experiments using bone marrow harboring inactivating mutations in *Tet2* but much more robust than what was observed with inactivating mutations in *Dnmt3a* (14-16), indicative of gene-specific effects of these mutations in the HSPC compartment. A particularly striking observation was that while the *Tet2* and *Dnmt3a* mutations in HSPCs tended to be multipotent and

represented in all progeny leukocytes, BMT experiments with the *JAK2*^{V617F} mutation displayed a nearly exclusive bias toward expansion into neutrophils and monocytes versus the lymphoid lineage. Consistent with these findings, a model of *Jak2*^{V617F} knock-in mice also display a myeloid bias of cell expansion (50,51). We and others also find that the *JAK2*^{V617F} mutation promotes the expression of CD41 in the LT-HSC population, a marker that is expressed on a subpopulation of myeloid-biased HSC that accumulate with age (36). Along these lines, lineage-restricted expansion is generally observed in patients with clonal hematopoiesis, typically with much higher mutant allele fractions in the myeloid population (52,53).

Although mice transplanted with *JAK2*^{V617F} bone marrow developed a strong expansion bias into myeloid cell populations, they also developed elevations in hemoglobin, platelets, and leukocytes that are associated with MPNs. These phenotypes are also observed in murine models of hematopoietic cell-specific *Jak2*^{V617F} expression (28–31). However, alterations in blood cell counts are generally not a feature of the clonal hematopoiesis that can arise from mutations in any 1 of multiple pre-leukemic genes including the *Jak2*^{V617F} variant. To account for these discrepant phenotypes between *JAK2*^{V617F}-mediated MPNs and clonal hematopoiesis, it has been proposed that heterogeneity among the HSC populations that acquire the *JAK2*^{V617F} mutation may contribute to the phenotypic diversity observed in this patient population (54). It is becoming increasingly recognized that distinct HSC subpopulations differ in their functional properties and display restricted lineage biases (55–59). Thus, it has been proposed that essential thrombocytopenia can result from a *JAK2*^{V617F} mutation that is acquired in megakaryocyte-restricted HSCs, whereas polycythemia vera can result when the mutation is acquired in HSCs that are destined for myeloid- or erythroid-restricted progeny (54). Support for these more complex lineage schemes comes from evidence of bypass pathways involving lineage-restricted progenitors that are self-renewing (56,57), and long-lived, lineage-biased HSCs that predominate in native hematopoiesis (58,60). Alternatively, it remains possible that clonal hematopoiesis and the diverse MPN disease phenotypes could result from the length of time that a patient harbors the mutation, the size of the clone, or the acquisition of additional driver gene mutations (61,62).

Previous studies have implicated *JAK2*^{V617F}-mediated clonal hematopoiesis without an MPN disease phenotype in cardiovascular disease (13). To model the effect of myeloid-restricted *JAK2*^{V617F} expression on the cardiovascular system, BMT experiments were conducted using lineage-negative cells that were transduced with a lentivirus vector expressing *JAK2*^{V617F} from the SP146/gp91 promoter/enhancer. This synthetic promoter/enhancer is active in myeloid cells of the blood and tissues (33,41), and it is more tissue restricted in this context than the LyzM promoter that is active in HSPCs in this context (30). Irradiated mice implanted with lineage negative cells transduced with the SP146/gp91-directed expression vector displayed high levels of transgene chimerism in the myeloid cells of the blood, but *JAK2*^{V617F} expression from this vector did not alter leukocyte, platelet, or hemoglobin levels. Mice treated in this manner were then subjected to the permanent LAD ligation model of myocardial infarction. In this model, myeloid-directed *JAK2*^{V617F} expression led to greater infarct size and a reduction in cardiac function that was associated with greater expression of IL-6 and IL-1β. To extend these studies, BMT using lineage negative cells transduced with the lentivirus vector expressing the *JAK2*^{V617F} allele from the myeloid-specific promoter/enhancer were also subjected to a model of pressure overload hypertrophy that is achieved by TAC. In this second model, myeloid-directed *JAK2*^{V617F} expression led to greater cardiac hypertrophy and fibrosis, which was accompanied by diminished cardiac function and increased lung congestion. Hearts from these mice also display greater macrophage infiltration and IL-6 expression. Based on these results, we hypothesize that clonal hematopoiesis that results in the expression of the *JAK2*^{V617F} mutation in circulating myeloid cells can contribute to myocardial disease independent of thrombocytosis, erythrocytosis or leukocytosis.

It is increasingly appreciated that inflammation plays a causal role in cardiovascular diseases (63–66). Here, we find that myeloid-directed *JAK2*^{V617F} expression can increase myocardial inflammation in murine models of heart failure and increase inflammatory responses in the THP-1 human monocytic cell line. Specifically, *JAK2*^{V617F} promotes the activating phosphorylation of STAT1 and increases the production of IL-6, IL-1β, tumor necrosis factor alpha, CCL2, and AIM2 in response to stimulation with LPS. Wild-type *JAK2* is normally associated with a cytokine receptor, and cytokine binding to its cognate receptor leads to the activation of *JAK2* via the trans-phosphorylation of a tyrosine residue in its activation loop (67). In contrast, the *JAK2*^{V617F} allele activates downstream targets without the requirement for cytokine stimulation, and it is therefore widely recognized as a constitutively active form. However,

binding to a cytokine receptor scaffold is still required for $JAK2^{V617F}$ to transmit a signal (40). While the receptors involved in $JAK2^{V617F}$ activation have been reported in several cell types, the receptors that confer this function in myeloid cells have not been elucidated. In the current study, we find that IFNGR1 is necessary for $JAK2^{V617F}$ to activate phosphorylated STAT1 signaling in THP-1 myeloid cells. Finally, because it has been reported that inflammation favors the expression of $JAK2^{V617F}$ hematopoietic cells to undergo clonal expansion relative to wild-type cells (38,39), we investigated whether the sterile inflammation brought about by infarction could accelerate the expansion of $JAK2^{V617F}$ mutant LT-HSCs. In a competitive BMT experiment, LAD ligation accelerated the expansion of vav1-$JAK2^{V617F}$ cells into the myeloid lineage. These data provide experimental evidence for a positive feedback loop where $JAK2^{V617F}$-mediated clonal hematopoiesis promotes cardiovascular disease, and vice versa, via modulation of inflammatory pathways.

A recent publication showed that $JAK2^{V617F}$ mutant neutrophils are prone to form neutrophil extracellular traps (NETs) and contribute to the thrombotic events that accompany myeloproliferative disease (68). NETs have been reported to promote cardiac dysfunction in the context of myocardial ischemia (69) and pressure overload (70). Thus, the formation of NETs could be another mechanism that can contribute to the cardiovascular consequences of the $JAK2^{V617F}$ mutation. However, JAK2 has cell type-specific functions, as it functions downstream of multiple receptors in different cell types to differentially activate specific downstream signaling pathways and produce different outcomes. Thus, in the current study, we focused on analyzing $JAK2^{V617F}$ mutations in the monocyte or macrophage population because they are widely recognized to be critical cells in cardiovascular disease models (64).

STUDY LIMITATIONS. In this study, we employed lentivirus-mediated expression of human $JAK2^{V617F}$ protein under synthetic promoter/enhancer to achieve myeloid-restricted expression of the protein to avoid confounding effects of polycythemia vera or essential thrombocythemia phenotypes. However, this is an overexpression and may not reflect the phenotype obtained from physiological levels of the driver gene mutation. Furthermore, these studies expressed the human JAK2 mutant in mouse hematopoietic cells, and this species mismatch could produce an additional confounding factor. Because of these limitations, further evaluation of $JAK2^{V617F}$ mutation in myeloid populations is warranted using more physiologically relevant models.

In addition, niche signals can shape tissue-resident immune cell function, For example, the transcriptomic landscapes of resident macrophage are dependent upon the tissue where they reside. Thus a deeper analysis of JAK2 mutant immune cells recruited to the heart could provide additional information about the pathogenic impact of JAK2-mediated clonal hematopoiesis in the setting of cardiac disease, which was not addressed in this study.

CONCLUSIONS

We show that $JAK2^{V617F}$ expression in HSPCs leads to the expansion of the mutant clones in a manner that is highly restricted to myeloid cells. This expression pattern differs markedly from HSPC that harbor mutations in *Tet2* or *Dnmt3a*, which display the ability to expand into all leukocyte populations in the competitive BMT model (14–16). Further, we developed a system to restrict $JAK2^{V617F}$ expression to differentiated blood myeloid cells following transduction of lineage-negative bone marrow cells that were implanted into lethally irradiated mice. Mice treated in this manner did not display alterations in blood cell or platelet levels, but they were more susceptible to myocardial inflammation and cardiac dysfunction in models of heart failure. We propose that $JAK2^{V617F}$ mutations can occur in a clonal subpopulation of HSC that exclusively gives rise to circulating myeloid cells that, in turn, contribute to cardiovascular disease risk through the overactivation of cytokine pathways. Thus, patients with $JAK2^{V617F}$-mediated clonal hematopoiesis may benefit form therapies that target pathways activated by this mutant kinase.

ACKNOWLEDGMENTS The authors thank Marieke Jones, PhD, and Data Services at the Health Sciences Library at the University of Virginia for advice on statistical analyses.

ADDRESS FOR CORRESPONDENCE: Dr. Kenneth Walsh, University of Virginia, Robert M. Berne Cardiovascular Research Center, 415 Lane Road, PO Box 801394, Suite 1010, Charlottesville, Virginia 22908. E-mail: kw9ar@virginia.edu.

PERSPECTIVES

COMPETENCY IN MEDICAL KNOWLEDGE: It is not clear why *JAK2*^{V617F} mutations in hematopoietic cells will lead to an MPN in some individuals and the condition of clonal hematopoiesis with no changes in blood cell counts in others. Furthermore, it is unknown how *JAK2*^{V617F}-mediated clonal hematopoiesis can contribute to cardiovascular disease risk independent of alterations in blood cell counts and pro-thrombotic complications associated with MPNs. Our competitive BMT studies in mice show that myeloid-restricted expression of the *Jak2*^{V617F} mutation will promote cardiac inflammation and dysfunction in models of heart failure in the absence of erythrocytosis, thrombosis, or leukocytosis.

TRANSLATIONAL OUTLOOK: These studies suggest that *JAK2*^{V617F}-mediated clonal hematopoiesis, in the absence of an MPN phenotype, can arise from the acquisition of these mutations in a hypothetical clonal population of progenitor cells that predominantly give rise to circulating myeloid cells. These *JAK2*^{V617F}-postive myeloid cells can contribute to cardiovascular disease risk through the overactivation of cytokine signaling. Individuals with *JAK2*^{V617F}-mediated clonal hematopoiesis may be protected from cardiovascular risk by JAK2 pathway inhibitors.

REFERENCES

1. Fuster JJ, Walsh K. Somatic mutations and clonal hematopoiesis: unexpected potential new drivers of age-related cardiovascular disease. Circ Res 2018;122:523–32.

2. Sano S, Wang Y, Walsh K. Clonal hematopoiesis and its impact on cardiovascular disease. Circ J 2018;83:2–11.

3. Jan M, Ebert BL, Jaiswal S. Clonal hematopoiesis. Semin Hematol 2017;54:43–50.

4. Busque L, Mio R, Mattioli J, et al. Nonrandom X-inactivation patterns in normal females: lyonization ratios vary with age. Blood 1996;88:59–65.

5. Busque L, Patel JP, Figueroa ME, et al. Recurrent somatic TET2 mutations in normal elderly individuals with clonal hematopoiesis. Nat Genet 2012;44:1179–81.

6. Goodell MA, Rando TA. Stem cells and healthy aging. Science 2015;350:1199–204.

7. Coombs CC, Zehir A, Devlin SM, et al. Therapy-related clonal hematopoiesis in patients with non-hematologic cancers is common and associated with adverse clinical outcomes. Cell Stem Cell 2017;21:374–382 e4.

8. Genovese G, Kahler AK, Handsaker RE, et al. Clonal hematopoiesis and blood-cancer risk inferred from blood DNA sequence. N Engl J Med 2014;371:2477–87.

9. Gibson CJ, Lindsley RC, Tchekmedyian V, et al. Clonal hematopoiesis associated with adverse outcomes after autologous stem-cell transplantation for lymphoma. J Clin Oncol 2017;35:1598–605.

10. Jaiswal S, Fontanillas P, Flannick J, et al. Age-related clonal hematopoiesis associated with adverse outcomes. N Engl J Med 2014;371:2488–98.

11. Loh PR, Genovese G, Handsaker RE, et al. Insights into clonal haematopoiesis from 8,342 mosaic chromosomal alterations. Nature 2018;559:350–5.

12. Zink F, Stacey SN, Norddahl GL, et al. Clonal hematopoiesis, with and without candidate driver mutations, is common in the elderly. Blood 2017;130:742–52.

13. Jaiswal S, Natarajan P, Silver AJ, et al. Clonal hematopoiesis and risk of atherosclerotic cardiovascular disease. N Engl J Med 2017;377:111–21.

14. Sano S, Oshima K, Wang Y, et al. Tet2-mediated clonal hematopoiesis accelerates heart failure through a mechanism involving the IL-1beta/NLRP3 inflammasome. J Am Coll Cardiol 2018;71:875–86.

15. Fuster JJ, MacLauchlan S, Zuriaga MA, et al. Clonal hematopoiesis associated with TET2 deficiency accelerates atherosclerosis development in mice. Science 2017;355:842–7.

16. Sano S, Oshima K, Wang Y, et al. CRISPR-mediated gene editing to assess the roles of Tet2 and Dnmt3a in clonal hematopoiesis and cardiovascular disease. Circ Res 2018;123:335–41.

17. Dorsheimer L, Assmus B, Rasper T, et al. Association of mutations contributing to clonal hematopoiesis with prognosis in chronic ischemic heart failure. JAMA Cardiol 2019;4:25–33.

18. Spivak JL. Myeloproliferative Neoplasms. N Engl J Med 2017;376:2168–81.

19. Tefferi A, Pardanani A. Myeloproliferative neoplasms: a contemporary review. JAMA Oncol 2015;1:97–105.

20. Nielsen C, Birgens HS, Nordestgaard BG, Bojesen SE. Diagnostic value of JAK2 V617F somatic mutation for myeloproliferative cancer in 49 488 individuals from the general population. Br J Haematol 2013;160:70–9.

21. Nielsen C, Birgens HS, Nordestgaard BG, Kjaer L, Bojesen SE. The JAK2 V617F somatic mutation, mortality and cancer risk in the general population. Haematologica 2011;96:450–3.

22. Sidon P, El Housni H, Dessars B, Heimann P. The JAK2V617F mutation is detectable at very low level in peripheral blood of healthy donors. Leukemia 2006;20:1622.

23. Xu X, Zhang Q, Luo J, et al. JAK2(V617F): Prevalence in a large Chinese hospital population. Blood 2007;109:339–42.

24. Abelson S, Collord G, Ng SWK, et al. Prediction of acute myeloid leukaemia risk in healthy individuals. Nature 2018;559:400–4.

25. Hinds DA, Barnholt KE, Mesa RA, et al. Germ line variants predispose to both JAK2 V617F clonal hematopoiesis and myeloproliferative neoplasms. Blood 2016;128:1121–8.

26. Xie M, Lu C, Wang J, et al. Age-related mutations associated with clonal hematopoietic expansion and malignancies. Nat Med 2014;20:1472–8.

27. Wang W, Liu W, Fidler T, et al. Macrophage inflammation, erythrophagocytosis, and accelerated atherosclerosis in Jak2 (V617F) mice. Circ Res 2018;123:e35–47.

28. Akada H, Yan D, Zou H, et al. Conditional expression of heterozygous or homozygous Jak2V617F from its endogenous promoter induces a polycythemia vera-like disease. Blood 2010;115:3589–97.

29. Mullally A, Lane SW, Ball B, et al. Physiological Jak2V617F expression causes a lethal myeloproliferative neoplasm with differential effects on hematopoietic stem and progenitor cells. Cancer Cell 2010;17:584–96.

30. Wang J, Hayashi Y, Yokota A, et al. Expansion of EPOR-negative macrophages besides erythroblasts by elevated EPOR signaling in erythrocytosis mouse models. Haematologica 2018;103:40–50.

31. Xing S, Wanting TH, Zhao W, et al. Transgenic expression of JAK2V617F causes myeloproliferative disorders in mice. Blood 2008;111:5109–17.

32. Georgiades P, Ogilvy S, Duval H, et al. VavCre transgenic mice: a tool for mutagenesis in hematopoietic and endothelial lineages. Genesis 2002;34:251–6.

33. Barde I, Laurenti E, Verp S, et al. Lineage- and stage-restricted lentiviral vectors for the gene therapy of chronic granulomatous disease. Gene Ther 2011;18:1087–97.

34. Sano S, Wang Y, Evans MA, et al. Lentiviral CRISPR/Cas9-mediated genome editing for the study of hematopoietic cells in disease models. J Vis Exp 2019;152:e59977.

35. Wang CX, Sather BD, Wang X, et al. Rapamycin relieves lentiviral vector transduction resistance in human and mouse hematopoietic stem cells. Blood 2014;124:913–23.

36. Gekas C, Graf T. CD41 expression marks myeloid-biased adult hematopoietic stem cells and increases with age. Blood 2013;121:4463–72.

37. Shi K, Zhao W, Chen Y, et al. Cardiac hypertrophy associated with myeloproliferative neoplasms in JAK2V617F transgenic mice. J Hematol Oncol 2014;7:25.

38. Arranz L, Sanchez-Aguilera A, Martin-Perez D, et al. Neuropathy of haematopoietic stem cell niche is essential for myeloproliferative neoplasms. Nature 2014;512:78–81.

39. Fleischman AG, Aichberger KJ, Luty SB, et al. TNFalpha facilitates clonal expansion of JAK2V617F positive cells in myeloproliferative neoplasms. Blood 2011;118:6392–8.

40. Lu X, Levine R, Tong W, et al. Expression of a homodimeric type I cytokine receptor is required for JAK2V617F-mediated transformation. Proc Natl Acad Sci U S A 2005;102:18962–7.

41. He W, Qiang M, Ma W, et al. Development of a synthetic promoter for macrophage gene therapy. Hum Gene Ther 2006;17:949–59.

42. Wang Y, Sano S, Oshima K, et al. Wnt5a-mediated neutrophil recruitment has an obligatory role in pressure overload-induced cardiac dysfunction. Circulation 2019;140:487–99.

43. Wang L, Zhang YL, Lin QY, et al. CXCL1-CXCR2 axis mediates angiotensin II-induced cardiac hypertrophy and remodelling through regulation of monocyte infiltration. Eur Heart J 2018;39:1818–31.

44. Liao X, Shen Y, Zhang R, et al. Distinct roles of resident and nonresident macrophages in nonischemic cardiomyopathy. Proc Natl Acad Sci U S A 2018;115:E4661–9.

45. Patel B, Bansal SS, Ismahil MA, et al. CCR2(+) monocyte-derived infiltrating macrophages are required for adverse cardiac remodeling during pressure overload. JACC Basic Transl Sci 2018;3:230–44.

46. Barbui T, Finazzi G, Falanga A. Myeloproliferative neoplasms and thrombosis. Blood 2013;122:2176–84.

47. Carobbio A, Finazzi G, Guerini V, et al. Leukocytosis is a risk factor for thrombosis in essential thrombocythemia: interaction with treatment, standard risk factors, and Jak2 mutation status. Blood 2007;109:2310–3.

48. Landolfi R, Di Gennaro L, Barbui T, et al. Leukocytosis as a major thrombotic risk factor in patients with polycythemia vera. Blood 2007;109:2446–52.

49. Campbell PJ, MacLean C, Beer PA, et al. Correlation of blood counts with vascular complications in essential thrombocythemia: analysis of the prospective PT1 cohort. Blood 2012;120:1409–11.

50. Lundberg P, Takizawa H, Kubovcakova L, et al. Myeloproliferative neoplasms can be initiated from a single hematopoietic stem cell expressing JAK2-V617F. J Exp Med 2014;211:2213–30.

51. Yang Y, Akada H, Nath D, Hutchison RE, Mohi G. Loss of Ezh2 cooperates with Jak2V617F in the development of myelofibrosis in a mouse model of myeloproliferative neoplasm. Blood 2016;127:3410–23.

52. Arends CM, Galan-Sousa J, Hoyer K, et al. Hematopoietic lineage distribution and evolutionary dynamics of clonal hematopoiesis. Leukemia 2018;32:1908–19.

53. Buscarlet M, Provost S, Zada YF, et al. Lineage restriction analyses in CHIP indicate myeloid bias for TET2 and multipotent stem cell origin for DNMT3A. Blood 2018;132:277–80.

54. Mead AJ, Mullally A. Myeloproliferative neoplasm stem cells. Blood 2017;129:1607–16.

55. Eaves CJ. Hematopoietic stem cells: concepts, definitions, and the new reality. Blood 2015;125:2605–13.

56. Sanjuan-Pla A, Macaulay IC, Jensen CT, et al. Platelet-biased stem cells reside at the apex of the haematopoietic stem-cell hierarchy. Nature 2013;502:232–6.

57. Yamamoto R, Morita Y, Ooehara J, et al. Clonal analysis unveils self-renewing lineage-restricted progenitors generated directly from hematopoietic stem cells. Cell 2013;154:1112–26.

58. Sun J, Ramos A, Chapman B, et al. Clonal dynamics of native haematopoiesis. Nature 2014;514:322–7.

59. Laurenti E, Gottgens B. From haematopoietic stem cells to complex differentiation landscapes. Nature 2018;553:418–26.

60. Haas S, Trumpp A, Milsom MD. Causes and consequences of hematopoietic stem cell heterogeneity. Cell Stem Cell 2018;22:627–38.

61. Chen E, Schneider RK, Breyfogle LJ, et al. Distinct effects of concomitant Jak2V617F expression and Tet2 loss in mice promote disease progression in myeloproliferative neoplasms. Blood 2015;125:327–35.

62. McKerrell T, Park N, Chi J, et al. JAK2 V617F hematopoietic clones are present several years before MPN diagnosis and follow different expansion kinetics. Blood Adv 2017;1:968–71.

63. Libby P. Interleukin-1 beta as a target for atherosclerosis therapy: biological basis of CANTOS and beyond. J Am Coll Cardiol 2017;70:2278–89.

64. Nahrendorf M. Myeloid cell contributions to cardiovascular health and disease. Nat Med 2018;24:711–20.

65. Ridker PM. Residual inflammatory risk: addressing the obverse side of the atherosclerosis prevention coin. Eur Heart J 2016;37:1720–2.

66. Swirski FK, Nahrendorf M. Cardioimmunology: the immune system in cardiac homeostasis and disease. Nat Rev Immunol 2018;18:733–44.

67. Jatiani SS, Baker SJ, Silverman LR, Reddy EP. Jak/STAT pathways in cytokine signaling and myeloproliferative disorders: approaches for targeted therapies. Genes Cancer 2010;1:979–93.

68. Wolach O, Sellar RS, Martinod K, et al. Increased neutrophil extracellular trap formation promotes thrombosis in myeloproliferative neoplasms. Sci Transl Med 2018;10:eaan8292.

69. Savchenko AS, Borissoff JI, Martinod K, et al. VWF-mediated leukocyte recruitment with chromatin decondensation by PAD4 increases myocardial ischemia/reperfusion injury in mice. Blood 2014;123:141–8.

70. Martinod K, Witsch T, Erpenbeck L, et al. Peptidylarginine deiminase 4 promotes age-related organ fibrosis. J Exp Med 2017;214:439–58.

KEY WORDS clonal hematopoiesis, left ventricular hypertrophy, myocardial infarction

APPENDIX For an expanded Methods section as well as supplemental figures and tables, please see the online version of this paper.

JACC: BASIC TO TRANSLATIONAL SCIENCE VOL. 4, NO. 6, 2019

EDITORIAL COMMENT

A New Murine Model of Clonal Hematopoiesis Investigates *JAK2*^{V617F} in Heart Failure*

Aniruddh P. Patel, MD,[a,b,c] Pradeep Natarajan, MD, MMSc[a,b,c]

Aging is often the strongest risk factor for diverse cardiovascular diseases. The mechanisms by which aging influences these conditions are poorly understood. A common feature of aging hematopoietic stem cells, whose progeny interface with and influence diverse organ systems, is the acquisition and selection of acquired mutations. When such mutations are clonally selective, they are linked to future risk of hematologic malignancy. Given the general infrequency of hematologic malignancy in the population and, thus, overall low absolute risk conferred, this phenomenon has been termed "clonal hematopoiesis of indeterminate potential" (CHIP; a.k.a., age-related clonal hematopoiesis [ARCH]).

Recent work indicates that CHIP is independently associated with other age-related phenotypes outside of cancer, most notably in atherosclerotic cardiovascular disease. Mutations in genes leading to CHIP commonly occur in methylation and transcriptional regulators such as *DNMT3A*, *TET2*, and *ASXL1*, as well as in genes promoting cellular growth and division such as *JAK2*. When individuals are sequenced very deeply, most individuals harbor deleterious mutations in these genes among very small populations of blood cells. By definition, CHIP is the presence of such mutations with a variant allele frequency (VAF) of at least 2%, indicating a degree of clonal expansion. Using this definition, 1% of individuals younger than 50 years of age are carriers, and 10% of individuals older than 65 years are carriers. In addition to increased risk for hematologic malignancy, there is a 1.4-fold all-cause mortality risk. Carriers are at increased risk for coronary artery disease and early onset myocardial infarction, independent of age. Atherogenic murine models of bone marrow *Tet2* and *Dnmt3a* deficiency are linked to heightened development of atherosclerosis (1).

Recent studies have begun to shed light on the associations and mechanistic underpinnings of CHIP and the development of congestive heart failure (CHF) under pathophysiologic stressors. Previous studies by Sano et al. (2,3) have demonstrated a role for *Tet2* deficiency in the incidence of greater cardiac dysfunction in pressure overload and chronic ischemia-induced CHF by using murine models of hematopoietic and myeloid-only *Tet2* deficiency. Furthermore, those studies implicated interleukin-1 beta (IL-1β) as the key mediator of *Tet2* deficiency and CHF development (2,3). By using a lentivirus vector and clustered regularly interspaced short palindromic repeats (CRISPR)-mediated gene editing, the authors demonstrated heightened cardiac hypertrophy, dysfunction, and fibrosis in response to angiotensin II infusion in the setting of murine

*Editorials published in *JACC: Basic to Translational Science* reflect the views of the authors and do not necessarily represent the views of *JACC: Basic to Translational Science* or the American College of Cardiology.

From the [a]Center for Genomic Medicine and Cardiovascular Research Center, Massachusetts General Hospital, Boston, Massachusetts; [b]Program in Population and Medical Genetics, Broad Institute of Harvard and Massachusetts Institute of Technology, Cambridge, Massachusetts; and the [c]Department of Medicine, Harvard Medical School, Boston, Massachusetts. Supported by National Heart, Lung, and Blood Institute grants R01HL148565 and R01HL148050 and Fondation Leducq grant TNE-18CVD04(Dr. Natarajan). Dr. Natarajan has received support from Amgen, Apple, and Boston Scientific; and is a scientific advisor to Apple and Blackstone Life Sciences. Dr. Patel is supported by National Heart, Lung, and Blood Institute grant T32HL007208.

The authors attest they are in compliance with human studies committees and animal welfare regulations of the authors' institutions and Food and Drug Administration guidelines, including patient consent where appropriate. For more information, visit the *JACC: Basic to Translational Science* author instructions page.

ISSN 2452-302X https://doi.org/10.1016/j.jacbts.2019.09.003

models with *Tet2*-deficient bone marrow versus wild-type bone marrow (3). Investigation in humans has further implicated the role of CHIP in CHF. In a study of 200 patients with prevalent CHF, individuals found to have mutations in *DNMT3A* and *TET2* had a 2.1-fold increased incidence of death or CHF hospitalization compared to those without these mutations (4).

The *JAK2* mutation V617F (*JAK2*^{V617F}) particularly is associated with an increased risk for atherosclerotic cardiovascular disease, potentially with distinct mechanisms. Prior studies linked *JAK2*^{V617F} with increased formation of neutrophil extracellular traps, extracellular strands of DNA and histone proteins expelled by neutrophils to trap microorganisms as part of innate immunity, thereby increasing the risk of thrombosis (5). However, the mechanistic relationship between the *JAK2*^{V617F} mutant and CHF remains unclear.

SEE PAGE 684

In this issue of *JACC: Basic to Translational Science*, Sano et al. (6) present transgenic mouse models of *JAK2*^{V617F} in clonal hematopoiesis and shed light on the mutant's role in response to models of CHF. The authors performed competitive *JAK2*^{V617F} transgenic mouse bone marrow transplantations into irradiated wild-type mice and demonstrate phenotypes similar to myeloproliferative neoplasms. These mice were shown to have increased de novo cardiac hypertrophy believed to be a response to myeloproliferative neoplasia, as previously observed. To more closely approximate CHIP (i.e., without notable blood cell count changes or neoplastic features), the authors also performed myeloid-specific *JAK2*^{V617F} transduction by using a lentivirus, limiting *JAK2*^{V617F} expression to neutrophils, monocytes, and macrophages (6). Importantly, these mice did not develop cardiac hypertrophy. In their model, the authors demonstrated that myeloid cells harboring the *JAK2*^{V617F} mutation displayed enhanced inflammatory properties dependent on downstream STAT signaling. After exposing these mice to stressors of coronary artery ligation-induced myocardial infarction and aortic constriction-induced pressure overload, the authors demonstrated that the expression of myeloid *JAK2*^{V617F} in mice led to accelerated cardiac remodeling, larger infarct size, and more cardiac dysfunction.

These studies continue to advance our understanding of CHIP, with prior models interrogating *Tet2* and *Dnmt3a*, and now new models for *JAK2* which help highlight its role in CHIP-related cardiovascular disease (3). The authors' myeloid-specific *JAK2*^{V617F} transgene expression model resulted in clonal hematopoiesis without affecting hematopoietic cell line counts, similar to CHIP (6).

This study provides additional evidence supporting CHIP as a risk factor of CHF development in murine heart failure models. Although this finding remains consistent with observations in humans that CHIP may exacerbate complications when CHF is manifest (4), data implicating CHIP for the onset of CHF in humans are currently lacking. Furthermore, because CHF is characterized by diverse causes and manifestations, it is unclear how homogenously CHIP may contribute to the risk of diverse CHF types. The study by Sano et al. (6) indicates that CHIP may exacerbate CHF risk across diverse genes under 2 distinct stressors, ischemia (i.e., coronary artery ligation) and pressure overload (i.e., transaortic clamp). Nevertheless, human validation of these types for heart failure are required to better understand clinical scope.

The authors demonstrated that human monocyte cells transduced by *JAK2*^{V617F} have greater expression of the inflammatory cytokines IL-1β, IL-6, tumor necrosis factor-alpha, and C-C chemokine ligand 2 when stimulated with lipopolysaccharide. Similarly, the authors show that myeloid-restricted *JAK2*^{V617F} transgenic mice undergoing coronary artery ligation express greater levels of IL-1β and IL-6 in the infarct zone. Recently, the authors implicated these interleukins in similar heart failure models for *Dnmt3a* and *Tet2* bone marrow deficiency (2). In prior studies, they mitigated cardiac maladaptation through inhibition of the pathway through an NLRP3 inflammasome inhibitor. The present study does not show similar rescue experiments, and it remains unclear whether consequential inflammatory changes from *JAK2*^{V617F} causally promote heart failure.

A general challenge of current CHIP murine models is the relatively rapid bone marrow reconstitution of hematopoietic cells with mutations of CHIP genes when altered bone marrow is transplanted. Limited longitudinal human analyses indicate relatively stable VAF over years. Nevertheless, our understanding of the kinetics and consequences of changing CHIP VAF is limited. Larger longitudinal analyses of CHIP in humans may help better inform the interpretation of murine models.

CHIP represents a new putative risk factor for CHF requiring human validation. The present

JACC: BASIC TO TRANSLATIONAL SCIENCE VOL. 4, NO. 6, 2019
OCTOBER 2019:698–700

paper by Sano et al. (6) shows consistent cardiac effects across multiple CHIP genes and murine models of heart failure. These exciting studies implicate a distinct pathophysiology not presently detected by current CHF risk prediction approaches nor addressed by current risk reduction strategies.

ADDRESS FOR CORRESPONDENCE: Dr. Pradeep Natarajan, Center for Genomic Medicine and Cardiovascular Research Center, Massachusetts General Hospital, 185 Cambridge Street, CPZN 3.184, Boston, Massachusetts 02114. E-mail: pnatarajan@mgh.harvard.edu. Twitter: @pnatarajanmd.

REFERENCES

1. Patel AP, Natarajan P. Completing the genetic spectrum influencing coronary artery disease: from germline to somatic variation. Cardiovasc Res 2019;115:830–43.

2. Sano S, Oshima K, Wang Y, et al. *Tet2*-mediated clonal hematopoiesis accelerates heart failure through a mechanism involving the IL-1β/NLRP3 inflammasome. J Am Coll Cardiol 2018;71:875–86.

3. Sano S, Oshima K, Wang Y, Katanasaka Y, Sano M, Walsh K. CRISPR-mediated gene editing to assess the roles of *Tet2* and *Dnmt3a* in clonal hematopoiesis and cardiovascular disease. Circ Res 2018;123:335–41.

4. Dorsheimer L, Assmus B, Rasper T, et al. Association of mutations contributing to clonal hematopoiesis with prognosis in chronic ischemic heart failure. JAMA Cardiol 2019;4:25–33.

5. Wolach O, Sellar RS, Martinod K, et al. Increased neutrophil extracellular trap formation promotes thrombosis in myeloproliferative neoplasms. Sci Transl Med 2018;10:eaan8292.

6. Sano S, Wang Y, Yura Y, et al. *JAK2*^{V617F}-mediated clonal hematopoiesis accelerates pathological remodeling in murine heart failure. J Am Coll Cardiol Basic Trans Science 2019;4:684–97.

KEY WORDS clonal hematopoiesis, heart failure, left ventricular hypertrophy

JACC: BASIC TO TRANSLATIONAL SCIENCE VOL. 4, NO. 6, 2019

PRECLINICAL RESEARCH

Cardioprotective Effects of VCP Modulator KUS121 in Murine and Porcine Models of Myocardial Infarction

Yuya Ide, MD,[a] Takahiro Horie, MD, PhD,[a] Naritatsu Saito, MD, PhD,[a] Shin Watanabe, MD, PhD,[a] Chiharu Otani, MD,[a] Yui Miyasaka, BSc,[a] Yasuhide Kuwabara, MD, PhD,[a] Tomohiro Nishino, MD, PhD,[a] Tetsushi Nakao, MD, PhD,[a] Masataka Nishiga, MD, PhD,[a] Hitoo Nishi, MD, PhD,[a] Yasuhiro Nakashima, MD, PhD,[a] Fumiko Nakazeki, MD, PhD,[a] Satoshi Koyama, MD, PhD,[a] Masahiro Kimura, MD,[a] Shuhei Tsuji, MD,[a] Randolph Ruiz Rodriguez, MD,[a] Sijia Xu, MD,[a] Tomohiro Yamasaki, MD,[a] Toshimitsu Watanabe, MD,[a] Masamichi Yamamoto, PhD,[b] Motoko Yanagita, MD, PhD,[b,c] Takeshi Kimura, MD, PhD,[a] Akira Kakizuka, MD, PhD,[d] Koh Ono, MD, PhD[a]

VISUAL ABSTRACT

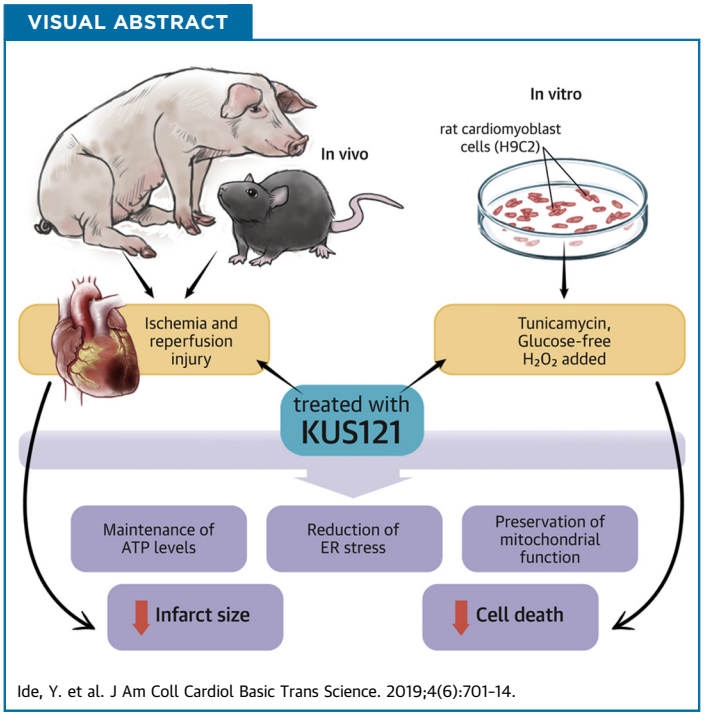

Ide, Y. et al. J Am Coll Cardiol Basic Trans Science. 2019;4(6):701–14.

HIGHLIGHTS

- **KUS121 was developed to selectively inhibit the adenosine triphosphatase activity of valosin-containing protein without affecting other cellular functions of valosin-containing protein.**
- **KUS121 preserved adenosine triphosphate levels, reduced endoplasmic reticulum stress, and suppressed cell death in H9C2 rat cardiomyoblast cells, treated with tunicamycin or hydrogen peroxide, or cultured in glucose-free medium.**
- **In murine ischemia and reperfusion injury models, KUS121 treatment after reperfusion attenuated the infarcted size and preserves cardiac function by maintaining adenosine triphosphate levels and reducing ER stress.**
- **In porcine ischemia and reperfusion injury models, intracoronary administration of KUS121 also attenuated the infarcted area in a dose-dependent manner.**
- **These results indicated that KUS121 is a promising novel therapeutic agent for myocardial infarction.**

ISSN 2452-302X https://doi.org/10.1016/j.jacbts.2019.06.001

ABBREVIATIONS AND ACRONYMS

AAR = area at risk

ATP = adenosine triphosphate

ATPase = adenosine triphosphatase

BiP = immunoglobulin heavy chain-binding protein

CHOP = C/EBP homologous protein

CMR = cardiac magnetic resonance

EF = ejection fraction

ER = endoplasmic reticulum

FRET = fluorescence resonance energy transfer

FS = fractional shortening

H_2O_2 = hydrogen peroxide

HF = heart failure

I/R = ischemia and reperfusion

IBMPFD = inclusion body myopathy associated with Paget's disease of bone and frontotemporal dementia

IHD = ischemic heart disease

KUS121 = Kyoto University Substance 121

LAD = left anterior descending artery

LV = left ventricular/ventricle

MI = myocardial infarction

PCI = percutaneous coronary intervention

TTC = triphenyltetrazolium chloride

TUNEL = terminal deoxynucleotidyl transferase dUTP nick-end labeling

VCP = valosin-containing protein

SUMMARY

No effective treatment is yet available to reduce infarct size and improve clinical outcomes after acute myocardial infarction by enhancing early reperfusion therapy using primary percutaneous coronary intervention. The study showed that Kyoto University Substance 121 (KUS121) reduced endoplasmic reticulum stress, maintained adenosine triphosphate levels, and ameliorated the infarct size in a murine cardiac ischemia and reperfusion injury model. The study confirmed the cardioprotective effect of KUS121 in a porcine ischemia and reperfusion injury model. These findings confirmed that KUS121 is a promising novel therapeutic agent for myocardial infarction in conjunction with primary percutaneous coronary intervention.
(J Am Coll Cardiol Basic Trans Science 2019;4:701–14)

Ischemic heart disease (IHD) is a leading cause of death worldwide. Of the 17.5 million cardiovascular deaths in 2012, an estimated 7.4 million deaths were due to IHD (1). In the United States, more than 360,000 people died of IHD in 2015, and IHD accounted for 43.8% of deaths from cardiovascular disease (2). In Japan, IHD accounted for 35.6% of deaths from heart disease in 2016 (3).

In patients with acute myocardial infarction (MI), early reperfusion therapy using primary percutaneous coronary intervention (PCI) is performed to reduce the infarct size and improve outcomes (4). However, when a larger infarct size remains after primary PCI, the rates of all-cause mortality and hospitalization for heart failure (HF) are still high (5). High mortality from HF and rehospitalization for HF are becoming serious concerns from both health care and medical cost perspectives (2,6).

To further reduce infarct sizes and improve clinical outcomes, new treatments in addition to early reperfusion therapy are needed. Indeed, drugs such as an inhibitor of Na^+/H^+ exchanger and cyclosporine A were reported to have cardioprotective effects in animal experiments (7) or in small clinical trials (8). However, these effects were not confirmed in multicenter, randomized, double-blind clinical trials (9,10). Although many other clinical trials of novel therapies for acute MI are ongoing, there are currently no therapeutic agents available to reduce infarct size and improve clinical outcomes (11).

SEE PAGE 715

Valosin-containing protein (VCP) is a member of the adenosine triphosphatase (ATPase) associated with diverse cellular activities family, and it is expressed ubiquitously in almost all cell types. As reported previously, in addition to ATPase activity, VCP is involved in various cellular functions, including proteasome-mediated protein degradation, endoplasmic reticulum (ER)-associated degradation, lysosomal protein degradation, autophagy, cell cycle progression, membrane fusion, and so on (12). Gain-of-function mutations in VCP have been reported to cause inclusion body myopathy associated with Paget's disease of bone and frontotemporal dementia (IBMPFD) (13), and IBMPFD-causing mutations in VCP result in elevated ATPase activity (14). The major clinical phenotypes of IBMPFD are myopathy, bone

From the [a]Department of Cardiovascular Medicine, Kyoto University Graduate School of Medicine, Kyoto, Japan; [b]Department of Nephrology, Kyoto University Graduate School of Medicine, Kyoto, Japan; [c]Institute for the Advanced Study of Human Biology, Kyoto University, Kyoto, Japan; and the [d]Laboratory of Functional Biology, Kyoto University Graduate School of Biostudies and Solution Oriented Research for Science and Technology, Kyoto, Japan. This work was supported by Ministry of Education, Culture, Sports, Science and Technology and Japan Society for the Promotion of Science Grant Nos. 18K15888 (to Dr. Ide), 17K09860 (to Dr. Horie), JP1605297 (to Dr. Kimura), 16H05151 (to Dr. Kakizuka), and 17H04177 and 17H05599 (to Dr. Ono), and a visionary research grant (Step) from the Takeda Science Foundation (to Dr. Ono). In relation to this manuscript, Kyoto University has applied for a patent (Tokugan 2018-078272). Drs. Ide, Horie, Saito, Kimura, Kakizuka, and Ono are named as inventors on the patent. Dr. Kakizuka owns stock in Kyoto Drug Discovery and Development Co., Ltd., a start-up company for the development of VCP modulators. All other authors have reported that they have no relationships relevant to the contents of this paper to disclose. The authors attest they are in compliance with human studies committees and animal welfare regulations of the authors' institutions and Food and Drug Administration guidelines, including patient consent where appropriate. For more information, visit the *JACC: Basic to Translational Science* author instructions page.

Manuscript received March 20, 2019; revised manuscript received June 12, 2019, accepted June 12, 2019.

lesions, and dementia, but it is notable that cardiac phenotypes, such as dilated cardiomyopathy, are also manifested in certain IBMPFD patients (15).

Kyoto University Substance 121 (KUS121) was developed to selectively inhibit the ATPase activity of VCP without affecting other cellular functions of VCP. Indeed, KUS121 has been shown to maintain cellular adenosine triphosphate (ATP) levels, reduce ER stress, and prevent cell death in vitro without showing any toxic effects (16). KUS121 has also been shown to elicit neuroprotective effects in murine retinitis pigmentosa models, murine glaucoma models, rat retinal ischemic injury models, and murine Parkinson's disease models (16–19).

Considering the cardiac phenotype in IBMPFD patients and the neuroprotective effect of KUS121 in vivo, we anticipated that KUS121 may produce a cardioprotective effect in IHD. In this study, we found that KUS121 preserved ATP levels, reduced ER stress, and suppressed cell death in H9C2 rat cardiomyoblast cells. Furthermore, in murine and porcine ischemia and reperfusion (I/R) injury models, KUS121 ameliorated cardiac damage and preserved cardiac function. These results indicated that KUS121 is a promising novel therapeutic agent for MI.

METHODS

This study was approved by the Kyoto University Ethics Review Board. Additional detailed methods are available in the Supplemental Appendix.

I/R INJURY MODELS IN MICE. In 8-week-old mice, the left anterior descending (LAD) coronary artery was ligated with a PE-10 tube. After 45 min of ischemia, reperfusion was induced by untying the knot and removing the tube. At 7 days after reperfusion, Masson's trichrome staining was performed to evaluate the infarcted area.

For quantification of heart ATP levels, I/R injury protocols using GO-ATeam2 mice were performed. ATeam biosensors are a series of fluorescence resonance energy transfer (FRET)-based indicators for ATP, which are able to estimate relative ATP levels in live cells in real time (20). Go-ATeam2 mice were developed by genetically integrating the GO-ATeam expression cassette into mice (M. Yamamoto, unpublished data, July 2019) (19); thus, the in vivo orange fluorescent protein and green fluorescent protein FRET ratio depends on the relative cellular ATP levels (21).

Analysis in murine IR injury models was performed by an experimenter who was blinded to treatment groups.

I/R INJURY MODELS IN PIGS. In 3-month-old pigs, the LAD was occluded using a 3.0 × 20-mm balloon (Terumo, Tokyo, Japan). After 60 min of occlusion, reperfusion was induced by deflation of the balloon.

At 7 days after reperfusion, to evaluate the infarcted area, gadolinium enhanced cardiac magnetic resonance (CMR) and double staining with triphenyltetrazolium chloride (TTC) and Evans blue were performed, and analyzed by an experimenter who was blinded to treatment groups.

STATISTICAL ANALYSIS. Measured data are presented as mean ± SEM. For statistical comparisons between 2 groups, unpaired Student's *t* test was used. For statistical analysis of 3 or more groups, 1-way analysis of variance was used. In 1-way analysis of variance, Sidak's post hoc test was performed to compare all pairs of groups and Dunnett's post hoc test to compare 1 group as a control with the other groups. A p value of <0.05 was considered as statistically significant. Statistical analyses were performed using GraphPad Prism 6 (GraphPad Software, San Diego, California).

RESULTS

VCP MESSENGER RNA IS EXPRESSED IN HUMAN AND MURINE HEARTS, ESPECIALLY IN CARDIOMYOCYTES. We first analyzed the expression levels of VCP messenger RNAs in various human organs (**Figure 1A**) and mice (**Figure 1B**). VCP expression levels in the human heart were comparable to that in central nervous tissues. VCP expression was also confirmed in the mouse heart and its expression in cardiomyocytes was 2-fold higher than in fibroblasts (**Figure 1C**).

KUS121 PRESERVES ATP LEVELS, REDUCES ER STRESS, AND SUPPRESSES CELL DEATH IN CULTURED H9C2 CELLS. To examine the cell protective effect of KUS121 on cardiomyocytes, H9C2 rat cardiomyoblast cells were treated with tunicamycin or cultured in glucose-free medium to induce cell death. KUS121 suppressed cell death and maintained ATP levels in tunicamycin-treated H9C2 cells in a dose-dependent manner (**Figures 2A to 2C**). KUS121 also preserved ATP levels and protected H9C2 cells against cell death when the cells were cultured in glucose-free medium (**Figures 2D and 2E**). KUS121 reduced ER stress, which was determined by the reduction in C/EBP homologous protein (CHOP) and immunoglobulin heavy chain-binding protein (BiP) levels in these conditions, without changing VCP expression levels (**Figures 2F and 2G**). In addition, KUS121 reduced hydrogen peroxide (H_2O_2)-induced H9C2 cell death (**Figure 2H**). KUS121 itself did not affect cell growth or cellular ATP levels, or CHOP, BiP, or VCP

FIGURE 1 VCP Is Expressed in Human and Murine Hearts, Especially in Cardiomyocytes

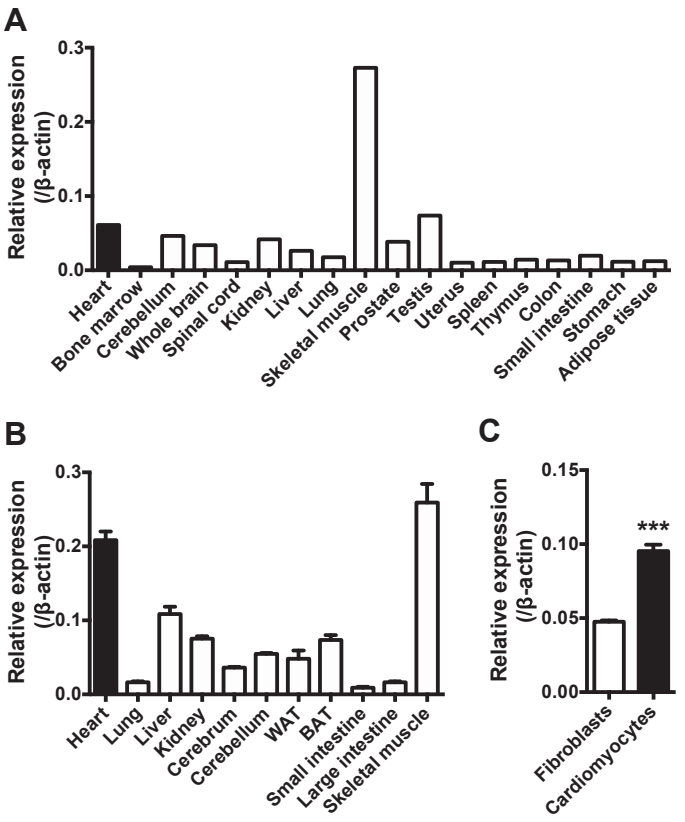

Expression levels of valosin-containing protein (VCP) in various **(A)** human organs and **(B)** mouse organs (n = 4). The human samples were from various sources, pooled from 1 or more healthy adults (Human Total RNA Master Panel II, Clontech Laboratories, Mountain View, California). Expression of β-actin was used as an internal control. **Black bars** indicate expression in hearts. **(C)** Comparison of VCP expression in cardiomyocytes (n = 4) with that in fibroblasts (n = 4). ***p < 0.001, using unpaired 2-tailed Student's *t* test. Data are presented as mean ± SEM. BAT = brown adipose tissue; WAT = white adipose tissue.

expression levels (Supplemental Figures 1A to 1C) in normal culture conditions.

KUS121 PRESERVES MITOCHONDRIAL FUNCTION AFTER TUNICAMYCIN TREATMENT. It is known that ER stress and ischemia affect mitochondrial functions (22–24); therefore, we examined mitochondrial functions using an XF96 extracellular flux analyzer (Agilent Technologies, Santa Clara, California). H9C2 cells were treated with tunicamycin in the absence or presence of KUS121 for 6 h, and the oxygen consumption rate was measured (**Figure 3A**). The numbers of H9C2 cells in these conditions were similar to that in normal culture (Supplemental Figure 2A). The parameters of mitochondrial respiration, such as basal respiration, ATP production–linked respiration, maximal respiration, spare respiratory capacity, and proton leak were calculated, as shown in Supplemental Figure 2B. The parameters of mitochondrial respiration were lower in H9C2 cells treated with tunicamycin than in control cells (**Figures 3B to 3F**). However, the parameters of mitochondrial respiration were preserved in tunicamycin and KUS121-treated cells, similar to those in normal cells without tunicamycin treatment. KUS121 also significantly increased mitochondrial respiration in normal culture conditions (Supplemental Figures 2C to 2H). Thus, the protective effects of KUS121 against H9C2 cell death are most likely mediated by ATP preservation, ER stress reduction, and conservation of mitochondrial functions.

KUS121 PRETREATMENT ATTENUATES CARDIAC DAMAGE AND PRESERVES CARDIAC FUNCTION IN MURINE ISCHEMIA AND REPERFUSION INJURY MODELS. Based on the in vitro cell protective effects on H9C2 cardiomyoblast cells, we next investigated whether KUS121 had protective effects on ischemic hearts by use of a murine I/R injury model. KUS121 was injected intraperitoneally at a dose of 160 mg/kg, which was followed by LAD coronary artery occlusion for 45 min (Supplemental Figure 3A). Subsequently, KUS121 was reinjected at the same dose once every 24 h for 6 days after reperfusion. Using Masson's trichrome staining at 7 days after reperfusion, the infarcted area-to-left ventricular (LV) area ratios in KUS121-treated mice were significantly lower than those in nontreated mice (control mice hereafter) (Supplemental Figures 3B and 3C). We also measured the infarcted area-to-area at risk (AAR) and AAR-to-LV ratios by double staining with TTC and Evans blue (Supplemental Figure 3D). The infarcted area-to-AAR ratios of KUS121-treated mice were significantly lower than were those in control mice, whereas the AAR-to-LV ratios were indistinguishable, compared with control mice (Supplemental Figures 3E and 3F). The expression of CHOP was significantly reduced in the border and remote zone, but not in the ischemic zone (Supplemental Figure 3G).

By echocardiographic analysis, both ejection fraction (EF) and fractional shortening (FS) in mice with I/R injury without KUS121 were reduced, compared with sham-operated mice, at 7 days after reperfusion. However, the systolic function of KUS121-treated mice was preserved at almost the same level as that in sham-operated mice (Supplemental Figures 4A to 4E). We also performed serial echocardiography at 1, 3, 7, 14, and 28 days after reperfusion (Supplemental Figure 3A). EF, FS, and LV systolic diameters were significantly preserved throughout the time course in KUS121-treated I/R mice, compared with I/R control mice (Supplemental Figures 4F to 4I).

FIGURE 2 KUS Preserves ATP Levels, Reduces Endoplasmic Reticulum Stress, and Suppresses Cell Death in Cultured Cells

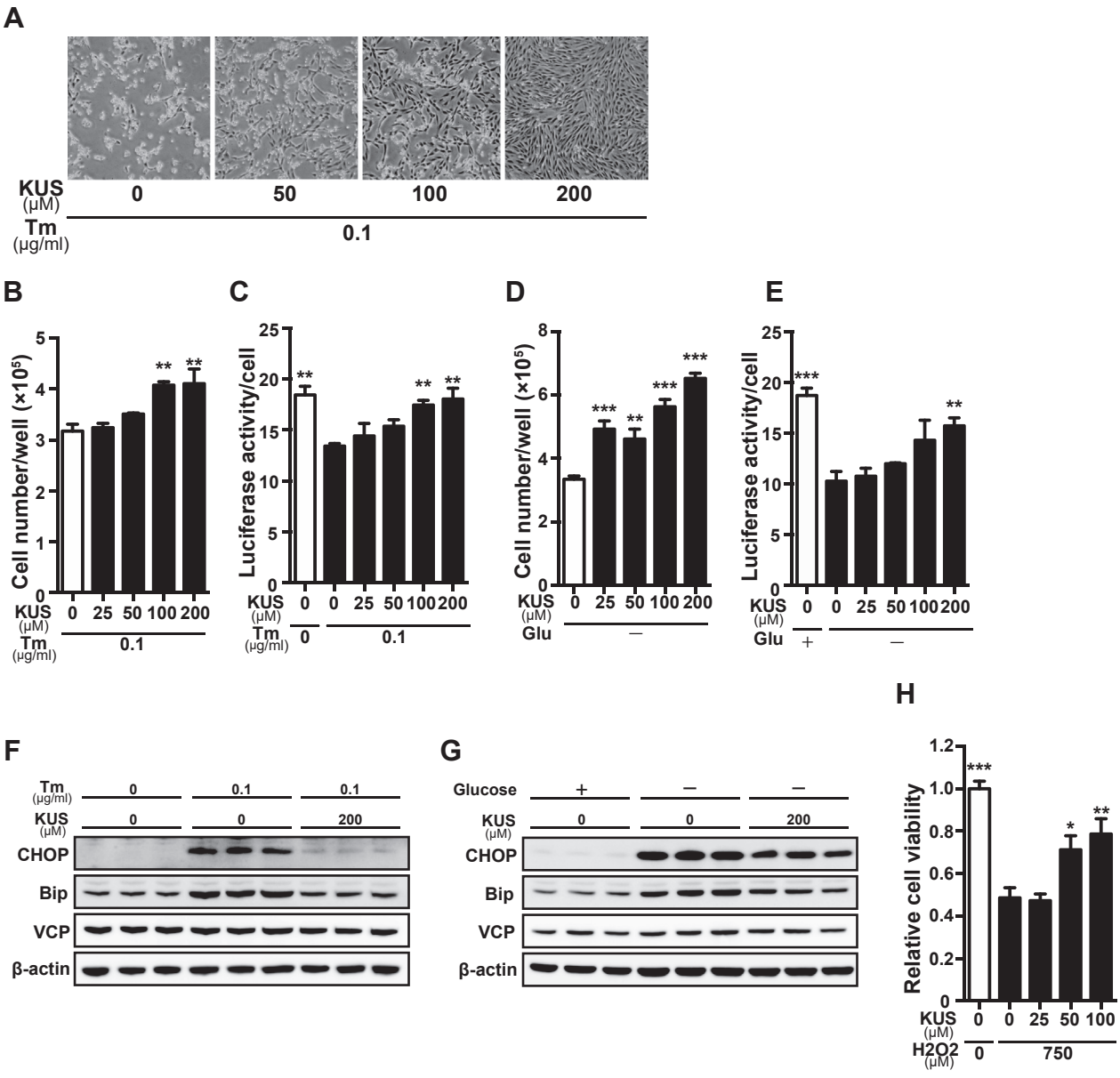

(A) Representative images of H9C2 rat cardiomyoblast cells cultured with tunicamycin (Tm) (0.1 μg/ml) for 48 h with different concentrations of Kyoto University Substance 121 (KUS) (50, 100, and 200 μM). **(B to E)** Number and adenosine triphosphate (ATP) levels of H9C2 cells **(B, C)** cultured with Tm (0.1 μg/ml) for 48 h or **(D, E)** cultured in glucose-free medium (Glu−) for 48 h, with different concentrations of KUS (25, 50, 100, and 200 μM) (n = 3). **(B, C)** **p < 0.01 vs. Tm (0.1 μg/ml) without KUS; **(D, E)** **p < 0.01, ***p < 0.001 vs. Glu− without KUS using 1-way analysis of variance with Dunnett's post hoc test. **(F, G)** Western blotting analysis of H9C2 cells **(F)** cultured with Tm (0.1 μg/ml) for 12 h or **(G)** cultured in Glu− for 24 h, with and without KUS (200 μM, n = 3). **(G)** Relative viability of H9C2 cells treated with hydrogen peroxide (H_2O_2) (750 μM) for 24 h with different concentrations of KUS (25, 50, and 100 μM) (n = 7). Viability of cells in normal culture conditions was the reference, indicated as 1. *p < 0.05, **p < 0.01, ***p < 0.001 vs. H_2O_2 (750 μM) without KUS using 1-way analysis of variance with Dunnett's post hoc test. All data are presented as mean ± SEM. BiP = immunoglobulin heavy chain-binding protein; CHOP = C/EBP homologous protein; VCP = valosin-containing protein.

FIGURE 3 KUS Preserves Mitochondrial Function After Tm Treatment

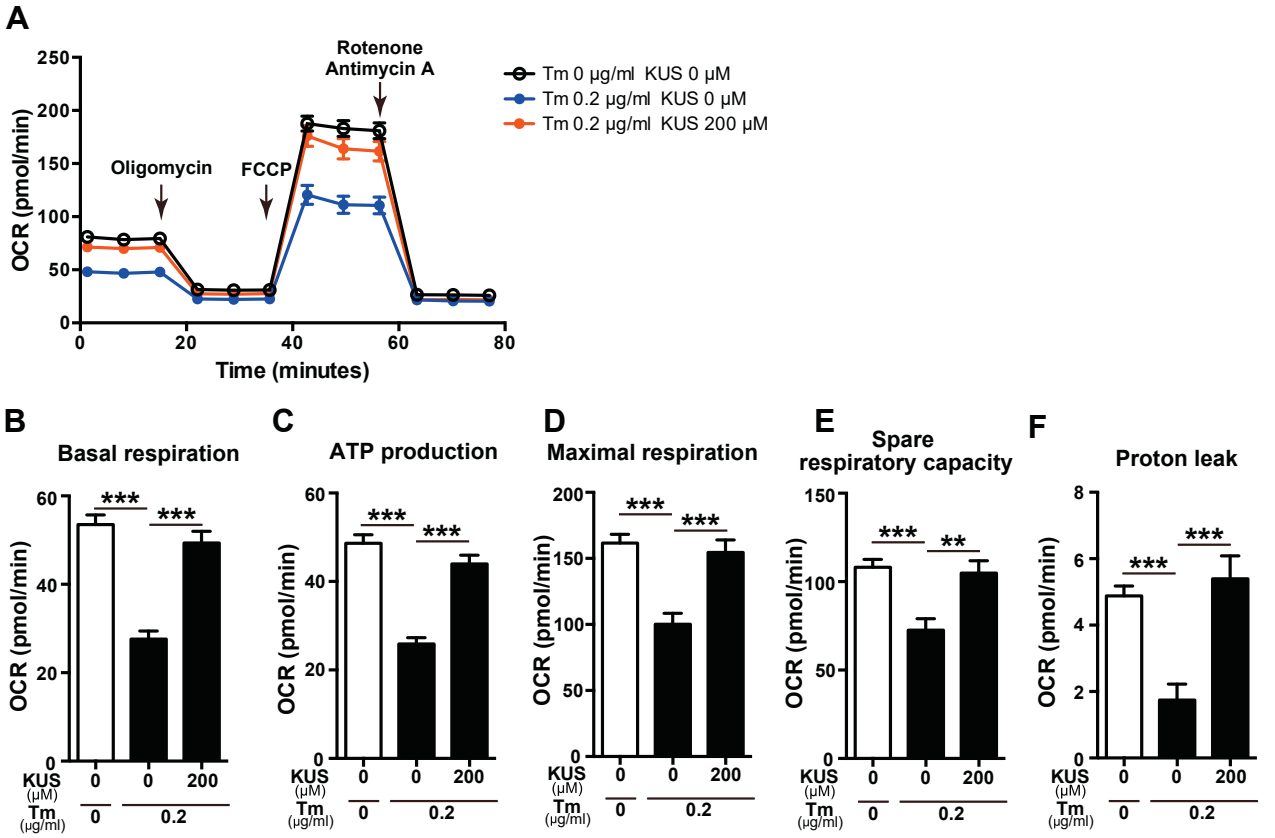

(A) Oxygen consumption rate (OCR) measured using an XF96 extracellular flux analyzer in H9C2 cells treated with Tm (0.2 μg/ml) and KUS (200 μM). After basal OCR was measured, oligomycin (2 μM), carbonyl cyanide-4-(trifluoromethoxy)phenylhydrazone (FCCP) (1 μM), and a mix of rotenone (1 μM) and antimycin A (1 μM), were added sequentially to assess mitochondrial respiration. OCR at each time point was obtained from an average of 10 replicate wells and presented as mean ± SEM. **(B to F)** Parameters of mitochondrial respiration: **(B)** basal respiration, **(C)** adenosine triphosphate (ATP) production–linked respiration, **(D)** maximal respiration, **(E)** spare respiratory capacity, and **(F)** proton leak. $^{**}p < 0.01$, $^{***}p < 0.001$, using 1-way analysis of variance with Sidak's post hoc test. Data are presented as mean ± SEM. Abbreviations as in Figure 2.

KUS121 TREATMENT AFTER REPERFUSION ALSO ATTENUATES THE INFARCTED SIZE AND PRESERVES CARDIAC FUNCTION. Next, we examined whether KUS121 could produce therapeutic benefits even when administered after I/R injury. Immediately after reperfusion, 80 mg/kg of KUS121 was injected intravenously, and the same amount was administered intraperitoneally (Figure 4A). Subsequently, KUS121 was repeatedly injected intraperitoneally at a dose of 160 mg/kg daily until 4 days after reperfusion. As a result, the infarcted area-to-LV area ratios were significantly reduced in KUS121-treated mice at 7 days after reperfusion compared with control mice (Figures 4B and 4C). The expression of CHOP was significantly reduced in the border zone (Figure 4D). In addition, to investigate the protective effects of KUS121 on cardiomyocyte apoptosis induced by I/R injury, we performed terminal deoxynucleotidyl transferase dUTP nick-end labeling (TUNEL) assays. The rate of apoptotic cardiomyocytes, defined as TUNEL-positive nuclei surrounded by troponin I, was significantly lower in KUS121-treated mice compared with control mice (Figures 4E and 4F).

Echocardiographic analysis at 7 days after reperfusion showed that both the EF and FS of KUS121-treated mice were better preserved than those of control mice (Figures 5A to 5E). Similar results were obtained in serial echocardiographic analyses of cardiac functions (Figures 4A and 5F to 5I).

KUS121 MAINTAINS ATP LEVELS IN ISCHEMIA AND REPERFUSION INJURY MODELS. To investigate whether KUS121 preserved ATP levels in vivo, we created I/R injury models using GO-ATeam2 mice. In

FIGURE 4 KUS121 Treatment After Reperfusion Attenuates Infarct Size and Reduces Cardiomyocyte Apoptosis

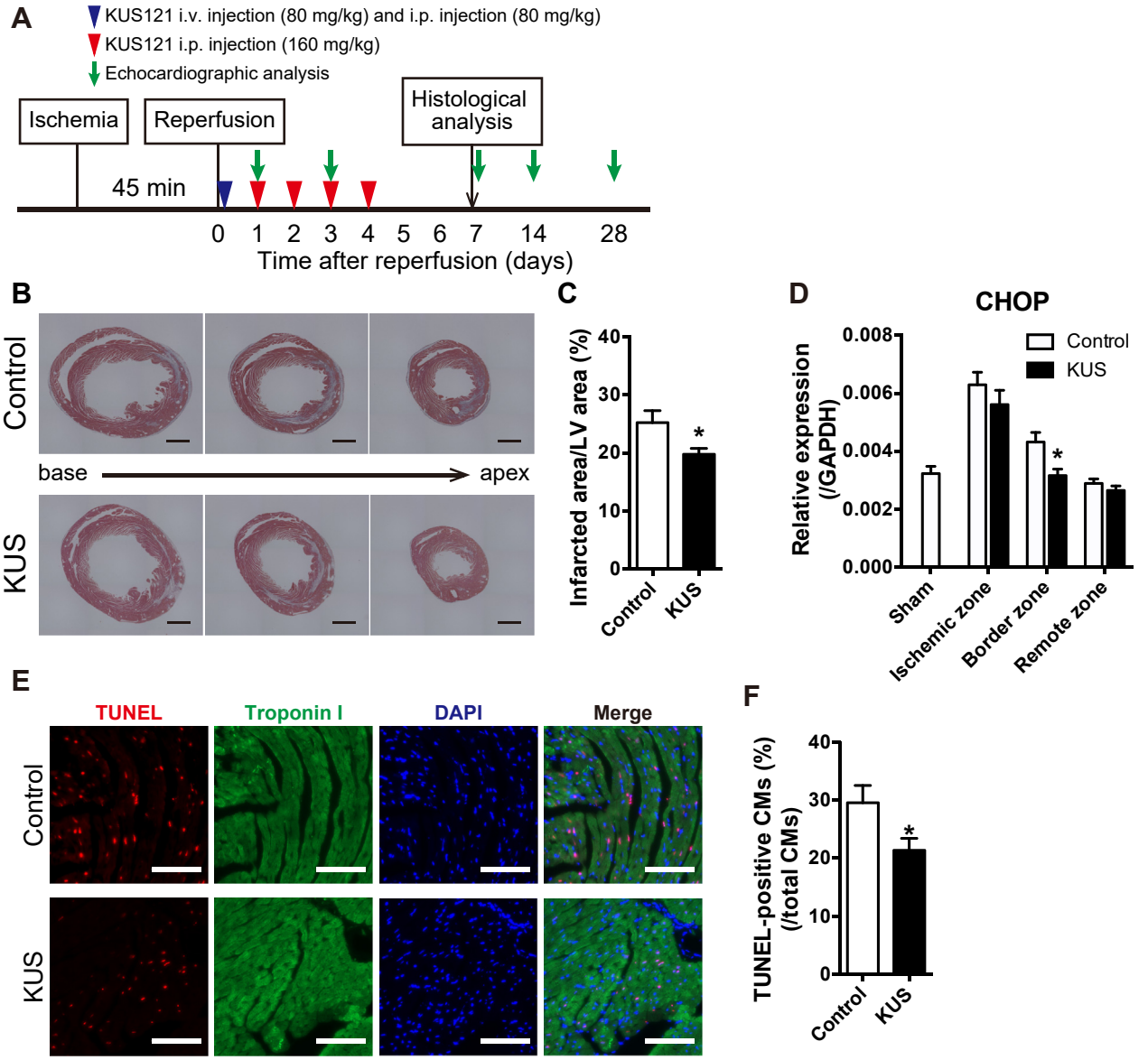

(A) Schematic diagram of ischemia and reperfusion (I/R) injury procedures and schedules of Kyoto University Substance 121 (KUS121) administration. **(B)** Representative images of Masson's trichrome staining in the short axis of left ventricles (LVs) at 7 days after I/R injury. **Black bars** indicate 1,000 μm. **(C)** Quantification of infarcted area in LVs at 7 days after I/R injury (control group, n = 7; KUS121 group, n = 10). *$p < 0.05$, using unpaired 2-tailed Student's *t* test. **(D)** Expression levels of CHOP in LVs at 1 h after I/R injury. LVs were divided into 3 parts: ischemic zone, border zone, and remote zone (sham group, n = 6; control group, n = 6; KUS121 group, n = 8). The expression level of glyceraldehyde 3-phosphate dehydrogenase (GAPDH) was used as an internal control. *$p < 0.05$, using unpaired 2-tailed Student's *t*-test. **(E)** Representative images of terminal deoxynucleotidyl transferase dUTP nick-end labeling (TUNEL) staining in LVs at 4 h after reperfusion. **White bars** indicate 100 μm. **(F)** Quantification of apoptotic cardiomyocytes (CMs), defined as TUNEL-positive cells surrounded by troponin I (control group, n = 6; KUS121 group, n = 6). *$p < 0.05$, using unpaired 2-tailed Student's *t*-test. All data are presented as mean ± SEM. i.p. = intraperitoneal; i.v. = intravenous; other abbreviations as in Figure 2.

the images, high FRET ratios (i.e., higher ATP levels) were pseudo-colored using warmer colors and low FRET ratios (i.e., lower ATP levels) using cooler colors (Supplemental Figure 5A). ATP levels in infarcted areas of KUS121-treated mice were significantly higher from 0 to 60 min after reperfusion (Supplemental Figures 5A and 5B) than were those of control I/R mice, when KUS121 was administered before ischemia, as shown in Supplemental Figure 3A. In noninfarcted areas of the LV, ATP levels in

FIGURE 5 KUS121 Treatment After Reperfusion Preserves Cardiac Function in I/R Injury Models

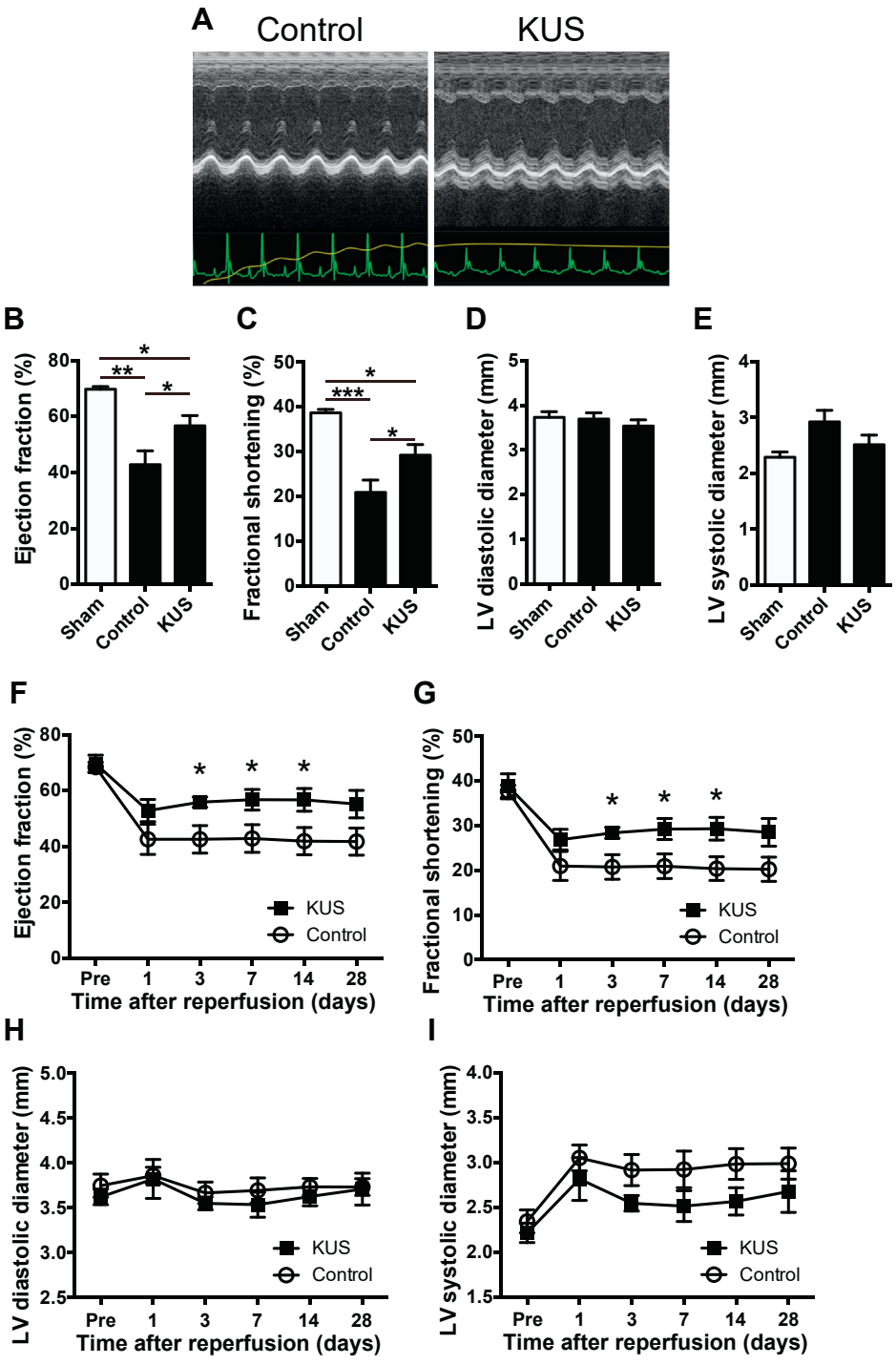

(A) Representative images of M-mode echocardiogram of control group and KUS-treated animals at 1 week after I/R injury. **(B to E)** Echocardiographic data 1 week after I/R injury. **(B)** Ejection fraction (EF), **(C)** fractional shortening (FS), **(D)** LV diastolic diameter, and **(E)** LV systolic diameter were measured (sham group, n = 4; control group, n = 6; KUS121 group, n = 6). *p < 0.05, **p < 0.01, ***p < 0.001, using 1-way analysis of variance with Sidak's post hoc test. **(F to I)** Echocardiographic data at the indicated time points after I/R injury. *p < 0.05, using unpaired 2-tailed Student's *t*-test. All data are presented as mean ± SEM. Abbreviations as in Figures 2–4.

FIGURE 6 KUS121 Treatment After Reperfusion Also Maintains ATP Levels in Ischemia and Reperfusion Injury Models

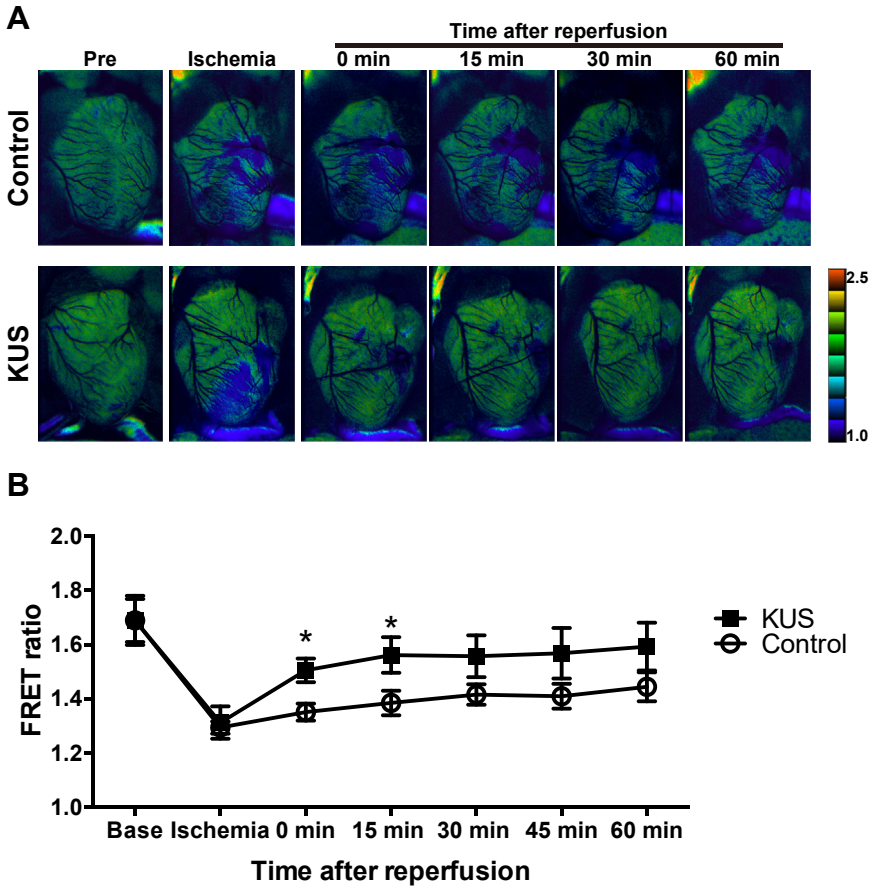

(A) Representative pseudocolor ratiometric fluorescence resonance energy transfer (FRET) images of whole hearts in I/R injury models of Go-ATeam2 mice. Pseudocolor images were obtained at various time points in ischemia and after reperfusion. In pseudocolor images, warmer colors represent high FRET ratios and cooler colors represent low FRET ratios. **(B)** Quantification of ATP levels in the infarcted area by FRET ratio (control group, n = 7; KUS121 group, n = 8). *p < 0.05, using unpaired 2-tailed Student's *t*-test. Data are presented as mean ± SEM. Abbreviations as in Figures 2 to 4.

KUS121-treated mice were also higher than those of control I/R mice (Supplemental Figure 5C). Although ATP levels in the right ventricle of KUS121-treated mice were similar to those of control mice (Supplemental Figure 5D), the relative ATP ratio in the infarcted area to that in the right ventricle was higher in KUS121-treated mice than in control mice (Supplemental Figure 5E).

Next, we examined whether KUS121 administration after reperfusion could also preserve ATP levels. As shown in **Figure 4A**, we administered the same amount of KUS121 immediately after reperfusion in I/R injury models of GO-ATeam2 mice. ATP levels in infarcted areas of KUS121-treated mice were the same as those of control mice during ischemia. However, ATP levels of KUS121-treated mice recovered immediately and significantly after KUS121 administration compared with control mice (**Figures 6A and 6B**). These data indicate that KUS121 was able to preserve ATP levels in I/R models in vivo.

BENEFICIAL EFFECTS ARE OBSERVED WITH A SINGLE ADMINISTRATION OF KUS121 AFTER REPERFUSION. We further examined whether a single KUS121 administration after reperfusion could benefit the infarcted area or not. As shown in **Figure 7A**, 25 mg/kg of KUS121 was injected intravenously, and the same amount was injected intraperitoneally immediately after reperfusion. The infarcted area-to-LV area ratio was significantly reduced in KUS121-treated mice at 7 days after reperfusion compared with control mice (**Figures 7B and 7C**). However, a dose of 16 mg/kg

FIGURE 7 Beneficial Effect of a Single Administration of KUS121 After Reperfusion

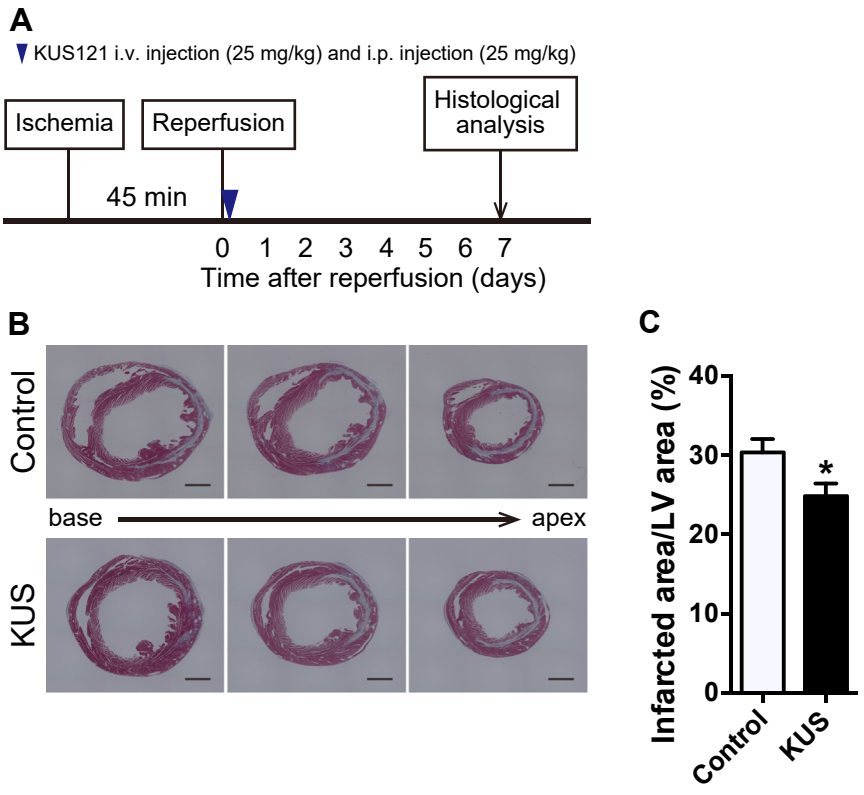

(A) Schematic diagram of I/R injury procedures and schedules of KUS121 administration. **(B)** Representative images of Masson's trichrome staining in the short axis of LVs at 7 days after I/R injury. **Black bars** indicate 1000 μm. **(C)** Quantification of infarcted area in LVs at 7 days after I/R injury (control group, n = 14; KUS121 group, n = 15). *p < 0.05, using unpaired 2-tailed Student's *t*-test. Data are presented as mean ± SEM. Abbreviations as in Figures 2–4.

KUS121 (Supplemental Figure 6A), failed to produce a beneficial effect (Supplemental Figures 6B and 6C).

KUS121 ATTENUATES THE INFARCTED AREA IN PORCINE I/R INJURY MODELS. Finally, we examined whether KUS121 could produce therapeutic effects in porcine I/R injury models. Reperfusion was induced after 60 min of endovascular LAD coronary artery occlusion, and KUS121 was administered by intracoronary injection at a dose of 0.64, 2.5, or 5.0 mg/kg for 3 min through the wire lumen of a balloon catheter immediately after reperfusion (**Figure 8A**). Using double-staining with TTC and Evans blue, the infarcted area-to-AAR ratios of KUS121-treated pigs were found to be significantly lower than were those of the control pigs in a dose-dependent manner, although the AAR-to-LV ratios of KUS121-treated pigs were the same as those of control pigs (**Figures 8B to 8D**). In addition, we confirmed that the appearance of infarcted areas, as determined using Masson's trichrome staining, was almost the same as that evaluated using TTC staining (Supplemental Figures 7A and 7B). We also evaluated the infarcted area by late gadolinium enhancement with CMR (**Figure 8E**). The infarcted area-to-LV area ratios in KUS121-treated pigs were also significantly lower than were those of control pigs (**Figure 8F**). These data demonstrate that KUS121 intracoronary administration provides significant benefits in the presence of cardiac damage in porcine I/R injury models.

DISCUSSION

In this study, we investigated the cardioprotective effects of KUS121 using murine I/R injury models that mimic reperfusion therapy for MI, and we showed that KUS121 administration even after reperfusion was able to maintain ATP levels and attenuate the infarcted area. Echocardiographic evaluation

FIGURE 8 KUS121 Attenuates Infarcted Areas in Porcine I/R Injury Models

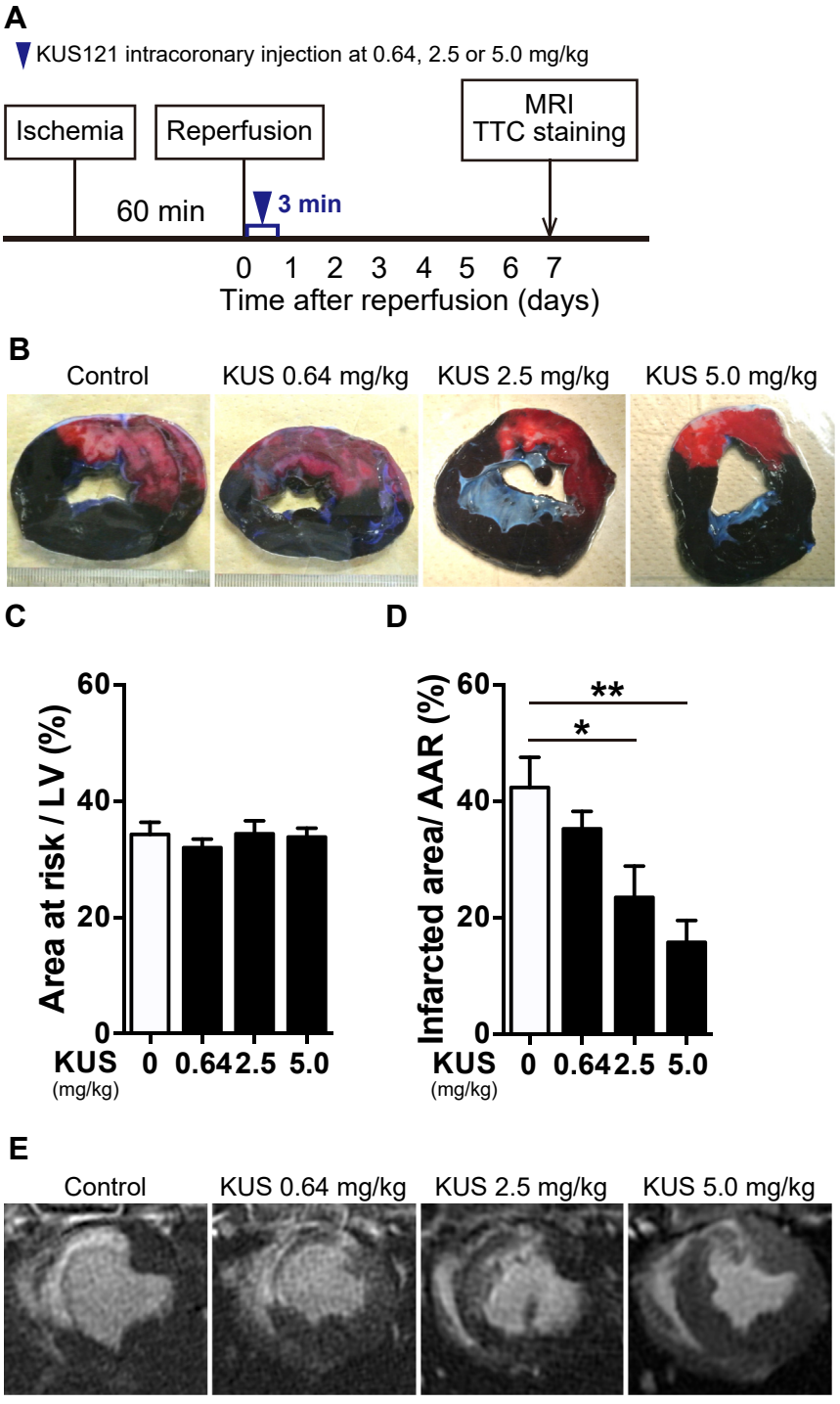

(A) Schematic diagram of I/R injury procedures in pigs. **(B)** Representative images of double-staining with triphenyltetrazolium chloride (TTC) and Evans blue in the short axis of LVs at 7 days after reperfusion. **(C, D)** Quantification of infarcted area-to-area at risk (AAR) ratio and AAR-to-LV ratio in double-staining with TTC and Evans blue (control group, n = 7; KUS121 group at 0.64 mg/kg, n = 4; at 2.5 mg/kg, n = 5; at 5.0 mg/kg, n = 5). *$p < 0.05$, **$p < 0.01$ vs. control group, using 1-way analysis of variance with Dunnett's post hoc test. **(E)** Representative images of late gadolinium enhancement on cardiac magnetic resonance (CMR) at 7 days after reperfusion. **(F)** Quantification of the infarcted area-to-LV ratio using CMR. *$p < 0.05$ vs. control group, using 1-way analysis of variance with Dunnett's post hoc test. All data are presented as mean ± SEM. Abbreviations as in Figures 2 and 4.

revealed that KUS121 administration preserved cardiac function at levels similar to those of normal mice. Notably, similar beneficial effects of KUS121 were also confirmed in a porcine I/R injury model using a single administration into the coronary artery in a dose-dependent manner.

This study demonstrated that KUS121 had cardioprotective effects in vivo by the same mechanisms as in in vitro analyses. Additionally, we also confirmed that the immediate cardio-protective effects of KUS121 within 24 h after IR injury were responsible for reducing the infarct size. Using Go-ATeam2 mice, we found that KUS121 treatment even after reperfusion maintained ATP levels in an I/R injury model, most likely due to the inhibition of ATP consumption by VCP or preservation of mitochondrial function observed in H9C2 cells. As reported previously (25), we examined the expression of CHOP in I/R injury and demonstrated that KUS121 treatment after reperfusion significantly reduced CHOP expression in border zone. This also suggested that KUS121 reduced ER stress in vivo and rescued the injured myocardium from cell death. KUS121 treatment also reduced cardiomyocyte apoptosis induced by I/R injury. In our in vitro experiment, KUS121 protected H9C2 cells from H_2O_2-induced cell death. As reported previously (26), H_2O_2 is considered to induce necrotic cell death rather than apoptotic cell death. Moreover, ER stress was also reported to induce necrotic cell death (27). This indicates that KUS 121 may protect cardiomyocytes from necrotic cell death by reducing ER stress. Thus, KUS121 is presumed to attenuate the infarct size by reducing both apoptotic and necrotic cell death.

KUS121 was developed to selectively inhibit the ATPase activity of VCP without affecting its other cellular functions, and previous studies demonstrated that KUS121 can maintain cellular ATP levels, reduce ER stress, and prevent cell death in vitro when challenged with many cell-death-inducing insults in many cell types (16–19). Consistent with the ability of KUS121 to maintain ATP levels and reduce ER stress, KUS121 has been reported to have neuroprotective effects in vivo (e.g., in models of murine retinitis pigmentosa, murine glaucoma, rat retinal ischemic injury, and murine Parkinson's disease) (16–19). In this study, we further demonstrated the close link among ER stress, decreased ATP levels, and cell death in the heart.

To the best of our knowledge, the cardioprotective mechanisms of KUS121 are quite different from other drugs that have been tested for the treatment of MI (7,28–30), making KUS121 virtually unique in its ability to maintain ATP levels in animal I/R injury models. Recently, LV mechanical support using Impella (Abiomed, Danvers, Massachusetts) was reported to reduce infarct size after I/R injury (31). This was possibly due to a reduction in excessive myocardial energy demand relative to supply, which would be similar in principle to KUS121 administration in our in vivo models.

It is especially noteworthy that KUS121 is able to reduce infarct size by administration even after reperfusion, especially through intracoronary injection. This can be easily performed after primary PCI in everyday clinical practice. Thus, we concluded that KUS121 is a promising compound that could be used in conjunction with primary PCI for the treatment of MI.

STUDY LIMITATIONS. We showed that KUS121 reduced the infarct size in murine and porcine I/R injury models by maintaining ATP levels and reducing ER stress, but the detailed mechanism of the link among ER stress, decreased ATP levels, and cell death remains to be elucidated. Further investigations are needed to fully explore the complex signaling mechanisms that are at play during MI and reperfusion.

In porcine models, we evaluated the infarct size only at 7 days after reperfusion, but we did not evaluate the effect of KUS121 at later time points. Moreover, we did not confirm the detailed safety of KUS121, although no obvious toxicity of KUS121 was observed in our study. We need to perform further studies with long-term follow-up to confirm the cardiac protective efficacy and safety of KUS121.

As previously reported (16,32), KUS121 was confirmed to inhibit the ATPase activity of recombinant VCP in vitro with half-maximal inhibitory concentration value of 330 nM, which is much lower than that of a VCP inhibitor, DBeQ (1 μM). However, we did not evaluate the specificity and off-target effects of KUS 121 in vivo. Further studies are need to elucidate them in vivo by analysis of the pharmacokinetics and pharmacodynamics of KUS121.

CONCLUSIONS

Here, we have shown that in I/R injury models, KUS121 reduced infarct size and preserved cardiac function by maintaining ATP levels and reducing ER stress. We also showed that this effect can be achieved by the administration of KUS121 only once after reperfusion, which was confirmed in porcine I/R models. Our study indicates that KUS121 is a promising therapeutic agent for MI in conjunction with primary PCI. Progression of studies leading to a

clinical trial of KUS121 is expected in the near future.

ACKNOWLEDGMENTS The authors thank Naoya Sowa for providing technical assistance. Extracellular flux analyses using XF96 were performed at the Medical Research Support Center, Graduate School of Medicine, Kyoto University. The authors acknowledge Prof. James Hejna (Kyoto University) for critical reading of the manuscript.

ADDRESS FOR CORRESPONDENCE: Dr. Koh Ono, Department of Cardiovascular Medicine, Kyoto University Graduate School of Medicine, 54 Shogoin-Kawahara-cho, Sakyo-ku, Kyoto 606-8507, Japan. E-mail: kohono@kuhp.kyoto-u.ac.jp. OR Dr. Akira Kakizuka, Laboratory of Functional Biology, Kyoto University Graduate School of Biostudies and Solution Oriented Research for Science and Technology, Kyoto 606-8501, Japan. E-mail: kakizuka@lif.kyoto-u.ac.jp.

PERSPECTIVES

COMPETENCY IN MEDICAL KNOWLEDGE: Although primary PCI is the only therapy for MI to reduce infarct size and improve outcomes, a larger infarction, even after primary PCI, results in a poorer prognosis. However, there are currently no therapies additional to primary PCI to further reduce infarct size and improve clinical outcomes. Our study demonstrated that KUS121 attenuated the infarct size in murine and porcine I/R injury models. These results indicate that KUS121 may be a novel therapy for MI in conjunction with primary PCI.

TRANSLATIONAL OUTLOOK: We expect that KUS121 will one day be used in clinical practice. However, further studies are needed to investigate the pharmacokinetics and pharmacodynamics of KUS121, especially those after intracoronary KUS121 administration. Additionally, we need to verify the detailed safety of KUS121. If these are confirmed, the cardioprotective effects of KUS121 may be evaluated in clinical trials.

REFERENCES

1. World Health Organization. Global Status Report on Noncommunicable Diseases 2014. Geneva, Switzerland: WHO Press, 2014.

2. Benjamin EJ, Virani SS, Callaway CW, et al. Heart Disease and Stroke Statistics—2018 Update: a report From the American Heart Association. Circulation 2018;137:e67–492.

3. Ministry of Health, Labour and Welfare. Vital statistics in Japan—trends up to 2016. Available at: https://www.mhlw.go.jp/english/database/db-hw/dl/81-1a2en.pdf. Accessed November 2018.

4. Levine GN, Bates ER, Blankenship JC, et al. 2015 ACC/AHA/SCAI Focused Update on Primary Percutaneous Coronary Intervention for Patients With ST-Elevation Myocardial Infarction: an update of the 2011 ACCF/AHA/SCAI Guideline for Percutaneous Coronary Intervention and the 2013 ACCF/AHA Guideline for the Management of ST-Elevation Myocardial Infarction. Circulation 2016;113:1135–47.

5. Stone GW, Selker HP, Thiele H, et al. Relationship between infarct size and outcomes following primary PCI patient-level analysis from 10 randomized trials. J Am Coll Cardiol 2016;67:1674–83.

6. Jencks SF, Williams MV, Coleman EA. Rehospitalizations among patients in the Medicare fee-for-service program. N Engl J Med 2009;360:1418–28.

7. Aihara K, Hisa H, Sato T, et al. Cardioprotective effect of TY-12533, a novel Na(+)/H(+) exchange inhibitor, on ischemia/reperfusion injury. Eur J Pharmacol 2000;404:221–9.

8. Piot C, Croisille P, Staat P, et al. Effect of cyclosporine on reperfusion injury in acute myocardial infarction. N Engl J Med 2008;359:473–81.

9. Kimura K, Nakao K, Shibata Y, et al. Randomized controlled trial of TY-51924, a novel hydrophilic NHE inhibitor, in acute myocardial infarction. J Cardiol 2016;67:307–13.

10. Cung T-T, Morel O, Cayla G, et al. Cyclosporine before PCI in patients with acute myocardial infarction. N Engl J Med 2015;373:1021–31.

11. Spath NB, Mills NL, Cruden NL. Novel cardioprotective and regenerative therapies in acute myocardial infarction: a review of recent and ongoing clinical trials. Future Cardiol 2016;12:655–72.

12. Meyer H, Weihl CC. The VCP/p97 system at a glance: connecting cellular function to disease pathogenesis. J Cell Sci 2014;127:3877–83.

13. Watts GDJ, Wymer J, Kovach MJ, et al. Inclusion body myopathy associated with Paget disease of bone and frontotemporal dementia is caused by mutant valosin-containing protein. Nat Genet 2004;36:377–81.

14. Manno A, Noguchi M, Fukushi J, Motohashi Y, Kakizuka A. Enhanced ATPase activities as a primary defect of mutant valosin-containing proteins that cause inclusion body myopathy associated with Paget disease of bone and frontotemporal dementia. Genes Cells 2010;15:911–22.

15. Hübbers CU, Clemen CS, Kesper K, et al. Pathological consequences of VCP mutations on human striated muscle. Brain 2007;130:381–93.

16. Ikeda HO, Sasaoka N, Koike M, et al. Novel VCP modulators mitigate major pathologies of rd10, a mouse model of retinitis pigmentosa. Sci Rep 2014;4:5970.

17. Nakano N, Ikeda HO, Hasegawa T, et al. Neuroprotective effects of VCP modulators in mouse models of glaucoma. Heliyon 2016;2:e00096.

18. Hata M, Ikeda HO, Kikkawa C, et al. KUS121, a VCP modulator, attenuates ischemic retinal cell death via suppressing endoplasmic reticulum stress. Sci Rep 2017;7:44873.

19. Nakano M, Imamura H, Sasaoka N, et al. ATP maintenance via 2 types of ATP regulators mitigates pathological phenotypes in mouse models of Parkinson's disease. EBioMedicine 2017;22:225–41.

20. Imamura H, Huynh Nhat KP, Togawa H, et al. Visualization of ATP levels inside single living cells with fluorescence resonance energy transfer-based genetically encoded indicators. Proc Natl Acad Sci U S A 2009;106:15651–6.

21. Nakano M, Imamura H, Nagai T, Noji H. Ca2+regulation of mitochondrial ATP synthesis visualized at the single cell level. ACS Chem Biol 2011;6:709–15.

22. Vannuvel K, Renard P, Raes M, Arnould T. Functional and morphological impact of ER stress on mitochondria. J Cell Physiol 2013;228:1802–18.

23. Lebeau J, Saunders JM, Moraes VWR, et al. The PERK Arm of the unfolded protein response regulates mitochondrial morphology during acute endoplasmic reticulum stress. Cell Rep 2018;22:2809–17.

24. Kwong JQ, Molkentin JD. Physiological and pathological roles of the mitochondrial permeability transition pore in the heart. Cell Metab 2015;21:206–14.

25. Miyazaki Y, Kaikita K, Endo M, et al. C/EBP homologous protein deficiency attenuates myocardial reperfusion injury by inhibiting myocardial apoptosis and inflammation. Arterioscler Thromb Vasc Biol 2011;31:1124–32.

26. Ali MAM, Kandasamy AD, Fan X, Schulz R. Toxicology in vitro Hydrogen peroxide-induced necrotic cell death in cardiomyocytes is independent of matrix metalloproteinase-2. Toxicol Vitr 2013;27:1686–92.

27. Ullman E, Fan Y, Stawowczyk M, Chen HM, Yue Z, Zong WX. Autophagy promotes necrosis in apoptosis-deficient cells in response to ER stress. Cell Death Differ 2008;15:422–5.

28. Malka A, Ertracht O, Bachner-Hinenzon N, Reiter I, Binah O. The cardioprotective efficacy of TVP1022 against ischemia/reperfusion injury and cardiac remodeling in rats. Pharmacol Res Perspect 2016;4:1–15.

29. Inagaki K, Chen L, Ikeno F, et al. Inhibition of delta-protein kinase C protects against reperfusion injury of the ischemic heart in vivo. Circulation 2003;108:2304–7.

30. Kim J-S. Reactive oxygen species, but not Ca2+ overloading, trigger pH- and mitochondrial permeability transition-dependent death of adult rat myocytes after ischemia-reperfusion. AJP Hear Circ Physiol 2006;290:H2024–34.

31. Saku K, Kakino T, Arimura T, et al. Left ventricular mechanical unloading by total support of Impella in myocardial infarction reduces infarct size, preserves left ventricular function, and prevents subsequent heart failure in dogs. Circ Heart Fail 2018;11:e004397.

32. Chou T-F, Brown SJ, Minond D, et al. Reversible inhibitor of p97, DBeQ, impairs both ubiquitin-dependent and autophagic protein clearance pathways. Proc Natl Acad Sci U S A 2011;108:4834–9.

KEY WORDS ATP, ER stress, KUS121, myocardial infarction

APPENDIX For supplemental methods and figures, please see the online version of this paper.

JACC: BASIC TO TRANSLATIONAL SCIENCE VOL. 4, NO. 6, 2019

EDITORIAL COMMENT

The Art of War in Drug Development*

Taro Kariya, MD, PhD, Kiyotake Ishikawa, MD, PhD

Drug development is one of the major goals of translational medicine, but for each victory in bringing a drug to market, there are all too many unseen candidate "corpses" relegated to the graveyard of drug discovery. In 2019, there were 16,181 drugs in the research and development (R&D) pipeline according to Pharma R & D Annual Review 2019 (1). Although this number represents an increase of 6.0% over the previous year, a consistently upward trend in the industry, those reaching registration numbered only 152, approximately 1.0% of those in the pre-registration phase (n = 14,585) in 2019. In addition to the low success rate of drug development, the time and cost of bringing a new drug from concept to market are growing, exceeding 10 years and $2.5 billion, respectively (2,3). Recently, various major pharmaceutical companies announced the termination of the following 6 phase III clinical trials of their anti-Alzheimer drugs, apparently because no effectiveness could be demonstrated compared to placebo in each trial: APECS (Efficacy and Safety Trial of Verubecestat [MK-8931] in Participants With Prodromal Alzheimer's Disease [MK-8931-019]; NCT01953601); AMARANTH (An Efficacy and Safety Study of Lanabecestat [LY3314814] in Early Alzheimer's Disease; NCT02245737); CREAD (A Study of Crenezumab Versus Placebo to Evaluate the Efficacy and Safety in Participants With Prodromal to Mild Alzheimer's Disease [AD]; NCT02670083); CREAD 2 (A Study of Crenezumab Versus Placebo to Evaluate the Efficacy and Safety in Participants With Prodromal to Mild Alzheimer's Disease [AD]; NCT03114657); ENGAGE (221AD301 Phase 3 Study of Aducanumab [BIIB037] in Early Alzheimer's Disease; NCT02477800); and EMERGE (221AD302 Phase 3 Study of Aducanumab [BIIB037] in Early Alzheimer's Disease; NCT02484547).

These sobering facts are stark reminders that the gate to victory in drug development is narrow indeed.

SEE PAGE 701

In this issue of *JACC: Basic to Translational Science*, the study by Ide et al. (4) reports a promising new drug for the reduction of myocardial ischemic injury. As suggested by its name, the Kyoto University substance 121 (KUS121) drug is a part of the drug discovery program at the Kyoto University. In the study (4), the authors showed that KUS121, a selective inhibitor of the ATPase activity of valosin-containing protein, reduced the size of myocardial infarction (MI) (e.g., 25% of the left ventricle) when it was given prior to ischemia or at the time of reperfusion in mice. After several experiments in mice, the authors extended the study to a pig model of 60-min ischemia-reperfusion and reproduced the beneficial effects observed in mice. Specifically, the single intracoronary administration of KUS121 at the time of reperfusion reduced infarct size in a dose-dependent manner in a clinically relevant animal model. The highest dose achieved a reduction of more than 50% in infarct size compared to that in the control group, highlighting its promising effect, which prompted further clinical translation of this drug. The mechanism of action seems to be multimodal. Using in vitro systems and mouse models, the authors showed inhibition of endoplasmic reticulum (ER) stress, preservation of mitochondrial function, and preservation

*Editorials published in *JACC: Basic to Translational Science* reflect the views of the authors and do not necessarily represent the views of *JACC: Basic to Translational Science* or the American College of Cardiology.

From the Cardiovascular Research Center, Icahn School of Medicine at Mount Sinai, New York, New York. Dr. Ishikawa is supported by American Heart Association grant 17SDG33410873 and U.S. National Institutes of Health grant R01 HL139963. Dr. Kariya has reported that he has no relationships relevant to the contents of this paper to disclose.

The authors attest they are in compliance with human studies committees and animal welfare regulations of the authors' institutions and Food and Drug Administration guidelines, including patient consent where appropriate. For more information, visit the *JACC: Basic to Translational Science* author instructions page.

ISSN 2452-302X https://doi.org/10.1016/j.jacbts.2019.09.002

JACC: BASIC TO TRANSLATIONAL SCIENCE VOL. 4, NO. 6, 2019
OCTOBER 2019:715–6

of myocardial ATP as potential contributors (4). The main strength of the study by Ide et al. (4) is its use of several experimental models from cells to pigs, rendering the study highly translational. Streamlined translational experiments certainly expedite the drug development process, and the authors already foresee a clinical trial.

Although a multimodal effect of the drug was extensively demonstrated by several approaches, it remained unclear which effect was most important for MI size reduction. Identifying the major effector of the drug is important because that would determine the most effective means of administering the drug for a particular disease. For example, if ATP preservation is the major effect of KUS121, administering the drug after reperfusion may not lead to a significant benefit. This seems not to be the case for KUS121, because the drug was also effective when given at the time of reperfusion. In addition, the lack of a difference in infarct size reduction between the drug given prior to ischemia and at the time of reperfusion (see Figure 4C and Online Figure 3C in the paper by Ide et al. [4]) suggests rather that ATP preservation is not the major effect or, at least, does not offer additional benefit when the drug is also administered at the time of reperfusion. Meanwhile, infarct size in mice given KUS121 just once at the time of reperfusion was approximately 25% in contrast to approximately 20% in animals given multiple doses after reperfusion. Although the infarct size of control animals probably differed because of a different study setting, multiple drug administrations might have resulted in additional infarct reduction. A potential beneficial effect produced by multiple administrations of KUS121 may be related to reduction of ER stress and subsequent attenuation of cell death signals, because theoretically, they can act during the post-reperfusion period. Unfortunately, the effect of additional doses after reperfusion was not tested in pigs. Therefore, the pig study suggests that a single intracoronary dose is effective, but whether it is sufficient to produce a maximal effect remains unknown. Additionally, the route of delivery also requires careful consideration. Although intracoronary delivery of KUS121 was likely to increase cardiac specificity in the pig study, intravenous injection could be combined before reperfusion if ATP preservation effect was achieved through this approach and offers benefit. Therefore, although the study by Ide et al. (4) demonstrated promising effects of KUS121 in multiple experimental models, there may be room for further improvement. Considering the number of candidate drugs that failed to gain entry into the armamentarium for managing MI, it is prudent for any regimen with the potential to achieve maximum benefit for reducing infarct size to be intensely scrutinized. For that purpose, understanding the major mechanisms of action of a drug is critically important.

In the ancient Chinese military treatise, "The Art of War," SunTzu wrote: "Thus we may say that if you know yourself and know your enemy, you will gain victory a hundred times out of a hundred. If you know yourself but do not know your enemy, you will meet one defeat for every victory. If you know neither yourself nor your enemy, you will never be victorious" (5). This quote from the 5th Century B.C. not only taught ancient generals about strategy on the battlefield, it also guides modern researchers in dealing with the difficult tasks inherent in drug development. Our understanding of the enemy (myocardial ischemic injury) is improving daily, but we are still far from "knowing" it. It is essential that our efforts to know ourselves (how the drug works) are painstaking in order not to become another drug corpse in the battle of drug development.

ACKNOWLEDGMENT The authors thank Dr. Kelly P. Yamada for critical reading of the manuscript.

ADDRESS FOR CORRESPONDENCE: Dr. Kiyotake Ishikawa, Cardiovascular Research Center, Mount Sinai School of Medicine, One Gustave L. Levy Place, Box 1030, New York, New York 10029-6574. E-mail: kiyotake.ishikawa@mssm.edu.

REFERENCES

1. Lloyd I. Pharma R&D Annual Review 2019. London: Pharma Intelligence, 2019.

2. Pammolli F, Magazzini L, Riccaboni M. The productivity crisis in pharmaceutical R&D. Nat Rev Drug Discov 2011;10:428–38.

3. DiMasi JA, Grabowski HG, Hansen RW. Innovation in the pharmaceutical industry: new estimates of R&D costs. J Health Econ 2016;47:20–33.

4. Ide Y, Horie T, Saito N, et al. Cardioprotective effects of VCP modulator KUS121 in murine and porcine models of myocardial infarction. J Am Coll Cardiol Basic Trans Science 2019;4:701–14.

5. SunTzu. The Art of War. London: Amber Books, 2011:20–1.

KEY WORDS drug discovery, ischemia reperfusion injury, KUS121, large animal, myocardial infarction

JACC: BASIC TO TRANSLATIONAL SCIENCE VOL. 4, NO. 6, 2019

PRECLINICAL RESEARCH

Acute Kidney Injury Induces Remote Cardiac Damage and Dysfunction Through the Galectin-3 Pathway

Mathilde Prud'homme, PHD,[a] Maxime Coutrot, MD, MSC,[a,b,*] Thibault Michel, MD, MSC,[a,*] Louis Boutin, MD, MSC,[a,b,*] Magali Genest, PHD,[a,d] Françoise Poirier, PHD,[c] Jean-Marie Launay, PHARMD, PHD,[a] Bocar Kane,[f] Satoshi Kinugasa, MD, PHD,[d] Niki Prakoura, PHD,[d] Sophie Vandermeersch,[d] Alain Cohen-Solal, MD, PHD,[a,e] Claude Delcayre, PHD,[a] Jane-Lise Samuel, MD, PHD,[a] Ravindra Mehta, MD,[g] Etienne Gayat, MD, PHD,[a,b] Alexandre Mebazaa, MD, PHD,[a,b] Christos E. Chadjichristos, PHD,[d,†] Matthieu Legrand, MD, PHD[a,b,h,†]

VISUAL ABSTRACT

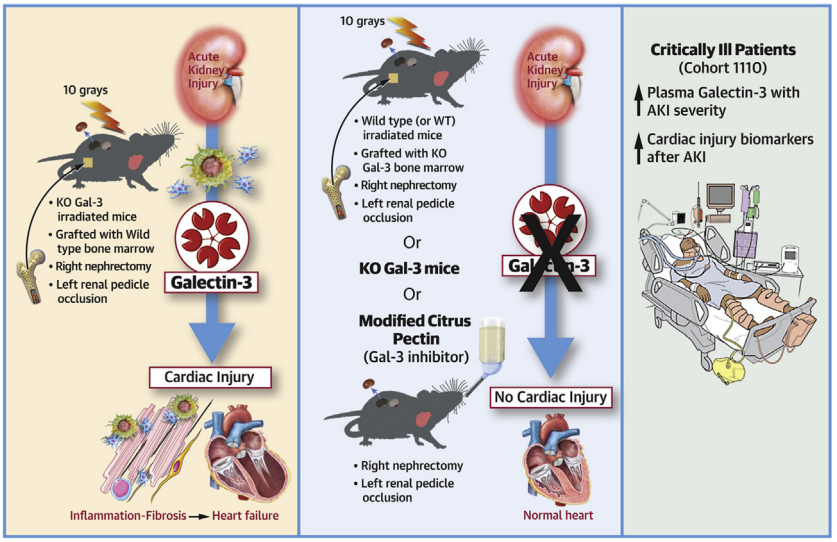

Prud'homme, M. et al. J Am Coll Cardiol Basic Trans Science. 2019;4(6):717–32.

HIGHLIGHTS

- **In 2 different mouse models, AKI increased Gal-3 expression and induced cardiac dysfunction, cardiac and systemic inflammation, cardiac macrophage infiltration, and fibrosis.**
- **Cardiac consequences of AKI were dependent on the Gal-3 pathway and were prevented using Gal-3 knockout mice or modified citrus pectin as a pharmaceutical inhibitor.**
- **Cardiac Gal-3 expression resulted from bone marrow-derived immune cells recruitment after AKI.**
- **In critically ill patients, development of AKI is associated with increased plasma Gal-3 levels and increased biomarkers of cardiac injury and damage.**

From the [a]INSERM UMR-S 942, Institut National de la Santé et de la Recherche Médicale (INSERM), Lariboisière Hospital, and INI-CRCT-F-CRIN, Paris, France; [b]AP-HP, St-Louis-Lariboisière Hospital, Department of Anesthesiology and Critical Care and Burn Unit, University Paris Diderot, Paris, France; [c]Institut Jacques Monod, Team: Morphogenesis, Homeostasis and Pathologies, Paris, France; [d]INSERM UMR-S 1155, Tenon Hospital, Paris, France; [e]Cardiology Department, Lariboisière Hospital, Paris, France; [f]UMS-28 Phénotypage du petit animal, Université Pierre et Marie Curie, Paris, France; [g]Department of Medicine, University of California-San Diego, San Diego, California; and the [h]Department of Anesthesiology and peri-operative Care, University of California San Francisco, United States. *Drs. Coutrot, Michel, and Boutin contributed equally to this work and are joint first authors. †Drs. Chadjichristos and Legrand contributed equally to this work and are joint senior authors. This work was supported by "Institut

ISSN 2452-302X https://doi.org/10.1016/j.jacbts.2019.06.005

ABBREVIATIONS AND ACRONYMS

AKI = acute kidney injury

BM = bone marrow

BUN = blood urea nitrogen

Cr = creatinine

eGFR = estimated glomerular filtration rate

Gal-3 = galectin-3

KO = knock-out

ICAM = intercellular adhesion molecule

ICU = intensive care unit

IL = interleukin

IR = ischemia-reperfusion

KDIGO = Kidney Disease Improving Global Outcome

MCP = modified citrus pectin

NT-proBNP = N-terminal-pro-brain natriuretic peptide

TGF = transforming growth factor

TNF = tumor necrosis factor

UUO = unilateral ureteral obstruction

WT = wild type

SUMMARY

Acute kidney injury is associated with increased risk of heart failure and mortality. This study demonstrates that acute kidney injury induces remote cardiac dysfunction, damage, injury, and fibrosis via a galectin-3 (Gal-3) dependent pathway. Gal-3 originates from bone marrow-derived immune cells. Cardiac damage could be prevented by blocking this pathway. (J Am Coll Cardiol Basic Trans Science 2019;4:717–32)

Acute kidney injury (AKI) has been associated with an increased risk of mortality (1), even in patients free of previous cardiovascular comorbidities (2). Furthermore, AKI has been associated with long-term cardiovascular events (3). Whether the occurrence of AKI only reflects the severity and magnitude of underlying disease or may contribute to remote organ injury remains uncertain. Remote cardiovascular injury may contribute to poor outcomes after AKI (4). AKI has also been associated with long-term cardiovascular events. This has been described in type 3 cardiorenal syndrome (or acute reno-cardiac syndrome) (5).

SEE PAGE 733

However, whether transient AKI can induce long-term cardiac injury remains unexplored. Cardiac fibrosis has been described as a key feature of chronic heart diseases (6). Galectin-3 (Gal-3) is a lectin that specifically binds to β-galactosides (7) expressed in many tissues, including the heart and kidney (8,9). In the heart, Gal-3 induction promotes myocardial fibrosis and heart failure progression (10,11). Gal-3 has been shown to be a key player in cardiac fibrosis induction and has been proposed as a prognostic biomarker for chronic heart failure (7). In the kidney, Gal-3 has also been shown to be upregulated after AKI (12). In the present study, we hypothesized that AKI can activate Gal-3–dependent pathways and promote cardiac injury. For this purpose, we explored the role of Gal-3 in cardiac injury after kidney injury. Moreover, a bone marrow (BM) graft from Gal-3 knock-out (KO) mice was used to determine the origin of Gal-3.

METHODS

ANIMALS. Two- to 4-month old male C57Bl6/J mice (Janvier laboratory, Le Genest-Saint-Isle, France) and C57Bl6/J KO mice for Galectin-3 [Gal-3 KO (13)] were used. All animals were randomized into different groups after baseline echocardiography. Methods of echocardiography, plasma assays, gene expression analysis, protein analysis, immunostaining, cardiac fibrosis evaluation, renal macrophage isolation, cell culture, and monocyte adhesion assays are detailed in the Supplemental Appendix.

Renal and hind limb ischemia-reperfusion injury. A right nephrectomy and left renal pedicle occlusion (25 min of ischemia), followed by reperfusion, were performed under anesthesia (intraperitoneal injection of ketamine: 100 mg/kg and xylazine: 20 mg/kg). Right kidneys were used as controls. Sham mice underwent the same procedure, except for renal pedicle occlusion and right nephrectomy (14). To understand the kinetics of the kidney–heart crosstalk after renal ischemia–reperfusion (IR), mice were killed at different time points after reperfusion (at 3, 6, 12, 24, 48, and 72 h, and at 28 days; n = 7 per group)

National de la Santé et de la Recherche Médicale (INSERM)" and by Paris Diderot University and the Société Française d'Anesthésie et de Réanimation (SFAR). Dr. Prud'homme was supported by a Ph.D. training grant from Paris Diderot University and "Groupe de Réflexion sur la Recherche Cardiovasculaire (GRRC)." Dr. Cohen-Solal has received grants and fees from Novartis, Servier, Vifor, AstraZeneca, and Merck & Co. Inc. Dr. Mehta has been a consultant, a member of the advisory board for Baxter, AM Pharma, CSL-Behring, Astute Medical Inc. Regulus, Akebia, Intercept, Mallinckrodt, and Ferring; and has received grants from Relypsa, Fresenius-Kabi; Fresenius, and Grifols. Dr. Gayat has been a consultant for Magnisense and Adrenomed; and has received research grants from Deltex Medical and Retia Medical. Dr. Legrand has received research support from Sphingotec; has received lecture fees from Baxter and Fresenius; and has received consultancy fees from Novartis. All other authors have reported that they have no relationships relevant to the contents of this paper to disclose.

The authors attest they are in compliance with human studies committees and animal welfare regulations of the authors' institutions and Food and Drug Administration guidelines, including patient consent where appropriate. For more information, visit the *JACC: Basic to Translational Science* author instructions page.

Manuscript received February 21, 2019; revised manuscript received May 29, 2019, accepted June 4, 2019.

FIGURE 1 **Renal IR Leads to Acute and Transient Renal Dysfunction With Increased Gal-3 Expression**

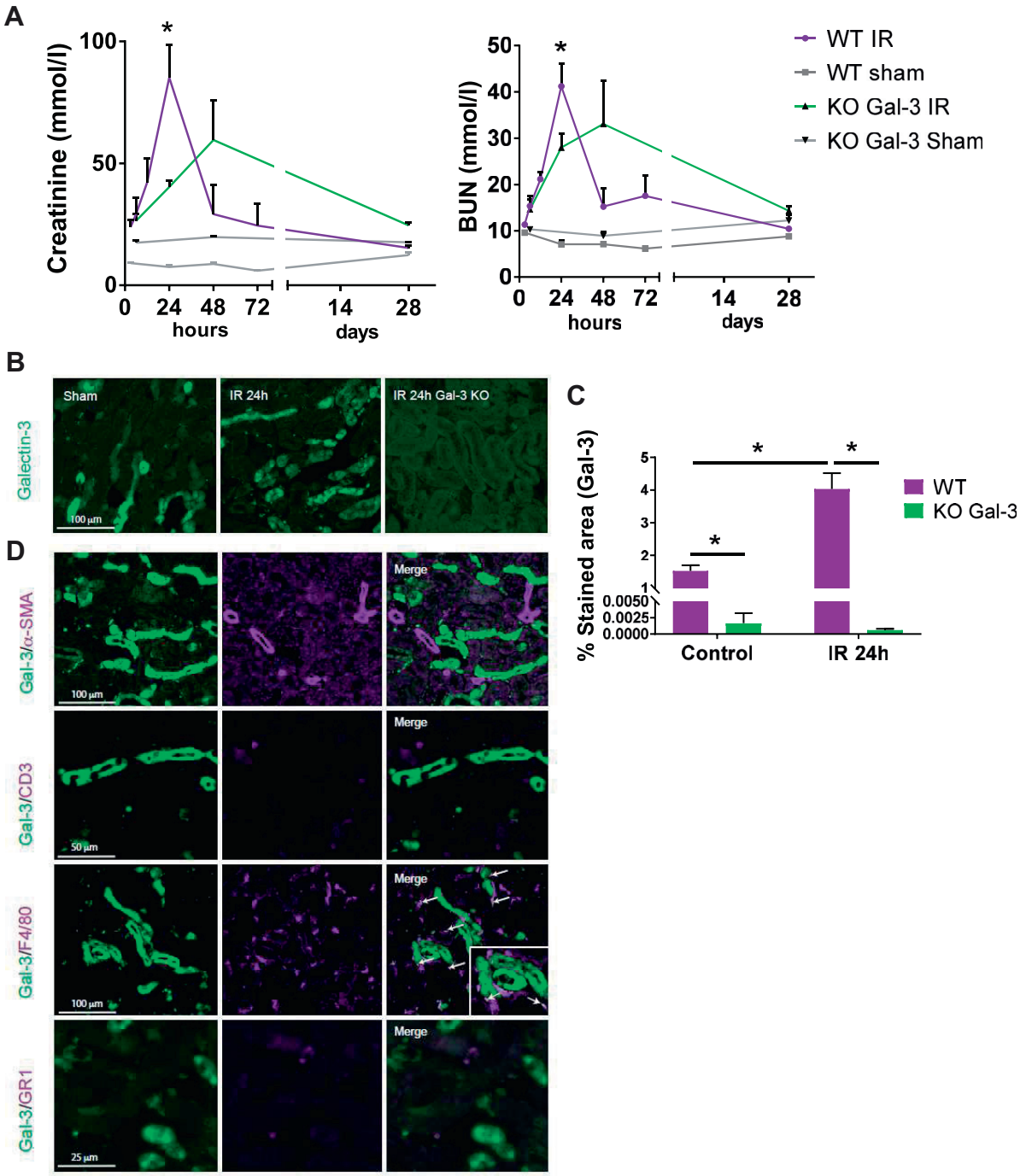

(A) Plasma assays performed in sham and ischemia–reperfusion IR mice showed an early and transient increase in creatinine and blood urea nitrogen (BUN) levels after IR compared with sham mice ($p < 0.001$; wild-type [WT] IR mice vs. WT sham mice). **(B)** Immunostaining showed increased galectin-3 (Gal-3) expression in kidney tissue, mainly in tubular cells, in response to renal IR. **(C)** Quantification of Gal-3 immunostaining of sham, IR 24-h WT, IR 2-h knockout (KO) Gal-3 groups. After IR, Gal-3 expression is increased in WT mice. **(D)** Gal-3 co-immunostaining with α-smooth muscle actin (SMA) (a marker of smooth muscle cells/myofibroblasts), CD3 (lymphocyte marker), F4/80 (macrophage marker), and GR1 (neutrophil marker) only showed co-localization of Gal-3 with F4/80, indicating that it was also expressed by infiltrated macrophages within the injured renal tissue after 24 h of IR **(white arrows)**. $n = 7$ to 14 for WT IR groups; $n = 4$ to 7 for KO IR; $n = 4$ for WT and $n = 4$ KO Gal-3 sham mice. Data are presented as mean ± SEM, and comparisons of medians were made using nonparametric Mann-Whitney U test. *$p < 0.05$.

FIGURE 2 Cardiac Inflammation After Renal IR

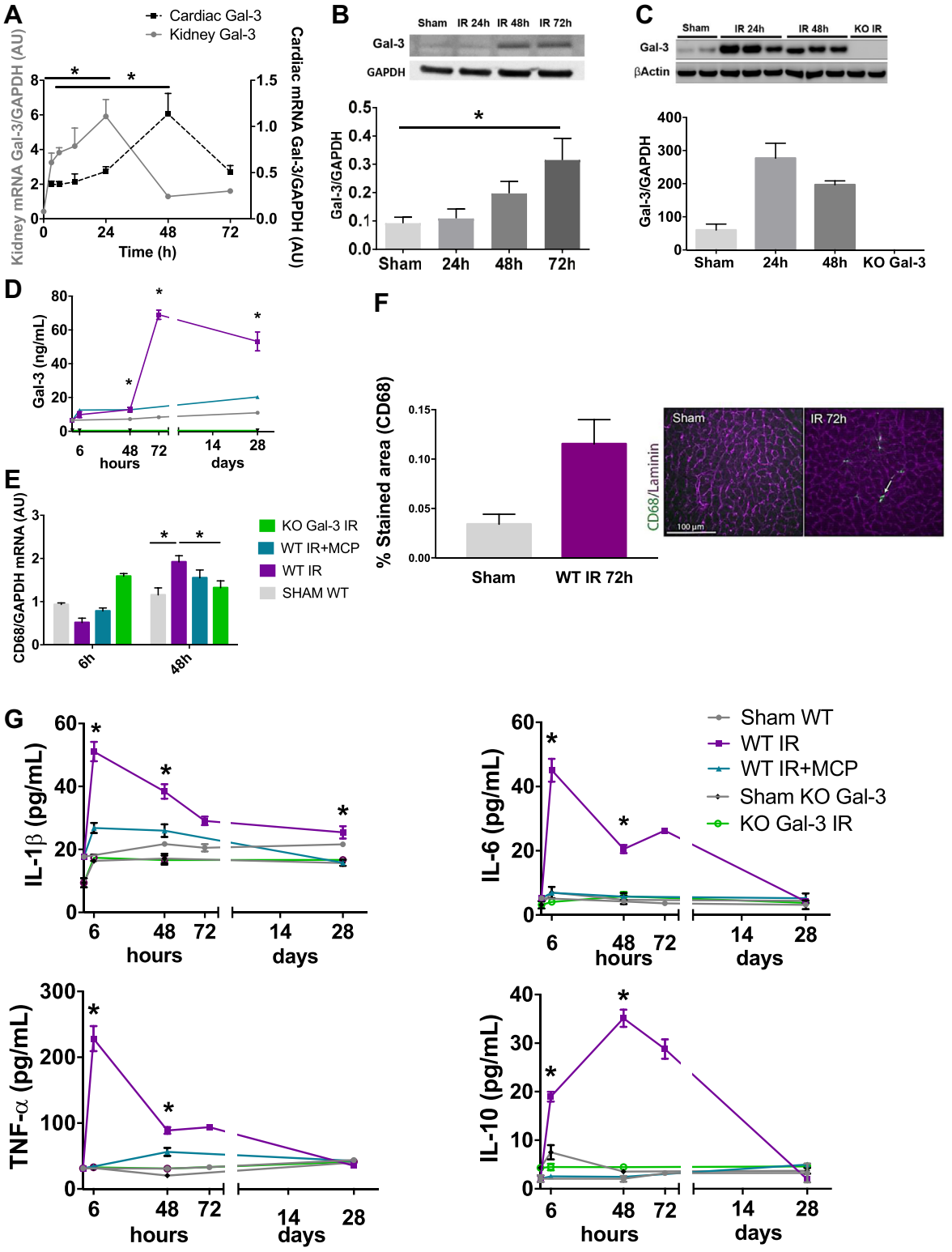

Continued on the next page

(Supplemental Figure 1A). Another mouse group was submitted to left femoral artery occlusion for 25 min, followed by reperfusion. These mice were killed 28 days after surgery (hind limb ischemia).

Bone marrow transplantation. Mice were irradiated at 10 grays (2 × 5 grays at 5-h interval) with filter, with a Faxitron irradiator (Faxitron, Tuscon, Arizona). After the second irradiation, mice were grafted with BM from wild-type (WT) or KO mice. At the end of the protocol, 2 groups of chimeric mice were obtained: WT mice grafted with KO Gal-3 bone marrow ($WT^{KO\ BM}$) and KO Gal-3 mice grafted with WT bone marrow ($KO^{WT\ BM}$). These chimeric mice were submitted to right nephrectomy and left renal IR injury, as described previously. Sham mice underwent the same procedure, except for right nephrectomy and left renal IR (Supplemental Figures 1B and 2).

Unilateral ureteral obstruction. A left ureteral obstruction was performed under anesthesia. The ureter was subsequently ligated in 2 places near the kidney. Sham mice underwent the same procedure, except for ureteral obstruction (Supplemental Figure 1C).

TREATMENTS. The Gal-3 inhibitor modified citrus pectin (MCP) was dissolved in drinking water (100 mg/kg/day). Mice were either pre-treated with MCP (IR+MCP) 3 days before surgery and during the time of reperfusion or treated 1 day after surgery (IR+MCP d+1).

HUMAN COHORT. The association among AKI, Gal-3, and cardiac injury was explored in the FROG-ICU (French and European Outcome Registry in Intensive Care Units) (NCT01367093). This study was an international observational study that included consecutive critically ill patients admitted to 23 intensive care units (ICUs) who received mechanical ventilation and/or vasopressors. The protocol was previously described elsewhere (15). In this subanalysis, patients with chronic kidney disease were excluded. The study population included 1,110 patients discharged from ICUs with neutrophil gelatinase-associated lipocalin data available on ICU admission and Gal-3 data available at ICU discharge. AKI was defined by the Kidney Disease Improving Global Outcome (KDIGO) definition (clinical AKI) or neutrophil gelatinase-associated lipocalin >150 ng/ml at ICU admission (subclinical AKI) (16,17). Plasmatic levels of cardiac injury and/or stress biomarkers were measured at ICU discharge (plasma Gal-3, N-terminal–pro-brain natriuretic peptide [NT-proBNP], and high-sensitivity troponin level). Interleukin (IL)–6 was measured as a biomarker of systemic inflammation.

STATISTICAL ANALYSIS. The primary endpoint was the association between Gal-3 expression and AKI. Results are expressed as mean ± SEM. A nonparametric Mann-Whitney U test was performed, unless otherwise stated. Levels of Gal-3 at discharge were compared using the Kruskal-Wallis test in the clinical cohort. Univariable and multivariable analyses using propensity score matching assessed the association between AKI and Gal-3 at ICU discharge in the clinical cohort. Variables included in the multivariable analysis were age, hypertension, chronic kidney disease, atrial fibrillation, liver disease, chronic heart failure, dyslipidemia, vascular disease, cancer, body mass index, heart rate, chronic obstructive pulmonary disease, Charlson score, simplified organ failure assessment score, simplified acute physiology score of 2, inotrope use, estimated glomerular filtration rate (eGFR) (using the Modified and Diet Renal Disease formula), septic shock, use of red blood cell transfusion, length of stay in the ICU, sex, and arterial blood pressure. Propensity score matching considered the probability that a patient with specific baseline characteristics had an AKI and then allowed

FIGURE 2 Continued

(A) Superposition of Gal-3 mRNA expression kinetics in the kidney and heart showed an early increase in Gal-3 in the kidney ($p < 0.001$; 24 h vs. 0 h), which preceded similar observations in the heart ($p < 0.001$; 48 h vs. 6 h). **(B)** Cardiac Gal-3 protein quantification confirmed this result, and increased cardiac Gal-3 levels were observed at 72 h compared with the sham group ($p = 0.016$). **(C)** Kidney Gal-3 protein levels after IR. **(D)** Gal-3 plasma levels began to increase at 48 h after IR compared with the sham group ($p = 0.037$), peaked at 72 h ($p = 0.017$ for WT IR mice vs. WT sham mice), and remained higher for 28 days compared with the sham group and modified citrus pectin (MCP)-treated mice ($p < 0.001$). **(E)** Cardiac CD68 mRNA increased at 48 h in WT IR mice ($p = 0.017$ vs. sham group) and was significantly higher than that in Gal-3 KO mice ($p = 0.03$). **(F)** CD68 immunostaining revealed positive cells at 72 h after reperfusion in IR mice compared with sham mice. Quantification confirmed increased Gal-3 expression in the heart. **(G)** Cytokine assays performed in plasma from WT (sham, IR, IR+MCP and IR+MCP d+1) and Gal-3 KO mice (sham and IR) showed a significant increase in interleukin (IL)-1-β, IL-6, IL-10, and tumor necrosis factor (TNF)-α levels at 6 and 48 h in WT IR mice, compared with WT IR+MCP ($p < 0.001$), KO IR ($p < 0.001$), and WT sham mice ($p < 0.001$). For **A**, n = 4 to 14. For **B and C**, n = 4 to 7 for the WT and sham groups. For **E and G**, n = 4 for sham, n = 7 to 14 for WT IR, n = 7 to12 for WT IR + MCP, n = 4 to 7 for KO Gal-3 IR. Data are presented as mean ± SEM, and comparisons of medians were made with the nonparametric Mann-Whitney U test. *$p < 0.05$. GADPH = glyceraldehyde 3-phosphate dehydrogenase; other abbreviations as in Figure 1.

FIGURE 3 At 28 Days, Kidney IR-Induced Cardiac Inflammation and Fibrosis Were Prevented in MCP-Treated and Gal-3 KO Mice

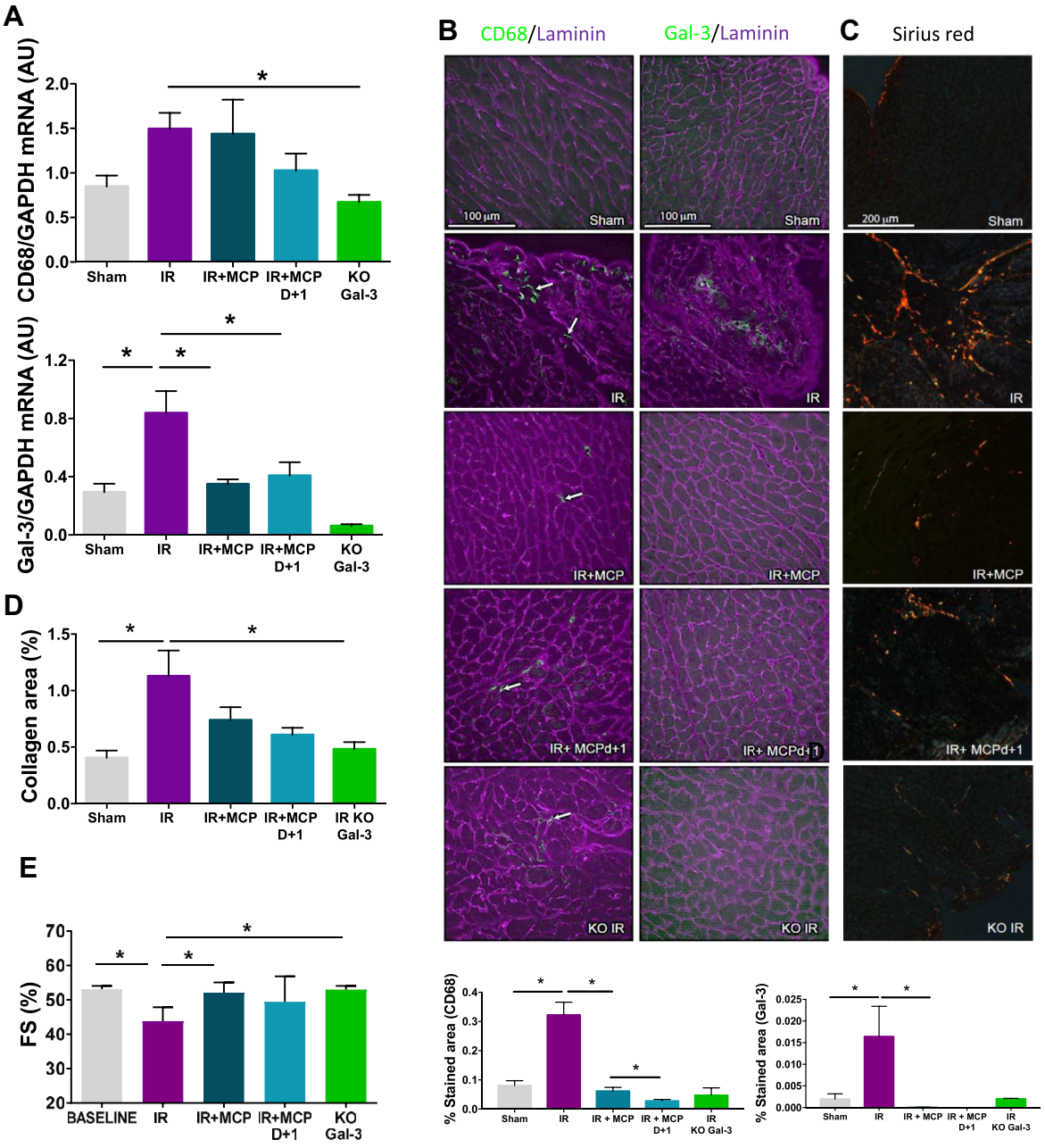

(A) Compared with the IR group, Gal-3 KO mice exhibited blunted cardiac inflammatory responses as indicated by lower CD68 mRNA in KO Gal-3 mice ($p = 0.007$). At 28 days, cardiac expression of Gal-3 remained high versus sham ($p = 0.028$). Mice treated with MCP had a lower cardiac expression of Gal-3 ($p = 0.008$ for WT IR vs. WR IR+MCP, and $p = 0.04$ for WT IR vs. WT IR+MCP day + 1 [d+1] comparisons). **(B)** Similar results were obtained after cardiac CD68 immunolabeling. CD68+ cells **(green)** were present in IR mice, whereas Gal-3 KO and MCP-treated mice showed the minimum CD68+ cells. Cardiac Gal-3 immunolabeling was positive in IR hearts but negative in treated mice. Quantification of Gal-3 and CD68 immunostainings confirmed the preceding observations ($p = 0.012$ for WT IR vs. WT IR+MCP and $p < 0.001$ for WT IR vs WT IR+MCP d+1 for CD68 immunostaining comparisons; $p < 0.001$ for both comparison WT IR vs. IR+MCP and WT IR vs. WT IR+MCP d+1 for Gal-3 immunostaining comparisons). **(C)** Sirius **red** coloration of the IR hearts treated with MCP (IR+MCP and IR+MCP d+1) and in Gal-3 KO mice revealed limited cardiac fibrosis. **(D)** Computer-assisted cardiac fibrosis evaluation confirmed these results ($p < 0.001$ for WT sham vs. WT IR and $p = 0.003$ for WT IR vs. KO Gal-3 IR). **(E)** Cardiac function assessed by the analysis of left ventricular fractional shortening (SF) was altered in response to IR ($p < 0.001$ baseline vs. IR) and rescued in KO-treated mice ($p = 0.002$ for IR vs IR + MCP and $p < 0.001$ for IR vs KO Gal-3). For **A to C**, $n = 5$ for sham group, $n = 7$ to 10 for WT IR, $n = 5$ to 6 for WT IR + MCP, $n = 5$ to 6 for WT IR + MCP d+1, and $n = 5$ to 8 for KO Gal-3 IR. For **E**, $n = 43$ for baseline echography and $n = 7$ for other groups. Data are presented as mean ± SEM and comparisons of medians were made with the nonparametric Mann-Whitney U test. *$p < 0.05$. Abbreviations as in Figures 1 and 2.

FIGURE 4 Gal-3 From BM-derived Cells, Including Macrophages, Is Sufficient to Induce Cardiac Fibrosis and Dysfunction

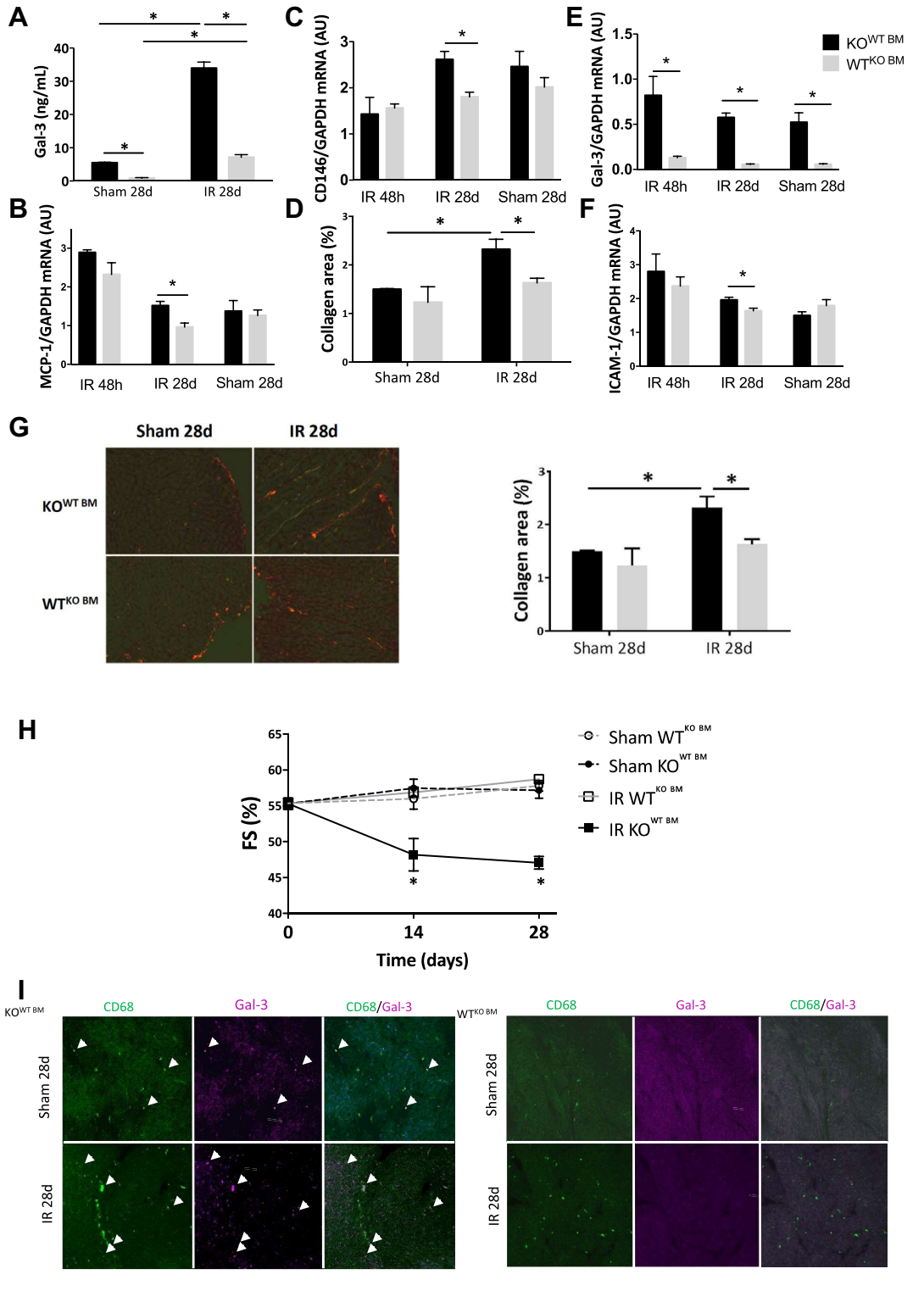

Continued on the next page

the comparison of Gal-3 levels in patients with or without AKI but with similar characteristics. The propensity score model included age, hypertension, chronic kidney disease, atrial fibrillation, liver disease, chronic heart failure, dyslipidemia, vascular disease, cancer, body mass index, heart rate, chronic obstructive pulmonary disease, Charlson score, simplified organ failure assessment score, simplified acute physiology score of 2, inotrope use, renal replacement therapy, eGFR (using the Modified and Diet Renal Disease formula), septic shock at admission, use of red blood cell transfusion during ICU stay, length of stay in the ICU, sex, and arterial blood pressure. Matching was performed according to the nearest neighbor approach within a caliper width of 0.2 (18). Imbalance between patients with and without AKI before and after propensity score matching was assessed using a standardized difference, considering <10% acceptable to define the study patients' characteristics balanced with respect to the previously described features. All statistical analyses were performed using R statistical software version 3.1.1 or above (The "R" Foundation for Statistical Computing, Vienna, Austria). A p value <0.05 was considered statistically significant.

RESULTS

AKI INDUCES GAL-3 EXPRESSION, CARDIAC INJURY, AND SYSTEMIC INFLAMMATION. After renal IR in WT mice, a transient increase in creatinine (Cr) and blood urea nitrogen (BUN) levels was observed 24 h post-reperfusion (**Figure 1A**). Cr and BUN returned to baseline within 48 h.

AKI induced an increase in kidney Gal-3 expression, mainly in tubular cells and monocytes at 24 h (**Figures 1B to 1D**). The increased expression of Gal-3 in monocytes was also confirmed in isolated renal macrophages (Supplemental Figure 3). This increase was followed by an increase in cardiac Gal-3 expression at 48 h (**Figure 2A**), which was confirmed at the protein level (**Figures 2B and 2C**). Cardiac tissue infiltration by inflammatory cells and systemic inflammation assessed with plasma cytokines and adhesion molecule levels measurements were observed during the first 72 h after IR. Plasma levels of Gal-3 increased, with a peak at 72 h, and remained elevated until day 28 (**Figure 2D**). *CD68* mRNA expression increased in the heart at 48 h (**Figure 2E**). Furthermore, hearts showed $CD68^+$ cells (infiltrating macrophages) (**Figure 2F**) and increased *MCP-1* mRNA expression at 72 h post IR versus that in sham mice (1.49 ± 1.0 vs. 4.1 ± 1.8; $p < 0.001$). Cytokines assays performed on plasma showed an increase in IL-1β, IL-6, IL-10, and tumor necrosis factor (TNF)-α levels at 6 and 48 h after IR (**Figure 2G**). Furthermore, adhesion of monocytes on endothelial monolayers was significantly increased after stimulation with recombinant Gal-3 (Supplemental Figure 4). Twenty-eight days after AKI, cardiac inflammation and fibrosis were observed. mRNA expression of both *CD68* and Gal-3 was increased (**Figure 3A**). Furthermore, $CD68^+$ and Gal-3^+ cells (**Figure 3B**) and increased collagen areas (**Figures 3C and 3D**) were observed.

Although cardiac function was normal during the first 72 h, IR induced a late increase in left ventricular diastolic diameter (Supplemental Table 1) and a decrease in fractional shortening (**Figure 3E**) 28 days after injury. At the anatomical level, kidney hypertrophy was observed 28 days after AKI and was not prevented by MCP treatment (Supplemental Table 1). Hind limb ischemia did not lead to cardiac dysfunction and injury, or changes in Gal-3 expression (Supplemental Figure 5).

FIGURE 4 Continued

(A) Plasmatic assays from chimeric mice $WT^{KO\ BM}$ mice (WT mice grafted with Gal-3 KO bone marrow [BM]) and $KO^{WT\ BM}$ mice (Gal-3 KO mice grafted with WT bone marrow) showed a difference in plasmatic Gal-3 level between sham $WT^{KO\ BM}$ and sham $KO^{WT\ BM}$ mice at 28 days. Furthermore, in response to IR, Gal-3 level was highly increased at 28 days post-IR in $KO^{WT\ BM}$ mice compared with sham mice ($p = 0.016$), whereas in $WT^{KO\ BM}$ mice, the Gal-3 increase was lower at 28 days post-IR ($p < 0.001$). Gal-3 level was lower in $WT^{KO\ BM}$ mice compared with $KO^{WT\ BM}$ mice ($p < 0.001$). **(B to F)** Interleukine (IL)-6 Cardiac CD146, monocyte chemoattractant protein (MCP)-1, Gal-3 and intercellular adhesion molecule (ICAM)-1 mRNAs expression were analyzed. CD146 and MCP-1 mRNA expression was higher in IR $KO^{WT\ BM}$ mice compare with IR $WT^{KO\ BM}$ mice ($p = 0.001$ for CD146, $p = 0.005$ for MCP-1). Gal-3 mRNA level did not alter in response to IR, but the level in $KO^{WT\ BM}$ mice was increased 6-fold vs $WT^{KO\ BM}$ mice (*$p < 0.001$ for all comparisons). **(G)** Sirius **red** coloration showed an increase in collagen fibers in response to IR in $KO^{WT\ BM}$ mice and blunted in $WT^{KO\ BM}$ mice. Computer-assisted cardiac fibrosis evaluation confirmed these results. **(H)** Echocardiography revealed a decline in fractional shortening after 28 days post-IR in $KO^{WT\ BM}$ mice that was prevented in $WT^{KO\ BM}$ mice ($p < 0.001$ for IR $KO^{WT\ BM}$ mice vs. IR $WT^{KO\ BM}$ mice at 14 and 28 days) **(I)** CD68/Gal-3 co-immunostaining performed on $WT^{KO\ BM}$ mice and $KO^{WT\ BM}$ mice showed CD68+ **(green)**/Gal-3+ **(purple)** cells in $KO^{WT\ BM}$ mice. CD68 staining appeared to be more important and grouped after acute kidney injury. No Gal-3 staining was observed in $WT^{KO\ BM}$ mice despite CD68+ cells in sham and IR mice. For 48 h and 28 days, $n = 4$ for sham $KO^{WT\ BM}$ mice, $n = 5$ for sham $WT^{KO\ BM}$ mice, $n = 5$ for IR $KO^{WT\ BM}$ mice, $n = 9$ for IR $WT^{KO\ BM}$ mice. Data are presented as mean ± SEM and comparisons of medians were made with the nonparametric Mann-Whitney U test. *$p < 0.05$. Abbreviations as in **Figure 1**.

FIGURE 5 Unilateral Ureteral Obstruction Leads to Cytokines Release, Cardiac Inflammation, Fibrosis and Dysfunction, Which Is Prevented in MCP Treated Mice

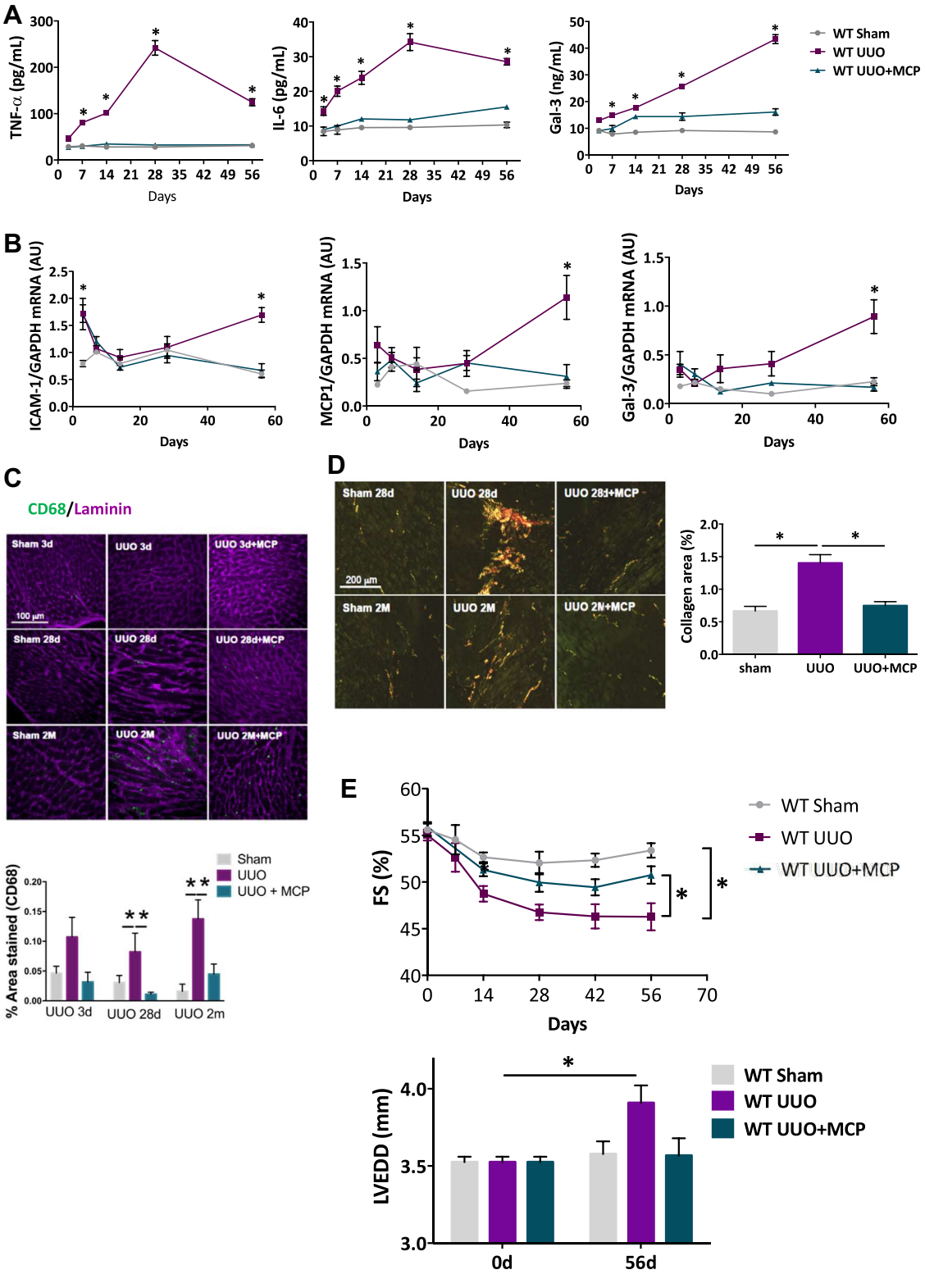

Continued on the next page

AKI-INDUCED CARDIAC INFLAMMATION, FIBROSIS, AND DYSFUNCTION IS GAL-3 DEPENDENT. Inactivation of Gal-3 by pharmacological inhibition (MCP treatment) and by genetic invalidation (Gal-3 KO mice) blunted cardiac consequences of AKI. Gal-3 inactivation prevented Gal-3 and cytokine release (Figures 2D and 2G), as well as cardiac endothelial activation (Figure 2H) during the first 72 h after renal IR. At 28 days post-AKI, Gal-3 inactivation prevented cardiac monocyte recruitment, Gal-3 increase (Figure 3B), cardiac fibrosis, and cardiac dysfunction (Figures 3C to 3E).

GAL-3 FROM BM-DERIVED CELLS IS RESPONSIBLE FOR CARDIAC DAMAGE. AKI was performed in a graft mouse model of BM. Chimeric mice were submitted to renal IR and killed 28 days post-reperfusion (Supplemental Figures 1B and 2). No variations in anatomical data were observed (Supplemental Table 2). Plasma Gal-3 levels were close to zero in sham $WT^{KO\ BM}$ mice. Furthermore, in response to renal IR, plasma Gal-3 levels were higher in $KO^{WT\ BM}$ than in $WT^{KO\ BM}$ mice (Figure 4A). No variation in plasmatic IL-6 levels was observed at 28 days post-IR (Figure 4B). Cardiac *CD146* and *MCP-1* mRNA levels, an endothelial and inflammatory marker, respectively, were lower in IR $WT^{KO\ BM}$ mice versus $KO^{WT\ BM}$ mice (Figures 4C and 4D). Cardiac *Gal-3* mRNA expression did not change between sham and IR mice but varied according to mice genotype. However, Gal-3 protein expression was slightly increased at 28 days after IR (Supplemental Figure 6). Cardiac Gal-3 mRNA expression was higher in $KO^{WT\ BM}$ mice than in $WT^{KO\ BM}$ mice (Figure 4E). Moreover, an increase in *ICAM-1* mRNA expression was observed in response to IR only in $KO^{WT\ BM}$ mice (Figure 4F). Furthermore, Sirius red staining showed a significant increase in cardiac interstitial fibrosis in response to IR in $KO^{WT\ BM}$ mice compared with sham mice, which was blunted in $WT^{KO\ BM}$ mice (Figure 4G). Echocardiography revealed a decrease in fractional shortening after IR only in $KO^{WT\ BM}$ mice (Figure 4H). Finally, CD68/Gal-3 co-staining in cardiac tissue showed $CD68^+/Gal\text{-}3^+$ cells in $KO^{WT\ BM}$ mice, whereas $CD68^+$ cells in $WT^{KO\ BM}$ mice were $Gal\text{-}3^-$ (Figure 4I).

CARDIAC DAMAGE AFTER AKI IS GAL-3 DEPENDENT BUT RENAL FUNCTION INDEPENDENT. Next, we assessed another model of renal injury, the unilateral ureteral obstruction (UUO), which does not affect renal function (Supplemental Figures 7A and 7B). Levels of Cr and BUN remained normal after UUO, whereas inflammation increased in the obstructed kidney. UUO+MCP mice were protected against renal inflammation (Supplemental Figure 7B). An increase in tubular dilatation was observed in both UUO and UUO+MCP mice at 15 days; an increase in right kidney weight (i.e., renal hypertrophy) was also observed at 2 months (Supplemental Figure 7B, Supplemental Table 3). Plasma levels of TNF-α, IL-6, IL-1β, and IL-10 were also increased after UUO and peaked at 28 days, except for IL-1β, which rapidly increased after surgery, peaked at 7 days, and then decreased and returned to baseline. The increase of cytokine levels was prevented by MCP treatment (Figure 5A, Supplemental Figure 8). Plasma levels of Gal-3 increased progressively during the 2 months of UUO (by 4-fold compared with sham group). In MCP-treated mice, the plasmatic increase of Gal-3 was blunted (Figure 5A). Similar signs of cardiac damage were observed compared with the renal IR model. An early (day 3) and transient cardiac increase in *ICAM-1* and late (2 months) increase in *ICAM-1, MCP-1*, and Gal-3 mRNA levels were observed in response to UUO, which were all prevented by MCP treatment (Figure 5B). At 28 days and 2 months, UUO induced cardiac inflammation and fibrosis, as shown by $CD68^+$cells (Figure 5C) and by an increase of interstitial collagen areas (Figure 5D). MCP treatment prevented fibrosis (Figures 5C and 5D). Importantly, UUO

FIGURE 5 Continued

(A) Cytokine assays performed in plasma showed a progressive increase in TNF-α, IL-6, and gal-3 levels until 28 days and 2 months respectively in response to UUO compared to WT UUO+MCP ($p < 0.001$ for comparisons at 28 days and 56 days) and WT sham mice ($p < 0.001$ for comparisons at 28 days and 56 days). **(B)** In response to UUO, cardiac mRNAs increased expressions of ICAM-1, MCP-1 and gal-3 compared to sham (UUO vs sham: $p < 0.001$ for ICAM-1, $p = 0.019$ for MCP-1, $p = 0.024$ for gal-3) were prevented in MCP treated mice at 2 months post-surgery (for UUO vs UUO+MCP: $p = 0.002$ for ICAM-1, $p < 0.001$ for MCP-1, $p = 0.002$ for gal-3). **(C)** CD68/Laminin immunostaining performed on cardiac tissue showed an increase in CD68+ cells in response to UUO from 28 days and less CD68+ cells in UUO+MCP. Quantification of CD68 staining confirmed the above observations. ($p = 0047$ for UUO vs sham and $p = 0.01$ for UUO vs UUO+MCP at 28 days; $p = 0.035$ for UUO vs sham and $p = 0.011$ for UUO vs UUO+MCP at 2 months). **(D)** Sirius red coloration revealed cardiac fibrosis afterat2 months of UUO. MCP treatment blunted collagen accumulation and deposition. Computer-assisted cardiac fibrosis evaluation confirmed these results ($p < 0.001$ for both comparisons UUO vs sham and UUO vs UUO+MCP). **(E)** Left ventricular Fractional shortening (FS) analysis by echocardiography after 2 months highlights a progressive decreasing in FS in response to UUO ($p = 0.01$ for UUO vs sham), prevented in treated mice ($p = 0.02$ for UUO vs UUO+MCP). Left ventricular end diastolic diameter (LVEDD) analysis revealed an increase in LVEDD after 2 months for UUO ($p = 0.043$ UUO vs sham), reflecting left ventricular dilatation. For different time points, $n = 4$ for WT sham UUO, $n = 5$-8 for WT UUO, $n = 6$-8 for WT UUO + MCP. Data are presented as mean ± SEM and comparisons of medians were made with non-parametric Mann-Whitney U test. *$p < 0.05$. Abbreviations as in Figures 1, 2, and 4.

FIGURE 6 **Plasma Gal-3 and AKI in Critically Ill Patients Discharged From ICU**

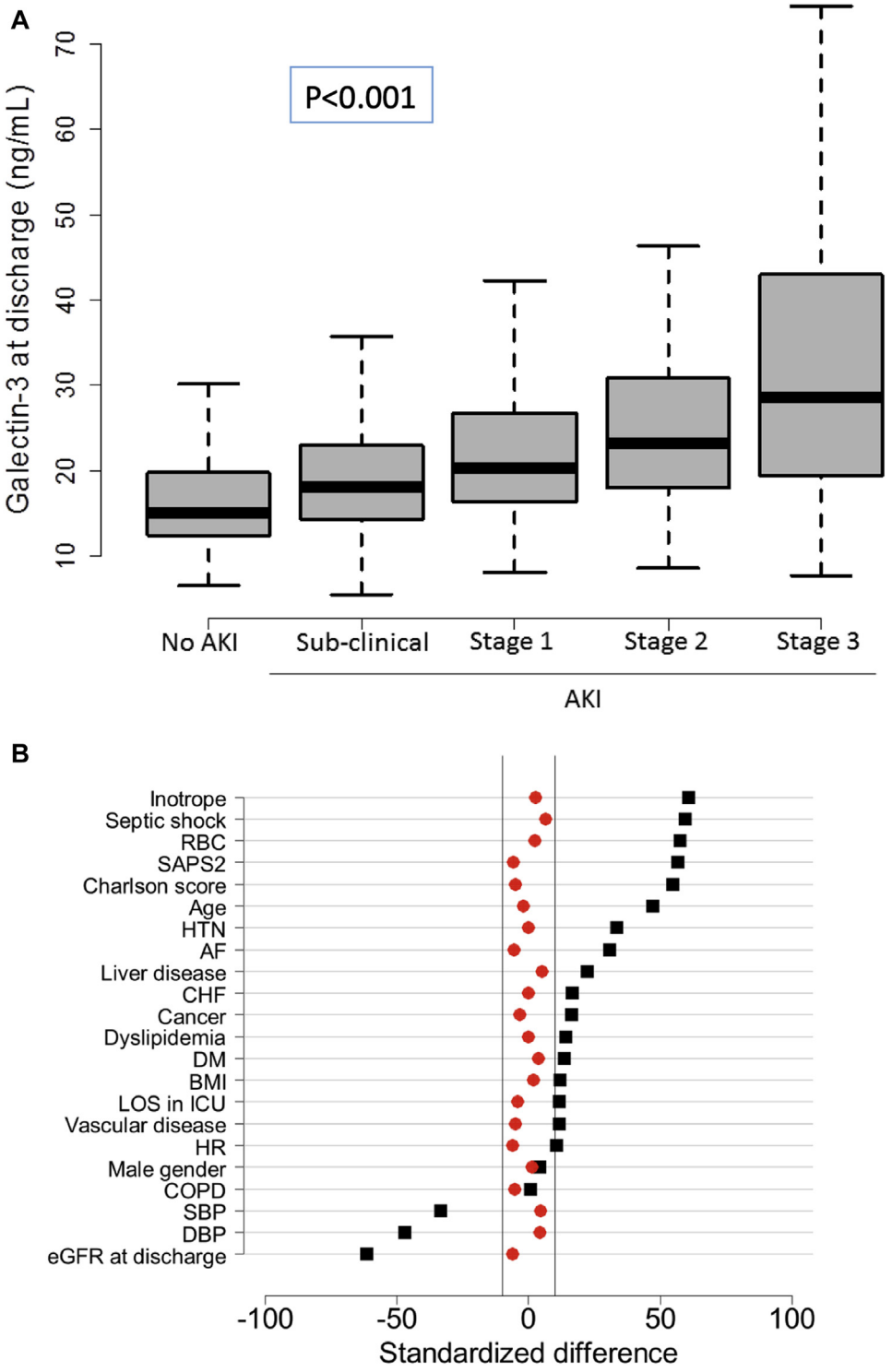

(A) Plasma Gal-3 level at hospital discharge according to AKI stage (sub-clinical, and stage 1, 2, or 3 of the KDIGO guidelines). We observed a stepwise increase of plasma Gal-3 level with AKI stages. **(B)** Graphical representation of imbalance in patients' characteristics before and after propensity score (PS) matching between no AKI and AKI patients (**Black squares** represents mean standardized difference [MSD] before PS-matching and the **red points** MSD after PS-matching). Abbreviations as in Figure 1.

induced left ventricular dilatation and a decrease in fractional shortening, which was prevented by MCP (**Figure 5E**).

AKI IS ASSOCIATED WITH GAL-3 EXPRESSION AND CARDIAC INJURY AT ICU DISCHARGE IN THE CLINICAL SETTING. In the clinical cohort, 645 (58%) patients developed AKI during ICU stay and were discharged alive (Supplemental Table 4), including 252 patients with subclinical AKI and 134, 65, and 194 patients with AKI KDIGO stages 1, 2, and 3, respectively. Plasma level of Gal-3 showed a stepwise increase with severity of AKI (from subclinical to stage 3) (**Figure 6**). Plasma level of Gal-3 was associated with AKI in univariable analysis (mean difference: 8.60 ng/ml; 95% CI: 7.04 to 10.15; $p < 0.001$) and remained significantly associated after adjustment for cofounding factors in multivariable analysis (mean difference: 5.13 ng/ml; 95% CI: 2.92 to 7.35; $p < 0.001$)). AKI was associated with increased biomarkers of cardiac injury (Gal-3, sST-2 and high-sensitivity troponin I), increased cardiac stress (NT-proBNP), and systemic inflammation (IL-6) at ICU discharge, even in patients who recovered their renal function (Supplemental Table 5).

DISCUSSION

In this study, we explored the impact of AKI on remote cardiac injury. Results showed that renal IR promoted the development of cardiac injury and fibrosis in part through the activation of the Gal-3 pathway. Gal-3 originated from BM-derived cells, including macrophages. Furthermore, by using the UUO model of renal disease we showed that cardiac injury occurred after renal damage even if renal function was not affected. Altogether, our data indicated that the activation of the Gal-3 pathway represents 1 of the causal links between AKI and cardiac injury.

Our findings provided important insights into cardiorenal syndrome type 3 or acute reno-cardiac syndrome (AKI leading to cardiac injury) pathophysiology (19). We hypothesized that AKI triggers the secretion of Gal-3, which promotes the development of cardiac injury by generating fibrosis.

Occurrence of AKI was associated with both short- and long-term risk of mortality in different settings (1). Furthermore, there was increasing evidence that AKI is associated with a risk of cardiovascular events (3,20). Recently, Go et al. (21) explored the association between AKI and the risk of cardiovascular events during the year following hospital discharge. Using a large database with propensity score matching, they observed that AKI was a risk factor for heart failure during the year following discharge. Such cardiovascular consequences of AKI may be causal (at least partially) in the poor outcomes of the injury. In this study, we explored the association between AKI and circulating expression of Gal-3 and cardiac injury in critically ill patients. We observed that patients who presented with AKI during ICU stay and survived had higher plasma Gal-3 levels at discharge, along with high plasma levels of biomarkers of cardiac injury and failure. Although renal function did affect the level of natriuretic peptides and troponin, eGFR did not appear to be the major determinant of these cardiac biomarker levels (22). Recent data showed similar diurnal variation in patients with and without chronic kidney disease, which suggested that decreased clearance is not the primary mechanism for elevated high-sensitivity cardiac troponin levels in the patients with renal failure (23). Importantly, elevated levels of natriuretic peptides and troponin were associated in many studies with cardiovascular events and outcome (24,25). Therefore, these biomarkers are still considered valid biomarkers of cardiovascular events in patients with renal failure. Finally, patients with AKI but who were discharged with eGFR >60 ml/min/1.73 m^2 showed elevated plasma biomarkers of cardiac damage compared with patients without AKI (Supplemental Table 5).

We used preclinical models to explore the pathophysiological roles of Gal-3 after AKI. In our models, acute cardiac response to renal injury was characterized by an early increase in plasmatic cytokine levels and cardiac injury. The acute cardiac response was followed by a late cardiac response that was characterized by systolic dysfunction and cardiac fibrosis. The early and late cardiac responses were Gal-3–dependent because they were prevented by MCP, a Gal-3 inhibitor, and in Gal-3 KO mice. Of note, the role of Gal-3 in remote cardiac injury was specifically linked to renal injury because hind limb IR did not induce any cardiac damage. Furthermore, Gal-3 remained elevated both in the plasma and heart in the preclinical models despite complete restoration of renal function.

In short-term animal experiments, AKI was shown to promote cellular apoptosis in the heart, followed by cardiac hypertrophy and fibrosis. Burchill et al. (26) observed cardiac hypertrophy and fibrosis 10 days after renal IR. Increased levels of immunoreactive *TNF-α*, *IL-1*, and *ICAM-1* mRNA were also reported in the heart within 48 h after renal IR (27). Furthermore, cardiomyocyte apoptosis was also observed and associated with cardiac dysfunction evaluated by

FIGURE 7 Schematic Representation of the Results From Initial Renal Injury to Cardiac Dysfunction, Including the Effects of Gal-3 Inhibition

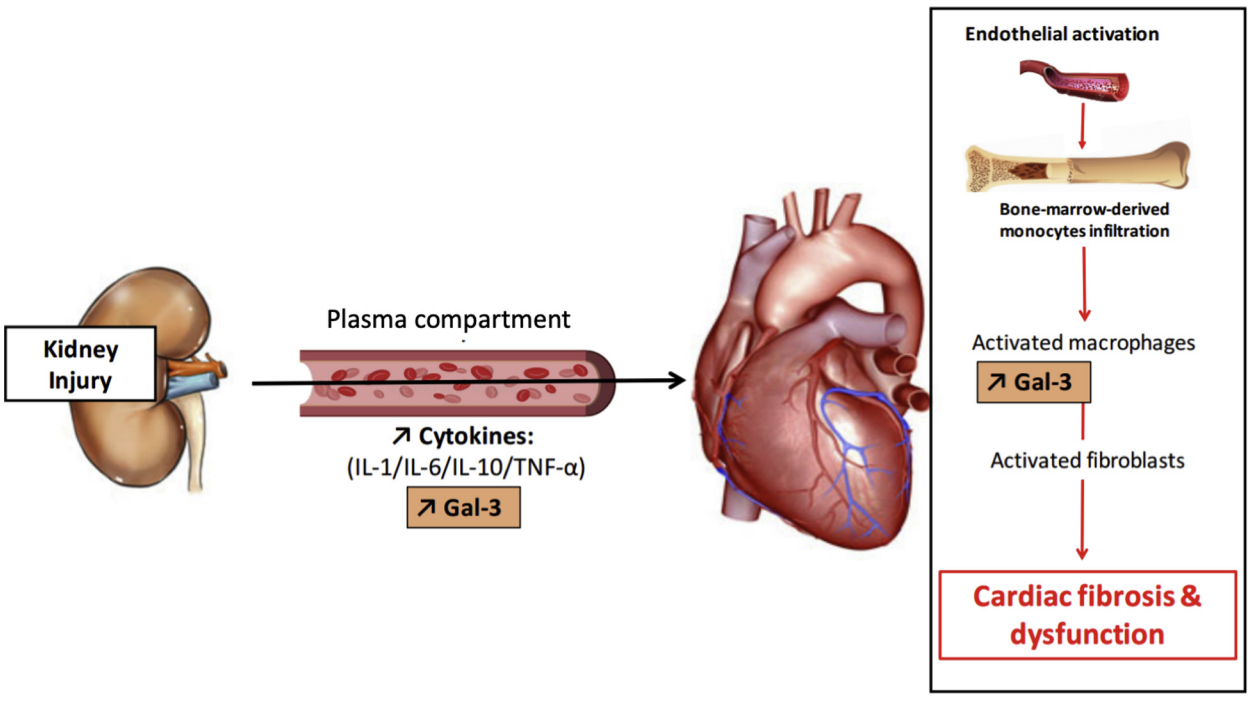

Renal injury induced transient renal dysfunction only in the IR model (increase in creatinine and blood urea nitrogen), as well as tubular cell response and macrophage activation, which led to an increase in Gal-3 expression. These features led to systemic inflammation by increasing levels of plasma cytokines (Il-1, IL-6, IL-10, and TNF-α) and Gal-3, which induced cardiac endothelial activation as shown by increased in ICAM-1, vascular cell adhesion molecule-1, monocyte chemoattractant protein-1 and connective tissue growth factor mRNA levels. Endothelial activation promoted monocyte infiltration in cardiac tissue; these monocytes differentiated into activated macrophages (increased CD68), thus expressing and secreting transforming growth factor (TGF)-β and Gal-3. TGF-β and Gal-3 may participate in the activation of fibroblasts leading to collagen type 1 and 3 synthesis and subsequent cardiac fibrosis and dysfunction. Treatment with MCP, Gal-3 deletion (Gal-3 KO mice), and WT mice grafted with Gal-3 KO BM, prevented the increase in plasma cytokines, Gal-3, cardiac Gal-3, fibroblast activation, and the increase in cardiac fibrosis, which therefore prevented cardiac dysfunction. Abbreviations as in **Figures 1, 2, and 4**.

echocardiography at 72 h (28). In another study, the macrophage chemokine osteopontin was increased, along with macrophage infiltration in the heart after 24 h of renal IR (29). In addition, increased TNF-α, IL-6, and IL-1β plasma concentrations were observed 3 h after renal IR (30). In our model, cytokine assays showed increased plasma cytokine levels in response to AKI during the acute stage (6 to 48 h). This increase was prevented in MCP-treated and Gal-3 KO mice. Martinez-Martinez et al. (8) showed that experimental hyperaldosteronism leads to cardiac fibrosis in a Gal-3–dependent pathway that is independent of blood pressure (8). The results from our study showed that AKI promoted Gal-3–dependent cardiac injury and inflammation, fibrosis, and systolic dysfunction.

Recently, macrophages were identified as key players in the development of heart failure (31). As we observed in our model, infiltration of macrophages was facilitated by the activation of the endothelium (which overexpresses its cell surface adhesion proteins, intercellular adhesion molecule-1, vascular cell adhesion molecule-1), which favored inflammatory cells transfer from the vascular compartment to the tissue. The role of Gal-3 as a chemokine was previously shown by Sano et al. (32), and in addition to that study, we showed that Gal-3 promotes monocyte adhesion (Supplemental Figure 4). Consequently, Gal-3 might have both chemoattractive and pro-adhesive effects locally in the damaged tissues. Gal-3 was already known for inducing fibrosis via the synthesis of TGF-β (33), but also by activating fibroblasts and collagen synthesis (34). The pro-fibrotic effect of Gal-3 was observed separately both in the kidney and the heart, making this lectin a serious promoter of type 3 cardiorenal syndrome. MCP is a complex water-soluble indigestible polysaccharide rich in β-galactose. The

carbohydrate chains of MCP are rich in galactose and are recognized by Gal-3 carbohydrate recognition domains. MCP's recognized mode of action is Gal-3 activity inhibition via carbohydrate recognition domains. There are currently no data that show anti-cytokinic or pro-cytokinic action of MCP via another pathway. However, we could not confirm the specificity of the carbohydrate recognition domain pathway mechanism of action of MCP.

AKI can induce systemic sympathetic nervous system and renin-angiotensin-aldosterone system activation (35). Although the increase in systemic arterial pressure was not sustained, increased vascular reactivity to angiotensin II was reported (36). Our group and others showed that activation of the renin-angiotensin-aldosterone system could promote cardiac and renal injuries (10,11). Gal-3 participates in the mechanisms of aldosterone-mediated myocardial damage. It is therefore also possible that activation of the renin-angiotensin-aldosterone system promotes endothelial injury in remote organs after AKI. These vascular consequences should be investigated in the future.

Finally, cardiac fibrosis has been extensively recognized as a key player in the development of heart failure. In our models, cardiac expression of Gal-3 was decreased in mice that received MCP compared with control mice and was associated with lower macrophage infiltration, which reflected a possible positive feedback of Gal-3 on macrophage recruitment. Thus, a decrease in cardiac Gal-3 expression may arise from direct synthesis inhibition as well as a decrease in macrophage recruitment.

We explored the source of Gal-3 in our models. Gal-3 can be expressed in different cell types including tubular and immune cells (37). In our model of renal IR, damaged tubules expressed Gal-3 and might also be the source of pro-inflammatory cytokine expression. In this study, the question of the source of cardiac Gal-3 after AKI was mainly explored using BM transplantation. We showed that renal IR led to an increase in Gal-3 expression, cardiac fibrosis, and dysfunction in WT mice, but this damage was prevented in $WT^{KO\ BM}$ mice. Furthermore, we observed cardiac CD68+/Gal-3+ cells by immunostaining only in $KO^{WT\ BM}$ mice, whereas $WT^{KO\ BM}$ mice did not express cardiac Gal-3. This set of experiments confirmed that cardiac Gal-3 arises from BM -derived immune cells, including macrophages. Souza et al. (38) showed in a mouse model of myocarditis that cardiac Gal-3 expression was high in macrophages, T cells, and fibroblasts using flux cytometry and confocal microscopy. Inhibition of Gal-3 by MCP or N-acetyl-D-lactosamine reduced cardiac inflammation and fibrosis and modulated the expression of pro-inflammatory genes in the heart.

Gal-3 appears to be a mandatory mediator for AKI-Induced cardiac damage because a specific blockage of the Gal-3 pathway prevented cardiac damage and injury. Gal-3 was shown to trigger immune cells and cytokines release. Inhibition of Gal-3 activity led to inhibition of macrophage recruitment and activation, and therefore, indirectly to a decrease in cytokine expression (e.g., TNF-α, IL-1, IL-6, IL-4, or IL-8 (34,39). The decrease in the expression of these cytokines led to the modulation of other cytokines in the downstream inflammatory cascade. Therefore, Gal-3 appeared upstream of the release of these cytokines. However, it remains to be tested whether blocking 1 of these downstream cytokines (IL-1, IL-6, TNF-α) would have cardioprotective effects as well.

A summary scheme of our results is shown in **Figure 7**. Kidney injury induces an increase in renal, circulating, and cardiac Gal-3 expression and in circulating cytokines levels. Kidney injury leads to cardiac damage via endothelium activation, monocyte recruitment, and finally development of cardiac fibrosis and dysfunction. Remote cardiac consequences of kidney injury are prevented in Gal-3 KO mice, MCP-treated mice, and in $WT^{KO\ BM}$ mice.

CONCLUSIONS

The Gal-3 pathway is involved in remote cardiac damage after AKI, which may be involved in AKI-associated poor outcomes. Cardiac Gal-3 originates from BM -derived cells. These findings open an area of clinical research with the aim of prevention of devastating consequences of AKI in humans.

ACKNOWLEDGMENTS The authors thank Pr Hang Korng Ea for discussions and help in Gal-3 KO mice strain development, Merval Régine, Polidano Evelyne, and Placier Sandrine for their technical assistance with the animal model, and Dr. Panagiotis Kavvadas for critical reading of the manuscript.

ADDRESS FOR CORRESPONDENCE: Dr. Matthieu M. Legrand, Department of Anesthesiology and Peri-Operative Care, University of California San Francisco, 500 Parnassus Avenue, E410, San Francisco, California 94117. E-mail: matthieu.legrand@ucsf.edu.

PERSPECTIVES

COMPETENCY IN MEDICAL KNOWLEDGE: AKI leads to remote cardiac injuries, including cardiac inflammation, acute dysfunction, and *in fine* fibrosis. These effects may contribute to poor outcomes after AKI. Remote cardiac injury after AKI is in part mediated by a Gal-3–dependant pathway that originates mainly from BM-derived immune cells.

TRANSLATIONAL OUTLOOK: Future research should examine inhibition of the Gal-3 pathway after AKI to prevent the adverse cardiac effects induced by AKI and to improve its prognosis.

REFERENCES

1. Sawhney S, Marks A, Fluck N, Levin A, Prescott G, Black C. Intermediate and long-term outcomes of survivors of acute kidney injury episodes: a large population-based cohort study. Am J Kidney Dis 2017;69:18–28.

2. Kaddourah A, Basu RK, Bagshaw SM, Goldstein SL, AWARE Investigators. Epidemiology of acute kidney injury in critically ill children and young adults. N Engl J Med 2017;376:11–20.

3. Parikh CR, Puthumana J, Shlipak MG, et al. Relationship of kidney injury biomarkers with long-term cardiovascular outcomes after cardiac surgery. J Am Soc Nephrol 2017;28:3699–707.

4. Yap SC, Lee HT. Acute kidney injury and extrarenal organ dysfunction: new concepts and experimental evidence. Anesthesiology 2012;116:1139–48.

5. Ronco C, McCullough P, Anker SD, et al. Cardiorenal syndromes: report from the consensus conference of the acute dialysis quality initiative. Eur Heart J 2010;31:703–11.

6. Ponikowski P, Voors AA, Anker SD, et al. 2016 ESC Guidelines for the diagnosis and treatment of acute and chronic heart failure: The Task Force for the diagnosis and treatment of acute and chronic heart failure of the European Society of Cardiology (ESC) Developed with the special contribution of the Heart Failure Association (HFA) of the ESC. Eur Heart J 2016;37:2129–200.

7. de Boer RA, Voors AA, Muntendam P, van Gilst WH, van Veldhuisen DJ. Galectin-3: a novel mediator of heart failure development and progression. Eur J Heart Fail 2009;11:811–7.

8. Martínez-Martínez E, Calvier L, Fernández-Celis A, et al. Galectin-3 blockade inhibits cardiac inflammation and fibrosis in experimental hyperaldosteronism and hypertension. Hypertension 2015;66:767–75.

9. Azibani F, Benard L, Schlossarek S, et al. Aldosterone inhibits antifibrotic factors in mouse hypertensive heart. Hypertension 2012;59:1179–87.

10. Vergaro G, Prud'homme M, Fazal L, et al. Inhibition of galectin-3 pathway prevents isoproterenol-induced left ventricular dysfunction and fibrosis in mice. Hypertension 2016;67:606–12.

11. Calvier L, Martinez-Martinez E, Miana M, et al. The impact of galectin-3 inhibition on aldosterone-induced cardiac and renal injuries. J Am Coll Cardiol HF 2015;3:59–67.

12. Dang Z, MacKinnon A, Marson LP, Sethi T. Tubular atrophy and interstitial fibrosis after renal transplantation is dependent on galectin-3. Transplantation 2012;93:477–84.

13. Colnot C, Fowlis D, Ripoche MA, Bouchaert I, Poirier F. Embryonic implantation in galectin 1/galectin 3 double mutant mice. Dev Dyn 1998;211:306–13.

14. Wei Q, Dong Z. Mouse model of ischemic acute kidney injury: technical notes and tricks. Am J Physiol Renal Physiol 2012;303:F1487–94.

15. Mebazaa A, Casadio MC, Azoulay E, et al. Post-ICU discharge and outcome: rationale and methods of the French and euROpean Outcome reGistry in Intensive Care Units (FROG-ICU) observational study. BMC Anesthesiol 2015;15:143.

16. Zarbock A, Kellum JA, Schmidt C, et al. Effect of early vs delayed initiation of renal replacement therapy on mortality in critically ill patients with acute kidney injury: the ELAIN randomized clinical trial. JAMA 2016;315:2190–9.

17. Ronco C, Legrand M, Goldstein SL, et al. Neutrophil gelatinase-associated lipocalin: ready for routine clinical use? An international perspective. Blood Purif 2014;37:271–85.

18. Austin PC. Some methods of propensity-score matching had superior performance to others: results of an empirical investigation and Monte Carlo simulations. Biom J Biom Z 2009;51:171–84.

19. Braam B, Joles JA, Danishwar AH, Gaillard CA. Cardiorenal syndrome-current understanding and future perspectives. Nat Rev Nephrol 2014;10:48–55.

20. Gammelager H, Christiansen CF, Johansen MB, Tønnesen E, Jespersen B, Sørensen HT. Three-year risk of cardiovascular disease among intensive care patients with acute kidney injury: a population-based cohort study. Crit Care Lond Engl 2014;18:492.

21. Go AS, Hsu C-Y, Yang J, et al. Acute kidney injury and risk of heart failure and atherosclerotic events. Clin J Am Soc Nephrol 2018;13:833–41.

22. Vickery S, Price CP, John RI, et al. B-type natriuretic peptide (BNP) and amino-terminal proBNP in patients with CKD: relationship to renal function and left ventricular hypertrophy. Am J Kidney Dis 2005;46:610–20.

23. van der Linden N, Cornelis T, Kimenai DM, et al. Origin of cardiac troponin T elevations in chronic kidney disease. Circulation 2017;136:1073–5.

24. van Kimmenade RRJ, Januzzi JL, Baggish AL, et al. Amino-terminal pro-brain natriuretic Peptide, renal function, and outcomes in acute heart failure: redefining the cardiorenal interaction? J Am Coll Cardiol 2006;48:1621–7.

25. Forfia PR, Watkins SP, Rame JE, Stewart KJ, Shapiro EP. Relationship between B-type natriuretic peptides and pulmonary capillary wedge pressure in the intensive care unit. J Am Coll Cardiol 2005;45:1667–71.

26. Burchill L, Velkoska E, Dean RG, et al. Acute kidney injury in the rat causes cardiac remodelling and increases angiotensin-converting enzyme 2 expression. Exp Physiol 2008;93:622–30.

27. Kelly KJ. Distant effects of experimental renal ischemia/reperfusion injury. J Am Soc Nephrol 2003;14:1549–58.

28. Sumida M, Doi K, Ogasawara E, et al. Regulation of mitochondrial dynamics by dynamin-related protein-1 in acute cardiorenal syndrome. J Am Soc Nephrol 2015;26:2378–87.

29. Tokuyama H, Kelly DJ, Zhang Y, Gow RM, Gilbert RE. Macrophage infiltration and cellular proliferation in the non-ischemic kidney and heart following prolonged unilateral renal ischemia. Nephron Physiol 2007;106:54–62.

30. Mitaka C, Si MKH, Tulafu M, et al. Effects of atrial natriuretic peptide on inter-organ crosstalk among the kidney, lung, and heart in a rat model of renal ischemia-reperfusion injury. Intensive Care Med Exp 2014;2:28.

31. Hulsmans M, Sager HB, Roh JD, et al. Cardiac macrophages promote diastolic dysfunction. J Exp Med 2018;215:423–40.

32. Sano H, Hsu DK, Yu L, et al. Human galectin-3 is a novel chemoattractant for monocytes and macrophages. J Immunol 2000; 165:2156–64.

33. Sharma UC, Pokharel S, van Brakel TJ, et al. Galectin-3 marks activated macrophages in failure-prone hypertrophied hearts and contributes to cardiac dysfunction. Circulation 2004;110: 3121–8.

34. Henderson NC, Mackinnon AC, Farnworth SL, et al. Galectin-3 expression and secretion links macrophages to the promotion of renal fibrosis. Am J Pathol 2008;172:288–98.

35. Hering D, Winklewski PJ. R1 autonomic nervous system in acute kidney injury. Clin Exp Pharmacol Physiol 2017;44:162–71.

36. Basile DP, Donohoe DL, Phillips SA, Frisbee JC. Enhanced skeletal muscle arteriolar reactivity to ANG II after recovery from ischemic acute renal failure. Am J Physiol Regul Integr Comp Physiol 2005;289:R1770–6.

37. Fernandes Bertocchi AP, Campanhole G, Wang PHM, et al. A role for galectin-3 in renal tissue damage triggered by ischemia and reperfusion injury. Transpl Int 2008;21: 999–1007.

38. Souza BS de F, Silva DN, Carvalho RH, et al. Association of cardiac galectin-3 expression, myocarditis, and fibrosis in chronic Chagas disease cardiomyopathy. Am J Pathol 2017;187: 1134–46.

39. Chung AW, Sieling PA, Schenk M, et al. Galectin-3 regulates the innate immune response of human monocytes. J Infect Dis 2013;207: 947–56.

KEY WORDS fibrosis, heart failure, inflammation, macrophages, renal failure

APPENDIX For an expanded Methods section as well as supplemental figures and tables, please see the online version of this paper.

JACC: BASIC TO TRANSLATIONAL SCIENCE VOL. 4, NO. 6, 2019

EDITORIAL COMMENT

The Kidney, Bone Marrow, and Heart Connection in Acute Kidney Injury

Role of Galecin-3*

Yang Chen, PhD, John C. Burnett, Jr, MD

In this issue of *JACC: Basic to Translational Science*, Prud'homme et al. (1) report that experimental acute kidney injury (AKI) in mice induces remote cardiac injury through the upregulation of a novel mediator galectin-3 (Gal-3). The major findings are that acute (up to 72 h) ischemia/reperfusion-induced AKI in mice stimulated an increase in Gal-3 expression in tubular inflammatory cells in the kidney and in cardiac tissues, with an increase in circulating levels of Gal-3. Along this line, ischemia/reperfusion also stimulated macrophage infiltration ($CD68^+$ cells) and an increase in plasma proinflammatory cytokines. With Gal-3 disruption (Gal-3 knockout [KO]), ischemia/reperfusion in KO mice abrogated the inflammatory response supported by decreases in cardiac $CD68^+$ cells and cytokines levels. Long-term (1-month) ischemia/reperfusion upregulated Gal-3 expression and induced cardiac injury and dysfunction with myocardial inflammation, fibrosis, decrease of fractional shortening, and an increase of left ventricular diastolic diameter. Gal-3 blockade with Gal-3 KO or pharmaceutical inhibition by modified citrus pectin significantly attenuated these abnormal myocardial events. The modified citrus pectin effect was confirmed in a second long-term (up to 2 months) model of kidney injury induced by unilateral ureteral obstruction, in which the obstruction increased Gal-3, inflammation, and fibrosis, and reduced fractional shortening. This second model was a rigorous test of the hypothesis of Prudhomme et al. (1) that the kidney communicates with the heart via Gal-3.

SEE PAGE 717

From a mechanistic perspective, an intriguing observation made by the investigators using the ischemia/reperfusion model together with Gal-3 KO mice bone marrow transplant revealed that Gal-3 originated from bone marrow mediated the pathophysiologic responses such as inflammation and fibrosis in the 1-month study. Additionally, in a highly translational study, the investigators performed a Gal-3 biomarker study in human AKI. Plasma Gal-3 at discharge from the hospital in a cohort of 645 critically ill patients with AKI showed a stepwise elevation, with severity of AKI from AKI-free, subclinical, stage 1, stage 2, and stage 3, supporting its role as an AKI biomarker.

AKI is characterized by an abrupt decline of renal function, with a decrease of glomerular filtration rate or urine output. It has a high prevalence rate especially in critically ill patients and is also a powerful risk factor for heart failure incidence. AKI remains a challenging clinical problem, and to date no therapies have been approved by the Food and Drug Administration for AKI patients. Thus, innovative AKI therapeutics represent an unmet clinical need. Here in this elegantly designed study, Prud'homme et al. (1) demonstrated that Gal-3 can serve as both a drug target for AKI-induced cardiac dysfunction and a biomarker for AKI.

*Editorials published in *JACC: Basic to Translational Science* reflect the views of the authors and do not necessarily represent the views of *JACC: Basic to Translational Science* or the American College of Cardiology.

From the Cardiorenal Research Laboratory, Department of Cardiovascular Medicine, Mayo Clinic, Rochester, Minnesota. This work was supported by AHA Predoctoral Fellowship 16PRE30770009 (Dr. Chen) and RO1 HL36634 (Dr. Burnett).

The authors attest they are in compliance with human studies committees and animal welfare regulations of the authors' institutions and Food and Drug Administration guidelines, including patient consent where appropriate. For more information, visit the *JACC: Basic to Translational Science* author instructions page.

ISSN 2452-302X https://doi.org/10.1016/j.jacbts.2019.09.001

There is no doubt that understanding the pathophysiology of AKI, discovering effective therapeutic targets, and identifying novel sensitive biomarkers will provide tremendous benefits for AKI therapeutics, thus improving the outcomes of patients with AKI. Indeed, recently published preclinical studies in large-animal AKI models have reported the potential of multiple promising innovative drugs, which includes targeting the particulate guanylyl cyclase A receptor pathway (2), adenosine A2 receptor signaling (3), and vascular endothelial growth factor (4), as well as suppressing CD47 (5). Furthermore, according to the Clinical Trials Register, investigational drugs targeting soluble guanylyl cyclase, particulate guanylyl cyclase A receptor, vitamin D receptor, CD28 receptor, p53 pathway, hepatocyte growth factor, and *N*-acetylcysteine are under way, with most of the studies centered on AKI prevention and treatment in patients undergoing cardiac surgery. In regard to biomarker studies, newly discovered noninvasive urinary biomarkers include c-type natriuretic peptide (2), liver fatty acid binding protein (6), and matrix metalloprotease 7 (7), which have demonstrated powerful predictive value in experimental or human studies.

The interconnecting pathophysiology and close interactions between the heart and kidney inevitably generate the challenge of cotargeting both organs for AKI. Previously, our laboratory reported that renal insufficiency induced myocardial apoptosis, fibrosis, and diastolic dysfunction (8). Similarly, as advanced by Prud'homme et al. (1), AKI, through circulating hormones or mediators, induces cardiac injury and dysfunction. The current Gal-3 inhibition studies, however, did not demonstrate noticeable improvement on renal function (creatinine and blood urea nitrogen levels) or renal hypertrophy, although significant improvements were observed in cardiac parameters. Optimizing the benefits of targeting both organs such as therapies activating particulate guanylyl cyclase A receptor and soluble guanylyl cyclase receptors can exert beneficial effects in both organs, as demonstrated by glomerular filtration rate elevation, vasorelaxation, and cardiac and renal antiremodeling (2,9). Further investigations to discover novel therapeutic targets or optimize the current drug targets are critical for the success of this cotargeting strategy.

This newly published study has several strengths. First, it elucidates the connection between AKI and remote cardiac damage, which is mediated by bone marrow Gal-3 upregulation. This new mechanism helps to understand the pathophysiology of the cardiorenal syndrome in such a setting and provides a promising new route of treating cardiorenal syndrome in AKI. Second, this study includes both acute and chronic intervention studies. Specifically, the acute study served to investigate the acute renal effects and the chronic study explored the long-term pharmaceutical feasibility of Gal-3 blockade. Furthermore, the study includes both mechanistic and biomarker studies, which conclude that Gal-3 not only is a mediator for AKI-induced cardiac injury but also may be a biomarker for AKI severity.

It is unclear what is the deleterious signal transmitted to the bone marrow from the injured kidney. Therefore, it will be of interest to investigate the hormonal or neural signals generated by the kidney and the causal relationship between the unknown signals and bone marrow Gal-3 formation. Furthermore, the authors did not mention the effect of modified citrus pectin or Gal-3 KO on cardiovascular hemodynamics such as blood pressure in the mice. This key information may further contribute to the cardiac improvement observed in the current study and should be studied. Additionally, future studies to investigate renin-angiotensin-aldosterone system modulation by Gal-3 suppression will be important because studies have previously documented the critical role of the system in inflammation and cardiac injury, with AKI initiation (2,10).

Gal-3 inhibition exerted potent cardiac protective effects in 2 kidney injury models but did not improve renal function or reduce renal structural abnormalities, which consequently may limit its use for AKI prevention or treatment itself. Thus, optimizing the dose, potency, and organ selectivity of a Gal-3 inhibitor to improve renal function such as increasing glomerular filtration rate or urine output is critical for the future development of a Gal-3 blockade strategy for AKI management. Additionally, from a therapeutic perspective, the authors may want to consider investigating disease models that focus on myocardial therapeutics with the use of Gal-3 inhibition. Future directions also include validating the therapeutic potential of Gal-3 inhibition in a large-animal model such as canines or porcines, which constitute a higher functional similarity and genetic homogeneity with humans.

Biomarker studies measuring plasma Gal-3 at admission (in addition to discharge) for critically ill patients may also help to identify patients who will later develop AKI. Additionally, given the distribution of Gal-3 in renal tubules and macrophages, it will be interesting to evaluate urinary Gal-3 levels in AKI patients. Effective preventive strategies and interventions can then be used to treat these patients at

an early stage of AKI. Considering the critical role of Gal-3 in cardiac injury, it is thus highly relevant to assess its predictive value for cardiovascular adverse outcomes in AKI patients.

Congratulations to the authors for such a well-designed, solid study and the novel findings of Gal-3 as a pathophysiologic mediator, a therapeutic target, and a biomarker for cardiorenal syndrome and AKI, and of the key role of bone marrow. These results highlight the essential role of Gal-3 in stimulating cardiac inflammation and fibrosis as a result of AKI. Indeed, this insult to the heart is independent of the type of renal injury. A Gal-3 suppression strategy may emerge as an effective, next-generation therapy for AKI-induced cardiac injury and related cardiorenal syndrome. Still, a need that remains is protecting the kidney and preserving renal function in AKI, in which a novel kidney-bone marrow-heart connection plays a key role.

ADDRESS FOR CORRESPONDENCE: Dr. John C. Burnett, Jr., Cardiorenal Research Laboratory, Department of Cardiovascular Medicine, Mayo Clinic, 200 First Street Southwest, Rochester, Minnesota 55905. E-mail: burnett.john@mayo.edu.

REFERENCES

1. Prud'homme M, Coutrot M, Michel T, et al. Acute kidney injury induces remote cardiac damage and dysfunction through the galectin-3 pathway. J Am Coll Cardiol Basic Trans Science 2019;4:717–32.

2. Chen Y, Harty GJ, Zheng Y, et al. CRRL269: a novel particulate uanylyl cyclase A receptor peptide activator for acute kidney injury. Circ Res 2019;124:1462–72.

3. Mehaffey JH, Money D, Charles EJ, et al. Adenosine 2A receptor activation attenuates ischemia reperfusion injury during extracorporeal cardiopulmonary resuscitation. Ann Surg 2019; 269:1176–83.

4. Bai Y, Zhang Y, Yang S, et al. Protective effect of vascular endothelial growth factor against cardiopulmonary bypass–associated acute kidney injury in beagles. Exp Ther Med 2018;15:963–9.

5. Xu M, Wang X, Banan B, et al. Anti-CD47 monoclonal antibody therapy reduces ischemia-reperfusion injury of renal allografts in a porcine model of donation after cardiac death. Am J Transplant 2018;18:855–67.

6. Greenberg JH, Zappitelli M, Jia Y, et al. Biomarkers of AKI progression after pediatric cardiac surgery. J Am Soc Nephrol 2018;29:1549–56.

7. Yang X, Chen C, Teng S, et al. Urinary matrix metalloproteinase-7 predicts severe AKI and poor outcomes after cardiac surgery. J Am Soc Nephrol 2017;28:3373–82.

8. Martin FL, McKie PM, Cataliotti A, et al. Experimental mild renal insufficiency mediates early cardiac apoptosis, fibrosis, and diastolic dysfunction: a kidney-heart connection. Am J Physiol Regul Integr Comp Physiol 2012;302: R292.

9. Chen Y, Burnett JC. Particulate guanylyl cyclase A/cGMP signaling pathway in the kidney: physiologic and therapeutic indications. Int J Mol Sci 2018;19:1006.

10. Ruiz-Ortega M, Ruperez M, Lorenzo O, et al. Angiotensin II regulates the synthesis of proinflammatory cytokines and chemokines in the kidney. Kidney Int 2002;62:S12–22.

KEY WORDS acute kidney injury, cardiorenal, galectin-3, inflammation

JACC: BASIC TO TRANSLATIONAL SCIENCE VOL. 4, NO. 6, 2019

TRANSLATIONAL MODEL

A Molecularly Detailed $Na_V1.5$ Model Reveals a New Class I Antiarrhythmic Target

Jonathan D. Moreno, MD, PhD,[a,b] Wandi Zhu, PhD,[b] Kathryn Mangold, MS,[b] Woenho Chung, BS,[b] Jonathan R. Silva, PhD[b]

VISUAL ABSTRACT

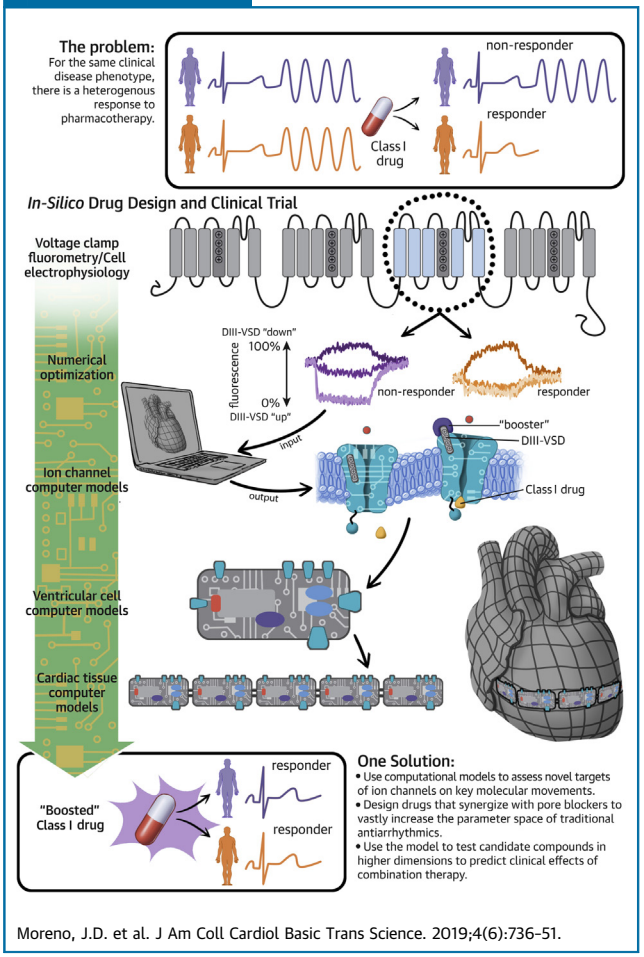

Moreno, J.D. et al. J Am Coll Cardiol Basic Trans Science. 2019;4(6):736–51.

HIGHLIGHTS

- **Antiarrhythmic therapies remain suboptimal due to our inability to predict how drug interactions with ion channels will affect the ability of the tissue to initiate and sustain an arrhythmia.**
- **We built a computational framework that allows for in silico design of precision-targeted therapeutic agents that simultaneously assesses antiarrhythmic markers of success and failure at multiple spatial and time scales. Using this framework, a novel in silico mexiletine "booster" was designed that may dramatically improve the efficacy of mexiletine in suppression of arrhythmia triggers.**

ISSN 2452-302X https://doi.org/10.1016/j.jacbts.2019.06.002

- **These results provide a roadmap for the design of novel molecular-based therapy to treat myriad arrhythmia syndromes, including ventricular tachycardia, heart failure arrhythmias, and inherited arrhythmia syndromes.**
- **In summary, computational modeling approaches to drug discovery represent a novel tool to design and test precision-targeted therapeutic agents. By exploiting nontraditional ion channel drug targets, an entirely new dimension can be added to the wide parameter space of traditional antiarrhythmic drugs to develop more precision-targeted and potent Class I therapeutic agents.**

ABBREVIATIONS AND ACRONYMS

APD = action potential duration

BCL2000 = basic cycle length of 2,000 ms

DIII-VSD = domain III voltage-sensing domain

EAD = early afterdepolarization

IC_{50} = half-maximal inhibitory voltage

LQT3 = long QT syndrome type 3

RFI = recovery from inactivation

SSA = steady-state availability

UDB = use-dependent block

$V_{1/2}$ = half-maximal voltage

VSD = voltage-sensing domain

SUMMARY

Antiarrhythmic treatment strategies remain suboptimal due to our inability to predict how drug interactions with ion channels will affect the ability of the tissues to initiate and sustain an arrhythmia. We built a multiscale molecular model of the Na^+ channel domain III (domain III voltage-sensing domain) to highlight the molecular underpinnings responsible for mexiletine drug efficacy. This model predicts that a hyperpolarizing shift in the domain III voltage-sensing domain is critical for drug efficacy and may be leveraged to design more potent Class I molecules. The model was therefore used to design, in silico, a theoretical mexiletine booster that can dramatically rescue a mutant resistant to the potent antiarrhythmic effects of mexiletine. Our framework provides a strategy for in silico design of precision-targeted therapeutic agents that simultaneously assesses antiarrhythmic markers of success and failure at multiple spatial and time scales. This approach provides a roadmap for the design of novel molecular-based therapy to treat myriad arrhythmia syndromes, including ventricular tachycardia, heart failure arrhythmias, and inherited arrhythmia syndromes.

Current antiarrhythmic treatment strategies remain suboptimal due to our inability to predict patient-specific responses. As evidenced by large clinical trials (e.g., CAST [Cardiac Arrhythmia Suppression Trial] [1], SWORD [Survival With Oral d-Sotalol] [2]), antiarrhythmic therapy can paradoxically increase arrhythmia burden compared with placebo and lead to increased risk of death. This outcome is due, in part, to the complex kinetics of the drug channel interaction that includes strong bidirectional feedback between how drugs alter the action potential waveform affecting voltage-dependent potency, as well as electrotonic coupling in tissue, which we (3) and others (4) have shown can lead to an even more complex response to drugs that may not be appreciated in single-cell studies. For both acquired and inherited arrhythmia syndromes, this scenario leads to a dangerous trial-and-error approach to choosing appropriate pharmacotherapy for patients. Furthermore, despite an enormous amount of research into antiarrhythmic drug therapy that has produced molecules with a wide range of pharmacokinetic properties, they all block a single target: the channel pore. Thus, targets of ion channels other than the channel pore may add an entirely new dimension to antiarrhythmic drug therapy.

SEE PAGE 752

Structurally, the alpha-subunit of Na^+ channels is formed by a monomer with 4 homologous domains (DI to DIV), each with 6 transmembrane subunits (S1 to S6). The S1-S4 of each domain forms the voltage-sensing domain (VSD), and S5-S6 forms the pore (5,6). Upon membrane depolarization, the VSDs activate and open the pore, allowing Na^+ entry into the

From the [a]Division of Cardiology, Department of Medicine, Washington University in St. Louis, St. Louis, Missouri; and the [b]Department of Biomedical Engineering, Washington University in St. Louis, St. Louis, Missouri. This work was supported by 5 T32 HL 7081-42 (Dr. Moreno) and R01-HL136553 (Dr. Silva). Dr. Silva is a member of the Board of Directors/Equity/Officer for SentiAR, Inc. All other authors have reported that they have no relationships relevant to the contents of this paper to disclose. Thomas Hund, MD, served as Guest Editor for this paper.

The authors attest they are in compliance with human studies committees and animal welfare regulations of the authors' institutions and Food and Drug Administration guidelines, including patient consent where appropriate. For more information, visit the *JACC: Basic to Translational Science* author instructions page.

Manuscript received March 21, 2019; revised manuscript received June 7, 2019, accepted June 7, 2019.

cell. Experimental recordings that monitor VSD conformation changes (voltage clamp fluorometry) have shown that VSD movement is modulated by binding of local anesthetics, and that when lidocaine binds to the Na^+ channel, it stabilizes the domain III VSD (DIII-VSD) in an activated conformation (7). Our recent experimental results (8) show that DIII-VSD dynamics significantly regulate mexiletine blockade of $Na_V1.5$, and the differential response of long QT syndrome type 3 (LQT3) carriers to mexiletine is due, in large part, to mutation-specific VSD dynamics.

To date, the myriad parameters within Na^+ channel kinetic models have been shown to have a significant impact on the ability of the heart to initiate and sustain an arrhythmia, and exploiting these parameters has been useful for understanding Na^+ channel pharmacology (9). However, it has not yet been possible to design targeted interventions that alter these parameters because they are not specifically connected to the channel structure.

The current study used our experimental results (8) to develop a computational model that tracks molecular DIII-VSD movement, Na^+ channel electrophysiology, and the response of both to mexiletine drug blockade for 2 LQT3 mutations: R1626P, shown to be mexiletine sensitive, and M1652R, shown to be mexiletine resistant. The fidelity of the model for these 2 mutants provides confidence that the relation between the DIII-VSD and channel gating is well represented by the model and allows us to predict novel therapeutic approaches based on this relation. This finding is clinically important; despite the common use of mexiletine in treating ischemia-related ventricular tachycardia in those without Na^+ channel mutations (WT), its effectiveness is suboptimal, necessitating high clinical doses, and plagued by numerous side effects. Our previous study confirms this lack of efficacy in WT channels.

To our knowledge, this is the first such multiscale computational model that explicitly displays the experimentally parameterized molecular underpinnings of drug efficacy from channel kinetics to higher dimensional cardiac fibers (10,11). Using the model as a therapeutic prediction tool, we then developed an in silico mexiletine "booster": a theoretical drug that alters DIII-VSD activation kinetics and significantly enhances drug efficacy. We propose that combination therapy with common pore blockers, enhanced by allosteric channel modulation, could dramatically alter the landscape for antiarrhythmic therapy by adding another dimension to the parameter space of drug efficacy. This approach would expand the number of patients who would receive clinical benefit from existing therapeutic agents and allow for a lower concentration of drugs to be used, decreasing off-target side effects.

METHODS

Computational Markov models of the WT, M1652R, and R1626P LQT3 mutants were formulated with and without the mexiletine drug channel interaction via numerical optimization from experimental data, as previously described (12,13). These models include both channel kinetics and voltage-clamp fluorescence describing the DIII-VSD movement. The drug channel model was incorporated into a computational model of the human ventricular myocyte (14) to assess cellular and tissue response to drug therapy. Our model incorporates experimental data from HEK cells and from the *Xenopus* cell expression system where appropriate.

Results for experimental data are expressed as mean ± SEM. Significance between groups was tested by using the Student's *t*-test. We have used a variety of figure types to best display the experimental data. The model-fitting plots are scatter plots of the summary experimental data (points, experiment) with the simulated model fits shown as linear overlays. The tissue data are displays of cellular action potential as well as simulated individual currents (e.g., Na^+ current). Summary data for the biotin experiments are shown as bar plots. Detailed methods are available in the Supplemental Information.

RESULTS

BIOPHYSICAL CHARACTERISTICS OF 2 LQT3 MUTANTS. We focused on the R1626P (RP) and the M1652R (MR) mutations because of their marked differential responses to mexiletine. Both mutations lie within the DIV S4 segment and produce an increased late Na^+ current ~0.7% to 1.0% of the peak current. Aside from a ~15 mV depolarizing shift in steady-state availability (SSA) for the MR mutation, and a ~8 mV hyperpolarization of the RP mutation, the electrophysiology of both mutations is similar (15). At resting membrane potential, however, the DIII-VSD of RP is nearly ~90% activated ("up" position), whereas the MR DIII-VSD is only ~50% activated (8).

DRUG-FREE MODEL DEVELOPMENT. We began by developing drug-free models of both mutations as well as wild type, which were easily fit with a well-established 8-state Markov model (3). The late currents of the mutations were simulated as slowly inactivating currents and were numerically optimized to yield 0.1%, 0.67%, and 1% late current (ratio to the

FIGURE 1 Model Schematic With Drug-Free Kinetics

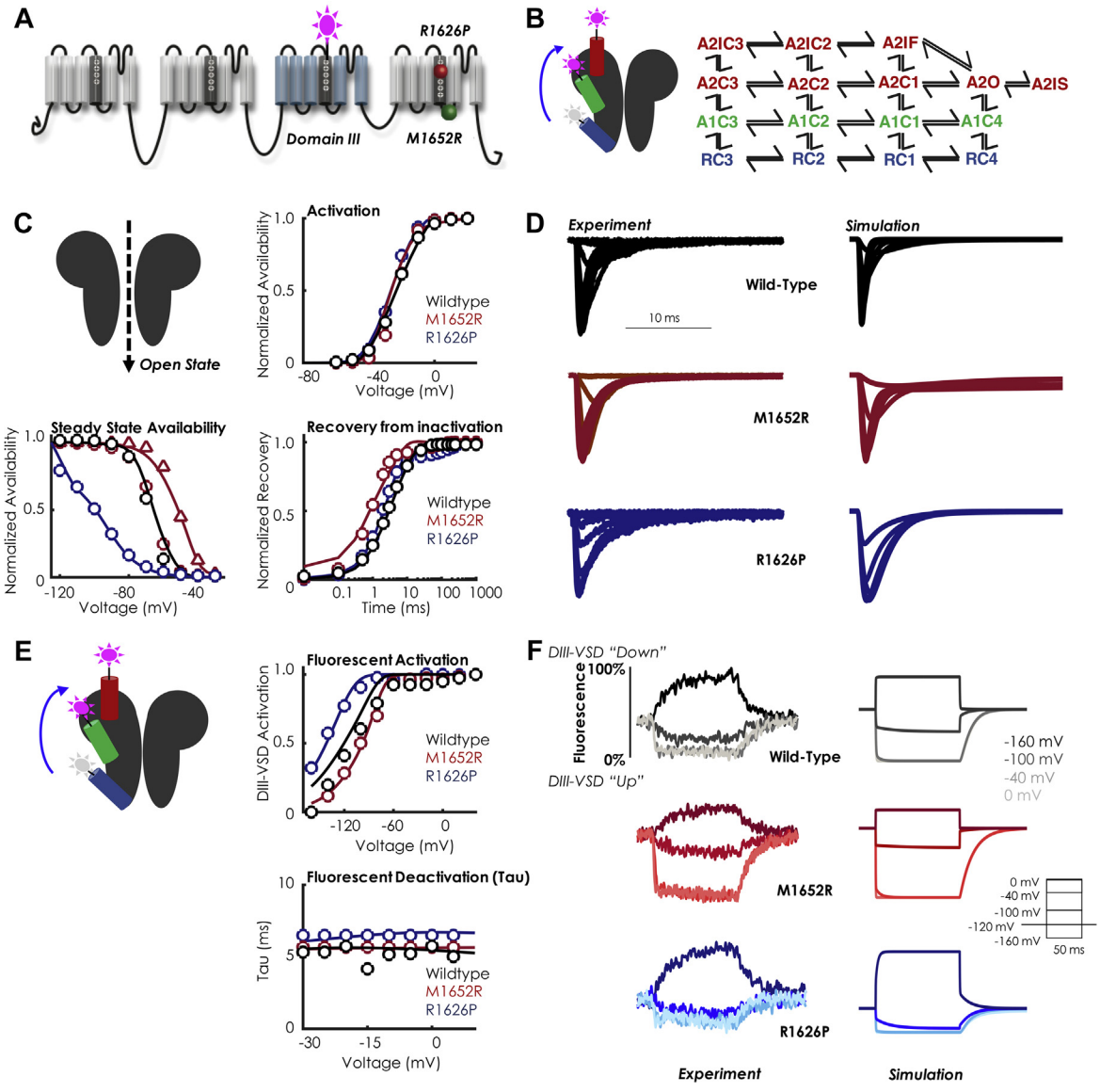

(A) Topology of the $Na_V1.5$ channel and location of the 2 long QT mutations with distinct mexiletine sensitivity, R1626P (**red ball**, sensitive) and M1652R (**green ball**, insensitive). A fluorophore is attached to domain III (DIII). **(B)** Schematic representation of the DIII voltage-sensing domain (DIII-VSD) in the Na^+ channel and corresponding Markov state-chain diagram of the drug-free Na^+ channel. The **blue** DIII-VSD is in a "down" or rested position and corresponds to the **blue** "R" states in the Markov model **(far right)**. The **green** DIII-VSD represents the first transition to a fluorescent regime labeled "A1" (first activated) and corresponds to the **green** "A1" states in the Markov model. The second transition to A2 is denoted with the **red** DIII-VSD, which represents a "fully up" state and corresponds to the "A2" states. As depicted, the model includes 16 states: 4 rested states ("R"), 4 first-activated states ("A1"), and 8 second-activated states ("A2"). The rate constants governing the transitions can be found in the Supplemental Material. **(C)** Current kinetics. In each panel, the **points** represent the experimental data, and the **solid lines** represent the model fits to the data. WT is shown in **black**, M1652R is shown in **red**, and R1626P is shown in **blue**. The **triangles** in the steady-state availability (SSA) plot indicate the HEK transformation of the SSA, detailed in the Supplemental Material. The model fits to current kinetics include steady-state availability, activation, recovery from inactivation, Tau of deactivation (not shown), and mean open time (for WT). Details of the protocols are given in the Supplemental Material. **(D)** Representative traces of currents in the 3 constructs. Shown at **left** is the experiment, **right** is the simulation. The channel was held at -120 mV to steady state and then pulsed to 0 mV for 25 ms. WT is in **black**, M1652R is in **red**, and R1626P is in **blue**. **(E)** Fluorescent kinetics. In each panel, the **points** represent the experimental data, and the **solid lines** represent the model fits to the data. WT is shown in **black**, M1652R is shown in **red**, and R1626P is shown in **blue**. Shown are fluorescent activation and deactivation. **(F)** Representative traces of fluorescence in the 3 constructs (WT, **black**; M1652R, **red**; R1626P, **blue**). Shown at **left** is the experiment, **right** is the simulation for 4 different test voltages (-160 mV, -100 mV, -40 mV, and 0 mV; the voltage protocol is shown in the **inset**). The experimental data for steady-state activation and recovery from inactivation are from Ruan et al. (15); the experimental data for SSA, fluorescent activation, and fluorescent tau are from Zhu et al. (8).

FIGURE 2 Mexiletine Drug-Binding Kinetics

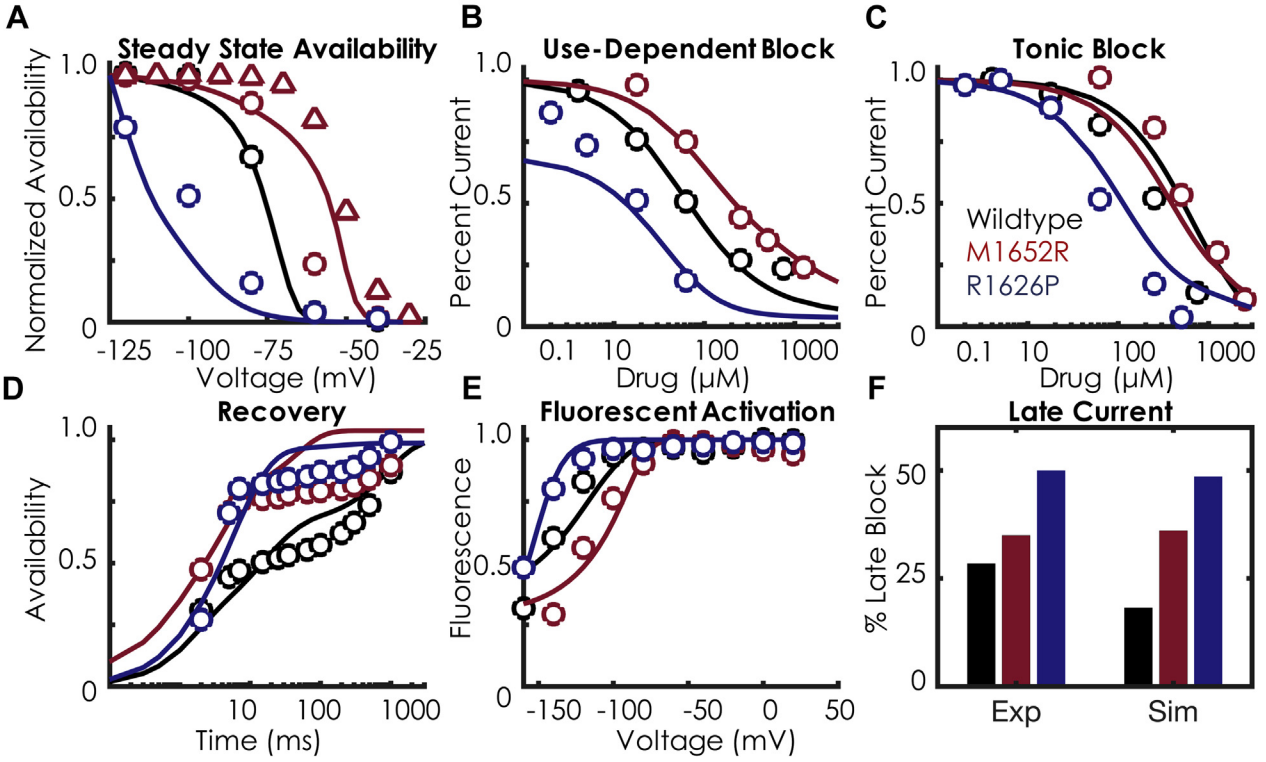

In each panel, the **points** represent the experimental data, and the **solid lines** represent the model fits to the data. WT is shown in **black**, M1652R is shown in **red**, and R1626P is shown in **blue**. **(A)** SSA with mexiletine 250 μM. As in **Figure 1**, the triangles represent the HEK transformation (Supplemental Material). There is a minimal shift in SSA with mexiletine, indicating minimal inactivated state binding. **(B)** Use-dependent block with mexiletine 0.1 to 1,000 μM. There is a 10 times differential sensitivity to mexiletine between MR **(blue)** and RP **(red)**. **(C)** Tonic block with mexiletine 0.1 to 1,000 μM. The marked differential sensitivity persists for tonic block, similar to the use-dependent block seen in **panel B**. **(D)** Recovery from inactivation at -100 mV with mexiletine 250 μM. **(E)** Fluorescent activation with 4,000 μM mexiletine. Note the marked hyperpolarization of all 3 constructs with mexiletine, indicating that mexiletine stabilizes DIII-VSD in the activated conformation. **(F)** Late block with mexiletine 75 μM. Similar to the experiment, there is increasing affinity of late current block (measured after 400 ms of a depolarizing pulse) between the 3 constructs: WT < M1652R < R1626P. Details of the protocols can be found in the Supplemental Material. Abbreviations as in **Figure 1**.

peak current) for the WT, M1652R, and R1626P constructs, respectively (15). We then focused on expanding the kinetic model to account for DIII-VSD movement, shown to be stabilized in an active conformation by mexiletine (8). Using voltage-clamp fluorometry methods previously described (16), the kinetics of DIII-VSD were simulated in response to channel activation. Briefly, by attaching a fluorescent tag to the DIII-VSD and expressing $Na_V1.5$ in a *Xenopus* oocyte cell expression system, we could simultaneously record current kinetics and DIII-VSD movement (16,17).

As can be seen in **Figure 1E**, much of the DIII-VSD movement occurs in a voltage range before Na^+ channels begin to activate. At -80 mV, the RP DIII-VSD is ~90% in the active position, whereas the MR DIII-VSD is only ~50% activated. Experimental data showing multiple time constants in response to depolarizing pulses of different durations suggest at least 2 active conformations of the DIII-VSD (16,18). Therefore, to best fit the fluorescent data, 3 regimes were added to the model: a row of resting closed states (RC1 - RC4) which represent DIII-VSD in a "down" position; a first-activated regime (A1C3 - A1C4), which represents the first activation of the DIII-VSD (DIII "moving up"); and a second-activated regime (A2 states) which represents the second-activation step of DIII-VSD (DIII "fully up") and contains the top 8 states. The full 16-state drug-free model is shown in **Figure 1B**. Fluorescence was then simulated by plotting the ratio of the sum of the A1 and A2 states to the total states. As detailed in the Supplemental Material, analysis of the half-maximal voltage ($V_{1/2}$) of DIII-VSD activation versus tonic

block with mexiletine allowed us to tease out the relative fluorescent contributions of the A1 and A2 states (Supplemental Figure 7).

One benefit of using a computational approach is that data from different expression systems can be reconciled by altering the appropriate parameters. For example, in simulating MR SSA, we chose to incorporate a 15 mV depolarizing shift of MR compared with WT to more closely simulate the results obtained by us and others (15) in the HEK expression system. Thus, in **Figure 1C** (SSA), the red circles represent data obtained in *Xenopus* oocytes, the red triangles represent the "HEK-transformed" SSA curve (+15 mV depolarization), and the solid red line represents the model fit. Overall, **Figure 1** shows that the resultant simulations (solid lines) match closely with the experimental data (points) and capture a wide range of channel kinetics.

Figures 1D and 1F present a side-by-side comparison of the simulated Na^+ channel currents and fluorescence traces in response to a voltage step protocol. As can be seen, for both mutations and WT, the activation of DIII-VSD to depolarized potentials is rapid and on the order of 3 to 5 ms, similar to current activation. At a membrane potential of -120 mV, WT is ~50% activated ("up"), MR is ~25% activated ("up"), and RP is ~75% activated ("up"). In general, over the physiological voltage range, the RP mutation traps the DIII-VSD in a relatively activated position, a necessary prerequisite for drug binding (discussed in the following section).

Experimentally, maximal fluorescence occurs at the most hyperpolarized potentials, which implies that the fluorescent molecule, TAMRA-MTS, is being quenched at elevated membrane voltages. Thus, DIII-VSD activation is inversely proportional to fluorescence, and the plots are normalized to the range of minimal to maximal fluorescence. As such, **Figure 1E** is labeled as "DIII-VSD activation" (which is equivalent to the DIII-VSD position in the membrane). This is congruent with **Figure 1F** labeling: at -160 mV, all constructs fluoresce maximally, shown as the upward deflection of the fluorescence curve. Upon depolarization, the fluorescence is quenched to 0%, as DIII-VSD is in an "up" position.

MEXILETINE DRUG-BOUND MODEL DEVELOPMENT. We next expanded the model to account for mexiletine drug binding. Our previous results suggested that the voltage dependence of DIII-VSD activation strongly correlates with tonic block by mexiletine (Figure 4 of Zhu et al. [8]). Briefly, tonic block, a measure of first-pulse block, is assessed at holding potentials before much closed-state inactivation occurs; thus, the apparent differences in tonic block seen for 15 different mutants were primarily accounted for by the difference in the DIII-VSD. For the RP mutation, the $V_{1/2}$ of DIII-VSD activation is -143 mV and has a 10-fold lower half-maximal inhibitory concentration (IC_{50}) for tonic block (69.5 μM), compared with MR, which has a $V_{1/2}$ of -100 mV and a tonic block IC_{50} of 624 μM. Our results, as well as others (15), suggest that the intrinsic affinity of mexiletine to the local anesthetic receptor for the mutants is likely the same, but the measured tonic block differences represent both contamination by the inactivated state and differences in DIII-VSD guarding the receptor. Taken together, we simulated mexiletine drug block as transitions only from the A2 states to the drug-bound states; in other words, DIII-VSD needs to be in a fully activated (A2 regime) position to allow for drug binding.

The resultant models after numerical optimization (Supplemental Material) are shown in **Figure 2**, with additional biophysical characterization shown in Supplemental Figure 2. As can be seen, the model simulations fit the experimental data over a wide range of pacing protocols and drug concentrations. Similar to the experimental data, there are marked differences in the affinities of mexiletine between the 2 mutants for both use-dependent block (UDB) and tonic block, with the RP mutation exhibiting a 10 to 15 times increased sensitivity to mexiletine compared with MR (tonic block: 69.5 μM vs. 625 μM; UDB: 16 μM vs. 240 μM). In the model, these differences are largely regulated by the difference in DIII-VSD activation (**Figure 2E**), given that the intrinsic affinity of mexiletine to the receptor for the 3 models was optimized to a constant affinity (156 μM). Recovery kinetics with mexiletine are similar between the 2 mutants (**Figure 2D**), which are both faster than WT. Application of mexiletine 4,000 μM stabilizes the DIII-VSD in the activated position (shifts the DIII-VSD to more hyperpolarized potentials) by 13 mV for RP (-156.8 mV vs. -143 mV) and by 22 mV for MR (-122.2 mV vs. -100 mV). Mexiletine application also slows recovery of DIII-VSD fluorescence ($Tau_{Recovery}$: RP 19.05 ms [experiment] vs. 19.02 ms [simulation]; MR 14.2 ms [experiment] vs. 14.2 ms [simulation after a depolarizing pulse to 20 mV). Late current block, the amount of current blocked by mexiletine 75 μM after a 400 ms depolarizing pulse, is shown in **Figure 2F**. The RP mutation is slightly more sensitive to late current block than MR (50% vs. 35% block).

CELLULAR SIMULATIONS RECAPITULATE DIFFERENTIAL SENSITIVITIES TO MEXILETINE. The next step was to incorporate our Na^+ channel models into the Grandi-Bers computational model of the human ventricular myocyte (14), with substitution of our Na^+

FIGURE 3 **Cellular Level Effects of Mex at Bradycardic Pacing**

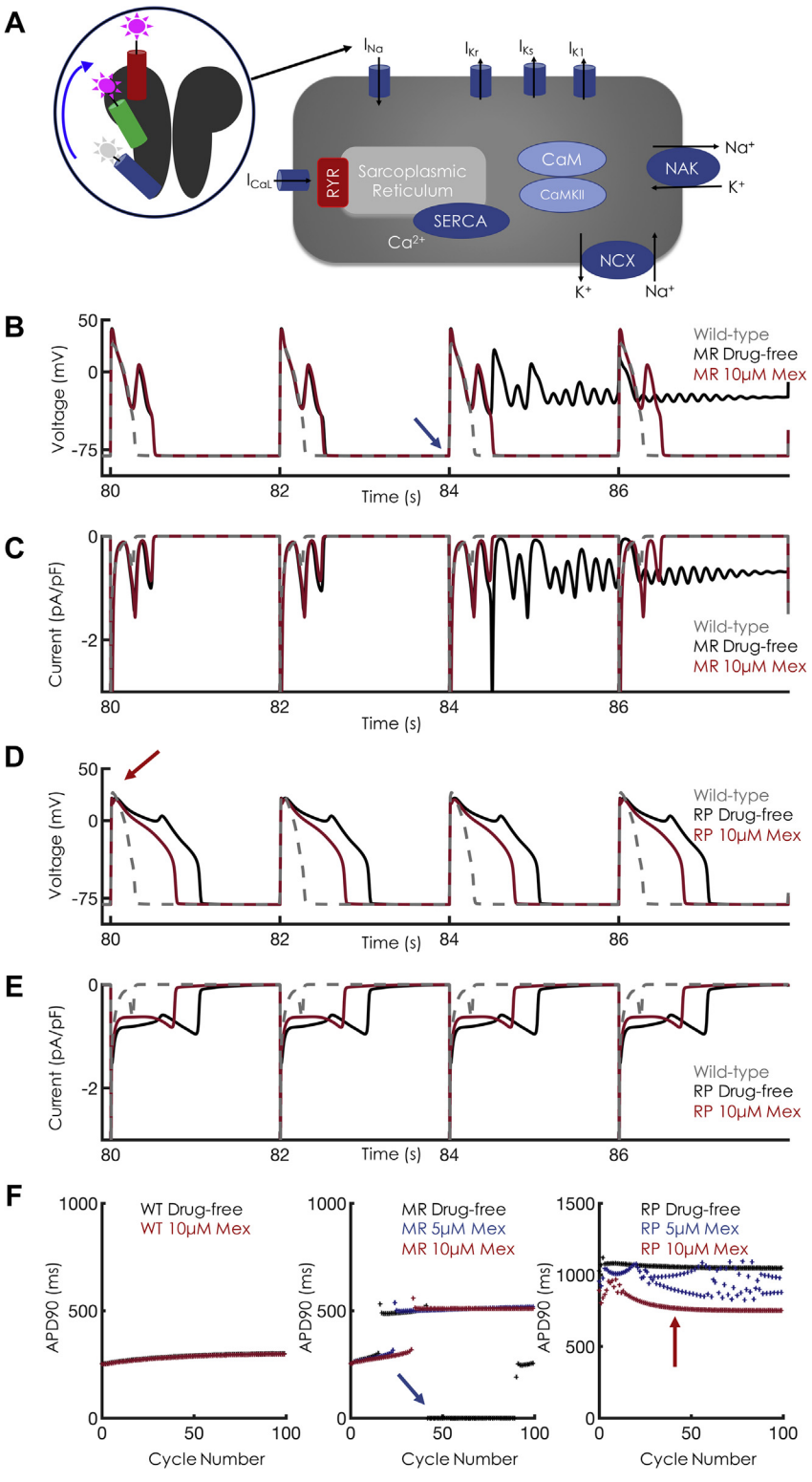

Continued on the next page

channel model for the baseline formulation and modification of the maximum chloride conductance of the baseline model for more accurate repolarization (Supplemental Material). We focused on a slow-pacing regime of 0.5 Hz (basic cycle length of 2,000 ms [BCL2000]) for our cellular simulations. In the drug-free conditions, both MR and RP display marked prolongation in action potential duration at 90% repolarization (APD_{90}), as well as sustained late Na^+ current (**Figures 3B and 3C**). Interestingly, the MR mutation displays chaotic behavior, including progressive APD prolongation until the onset of early afterdepolarizations (EADs), a hallmark bradycardic arrhythmia trigger, as well as salvos of sustained depolarization (**Figure 3B**, Supplemental Figure 4). Application of mexiletine 10 μM (high clinical concentration) is unable to normalize APD_{90}: ~509 ms versus ~523 ms in the drug-free condition. In contrast, the RP mutation shows stable EADs, with an APD_{90} of ~1,047 ms in the absence of drug. Application of mexiletine 10 μM is able to decrease the APD_{90} of RP by 28% and abolish the EAD triggers, similar to clinical results (Figure 2 in Ruan et al. [15]). As expected, mexiletine had negligible effects on WT APD_{90}. Consistent with other Class Ib antiarrhythmic drugs, mexiletine 10 μM has negligible effects on maximum upstroke velocity (Supplemental Figure 3).

DEVELOPMENT OF A MEXILETINE "BOOSTER". Given mexiletine's safety and widespread use in the clinic, we hypothesized that combination therapy with mexiletine and a "booster" drug might synergize for more potent antiarrhythmic effects. Because mexiletine sensitivity between RP and MR seems to be driven by the relative position of the DIII-VSD, we hypothesized that by holding the DIII-VSD in an "up" and activated position, we could enhance the efficacy of mexiletine for patients found to be mexiletine resistant (e.g., MR mutants). We thus turned to the computational model to design (i.e., in silico) a mexiletine booster and then tested its efficacy in combination with mexiletine.

This concept was first tested experimentally (**Figure 4**). We used MTSEA-biotin (biotin) to alter the conformation of the DIII-VSD. It was previously shown that extracellular application of biotin can modulate the cysteine residue at the 1,306 location (7,19). It stabilizes the DIII-VSD in an activated position in R1306C channels. We engineered the R1306C mutation as a biotin target, as well as an R1306C M1652R double mutation into $Na_V1.5$, and expressed the mutant channels in the HEK cell expression system. As shown in these previous studies, application of biotin to R1306C channel decreases peak Na^+ current, which stabilized ~20 min after biotin perfusion. The decrease in Na^+ current amplitude suggests that MTSEA-biotin binds to the cysteine residue and modulates the DIII-VSD conformation. We also observed a reduction in peak Na^+ current in the double-mutant R1306C M1652R 20 min after biotin application (**Figure 4B**). Biotin caused a small depolarizing shift in the activation (conductance-voltage [GV]) curve, but no effect on the SSA curve, for the R1306C channel (**Figure 4C**). Similar to the M1652R channel, the double-mutant R1306C M1652R channel exhibited a large depolarizing shift in the SSA curve compared with the R1306C channel (R1306C $V_{1/2}$ = -79.5 ± 1.2 mV; R1306C M1652R $V_{1/2}$ = -59.0 ± 2.7 mV) (**Figures 4C and 4D**). This depolarizing shift increases the availability of the channel (gain of function). Notably, when the R1306C M1652R channel was modified with a biotin, the SSA curve was shifted to hyperpolarizing potentials ($V_{1/2}$ = -66.1 ± 3.8 mV). Thus, biotin partially corrects the alteration of the SSA curve caused by the M1652R mutation.

Finally, we tested block by mexiletine 50 μM in R1306C and R1306C M1652R channels modified by biotin. There was a significant 81% and 146% increase in tonic block in the R1306C and R1306C M1652R

FIGURE 3 Continued

(A) Schematic of single-cell simulations. The Markov model representation of the Na^+ channel was placed into an action potential (AP) model, replacing the standard Hodgkin-Huxley formulation. **(B)** Single-cell APs at basic cycle length 2,000 ms (BCL2000) for M1652R. In the absence of mexiletine (Mex), the M1652R mutation displays chaotic behavior with failure to repolarize **(black trace)**. Application of Mex 10 μM **(red trace)** induced single early afterdepolarizations (EADs) but enhanced repolarization. Wild type, drug free is shown in **gray**. **(C)** Na^+ currents for the corresponding APs shown in panel B. Note that the drug-free condition induces sustained inward current **(black trace)**. Despite high clinical Mex (10 μM), Na^+ channels reactivate, which causes the EADs shown in **B**. **(D)** Single-cell APs at BCL2000 for R1626P. In the absence of Mex, the R1626P shows characteristic EADs and a markedly prolonged AP duration (APD, **black trace**). Application of Mex 10 μM **(red)** successfully abolished the EADs, leading to monotonic repolarization but still with a prolonged APD compared with wild type **(gray trace)**. **(E)** Na^+ currents for the corresponding APs shown in **D**. Note the shortened late inward Na^+ current with application of Mex. **(F)** APD as a function of cycle number for 100 beats at BCL2000 (corresponding to the APs shown in **B and D**). Note in the M1652R panel, the **blue arrow** at beat 42 corresponds to the **blue arrow in B** depicting the onset of a failure of the repolarization regime. For the R1626P mutation, the **red arrow** corresponds to beat 40, shown in **D**. Note the beat-to-beat APD variability with Mex 5 μM **(blue trace)**. After early chaos (first 10 beats), Mex 10 μM induces monotonic repolarization (absence of EADs), shown as the **red curve in F (far right)**.

FIGURE 4 Effects of Biotin on the DIII-VSD and Optimization of a Mex "Booster"

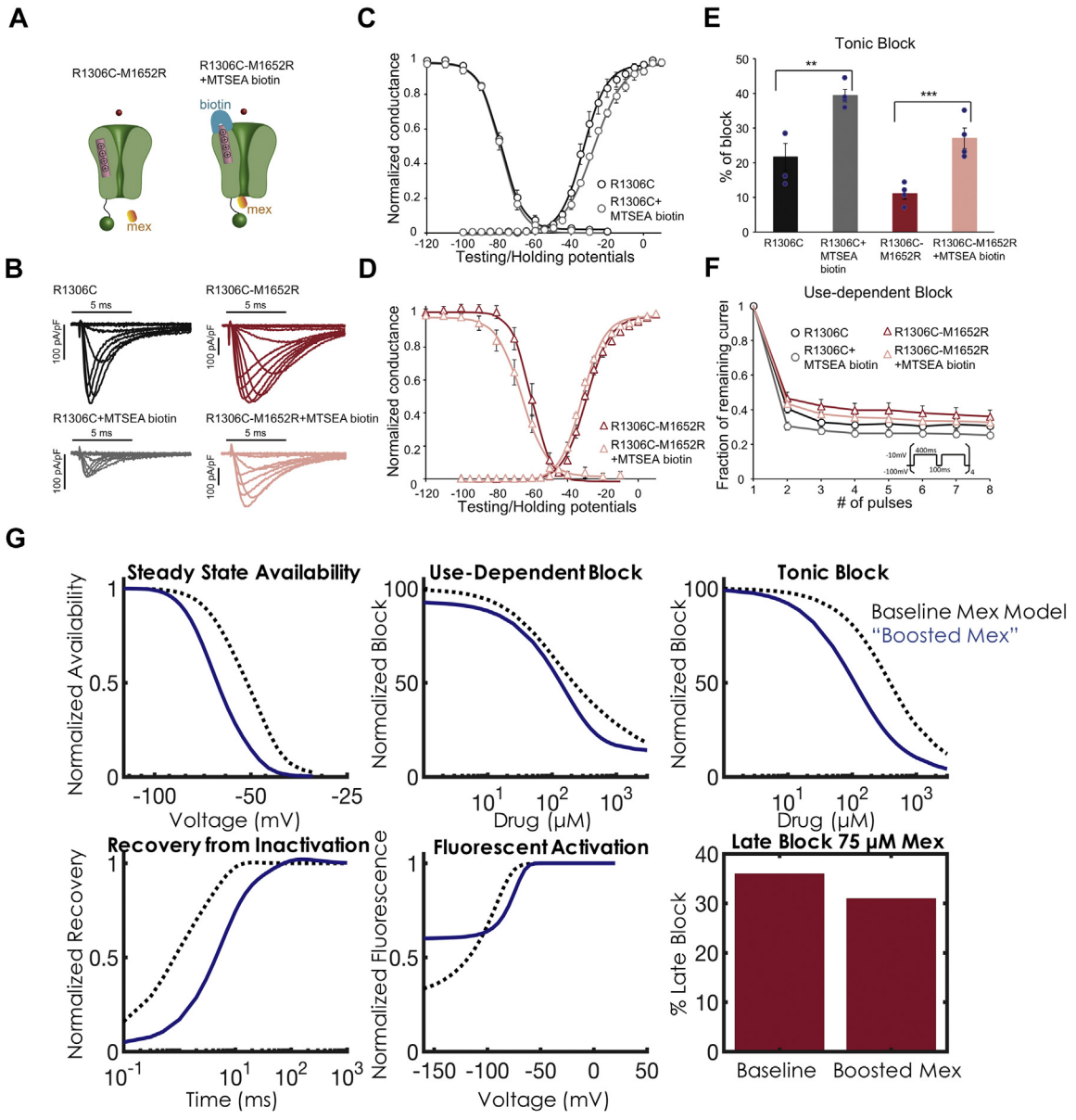

(A) Schematic of the Na^+ channel with the double-mutation R1306C M1652R. Application of MTSEA-biotin traps the DIII-VSD **(pink)** in the activated position. **(B)** Representative current traces of the R1306C and R1306C M1652R channels before and 20 min after MTSEA-biotin 20 μM perfusion. Peak current amplitude for both constructs decreased after MTSEA-biotin application. **(C)** Effects of biotin on channel activation (conductance-voltage [GV]) and SSA of the R1306C channel. Application of biotin induces a small right shift in the GV curve. Results are expressed as mean ± SEM from a group of 4 to 6 cells. **(D)** Effect of biotin on GV and SSA of the M1652R R1306C double mutant. Biotin induces a hyperpolarizing shift in SSA, compared with control. **(E)** Summary data of tonic block. Application of MTSEA-biotin to both mutants induces a significant ~2 times increase in tonic block for Mex 50 μM. Significance was determined by using the Student's *t*-test. $^{**}p < 0.01$, $^{***}p < 0.005$. **(F)** Use-dependent block (UDB) for Mex 50 μM. UDB is measured by applying eight 400 ms depolarizing pulses at a 2 Hz frequency to mimic a tachycardia condition. Although there was a trend of decreasing availability after biotin for both constructs, the changes were not significant. **(G)** Optimization of a Mex booster. Starting with the optimized parameters from the M1652R mutation (baseline Mex model shown in the **black dashed curve**), the parameters for DIII-VSD movement were optimized to induce a 15 mV hyperpolarization in SSA and a 2-fold increase in tonic block and UDB. After optimization, the Mex booster is shown in **blue**. As in **D**, the "booster" rescues SSA back to WT. UDB **(top middle)** and tonic block **(top right)** exhibit marked increased affinity with the Mex booster **(blue trace)** compared with the baseline Mex model **(black dashed traces)**. Recovery from inactivation **(bottom left)**, fluorescent activation **(bottom middle)**, and late block **(bottom right)** with Mex 75 μM are plotted in the same fashion, but these 3 protocols were not used for optimization. They serve as model predictions (details are given in the text). Abbreviations as in Figures 1 and 3.

channels, respectively (Figure 4E). In addition, for the double mutant, mexiletine 50 μM blocks 17.4 ± 6.1% late current; the addition of biotin and mexiletine 50 μM blocks 65.3 ± 5.6% late current ($p = 0.004$). It is noteworthy that the late current was quantified 50 ms after a depolarization pulse of -40 mV. For mexiletine UDB, there was no significant difference between channels with or without biotin (Figure 4F). This result is possibly due to MTSEA-biotin immobilization of the DIII-VSD in the activated conformation, which eliminates dynamic control of channel gating by the DIII-VSD. Overall, these experiments are congruent with our hypothesis that "pulling up" the DIII-VSD with a small molecule has the potential to enhance mexiletine efficacy.

To design an in silico booster, we modified the rates of the DIII-VSD movement in the drug-free model of MR (i.e., ax, bx, ay, by, a3, b3), while keeping the drug-bound rates constant, to simulate a 15 mV hyperpolarizing shift of SSA (in the absence of mexiletine) and a 2-fold increase in tonic block and UDB in the presence of mexiletine. The results of simulated biotin are shown in Figure 4G. As can be seen, in silico biotin shifts the SSA back to WT and significantly increases both tonic block (IC_{50} 105 μM vs. 400 μM) and UDB (IC_{50} 125 μM vs. 200 μM). We simulated the effects of recovery from inactivation (RFI), DIII fluorescence, and late block as confirmatory validation (e.g., these protocols were not used in the optimization routine). Thus, our model predicts that when DIII-VSD is held up, which shifts SSA, recovery from inactivation is slowed. Furthermore, even at significantly hyperpolarized potentials, DIII-VSD remains in the up and activated position. Interestingly, we found no appreciable increased late current blockade (as a percentage of peak current block), although an examination at the actual Na^+ current trace (Figure 4G) exhibited markedly less late current compared with drug-free conditions.

When application of boosted mexiletine was simulated in single cells, a dramatic response in the M1652R mutation was observed. Figure 5A shows the movement of the DIII-VSD during the action potential for the 3 constructs. For WT, the DIII-VSD transits between 92% and 100% "up" during an action potential. For RP, the DIII-VSD remains nearly 100% up throughout the entire duration of the action potential, underlying the sensitivity of RP to mexiletine. In contrast, the DIII-VSD of MR, even with mexiletine 10 μM, transits between 75% and 100% activated, with most of the cardiac cycle at 75% (during diastole). Application of boosted mexiletine holds "up" the DIII-VSD to ~90% (similar to WT) and allows increased mexiletine access. In Figure 5B, the action potentials Na^+ current and APD_{90} are plotted in response to boosted mexiletine in a fashion similar to that shown in Figure 3. Combination therapy dramatically shortened APD and late Na^+ current and rescued the phenotype to resemble WT. This boost is further shown with the monotonic, stable APDs as a function of cycle in Figure 5B. In sum, a mexiletine booster that was designed to hold up DIII-VSD in drug-free conditions enhances mexiletine efficacy and normalizes cellular markers of arrhythmia.

To further characterize the efficacy of the mexiletine booster, an in silico dose-finding experiment was conducted in which we quantified the "equivalent dose" of mexiletine that would be needed to achieve comparable results with the combined booster + mexiletine 10 μM; the experiment used simulations in increments of 5 μM mexiletine, starting from the maximum therapeutic dose (10 μM). As can be seen in Figure 6, achieving similar APD shortening at BCL2000 with combination therapy (combined booster + mexiletine 10 μM) would require mexiletine 40 μM monotherapy, a 400% increase over the therapeutic limit used clinically. Thus, the use of a mexiletine booster allows increased efficacy without a concomitant increase in potentially adverse supratherapeutic dosages of mexiletine.

1-DIMENSIONAL TISSUE SIMULATIONS CONFIRM THE ANTIARRHYTHMIC EFFICACY OF A MEXILETINE BOOSTER WITHOUT INDUCING CONDUCTION BLOCK. We then simulated the effects of mexiletine alone and boosted mexiletine in a 100-cell 1-dimensional cardiac fiber. As with the single-cell results, there was sustained APD lengthening throughout a 1-dimensional simulation of a 100-cell cardiac fiber for both RP and MR. The 49th and 50th beats of a simulation at a BCL2000 were plotted. For the MR mutation, these beats are in the sustained depolarization regime. Application of mexiletine 10 μM (Figures 7B and 7C) shortened the APD for each mutant, but EADs persisted for the MR mutation. In contrast, boosted mexiletine (Figure 7D) proves efficacious in rescuing the MR mutation back to the WT phenotype.

Lastly, we assessed for conduction block by measuring conduction velocity throughout a 1-dimensional fiber using the same simulation conditions as in Figure 7 (100 cells, BCL2000, 50 beats). Within the therapeutic range of drug concentrations and pacing conditions seen clinically, mexiletine exhibited a strong degree of safety. The full analysis can be found in the Supplemental Material.

FIGURE 5 Effects of "Boosted" Mex Cellular Dynamics

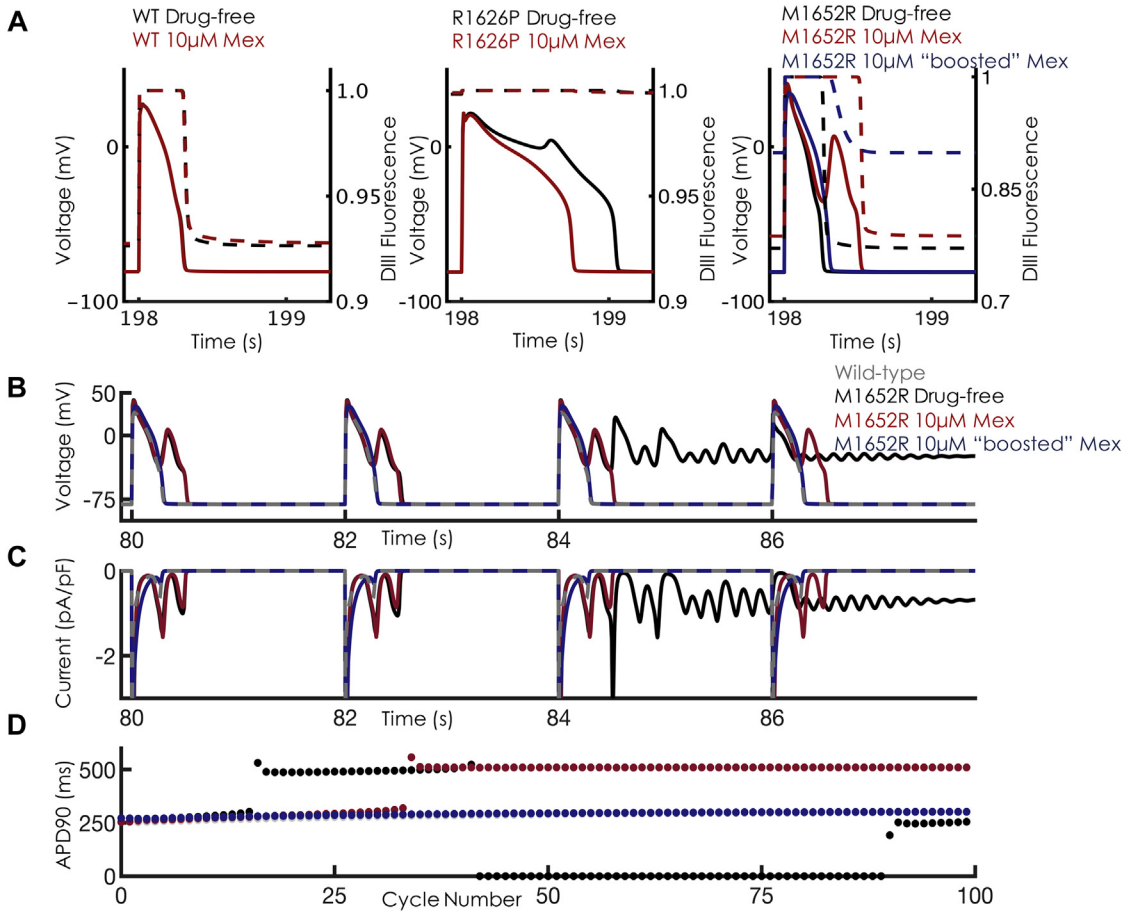

(A) Overlay of APs and DIII-VSD fluorescence in the absence **(black)** and presence **(red)** of Mex 10 μM for WT **(left)**, R1626P **(middle)**, and M1652R **(right)**. In response to voltage depolarization (the AP), the DIII-VSD **(dashed lines)** fluoresces before decaying to its resting value at -80 mV (~93% for WT). For R1626P, the DIII-VSD remains 100% activated throughout the duration of the AP. In M1652 **(far right)**, the DIII-VSD relaxes to ~75%, activated both in the presence and absence of Mex. Application of "boosted" Mex "holds up" the DIII-VSD to ~90% **(dashed blue trace)**. **(B)** The effects of "boosted" Mex (Mex 10 μM + "booster") on APs. "Boosted" Mex **(shown in blue)** abolishes EAD triggers, failed repolarization, and normalizes the AP toward WT **(gray trace)**. **(C)** Late Na^+ current is dramatically decreased, with a monotonic decrease back to baseline after each AP, similar to WT. **(D)** APD as a function of cycle number for 100 beats at BCL2000 corresponding to the APs shown in **B**. Note that with "boosted Mex" **(blue dots)**, there is normalization of APD similar to WT. Abbreviations as in Figures 1 and 3.

DISCUSSION

Despite numerous clinical failures (2,20), antiarrhythmic drug therapy remains a cornerstone for the pharmacological management of ventricular arrhythmia. To date, all antiarrhythmic drugs are variations on a similar theme: blockade of the channel pore with varying pharmacokinetic parameters leading to varied and often unpredictable efficacy. Greer-Short et al. (21) recently reported suppression of late current in LQT3-associated mutants by narrowing intracellular cleft separation, a mechanism that depends on the local clustering of Na^+ channels at the intercalated disc. However, given the current limitations and pressing need for novel therapeutic agents, we asked the question, can we use modulators of the channel other than the pore as novel drug targets to increase the dimensionality of the classic antiarrhythmic drugs?

To create our model, 2 unique LQT3 mutations were used as "guideposts," given their varied clinical responses to mexiletine (8,15,22). These data allowed us to integrate our experimental findings into a model of the Na^+ channel that is able to explicitly represent the molecular movements shown to be critical for mexiletine drug efficacy. To our knowledge, this

FIGURE 6 Dose-Finding Strategy for Equivalence Between Mex and Mex + Booster

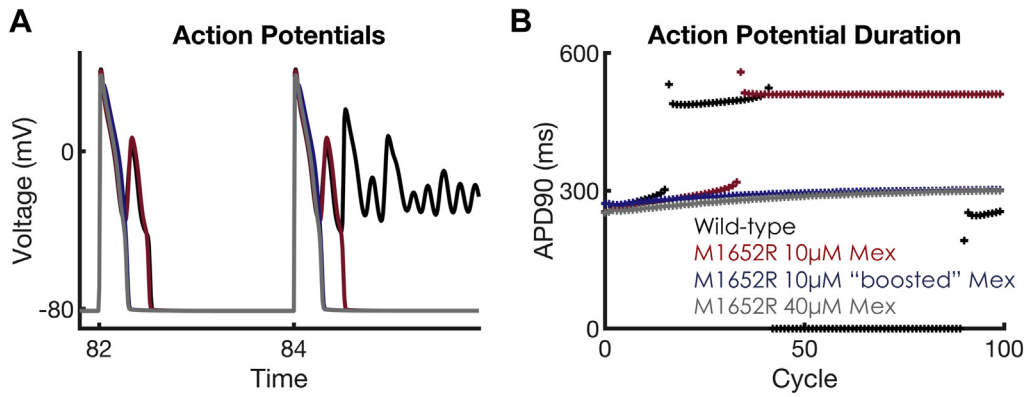

(A) Shown are APs at BCL2000, equivalent to Figure 5, at the juncture where the M1652R mutation starts the failure of the repolarization regime. After dose finding, Mex 40 μM gives APD shortening similar to that of Mex 10 μM + booster. **(B)** APD over the course of 100 cycles at BCL2000. The addition of Mex 10 μM **(red trace)**, induces repolarization at every beat, but EADs persist. This was abolished with Mex 10 μM + booster **(blue)**. To achieve equivalent APD shortening with Mex monotherapy would require Mex 40 μM **(gray)**, a 4-fold increase from the upper therapeutic range of Mex used clinically. APD_{90} = action potential duration at 90% repolarization; other abbreviations as in Figures 1 and 3.

analysis is the first such computational model to represent targetable molecular movements responsible for drug efficacy.

DRUG-FREE MODEL DEVELOPMENT. Mathematical models to describe ion channel kinetics have proven effective at elucidating mechanisms of both normal ion channel gating as well as mutations causing aberrant channel function. State-dependent modeling has allowed for the description of the drug interaction with theoretical channel conformations, which underlie the complex kinetics and emergent behavior seen clinically (12,23,24). However, aside from the "open" state, all other states in previous models did not map to a specific, targetable structural correlate. The models presented here represent the next generation of kinetic modeling: combining electrophysiology kinetic data with molecular-level structural insight (10,17).

We focused on the DIII-VSD for a number of reasons. It is becoming increasingly clear that the 4 VSDs can exhibit subtle dynamic changes and cause a bidirectional effect on pore conformation. Previous studies showed that lidocaine, a Class Ib antiarrhythmic drug binding to the pore, affects DIII-VSD dynamics (7,25), and we previously found that LQT3 variants can alter DIII-VSD activation; DI, DII, and DIV seem to play less of a role (8). Thus, we focused our efforts at incorporating DIII-VSD movement into a kinetic-based model of the Na^+ channel.

We began by using 2 LQT3 mutations to parameterize our kinetic model: R1626P, a mexiletine-sensitive mutation, and M1652R, a mexiletine-resistant mutation, in addition to wild type. When mexiletine was given to a carrier of M1652R, there was no change in QT interval, and the patient subsequently developed sudden cardiac death (ventricular fibrillation). In contrast, a carrier of the R1626P mutation exhibited a 12.5% reduction in QT interval and has remained alive with no cardiac events after 7 years of follow-up at the time of publication (15). Thus, these 2 mutants served as a natural starting point. After numerical optimization, the final models incorporated a wealth of electrophysiological data that captured current kinetics over a wide range of pacing protocols, as well as fluorescent data that tracked the DIII-VSD molecular movement in response to changes in membrane voltage.

MEXILETINE DRUG BLOCKADE. We then expanded these models to account for mexiletine drug blockade, with representations for drug access derived from the modulated and guarded receptor hypotheses (26–28), microscopic reversibility (29), DIII-VSD results (8), and clinical effects of mexiletine (15,22). Our constraint requiring equivalent affinity of mexiletine to the local anesthetic receptor for each mutation, verified experimentally by us (8) and others (15), ensured that the observed differences in the model simulations were a direct result of DIII-VSD movement. The cellular and tissue simulations recapitulated the

FIGURE 7 Effects of Mex on a 100-Cell 1D Cardiac Fiber

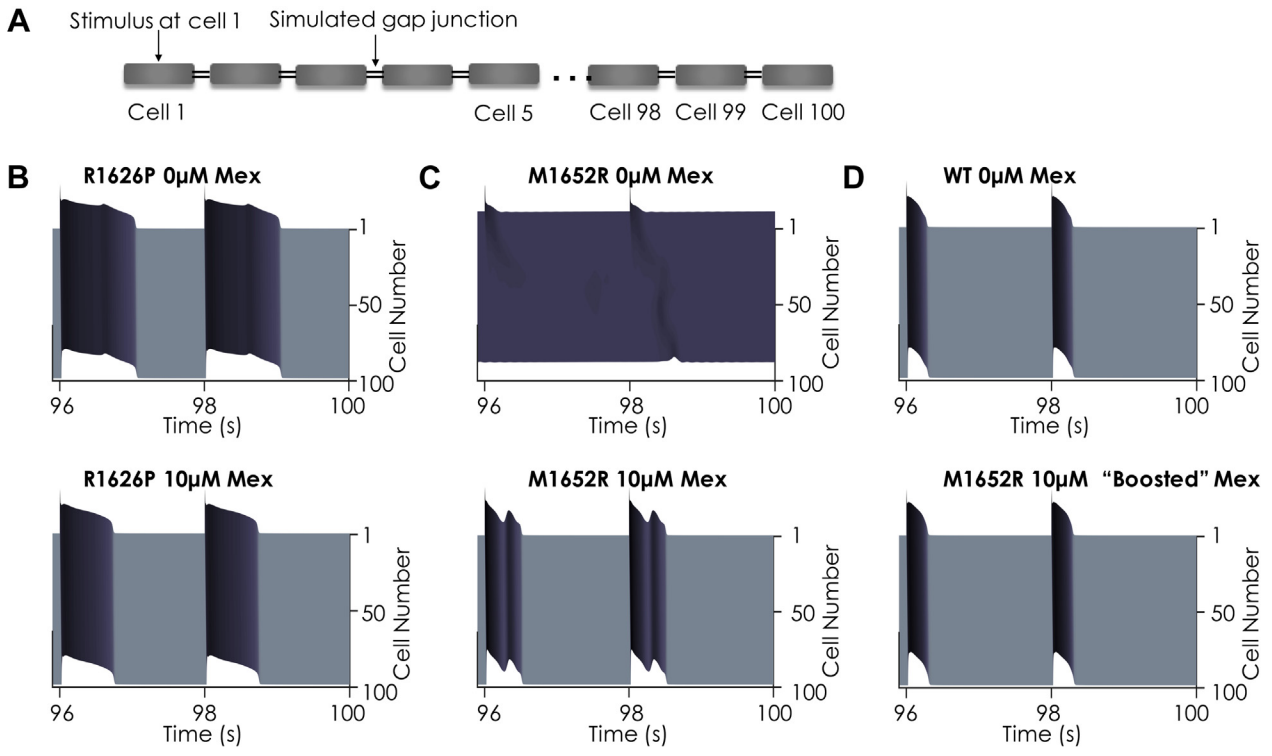

Note that for all panels, time is on the x axis, cell number is on the y axis (1→100), and voltage is in the z axis. Full details of the fiber simulation are in the Supplemental Material. The last 2 beats of a 50-beat simulation at BCL2000 are shown for each condition. **(A)** Schematic of a 1-dimensional (1D) cardiac fiber. Single ventricular myocytes were electrotonically "coupled together" by simulated gap junctions. The fiber was stimulated at cell 1, and currents and transmembrane voltage were recorded for each cell in the cardiac fiber. **(B)** In the absence of Mex **(top)**, the R1626P mutation shows EADs that persist throughout fiber. Application of Mex 10 μM **(bottom)** normalizes the AP. **(C)** For the M1652R mutation in the absence of Mex, the 49th and 50th beats represent a failure of the repolarization regime, indicating sustained arrhythmia **(top)**. Mex (10 μM) repolarizes the membrane, but sustained EADs are present throughout the fiber **(bottom)**. **(D)** The WT drug-free model shows narrow APs that easily propagate throughout the fiber **(top)**. When the M1652R mutation is treated with 10 μM of "boosted" Mex **(bottom)**, the AP normalizes dramatically and resembles the WT phenotype. Abbreviations as in **Figures 1 and 3**.

effects seen clinically: therapeutic doses of mexiletine failed to normalize the marked APD prolongation and emergent EAD triggers seen in the M1652R mutation. In the extended time course for the M1652R mutation (Supplemental Figure 4), chaotic behavior was noted, with salvos of sustained membrane depolarization preceded by increasing APD, strikingly similar to the 2:1 atrioventricular block as well as sudden cardiac death/ventricular fibrillation at the whole heart level seen clinically (15). Conversely, the R1626P mutation exhibited a 28% reduction in APD_{90} from baseline with mexiletine 10 μM, similar to clinical results.

We chose to simulate slow pacing frequencies, given that LQT3 arrhythmia syndromes are bradycardia dependent, happening mostly during sleep and periods of inactivity (30). Often, they are much less pronounced during normal (and fast) heart rates, given the rate-dependent QT shortening. This rate dependence can best be seen in Supplemental Figure 9: both mutations clearly display pathologic QT prolongation (as seen clinically [15]). Based on our simulations, the M1652R displays marked variation in rate-dependent APD, with severe prolongation only at bradycardic pacing. The important overall distinction, however, is that M1652R remains resistant to therapeutic mexiletine (**Figure 3**), whereas R1626P can effectively be treated with current therapies even at tachycardic pacing (dashed blue traces in Supplemental Figure 9 represent mexiletine 10 μM).

Based on our modeling, we found that R1626P significantly prolonged the QT interval even more than M1652R in single-cell simulations. Furthermore, **Figure 3F** shows that mid-dose mexiletine (5 μM) was not particularly effective for the R1626P mutation, which displays beat-to-beat variability in APD. However, we found no simulations that suggested further

degeneration of this variability (e.g., sustained failure of repolarization for example), as was seen with M1652R (Supplemental Figure 4). Simulating a clinical approach, we found that we could overcome this chaotic behavior by applying high-dose mexiletine (10 μM) with R1626P. Whether beat-to-beat variability versus EADs play more of a proarrhythmic role is still unclear clinically, although these mechanisms are likely a continuum of similar phenomena (e.g., EADs can lead to beat-to-beat variability and vice versa).

RATIONAL DESIGN OF MEXILETINE BOOSTER. We then sought to leverage computational modeling to rationally design a precision-targeted, molecularly based therapy to enhance mexiletine. The data explicitly reveal 3 positions of the DIII-VSD and suggest a fourth: 1) the rested position (R), in which DIII-VSD is in a "down" position, drug is inhibited from receptor access, and the DIII-VSD is maximally fluorescent; 2) the first activated state (A1), in which the DIII-VSD has moved progressively "up" in the membrane and fluorescence starts to quench, but the receptor is still blocked; 3) the second activated state (A2), in which DIII is fully "up" and fluorescence is maximally quenched, and which allows for drug binding; and 4) DIII-VSD is fully "up" but the channel has shifted to a kinetically inactivated regime. This fourth regime is based on our biotin experiment (**Figure 4**), as well as our previous studies (8,18), which strongly suggest that the DIII-VSD plays a critical role in channel inactivation.

Our approach to designing an in silico mexiletine booster was therefore to optimize the drug-free rate constants responsible for DIII-VSD movement in the MR mutation to simulate the hyperpolarizing shift in SSA of MR back to WT, and a 2-fold increase in tonic block and UDB. Simply by changing the rates governing the drug-free DIII-VSD movement, we were able to simulate the effects of "holding up" DIII-VSD on drug binding. In our computational simulations (**Figure 5A**), the mexiletine booster effectively "trapped" DIII-VSD in the up position throughout the action potential and revealed a crucial result: a relatively small change in DIII-VSD fluorescence at resting membrane potential (75% vs. 90% with the mexiletine booster) had a dramatic effect on mexiletine's clinical efficacy.

CLINICAL UTILITY AND IMPLICATIONS. Mexiletine remains widely prescribed, most commonly for malignant ventricular tachycardia. In contrast to flecainide, it can be used in both structurally normal and abnormal, infarcted hearts. It is often used as an oral lidocaine analogue in those patients who derived clinical benefit from intravenous lidocaine. It is preferred over amiodarone for long-term management of ventricular arrhythmia, given the long-term consequences of chronic amiodarone therapy (pulmonary, liver, thyroid, and cornea deposition). Interestingly, mexiletine has also been used to treat neuropathic pain (31). Although widely used, tolerance to mexiletine is inversely proportional to the dose, with gastrointestinal distress and nausea often limiting high therapeutic concentrations.

As a necessary first step and proof-of-concept, we focused on 2 LQT3 mutations that represent the "extremes" of DIII-VSD sensitivity to mexiletine. By framing the modeling study in terms of these 2 mutations, however, we were able to delineate the putative molecular mechanism that underlies $Na_V1.5$ sensitivity to mexiletine, regardless of the presence or absence of a mutation. In our previous study (8), we further found a strong correlation between DIII-VSD activation and mexiletine sensitivity (Figure 4 and Online Table II in the paper by Zhu et al. [8]). We also found that WT channels are not particularly sensitive to mexiletine, obviating high doses of mexiletine used clinically with increased side effects for modest therapeutic benefit. Thus, it is conceivable that the booster strategy could work for WT channels implicated in varied cardiac arrhythmia syndromes (e.g., ventricular tachycardia in which mexiletine is commonly used) by further hyperpolarizing the WT DIII-VSD activation voltage, which would result in increased WT sensitivity.

Drug development remains a markedly expensive and time-consuming endeavor fraught with potential failure throughout the development cycle. The computational modeling approach presented here may be a novel strategy to increase the chances of success by rationally designing drugs in silico while simultaneously assessing markers of success and failure at multiple spatial and time scales. The strength of computational modeling is highlighted by a few key results; namely, we were able to rationally design a drug molecule based on key molecular movements of the Na^+ channel, and then test those predictions in coupled higher dimensional tissue. Second, we were able to perform an in silico safety analysis to assess for hallmark proarrhythmic sequelae of Class I drugs, namely conduction block. Finally, we were able to use the model to quantify the strength of our mexiletine booster through an "equivalence" dose-finding simulation. Rather than de novo drug design of a new antiarrhythmic drug, our model suggests a potential polypharmaceutical strategy to use 2 drugs with synergistic effects: a commonly prescribed antiarrhythmic drug that accesses the local anesthetic drug receptor on the Na^+ channel combined with a

DIII-VSD modulator for increased antiarrhythmic efficacy. As shown in the state-dependent drug-binding analysis of Supplemental Figures 3 and 4, a relatively small increase in DIII-VSD movement can have a dramatic effect on therapeutic doses of mexiletine.

This "boosted" approach, or pharmacokinetic enhancement, has been used previously with notable examples, including human immunodeficiency virus antiretroviral agents, drugs for Parkinson's disease, and cancer immunotherapy. The addition of a "booster," in this case an allosteric modulator, combined with a pore blocker adds an entirely new dimension to the existing parameter space of antiarrhythmic drug efficacy. Although we tested this approach with LQT3 and mexiletine, we expect that a similar strategy is widely applicable to those with malignant and refractory ventricular tachycardia both from ischemic heart failure and nonischemic, inherited arrhythmia syndromes. We further expect that boosting other Class I drugs could yield similar benefit.

STUDY LIMITATIONS. Although the Na^+ channel model is highly complex and is coupled with a highly parameterized human ventricular myocyte computational model, it represents a simplification of the true underlying pathophysiology. The molecular movements include only the contribution from the DIII-VSD, as our experimental results (8) suggest that this domain is the most important for determining Class I antiarrhythmic drug efficacy. Future studies may incorporate the contribution of the DIV-VSD as a next step. As noted, all current Class I drugs are designed to have different binding rates and affinities to the channel pore; a "booster" allows for the modulation of the state of the channel. However, it is possible that activation of DIII-VSD may be proarrhythmic. Based on our simulations, our in silico booster molecule seems to be extremely effective as an adjunct therapeutic strategy with mexiletine and could be a clinically useful therapy. However, such a molecule does not currently exist, and in fact, despite the existence of DIV-VSD-binding molecules, we are aware of no DIII-VSD molecule currently in clinical development. We further note that we used a saturating concentration of biotin, and our simulations of "booster" necessarily pushed the DIII-VSD into a nearly complete "upward" position to fit the desired higher affinity tonic and use-dependent block. Theoretically, one could pursue further dose-finding strategies to "fine-tune" the desired therapeutic effects of the "booster" molecule. Although a booster does not exist currently, this study provides a rationale to pursue such a molecule.

CONCLUSIONS

We have developed a model of the Na^+ channel that for the first time includes explicit representation of the molecular movements which shape the action potential and form the basis of the differential sensitivity to the common antiarrhythmic drug mexiletine. After expanding the model to account for the pharmacokinetic variables of mexiletine drug binding and the role of the DIII-VSD, the model was used to develop a precision-targeted mexiletine booster that was able to effectively rescue a mexiletine-resistant LQT3 mutation. Our results suggest a promising future avenue of drug development, namely exploitation of nontraditional ion channel drug targets, which allows for precision-targeted and mutation-specific pharmacotherapy for both LQT3 mutations and an enhanced mexiletine for ventricular tachycardia, with a more favorable side effect profile.

ADDRESS FOR CORRESPONDENCE: Dr. Jonathan R. Silva, Department of Biomedical Engineering, Washington University in St. Louis, One Brookings Drive, Whitaker Hall, Room 290G, St. Louis, Missouri 63130. E-mail: jonsilva@wustl.edu.

PERSPECTIVES

COMPETENCY IN MEDICAL KNOWLEDGE: Class I antiarrhythmic therapies remain suboptimal given the inability to predict efficacy and potential proarrhythmic side effects. The Class Ib drug mexiletine has been show to have differential efficacy based on key molecular determinants of the Na+ channel. This study used computational modeling to understand the molecular basis of drug efficacy, and then designed an in-silico mexiletine booster that could improve efficacy.

TRANSLATIONAL OUTLOOK: Drug discovery remains expensive, time-consuming, and has an unacceptably high failure rate. Computational modeling approaches to drug discovery represent a novel tool to design and test precision-targeted therapeutic agents, premised on a detailed understanding of the molecular underpinnings of drug efficacy. By exploiting nontraditional ion channel drug targets, we can add an entirely new dimension to the wide parameter space of traditional antiarrhythmic drugs to develop more precision-targeted and potent Class I therapeutic agents.

REFERENCES

1. Echt DS, Liebson PR, Mitchell LB, et al. Mortality and morbidity in patients receiving encainide, flecainide, or placebo. The Cardiac Arrhythmia Suppression Trial. N Engl J Med 1991;324:781–8.

2. Waldo AL, Camm AJ, deRuyter H, et al. Effect of d-sotalol on mortality in patients with left ventricular dysfunction after recent and remote myocardial infarction. The SWORD Investigators. Survival With Oral d-Sotalol. Lancet 1996;348:7–12.

3. Moreno JD, Zhu ZI, Yang PC, et al. A computational model to predict the effects of class I anti-arrhythmic drugs on ventricular rhythms. Sci Transl Med 2011;3:98ra83.

4. Starmer CF. How antiarrhythmic drugs increase the rate of sudden cardiac death. Int J Bifurcation Chaos 2002;12:1953–68.

5. Payandeh J, Scheuer T, Zheng N, Catterall WA. The crystal structure of a voltage-gated sodium channel. Nature 2011;475:353–8.

6. Balser JR. The cardiac sodium channel: gating function and molecular pharmacology. J Mol Cell Cardiol 2001;33:599–613.

7. Sheets MF, Hanck DA. Molecular action of lidocaine on the voltage sensors of sodium channels. J Gen Physiol 2003;121:163–75.

8. Zhu W, Mazzanti A, Voelker TL, et al. Predicting patient response to the antiarrhythmic mexiletine based on genetic variation. Circ Res 2019;124:539–52.

9. Beaumont J, Davidenko N, Davidenko JM, Jalife J. Spiral waves in two-dimensional models of ventricular muscle: formation of a stationary core. Biophys J 1998;75:1–14.

10. Silva JR. How to connect cardiac excitation to the atomic interactions of ion channels. Biophys J 2018;114:259–66.

11. Mangold KE, Brumback BD, Angsutararux P, et al. Mechanisms and models of cardiac sodium channel inactivation. Channels (Austin) 2017;11:517–33.

12. Moreno JD, Lewis TJ, Clancy CE. Parameterization for in-silico modeling of ion channel interactions with drugs. PLoS One 2016;11:e0150761.

13. Teed ZR, Silva JR. A computationally efficient algorithm for fitting ion channel parameters. MethodsX 2016;3:577–88.

14. Grandi E, Pasqualini FS, Bers DM. A novel computational model of the human ventricular action potential and Ca transient. J Mol Cell Cardiol 2010;48:112–21.

15. Ruan Y, Liu N, Bloise R, Napolitano C, Priori SG. Gating properties of SCN5A mutations and the response to mexiletine in long-QT syndrome type 3 patients. Circulation 2007;116:1137–44.

16. Varga Z, Zhu W, Schubert AR, et al. Direct measurement of cardiac Na+ channel conformations reveals molecular pathologies of inherited mutations. Circ Arrhythm Electrophysiol 2015;8:1228–39.

17. Zhu W, Varga Z, Silva JR. Molecular motions that shape the cardiac action potential: insights from voltage clamp fluorometry. Prog Biophys Mol Biol 2016;120:3–17.

18. Hsu EJ, Zhu W, Schubert AR, Voelker T, Varga Z, Silva JR. Regulation of Na+ channel inactivation by the DIII and DIV voltage-sensing domains. J Gen Physiol 2017;149:389–403.

19. Sheets MF, Hanck DA. Outward stabilization of the S4 segments in domains III and IV enhances lidocaine block of sodium channels. J Physiol 2007;582 Pt 1:317–34.

20. Preliminary report: effect of encainide and flecainide on mortality in a randomized trial of arrhythmia suppression after myocardial infarction. The Cardiac Arrhythmia Suppression Trial (CAST) Investigators. N Engl J Med 1989;321:406–12.

21. Greer-Short A, George SA, Poelzing S, Weinberg SH. Revealing the concealed nature of long-QT type 3 syndrome. Circ Arrhythm Electrophysiol 2017;10:e004400.

22. Mazzanti A, Maragna R, Faragli A, et al. Gene-specific therapy with mexiletine reduces arrhythmic events in patients with long QT syndrome type 3. J Am Coll Cardiol 2016;67:1053–8.

23. Moreno JD, Clancy CE. Using computational modeling to predict arrhythmogenesis and antiarrhythmic therapy. Drug Discov Today Dis Models 2009;6:71–84.

24. Roberts BN, Yang PC, Behrens SB, Moreno JD, Clancy CE. Computational approaches to understand cardiac electrophysiology and arrhythmias. Am J Physiol Heart Circ Physiol 2012;303:H766–83.

25. Arcisio-Miranda M, Muroi Y, Chowdhury S, Chanda B. Molecular mechanism of allosteric modification of voltage-dependent sodium channels by local anesthetics. J Gen Physiol 2010;136:541–54.

26. Hille B. Local anesthetics: hydrophilic and hydrophobic pathways for the drug-receptor reaction. J Gen Physiol 1977;69:497–515.

27. Starmer CF, Lastra AA, Nesterenko VV, Grant AO. Proarrhythmic response to sodium channel blockade. Theoretical model and numerical experiments. Circulation 1991;84:1364–77.

28. Hondeghem LM, Katzung BG. Antiarrhythmic agents: the modulated receptor mechanism of action of sodium and calcium channel-blocking drugs. Annu Rev Pharmacol Toxicol 1984;24:387–423.

29. Colquhoun D, Dowsland KA, Beato M, Plested AJ. How to impose microscopic reversibility in complex reaction mechanisms. Biophys J 2004;86:3510–8.

30. Ruan Y, Liu N, Priori SG. Sodium channel mutations and arrhythmias. Nat Rev Cardiol 2009;6:337–48.

31. Chabal C, Jacobson L, Mariano A, Chaney E, Britell CW. The use of oral mexiletine for the treatment of pain after peripheral nerve injury. Anesthesiology 1992;76:513–7.

KEY WORDS arrhythmias, computational biology, ion channels, pharmacology, translational studies

APPENDIX For supplemental information and figures, please see the online version of this paper.

JACC: BASIC TO TRANSLATIONAL SCIENCE VOL. 4, NO. 6, 2019

EDITORIAL COMMENT

How to Boost Efficacy of a Sodium Channel Blocker

The Devil Is in the Details*

Madison B. Nowak, BS, Vrishti M. Phadumdeo, BS, Seth H. Weinberg, PhD

The development of antiarrhythmic therapies is a costly endeavor. Computational models have increasingly been included in the drug development pipeline as a method to screen potentially proarrhythmic compounds and provide a critical link between protein scale perturbations (e.g., ion channel mutations) and tissue scale behavior (e.g., arrhythmia episodes). As experiments have more clearly elucidated ion channel dynamics, computational models too need to incorporate more detailed representations of channel responses.

The earliest models of the cardiac sodium channel ($Na_v1.5$) used Hodgkin-Huxley–type gating variables to reproduce the kinetics associated with channel activation and inactivation. Although these types of models can reproduce important channel properties, a key limitation is that channel activation and inactivation are assumed to be independent. Markov chain models were subsequently developed to address this limitation and to represent multiple distinct closed, open, and inactivated channel states. This framework was also critical to more accurately model drugs that target ion channels. Simply put, a drug may only access its binding site when the channel is in specific states; therefore, representing state-specific binding rates is critical. Moreno et al. (1) previously applied such an in silico approach to explain the paradoxically proarrhythmic response of the sodium channel blocker flecainide.

Sodium channel Markov models have been expanded to account for several variants of gain-of-function mutations in the *SCN5A* gene, encoding the alpha subunit of the $Na_v1.5$ channel, that are associated with long QT type 3 syndrome (LQT3). Although the phenotypes associated with these variants are similar, a late sodium current which prolongs the action potential duration (APD), the mechanism by which the late current manifest differs among variants. This suggests that a "one size fits all" therapy to treat LQT3 may be problematic.

Recent work by Zhu et al. (2) illustrated that the picture is indeed even more complicated. That study used voltage-clamp fluorometry, an elegant technique in which a fluorophore is tethered to each of the 4 voltage-sensitive domains (VSDs) of the $Na_v1.5$ alpha subunit to monitor VSD movement simultaneously with channel current (2). The study found that activation of the VSD of the third $Na_v1.5$ domain (DIII-VSD) varied significantly across 15 LQT3 variants and, critically, that DIII-VSD activation and channel inhibition by the sodium channel blocker mexiletine were correlated. Thus, the complex picture begins to emerge: 1) VSDs regulate channel gating processes and transitions between channel states; 2) VSD kinetics are altered differently for different LQT3 variants; and 3) drug binding depends on VSD activation.

SEE PAGE 736

In this issue of *JACC: Basic to Translational Science*, Moreno et al. (3) for the first time developed a computational model of the sodium channel that incorporated all of these critical details: channel mutations, DIII-VSD movement, and drug binding. The authors focused on 2 LQT3 mutant variants,

*Editorials published in *JACC: Basic to Translational Science* reflect the views of the authors and do not necessarily represent the views of *JACC: Basic to Translational Science* or the American College of Cardiology.

From the Department of Biomedical Engineering, Ohio State University, Columbus, Ohio. The authors have reported that they have no relationships relevant to the contents of this paper to disclose.

The authors attest they are in compliance with human studies committees and animal welfare regulations of the authors' institutions and Food and Drug Administration guidelines, including patient consent where appropriate. For more information, visit the *JACC: Basic to Translational Science* author instructions page.

ISSN 2452-302X https://doi.org/10.1016/j.jacbts.2019.09.004

R1626P (RP), which is highly sensitive to mexiletine, and M1652R (MR), which is minimally sensitive to mexiletine (2). They then used voltage-clamp fluorometry to show that the mexiletine-sensitive RP mutant channels had enhanced DIII-VSD activation, whereas the mexiletine-resistant MR mutant channels had reduced DIII-VSD activation. Next, the authors developed a Markov model of the wild-type (WT) and mutant sodium channels, representing distinct drug-free and drug-bound VSD states and gating conformations that accurately reproduced experimental measurements of voltage-, time-, and drug concentration-dependent channel activities, including mexiletine blockage of late sodium current. One key aspect of the modeling approach was that the authors assumed that the intrinsic affinity of mexiletine for the channel was constant between the variants. Thus, the different drug responses of the WT and the 2 mutants emerged from the dynamics of DIII-VSD activation and channel gating.

Bridging the scale from ion channel to cellular response, the authors next incorporated the sodium channel model into a human ventricular myocyte model. Simulations of myocytes with the mutant channels displayed a sustained late sodium current, the hallmark of the LQT3 phenotype. Myocytes with the RP mutant illustrated significant APD prolongation and early after-depolarizations (EADs). Treatment with a maximal clinical dose of 10 μmol of mexiletine abolished EADs and shortened APD, although not to WT levels. In contrast, myocytes with the MR mutant displayed highly irregular repolarization, with significant APD prolongation, EADs, and periods of repolarization failure; 10 μmol of mexiletine delayed the onset of EADs but failed to suppress them or APD prolongation.

Based on the relationship between DIII-VSD activation and mexiletine channel blockage, Moreno et al. (3) then insightfully hypothesized that mexiletine efficacy in the MR mutant could be enhanced or "boosted" by combining mexiletine with an agent that promoted DIII-VSD activation. The authors performed a proof-of-concept demonstration experimentally by introducing a second mutation, R1306C, which, in conjunction with extracellular application of biotin, stabilized DIII-VSD in an activated position. Consistent with the hypothesis, these modifications enhanced late sodium current blockage. The authors then pushed the computational predictions further by altering only DIII-VSD movement rates. The authors designed an in silico mexiletine booster with enhanced DIII-VSD activation. Simulations in MR mutant myocytes with the "boosted" mexiletine showed late sodium current was reduced to nearly WT levels and suppressed EADs and APD prolongation. The authors concluded by scaling predictions to the tissue level, illustrating that EADs are similarly suppressed by boosted mexiletine in a 1-dimensional cardiac fiber.

The authors are to be commended for proposing a novel strategy for developing new antiarrhythmic drugs, as the booster strategy deviates from the typical approach of solely targeting the ion channel pore and draws from considerable insights into the molecular mechanisms underlying drug action on the sodium channel. The study also predicts that the booster combination therapy would enable a greatly reduced drug dose, which in turn mitigates potentially off-target side effects. Although Moreno et al. (3) focused specifically on the cardiac sodium channel, the concept of altering VSD activation to enhance drug binding responses can be applied to other channels and should be explored further as a new approach to increasing drug efficacy.

The proposed strategy illustrated by Moreno et al. (3) introduces a new dimension in ion channel drug-targeting development. However, the translational application of such a strategy faces significant hurdles. The experimental demonstration of enhanced DIII-VSD activation using extracellular application of biotin also required the introduction of an additional point mutation in the *SCN5A* gene and, thus, is far from ideal for patient therapy. A more likely approach would involve the use of a hypothetical molecule that targets the DIII-VSD, but as the authors note, no such molecule has been identified. However, this study can motivate the exploration for and development of agents targeting and modifying channel VSDs.

With increased biophysical detail comes increased model complexity. The full sodium channel Markov model incorporating the combinations of DIII-VSD states, channel gating, and drug-free and drug-bound states results in 40 distinct channel states and introduces more than 80 parameters, despite constraints from microscopic reversibility and additional assumptions. To further motivate the development of such VSD-targeting therapeutics, new in silico predictions demonstrating the robustness of the proposed strategy would be particularly valuable (e.g., by performing parameter sensitivity analysis and population-based simulations).

Further challenges arise after considering the strong evidence for multiple pools of $Na_v1.5$ channels in different regions of the cell, with distinct interacting regulatory proteins and channel kinetics (4). Differences in regulatory proteins in turn may result in different responses to therapeutics modulating DIII-VSD activation. Accounting for distinct $Na_v1.5$

pools is particularly critical in LQT3, as the present authors recently showed that $Na_v1.5$ preferential localization at the intercalated disk can reduce the late sodium current and suppress EAD formation (5).

Despite these additional qualifications, the study by Moreno et al. (3) proposes several significant advances in computational modeling and drug design approaches. The strategy of predicting the drug response of a specific genetic variant and then enhancing drug efficacy by targeting nonporous channel regions could become a critical tool in the design of new antiarrhythmic therapies.

ADDRESS FOR CORRESPONDENCE: Dr. Seth H. Weinberg, The Ohio State University, Biomedical Engineering, 1080 Carmack Road, Columbus, Ohio 43210. E-mail: weinberg.147@osu.edu.

REFERENCES

1. Moreno JD, Zhu ZI, Yang PC, et al. A computational model to predict the effects of class I anti-arrhythmic drugs on ventricular rhythms. Sci Transl Med 2011;3:83.

2. Zhu W, Mazzanti A, Voelker TL, et al. Predicting patient response to the antiarrhythmic mexiletine based on genetic variation. Circ Res 2019;124:539–52.

3. Moreno JD, Zhu W, Mangold K, Chung W, Silva JR. A molecularly detailed $Na_v1.5$ model reveals a new class I antiarrhythmic target. J Am Coll Cardiol Basic Trans Science 2019;4:736–51.

4. Shy D, Gillet L, Abriel H. Cardiac sodium channel $Na_v1.5$ distribution in myocytes via interacting proteins: the multiple pool model. Biochim Biophys Acta 2013;1833:886–94.

5. Greer-Short A, George SA, Poelzing S, Weinberg SH. Revealing the concealed nature of long-QT type 3 syndrome. Circ Arrhythm Electrophysiol 2017;10:e004400.

KEY WORDS arrhythmia, computational biology, ion channels, pharmacology, translational studies

JACC: BASIC TO TRANSLATIONAL SCIENCE VOL. 4, NO. 6, 2019

STATE-OF-THE-ART REVIEW

Angiopoietin-Like 3

From Discovery to Therapeutic Gene Editing

Xiao Wang, PhD, Kiran Musunuru, MD, PhD, MPH, ML

JACC: BASIC TO TRANSLATIONAL SCIENCE CME/MOC/ECME

This article has been selected as this month's *JACC: Basic to Translational Science* CME/MOC/ECME activity, available online at http://www.acc.org/jacc-journals-cme by selecting the *JACC* Journals CME/MOC/ECME tab.

Accreditation and Designation Statement

The American College of Cardiology Foundation (ACCF) is accredited by the Accreditation Council for Continuing Medical Education (ACCME) and the European Board for Accreditation in Cardiology (EBAC) to provide continuing medical education for physicians.

The ACCF designates this Journal-based CME/MOC/ECME activity for a maximum of 1 AMAPRA Category 1 Credit or 1 EBAC Credit. Physicians should only claim credit commensurate with the extent of their participation in the activity.

Successful completion of this CME activity, which includes participation in the evaluation component, enables the participant to earn up to 1 Medical Knowledge MOC point in the American Board of Internal Medicine's (ABIM) Maintenance of Certification (MOC) program. Participants will earn MOC points equivalent to the amount of CME credits claimed for the activity. It is the CME activity provider's responsibility to submit participant completion information to ACCME for the purpose of granting ABIM MOC credit.

Angiopoietin-Like 3: From Discovery to Therapeutic Gene Editing will be accredited by the European Board for Accreditation in Cardiology (EBAC) for 1 hour of External CME credits. Each participant should claim only those hours of credit that have actually been spent in the educational activity. The Accreditation Council for Continuing Medical Education (ACCME) and the European Board for Accreditation in Cardiology (EBAC) have recognized each other's accreditation systems as substantially equivalent. Apply for credit through the post-course evaluation.

Method of Participation and Receipt of CME/MOC/ECME Certificate

To obtain credit for *JACC: Basic to Translational Science* CME/MOC/ECME, you must:

1. Be an ACC member or JACBTS subscriber.
2. Carefully read the CME/MOC/ECME-designated article available online and in this issue of the *journal*.
3. Answer the post-test questions. At least 2 questions provided must be answered correctly to obtain credit.
4. Complete a brief evaluation.
5. Claim your CME/MOC/ECME credit and receive your certificate electronically by following the instructions given at the conclusion of the activity.

CME/MOC/ECME Objective for This Article: Upon completion of this activity, the learner should be able to: 1) discuss the role of cholesterol testing to stratify cardiovascular risk; 2) compare different pharmacologic strategies for treatment of hyperlipidemia; and 3) discuss the potential role for ANGPTL3 directed therapies for hyperlipidemia.

CME/MOC/ECME Editor Disclosure: CME/MOC/ECME Editor L. Kristin Newby, MD, is supported by research grants from Amylin, Bristol-Myers Squibb Company, GlaxoSmithKline, Sanofi, Verily Life Sciences (formerly Google Life Sciences), the MURDOCK Study, NIH, and PCORI; receives consultant fees/honoraria from BioKier, DemeRx, MedScape/TheHeart.org, Metanomics, Philips Healthcare, Roche Diagnostics, CMAC Health Education & Research Institute; serves as an Officer, Director, Trustee, or other fiduciary role for the AstraZeneca HealthCare Foundation and the Society of Chest Pain Centers (now part of ACC); and serves in another role for the American Heart Association and is the Deputy Editor of *JACC: Basic to Translational Science*.

Author Disclosures: Dr. Musunuru is an unpaid scientific advisor to Verve Therapeutics. The authors have reported that they have no relationships relevant to the contents of this paper to disclose.

Medium of Participation: Online (article and quiz).

CME/MOC/ECME Term of Approval

Issue Date: October 2019
Expiration Date: September 30, 2020

From the Department of Medicine and Department of Genetics, Cardiovascular Institute, Perelman School of Medicine at the University of Pennsylvania, Philadelphia, Pennsylvania. Dr. Musunuru is an unpaid scientific advisor to Verve Therapeutics. The authors have reported that they have no relationships relevant to the contents of this paper to disclose.

The authors attest they are in compliance with human studies committees and animal welfare regulations of the authors' institutions and Food and Drug Administration guidelines, including patient consent where appropriate. For more information, visit the *JACC: Basic to Translational Science* author instructions page.

Manuscript received January 16, 2019; revised manuscript received May 11, 2019, accepted May 15, 2019.

ISSN 2452-302X https://doi.org/10.1016/j.jacbts.2019.05.008

JACC: BASIC TO TRANSLATIONAL SCIENCE VOL. 4, NO. 6, 2019
OCTOBER 2019:755–62

Angiopoietin-Like 3

From Discovery to Therapeutic Gene Editing

Xiao Wang, PhD, Kiran Musunuru, MD, PhD, MPH, ML

HIGHLIGHTS

- **Individuals with ANGPTL3 loss-of-function mutations have reduced cholesterol levels, triglyceride levels, and risk of coronary heart disease, making ANGPTL3 a potential therapeutic target.**
- **An antisense oligonucleotide inhibitor of ANGPTL3 and a monoclonal antibody against ANGPTL3 have been advanced into clinical trials, with encouraging results to date.**
- **A distinct approach to targeting ANGPTL3 would be therapeutic gene editing in patients to induce permanent loss of function mutations mimicking those in individuals with naturally occurring cardioprotective mutations.**

SUMMARY

Hyperlipidemia is a major causal risk factor for atherosclerosis and coronary heart disease (CHD). Angiopoietin-like 3 (ANGPTL3) has emerged as a promising molecular target to reduce CHD risk due to its regulation of all 3 major lipid traits: low-density lipoprotein cholesterol, high-density lipoprotein cholesterol, and triglycerides. Here, the authors review the discovery of ANGPTL3, the role of ANGPTL3 in lipoprotein metabolism, and the genetic association between naturally occurring ANGPTL3 loss-of-function mutations and CHD. In light of the favorable consequences of ANGPTL3 deficiency, various therapeutic strategies to target ANGPTL3 are currently in development, including a monoclonal antibody, an antisense oligonucleotide, and gene editing. (J Am Coll Cardiol Basic Trans Science 2019;4:755–62)

Over the last few decades, tremendous progress has been made in understanding and decreasing the incidence of coronary heart disease (CHD). Low-density lipoprotein cholesterol (LDL-C) has been established as a major causal risk factor for atherosclerosis and CHD. Remarkable efforts have been made to develop LDL-lowering therapies, and statins have been proven to be an effective means of reducing the risk of CHD. However, even with the use of statin therapy, there remains a large residual risk of CHD, particularly in patients with familial hypercholesterolemia (1). In light of these observations, an intensive search for new molecular targets to further reduce CHD risk is ongoing. In 2015, the efficacy of alirocumab and evolocumab, 2 human monoclonal antibody-based drugs that target proprotein convertase subtilisin/kexin type 9 (PCSK9), was confirmed with respect to the reduction of LDL-C levels in patients (2,3).

Despite advances in the development of lipid-lowering therapies, clinical trials have shown that a substantial risk of cardiovascular disease persists even when receiving currently recommended medical therapy. For example, in 1 trial involving patients who had an acute coronary syndrome, the lowering of LDL-C levels to a median of 54 mg/dl with the use of a statin plus ezetimibe was found to prevent only a slightly higher proportion of events than treatment with a statin alone; the difference in absolute risk associated with the 2 regimens was only 2 proportion points, and approximately one-third of both sets of patients had a major cardiovascular event within 7 years (4). A similarly small reduction in the absolute risk of coronary events was found among patients whose levels of LDL-C were reduced to 30 mg/dl with the use of a PCSK9 inhibitor (5). In addition, researchers have continued to search for additional molecular targets that are particularly relevant for the treatment of patients with homozygous familial hypercholesterolemia (hoFH) who have genetic deficiency of the LDL receptor. Since the efficacy of both statins and PCSK9 antibody therapies largely depends on functional LDL receptors, patients with hoFH show limited responses to both therapies.

One such promising molecular target is angiopoietin-like 3 (ANGPTL3). ANGPTL3 belongs to a

subfamily of angiopoietin-like proteins involved in the regulation of plasma lipid metabolism. ANGPTL3 is secreted from liver and was first identified via positional cloning of a hypolipidemic mouse strain (6). ANGPTL3 is unique in that it regulates all 3 major lipid traits: LDL-C, high-density lipoprotein cholesterol (HDL-C), and triglycerides. The primary action of ANGPTL3 is to inhibit lipoprotein lipase (LPL), which hydrolyzes the triglycerides carried in triglyceride-rich lipoproteins in the circulation (7). ANGPTL3 also inhibits endothelial lipase to modulate HDL-C metabolism (8). The mechanism by which ANGPTL3 regulates LDL-C remains unclear (9).

DISCOVERY OF ANGPTL3

The *Angptl3* gene was identified by positional cloning of the mutation responsible for the hypolipidemia phenotype in KK/San mice, a sub-strain of KK mice that have moderate obesity, abnormally high levels of plasma insulin (hyperinsulinemia), glucose (hyperglycemia), and lipids (hyperlipidemia). There is a 4-bp insertion in exon 6 of *Angptl3* in KK/San mice, introducing a premature stop codon. KK/San mice have lower levels of triglycerides, total cholesterol, and non-esterified fatty acids in the circulation compared to KK mice. Using adenovirus expressing human or mouse ANGPTL3 rescued the lower levels of triglycerides, total cholesterol, and non-esterified fatty acids in KK/San mice. The same treatment also increased triglycerides and total cholesterol levels in wild-type (WT) C57BL/6 mice (6). These data proved that disruption of *Angptl3* is responsible for the hypolipidemia in KK/San mice and that ANGPTL3 regulates circulating triglycerides and total cholesterol levels in mouse.

ANGIOPOIETIN-LIKE PROTEINS. ANGPTL3 belongs to a family of 8 angiopoietin-like proteins (ANGPTL1 to ANGPTL8) that share a similar structure and carry out related functions. Seven of 8 angiopoietin-like proteins (ANGPTL1 to ANGPTL7) contain a signal peptide, an N-terminal coiled-coil domain, a linker region, and a C-terminal fibrinogen-like domain (FLD) (10). ANGPTL8 differs from the other angiopoietin-like proteins in that it lacks a C-terminal FLD (11). Similar to other angiopoietin-like proteins, ANGPTL3 undergoes cleavage; the cleavage site is at amino acid residues 221-Arg-Ala-Pro-Arg-224, which yields separate fragments containing the coiled-coil domain and the FLD (12). ANGPTL3 is found in the plasma as full-length and truncated forms. ANGPTL3 is cleaved intracellularly by furin (also known as PCSK3) and extracellularly mainly by PACE4 (also known as PCSK6) (13). The truncated form of ANGPTL3 is more active, and cleavage enhances the ability of ANGPTL3 to inhibit lipoprotein lipase and regulate plasma levels of triglycerides both in vitro (11) and in vivo (12).

Similar to ANGPTL3, another 2 members of the angiopoietin-like protein family—ANGPTL4 and ANGPTL8—are involved in the regulation of plasma lipid metabolism. ANGPTL4 is highly expressed in the liver and adipose tissue and upregulated by fasting and hypoxia (14,15). ANGPTL4 forms dimers and tetramers before secretion and undergoes cleavage at a canonical proprotein convertase cleavage site, 161-Arg-Arg-Lys-Arg-164, after secretion (16). The N-terminal fragment remains oligomerized after cleavage, binds transiently to LPL, and converts LPL from catalytically active dimers to inactive monomers to decrease its activity (17). *Angptl4* knockout mice have lower triglyceride levels and modestly lower cholesterol levels (18). However, when *Angptl4* knockout mice were fed a high-fat diet, they showed reduced viability associated with lipogranulomatous lesions, which raises a significant safety concern with respect to the proposed targeting of ANGPTL4 for the treatment of dyslipidemia and atherosclerosis (18,19).

ANGPTL8 is an atypical member of the angiopoietin-like protein family because of its lack of a C-terminal FLD, but it does share structural homology with the N-terminal domains of ANGPTL3 and ANGPTL4 (20,21), and it can inhibit LPL and thereby regulate triglyceride metabolism (11).

ABBREVIATIONS AND ACRONYMS

ANGPTL3 = angiopoietin-like 3

ASO = antisense oligonucleotide

CHD = coronary heart disease

HDL-C = high-density lipoprotein cholesterol

hoFH = homozygous familial hypercholesterolemia

LDL-C = low-density lipoprotein cholesterol

PCSK9 = proprotein convertase subtilisin/kexin type 9

***ANGPTL3* GENETICS AND PLASMA LIPIDS.** Genome-wide association studies and exome sequencing studies have identified associations between loss-of-function genetic variants in the *ANGPTL3* gene and low levels of plasma LDL-C, HDL-C, and triglycerides (22,23). The *ANGPTL3* coding regions were sequenced in 3,551 individuals in the Dallas Heart Study, and a total of 35 nonsynonymous sequence variations (nonsense, missense, frameshift, and splice-site mutations) were identified. An excess of sequence variants in the lowest quartile for plasma triglyceride levels (14 vs. 5 variants) approached the nominal significance threshold ($p = 0.06$). In vitro functional studies revealed that all *ANGPTL3* missense variants that were associated with low plasma triglyceride levels interfered either with the synthesis or secretion of the protein or with the ability of the ANGPTL3 protein to inhibit LPL activity (24).

JACC: BASIC TO TRANSLATIONAL SCIENCE VOL. 4, NO. 6, 2019
OCTOBER 2019:755–62

CENTRAL ILLUSTRATION **ANGPTL3 Deficiency Protects People From Coronary Artery Disease**

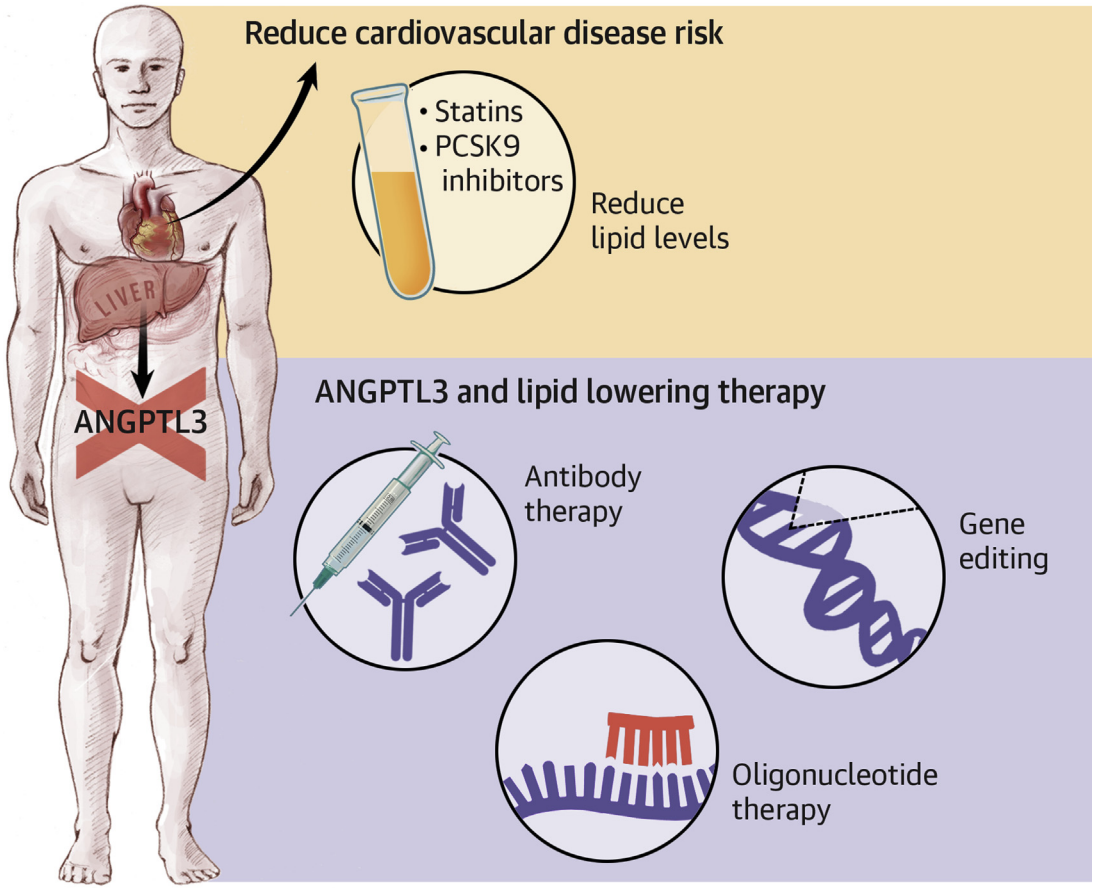

Wang, X. et al. J Am Coll Cardiol Basic Trans Science. 2019;4(6):755–62.

Despite the use of statins and PCSK9 inhibitors, there remains residual risk of coronary heart disease (CHD). ANGPTL3 has emerged as a promising molecular target to further reduce CHD risk due to its regulation of all 3 major lipid traits: low-density lipoprotein cholesterol, high-density lipoprotein cholesterol, and triglycerides. In light of the favorable consequences of ANGPTL3 deficiency, various therapeutic strategies to target ANGPTL3 are currently in development, including a monoclonal antibody, an antisense oligonucleotide, and gene editing.

Exome sequencing of 2 siblings with combined hypolipidemia, characterized by extremely low plasma levels of LDL-C, HDL-C, and triglycerides, led to the identification of 2 loss-of-function variants in *ANGPTL3* as the cause. The siblings were compound heterozygotes for 2 distinct nonsense mutations (S17X and E129X) (23). Since the publication of this study, additional mutations in *ANGPTL3* have been identified in combined hypolipidemia subjects without *APOB* gene mutations (25–27).

ANGPTL3 AND CORONARY HEART DISEASE. Numerous animal models, such as inactivation of ANGPTL3 by an antibody (9), inhibition by an antisense oligonucleotide (ASO) (28), and genetic knockout of *Angptl3* (29), support that ANGPTL3 regulates plasma lipid levels. In humans, individuals bearing 2 nonsense mutations in *ANGPTL3* have familial combined hypolipidemia. The individuals with complete ANGPTL3 deficiency showed no evidence of coronary atherosclerotic plaque (30). Predicted loss-of-function (LOF) variants (nonsense, frameshift, and splice-site) in *ANGPTL3* are rare in the general population, found in only ~1 in 300 individuals in the United States, limiting the power of association analyses seeking to link LOF *ANGPTL3* variants to coronary artery disease risk (30). Accordingly, a mouse

model was used to functionally classify *ANGPTL3* missense variants as LOF versus neutral. WT human *ANGPTL3* and each *ANGPTL3* missense variant were reconstituted in the livers of *Angptl3* knockout mice by adenoviral expression. Missense variants were defined as LOF if they conferred <25% of WT activity as assessed by percent change in circulating triglyceride and cholesterol levels induced by heterologous gene expression. Eleven rare missense variants predicted to be damaging by 5 in silico prediction algorithms underwent functional validation in a mouse model, of which only 2 (p.Asp42Asn and p.Thr383Ser) were functionally validated as LOF. With the inclusion of nonsense, frameshift, and splice-site mutations along with the 2 LOF missense variants, there was a 34% lower risk of CHD among carriers of an *ANGPTL3* LOF mutation compared with non-carriers in a meta-analysis of 21,980 patients with CHD and 158,200 control individuals (30). Subsequently, a different group reported that individuals carrying LOF variants in *ANGPTL3* had a 41% lower risk of CHD than non-carriers (31).

ANGPTL3 AND LIPID-LOWERING THERAPY. In light of the favorable consequences of ANGPTL3 deficiency, an ASO inhibitor of *ANGPTL3* and a monoclonal antibody against ANGPTL3 have been advanced into clinical trials, with encouraging results so far (28,31) (**Central Illustration**). The group that developed the ASO have performed studies in a variety of mouse models and humans. They found that after administration of the ASO, hepatic *Angptl3* mRNA expression and plasma ANGPTL3 protein levels were significantly decreased in the mouse models they tested, including WT C57BL/6 mice, low-density lipoprotein receptor (LDLR) knockout mice($Ldlr^{-/-}$), double-knockout mice ($Apoc3^{-/-}$ and $Ldlr^{-/-}$), heterozygous mice ($Apoc3^{+/-}$ and $Ldlr^{-/-}$), mice with diet-induced obesity, and mice overexpressing human apolipoprotein C-III. The ASO decreased only triglyceride levels, not LDL-C or HDL-C, in C57BL/6 mice on standard chow, whereas in various hypercholesterolemic mouse models, the ASO resulted in reductions in levels of triglycerides (35% to 85%), LDL-C (7% to 64%), and HDL-C (3% to 23%). In addition, the ASO decreased liver triglyceride secretion and accumulation and improved insulin sensitivity, measured by means of intraperitoneal glucose tolerance and insulin tolerance testing in mice with diet-induced obesity. The ASO also slowed the progression of atherosclerosis in LDLR knockout mice.

Subsequently, a randomized placebo-controlled phase 1 clinical trial of an *ANGPTL3* ASO was conducted (28). Forty-four healthy human participants were randomly assigned to receive subcutaneous injections of the ASO or a placebo in a single dose or multiple doses. Among the single-dose groups at day 15, the investigators observed lower levels of ANGPTL3 protein, triglycerides, very low-density lipoprotein cholesterol, non-HDL cholesterol, and total cholesterol in the ASO group compared with placebo group. However, these differences were not significant, probably due to the small sizes of the groups (N = 3 for each group). Among the multiple-dose groups, they observed dose-dependent reductions of ANGPTL3 protein, triglycerides, non-HDL cholesterol, and apolipoprotein C-III in the ASO groups than in the placebo group.

Another group developed a fully human monoclonal antibody with high affinity for ANGPTL3. Intravenous administration of the antibody to normal C57BL/6 mice decreased plasma triglyceride levels by ≥50% and increased the LPL activity (9). Chronic administration of the antibody to dyslipidemic C57BL/6 mice reduced triglyceride, LDL-C, and HDL-C levels in the circulation without any changes in the triglyceride content of the liver, adipose, or heart. The investigators extended their observations to non-human primates by assessing the effect of the antibody on circulating lipid levels in cynomolgus monkeys (9). The antibody produced robust reductions in circulating triglycerides and non-HDL cholesterol in a dose-dependent way. It did not alter the plasma levels of LDL-C, perhaps due to those levels being low at baseline. The investigators also reported that inhibition of ANGPTL3 by the antibody could significantly decrease atherosclerotic lesion size compared to a control antibody in a mouse model of atherosclerosis (31).

A randomized placebo-controlled phase I clinical trial was performed to assess the safety, side effect profile, and pharmacodynamics of the antibody (31). A total of 83 healthy human volunteers with mildly to moderately elevated levels of triglycerides or LDL-C entered a single-ascending-dose trial. The antibody caused dose-dependent reductions in triglyceride levels of up to 76% and LDL-C levels of up to 23%. In addition, a single-group, open-label clinical trial of the antibody was conducted with 9 patients with homozygous familial hypercholesterolemia (hoFH). They received the antibody for 4 weeks, and their LDL-C levels were decreased by ~50% at week 4, although the patients were already taking aggressive lipid-lowering therapy (32).

***ANGPTL3* AND THERAPEUTIC GENE EDITING.** Another approach to target *ANGPTL3* is via gene

editing to induce permanent LOF mutations in vivo (**Central Illustration**). Since the first report of successful use in mammalian cells in 2013, CRISPR-Cas9 technology has emerged as a promising gene editor for therapeutic applications due to its efficiency and ease of use (33).

CRISPR-Cas9 introduces a double-strand DNA break at a desired site in the genome. This activates endogenous DNA repair pathways, either nonhomologous end-joining (NHEJ) or homology-directed repair (HDR), to fix the break (34). NHEJ is the default repair pathway in all cells, in which the free ends from the DNA break are reconnected. However, NHEJ is an error-prone process and results in introduction of insertions or deletions (indels) at the site of the break. NHEJ can introduce frameshift mutations into a targeted gene, thereby disrupting the gene. By contrast, the cell can accurately repair a DNA break through HDR, which occurs only in proliferating cells. HDR uses a template DNA strand to achieve high-fidelity repair, and if a repair template has matching sequence to the site of the break but also has a custom-made DNA mutation, the mutation can be introduced into the genome. However, introducing a specific mutation at the site with HDR is usually inefficient, and the efficiency in vivo in adult animals is very low (<1%), which limits its use to correct a disease-causing mutation (35). Another major concern about using a gene editor is that it might also cleave the genome at other sites and cause off-target mutations.

To circumvent these problems, CRISPR-Cas9 has been adapted so that it can directly alter specific nucleotides in the DNA sequence without generating double-strand breaks and without the need for a repair template—a phenomenon known as base editing (36-40). A fusion protein with a catalytically impaired Cas9 protein and a cytosine deaminase domain adapted from an RNA-editing or DNA-editing enzyme confers the ability to convert cytosine bases at the CRISPR-Cas9 target site into thymine bases.

The use of base editor 3 (BE3) successfully introduced LOF *Angptl3* mutations into liver cells in mice (41). The investigators first screened potential sites of base-edited nonsense mutations in *Angptl3* in Neuro-2a cells and identified high BE3 activity at the codon Gln-135 site. Then they produced an adenoviral vector expressing BE3 targeting *Angptl3* Gln-135 and injected the vector into C57BL/6J mice. This resulted in significantly reduced plasma ANGPTL3, triglyceride, and total cholesterol levels (49%, 31%, and 19%, respectively). In hyperlipidemic LDLR knockout mice, even larger effects were observed. After treatment, triglycerides and cholesterol were reduced by 56% and 51%, respectively. Overall, this proof-of-concept study showed the ability to efficiently introduce LOF mutations in dyslipidemia-associated genes in vivo with significant lipid-lowering effects.

Several aspects make ANGPTL3 an attractive target for gene editing. First, naturally occurring LOF mutations in *ANGPTL3* protect against coronary artery disease without causing serious adverse health consequences (30,31), even in the homozygous or compound heterozygous state (i.e., full knockout of gene function) (23,30). Second, ANGPTL3 is primarily expressed in hepatocytes and secreted into the bloodstream. The liver is an ideal organ for in vivo gene editing because of its accessibility for various delivery methods. Lastly, inhibition of *ANGPTL3* requires only the introduction of inactivating mutations, which is easier to achieve than precisely correcting a specific gene mutation.

Will in vivo gene editing approaches translate into the clinic and provide a potential preventive strategy for CHD in humans? The primary benefit of in vivo gene editing is that it could ultimately yield a 1-shot, long-term therapy that would permanently modify a target gene, removing the need for repeated administration of drugs. Before consideration of translation into the clinic, ethical and regulatory challenges as well as technical issues must be addressed.

The first concern about in vivo gene editing from the scientific community has been the potential for off-target mutagenesis. It has the potential to introduce unanticipated mutations that cause oncogenesis, promoting a different disease than the 1 being treated. Second, unintended on-target mutagenesis requires more characterization before gene editing can be used as a therapy in humans because it causes irreversible genetic changes with possible serious adverse effects. Third, there might be the potential for toxicity or immune responses on delivery, and methods of safe delivery will need to be refined. Adeno-associated viruses are the preferred viral delivery vehicle compared with adenoviral vectors for use in humans because of safety concerns (42,43). However, the size limitation of each adeno-associated virus vector makes it challenging to deliver a gene editor, especially a base editor. A nonviral solution would be the use of lipid nanoparticles to deliver gene editing tools into hepatocytes (44,45).

Despite these challenges, *ANGPTL3* is a promising gene editing target for potential clinical translation.

The best candidates for first-in-human studies would be hoFH patients because they show limited response to current LDL-lowering therapies and the potential benefits might substantially outweigh the risks. With a demonstration of efficacy as well as safety in these selected patients, gene-editing therapies could then be considered for broader groups of patients at risk for CHD.

ADDRESS FOR CORRESPONDENCE: Dr. Kiran Musunuru, Department of Medicine and Department of Genetics, Cardiovascular Institute, Perelman School of Medicine at the University of Pennsylvania, 3400 Civic Center Boulevard, Building 421, 11-104 Smilow Center, Philadelphia, Pennsylvania 19104. E-mail: kiranmusunuru@gmail.com.

REFERENCES

1. Bonanni L, Cutolo A, Dalla Vestra M. Novel Approaches for the treatment of familial hypercholesterolemia. Exp Clin Endocrinol Diabetes 2016;124:583–7.

2. Robinson JG, Farnier M, Krempf M, et al. Efficacy and safety of alirocumab in reducing lipids and cardiovascular events. N Engl J Med 2015;372:1489–99.

3. Sabatine MS, Giugliano RP, Wiviott SD, et al. Efficacy and safety of evolocumab in reducing lipids and cardiovascular events. N Engl J Med 2015;372:1500–9.

4. Cannon CP, Blazing MA, Giugliano RP, et al. Ezetimibe added to statin therapy after acute coronary syndromes. N Engl J Med 2015;372:2387–97.

5. Sabatine MS, Giugliano RP, Keech AC, et al. Evolocumab and clinical outcomes in patients with cardiovascular disease. N Engl J Med 2017;376:1713–22.

6. Koishi R, Ando Y, Ono M, et al. Angptl3 regulates lipid metabolism in mice. Nat Genet 2002;30:151–7.

7. Shimizugawa T, Ono M, Shimamura M, et al. ANGPTL3 decreases very low density lipoprotein triglyceride clearance by inhibition of lipoprotein lipase. J Biol Chem 2002;277:33742–8.

8. Shimamura M, Matsuda M, Yasumo H, et al. Angiopoietin-like protein3 regulates plasma HDL cholesterol through suppression of endothelial lipase. Arterioscler Thromb Vasc Biol 2007;27:366–72.

9. Gusarova V, Alexa CA, Wang Y, et al. ANGPTL3 blockade with a human monoclonal antibody reduces plasma lipids in dyslipidemic mice and monkeys. J Lipid Res 2015;56:1308–17.

10. Mattijssen F, Kersten S. Regulation of triglyceride metabolism by Angiopoietin-like proteins. Biochim Biophys Acta 2012;1821:782–9.

11. Quagliarini F, Wang Y, Kozlitina J, et al. Atypical angiopoietin-like protein that regulates ANGPTL3. Proc Natl Acad Sci U S A 2012;109:19751–6.

12. Ono M, Shimizugawa T, Shimamura M, et al. Protein region important for regulation of lipid metabolism in angiopoietin-like 3 (ANGPTL3): ANGPTL3 is cleaved and activated in vivo. J Biol Chem 2003;278:41804–9.

13. Essalmani R, Susan-Resiga D, Chamberland A, et al. Furin is the primary in vivo convertase of angiopoietin-like 3 and endothelial lipase in hepatocytes. J Biol Chem 2013;288:26410–8.

14. Kersten S, Mandard S, Tan NS, et al. Characterization of the fasting-induced adipose factor FIAF, a novel peroxisome proliferator-activated receptor target gene. J Biol Chem 2000;275:28488–93.

15. González-Muniesa P, de Oliveira C, Pérez de Heredia F, Thompson MP, Trayhurn P. Fatty acids and hypoxia stimulate the expression and secretion of the adipokine ANGPTL4 (angiopoietin-like protein 4/fasting-induced adipose factor) by human adipocytes. J Nutrigenet Nutrigenomics 2011;4:146–53.

16. Yin W, Romeo S, Chang S, Grishin NV, Hobbs HH, Cohen JC. Genetic variation in ANGPTL4 provides insights into protein processing and function. J Biol Chem 2009;284:13213–22.

17. Sukonina V, Lookene A, Olivecrona T, Olivecrona G. Angiopoietin-like protein 4 converts lipoprotein lipase to inactive monomers and modulates lipase activity in adipose tissue. Proc Natl Acad Sci U S A 2006;103:17450–5.

18. Desai U, Lee EC, Chung K, et al. Lipid-lowering effects of anti-angiopoietin-like 4 antibody recapitulate the lipid phenotype found in angiopoietin-like 4 knockout mice. Proc Natl Acad Sci U S A 2007;104:11766–71.

19. Lichtenstein L, Mattijssen F, de Wit NJ, et al. Angptl4 protects against severe proinflammatory effects of saturated fat by inhibiting fatty acid uptake into mesenteric lymph node macrophages. Cell Metab 2010;12:580–92.

20. Fu Z, Yao F, Abou-Samra AB, Zhang R. Lipasin, thermoregulated in brown fat, is a novel but atypical member of the angiopoietin-like protein family. Biochem Biophys Res Commun 2013;430:1126–31.

21. Zhang R. Lipasin, a novel nutritionally-regulated liver-enriched factor that regulates serum triglyceride levels. Biochem Biophys Res Commun 2012;424:786–92.

22. Willer CJ, Sanna S, Jackson AU, et al. Newly identified loci that influence lipid concentrations and risk of coronary artery disease. Nat Genet 2008;40:161–9.

23. Musunuru K, Pirruccello JP, Do R, et al. Exome sequencing, ANGPTL3 mutations, and familial combined hypolipidemia. N Engl J Med 2010;363:2220–7.

24. Romeo S, Yin W, Kozlitina J, et al. Rare loss-of-function mutations in ANGPTL family members contribute to plasma triglyceride levels in humans. J Clin Invest 2009;119:70–9.

25. Martín-Campos JM, Roig R, Mayoral C, et al. Identification of a novel mutation in the ANGPTL3 gene in two families diagnosed of familial hypobetalipoproteinemia without APOB mutation. Clin Chim Acta 2012;413:552–5.

26. Noto D, Cefalù AB, Valenti V, et al. Prevalence of ANGPTL3 and APOB gene mutations in subjects with combined hypolipidemia. Arterioscler Thromb Vasc Biol 2012;32:805–9.

27. Pisciotta L, Favari E, Magnolo L, et al. Characterization of three kindreds with familial combined hypolipidemia caused by loss-of-function mutations of ANGPTL3. Circ Cardiovasc Genet 2012;5:42–50.

28. Graham MJ, Lee RG, Brandt TA, et al. Cardiovascular and metabolic effects of ANGPTL3 antisense oligonucleotides. N Engl J Med 2017;377:222–32.

29. Fujimoto K, Koishi R, Shimizugawa T, Ando Y. Angptl3-null mice show low plasma lipid concentrations by enhanced lipoprotein lipase activity. Exp Anim 2006;55:27–34.

30. Stitziel NO, Khera AV, Wang X, et al. ANGPTL3 deficiency and protection against coronary artery disease. J Am Coll Cardiol 2017;69:2054–63.

31. Dewey FE, Gusarova V, Dunbar RL, et al. Genetic and pharmacologic inactivation of ANGPTL3 and cardiovascular disease. N Engl J Med 2017;377:211–21.

32. Gaudet D, Gipe DA, Pordy R, et al. ANGPTL3 inhibition in homozygous familial hypercholesterolemia. N Engl J Med 2017;377:296–7.

33. Musunuru K. Genome editing: the recent history and perspective in cardiovascular diseases. J Am Coll Cardiol 2017;70:2808–21.

34. West SC. Molecular views of recombination proteins and their control. Nat Rev Mol Cell Biol 2003;4:435–45.

35. Yang Y, Wang L, Bell P, et al. A dual AAV system enables the Cas9-mediated correction of a metabolic liver disease in newborn mice. Nat Biotechnol 2016;34:334–8.

36. Komor AC, Kim YB, Packer MS, Zuris JA, Liu DR. Programmable editing of a target base in genomic DNA without double-stranded DNA cleavage. Nature 2016;533:420–4.

37. Nishida K, Arazoe T, Yachie N, et al. Targeted nucleotide editing using hybrid prokaryotic and vertebrate adaptive immune systems. Science 2016;353(6305). pii:aaf8729.

38. Ma Y, Zhang J, Yin W, Zhang Z, Song Y, Chang X. Targeted AID-mediated mutagenesis (TAM) enables efficient genomic diversification

in mammalian cells. Nat Methods 2016;13:1029–35.

39. Hess GT, Frésard L, Han K, et al. Directed evolution using dCas9-targeted somatic hypermutation in mammalian cells. Nat Methods 2016;13:1036–42.

40. Kim YB, Komor AC, Levy JM, Packer MS, Zhao KT, Liu DR. Increasing the genome-targeting scope and precision of base editing with engineered Cas9-cytidine deaminase fusions. Nat Biotechnol 2017;35:371–6.

41. Chadwick AC, Evitt NH, Lv W, Musunuru K. Reduced blood lipid levels with in vivo CRISPR-Cas9 base editing of ANGPTL3. Circulation 2018;137:975–7.

42. Muruve DA. The innate immune response to adenovirus vectors. Hum Gene Ther 2004;15:1157–66.

43. Gregory SM, Nazir SA, Metcalf JP. Implications of the innate immune response to adenovirus and adenoviral vectors. Future Virol 2011;6:357–74.

44. Yin H, Song CQ, Dorkin JR, et al. Therapeutic genome editing by combined viral and non-viral delivery of CRISPR system components in vivo. Nat Biotechnol 2016;34:328–33.

45. Wang M, Zuris JA, Meng F, et al. Efficient delivery of genome-editing proteins using bioreducible lipid nanoparticles. Proc Natl Acad Sci U S A 2016;113:2868–73.

KEY WORDS coronary artery disease, genetics, lipids